

The synthesis and ion-exchange
chemistry of vanadium doped
natisite and paranatisite.

By

Phillippa Patterson

A thesis submitted in partial fulfilment for the
requirements for the degree of MSc (by Research)
at the University of Central Lancashire.

May 2018

STUDENT DECLARATION FORM



Concurrent registration for two or more academic awards

I declare that while registered as a candidate for the research degree, I have not been a registered candidate or enrolled student for another award of the University or other academic or professional institution

Material submitted for another award

I declare that no material contained in the thesis has been used in any other submission for an academic award and is solely my own work

Collaboration

Where a candidate's research programme is part of a collaborative project, the thesis must indicate in addition clearly the candidate's individual contribution and the extent of the collaboration. Please state below:

Signature of Candidate:

A handwritten signature in black ink, appearing to be "A. B. B.", written over a horizontal line.

Type of Award

MSc (by Research)

School

School of Physical Sciences and Computing

Abstract

With 440 commercial nuclear reactors in use globally, nuclear energy contributes to 11 % of the world's energy demands^[1]. Like most forms of energy, nuclear energy generates waste. To help manage contaminated aqueous streams generated from the nuclear cycle, i.e., reactor primary coolant and the clean-up of spent fuel systems, ion exchange media are being utilised^[2].

This thesis focuses upon the synthesis of vanadium-paranatisite and vanadium-natisite, inorganic zeotypes^[3], which have not been previously reported. Optimisation of the synthesis showed that with an increased percentage of vanadium the time taken for the progressive transformation of vanadium-paranatisite to vanadium-natisite increased. 5 %-vanadium-paranatisite and natisite formed during 7 and 72 hours of synthetic heating, whilst 10 %-vanadium-paranatisite and natisite formed during 72 and 288 hours, respectively. Increasing the percentage of vanadium also showed to increase the crystallinity of the vanadium-paranatisite framework, with attempts to form Ti-paranatisite failing.

The respective abilities of vanadium-paranatisite and vanadium-natisite to remove ions commonly found within nuclear waste such as strontium, cesium, cobalt, cerium (inactive surrogate for plutonium) and neodymium (inactive surrogate for uranium) was also investigated. The results showed that both vanadium-paranatisite and vanadium-natisite have the potential to act as ion exchange media for the removal of radioactive ions from aqueous effluent within the nuclear industry.

Vanadium-paranatisite and vanadium-natisite frameworks showed higher affinities towards strontium and cobalt. During ion exchanges involving

vanadium-paranatisite, up to 32 % (± 0.62) and 29 % (± 0.82) of strontium and cobalt ions respectively, were exchanged during a 24 hour period. Ion exchanges involving vanadium-natisite showed that up to 30 % (± 0.53) and 28 % (± 0.26) of strontium and cobalt ions respectively, were exchanged in the same 24 hour period.

Further to this, vanadium-paranatisite frameworks showed increased affinities for all the ions tested when compared with vanadium-natisite. A plausible reason for the increased affinity shown by vanadium-paranatisite could be due to the structure. Unlike natisite, which is a layered titanium silicate, the framework of paranatisite is less regimented, with exchangeable cations fragmented throughout the framework.

Acknowledgments

I would first like to thank Dr. Jennifer Readman without whom, this project would not have started. Her expertise, ensuring I got on the right train to conferences and got home safely in one piece is of much thanks and shows her willingness for her students to do well.

To Prof. Harry Eccles, who sat down with me on a weekly basis to answer all my queries upon waste management and treatment as well as reading my thesis. His knowledge and expertise around the subject is to be admired and respected.

A further thanks to Reece Hall, whom throughout this project and the entirety of my time at UCLan, has took me under his wing and ensured that every 'quick question' I asked was answered. From teaching me how to use the analytical equipment to ensuring I was ok on trips, his patience to help is and will always be deeply appreciated.

To Nazesh Sajjad, my greatest thanks and apologies for the numerous questions and texts on structural refinements. Without your help there is no doubt in my mind that I would still be stuck trying to refine my structures. For also bearing with me on trips without any choice and making sure that I got on the right train home is of appreciation.

Finally, and by no means least, to the analytical staff, Jim Donnelley, Tamar Gracia, Peter Bentley and Sameera Mahroof. The analytical staff have been there daily, showing continual patience and vast expertise throughout my entire time at UCLan. Answering the same questions and fixing the same problems so that the results of this thesis and coursework throughout the years could be obtained and analysed.

List of Abbreviations

UK	United Kingdom
ONR	Office of Nuclear Regulations
EA	Environmental Agency
SPEA	Scottish Environmental Agency
NRW	Natural Resources Wales
DFT	Department for Transport
NDA	National Decommissioning Agency
SLC	Site Licensing Companies
HLW	High-Level Waste
ILW	Intermediate-Level Waste
LLW	Low-Level Waste
GDF	Geological Disposal Facilities
PUREX	Plutonium Uranium Redox Extraction
THORP	Thermal Oxide Reprocessing Plant
Magnox	Magnesium Alloy Graphite Moderated Gas Cooled Uranium Oxide
GAEX	Group Actinide Extraction Process
EU	European Union
AGR	Advanced Gas-cooled Reactor
PWR	Pressurised Water Reactor
MOX	Mixed Oxide
SIXEP	Site Ion Exchange Plant
IZA	International Zeolite Association
3 D	Three Dimensional

S4R	Single Four Ring
S6R	Single Six Ring
D4R	Double Four-Ring
D6R	Double Six-Ring
ZSM-5	Zeolite Socony Mobil-5
MASWEP	Medium Active Waste Export Plant
Silicotitanate	CST
ETS-10	Engelhard Titanium Silicate 10
XRD	X-Ray Diffraction
XRF	X-Ray Fluorescence
ICP-MS	Inductively Coupled Plasma- Mass Spectroscopy
SEM	Scanning Electron Microscopy
EDX	Energy Dispersive X-Ray Spectroscopy
R_{wp}	Weighted Profile R-Factor
R_{exp}	Expected R-Factor
ICP-OES	Inductively Coupled Plasma-Optical Emission Spectroscopy
ICP	Inductively Coupled Plasma
Ti-Paranatisite	Titanium-Paranatisite
Ti-Natisite	Titanium-Natisite
Occ	Occupancy
Beq	Isotropic Temperature Factor
Na1/ Na2/ Na3	1 st / 2 nd / 3 rd Sodium Environment
O1/ O2/ O3/ O4	1 st / 2 nd / 3 rd / 4 th Oxygen Environment
Ti1/ Ti2	1 st / 2 nd Titanium Environment

Si1

1st Silicon Environment

M1

Method 1

M2

Method 2

List of Equations

Equation 1: General Zeolite Formula

Equation 2: Path Difference between the Waves Reflected at Points A and B

Equation 3: Bragg's Law

Equation 4: Intensity Factor

Equation 5: Structure Factor

List of Figures

Figure 1 : Outline of the way in which Radioactive Waste Generated from the Nuclear Industry, in the Public Sector, is Dealt with.....	Pg. 2
Figure 2 : Diagram of Alpha, Beta and Gamma Penetration Capabilities.....	Pg. 3
Figure 3 : A Chart to Show the Composition of Radioactive Waste.....	Pg. 5
Figure 4 : Schematic Diagram of Open and Closed Fuel Cycles...	Pg. 7
Figure 5 : Illustration of Primary Building Blocks of Zeolites.....	Pg. 14
Figure 6 : Illustration of Secondary Building Blocks of Zeolites Forming Single Four Ring (S4R) and Single Six Ring (S6R) Structures.....	Pg. 14
Figure 7 : Illustration of Double Four Ring Structures (D4R) Forming β Cages and Double Six Ring (D6R) Structures Forming α Cages.....	Pg. 15
Figure 8 : Structural Representation of Clinoptilolite.....	Pg. 19
Figure 9 : Structural Representation of Sitinakite.....	Pg. 23
Figure 10: Structural Representation of Engelhard Titanium Silicate 10.....	Pg. 25
Figure 11: Structural Representation of Paranatisite.....	Pg. 26
Figure 12: Structural Representation of Natisite	Pg. 27
Figure 13: Illustration of Bragg's Law.....	Pg. 30
Figure 14: Illustration of the Production of Secondary X-rays from L and M Shells.....	Pg. 34

Figure 15: Schematic Diagram of the Inductively Coupled Plasma-Mass Spectroscopy Technique.....	Pg. 37
Figure 16: X-Ray Diffraction Pattern of 10 %-Vanadium Doping Following 7 Day Synthesis.....	Pg. 43
Figure 17: Stack View of X-Ray Diffraction Patterns Following the Successive Transformation of 10 %-Vanadium-Paranatisite to 10 %-Vanadium-Natisite.....	Pg. 45
Figure 18: Close Stack View of X-Ray Diffraction Patterns Following the Successive Transformation of 10 %-Vanadium-Paranatisite to 10 %-Vanadium-Natisite.....	Pg. 46
Figure 19: Peak Analysis at 32.00 ° - 33.00 ° Following the Successive Transformation of 10 %-Vanadium-Paranatisite to 10 %-Vanadium-Natisite.....	Pg. 47
Figure 20: SEM Images of Synthesised Material following 3-12 Day Synthesis.....	Pg. 50
Figure 21: Overlay of Amorphous and Crystalline 5 %-Vanadium-Paranatisite XRD Patterns with known Ti-Paranatisite Literature.....	Pg. 54
Figure 22: Overlay of 10 %-Vanadium-Paranatisite XRD Pattern with known Ti-Paranatisite Literature.....	Pg. 56
Figure 23: Final Rietveld Fit of 10 %-Vanadium-Paranatisite.....	Pg. 60
Figure 24: Ti1 Octahedrally Coordinated to O2 and O3 Atoms.....	Pg. 61
Figure 25: Ti2 Coordinated in a Square Pyramidal Environment to O1 and O4 Atoms.....	Pg. 61

Figure 26: Si1 Coordinated in a Tetrahedrally Coordinated Environment to O1 and O2 Atoms.....	Pg. 62
Figure 27: Na1 in a Six Coordinated Environment to O2 and O3 Atoms.....	Pg. 62
Figure 28: Na2 Coordinated in an Octahedral Environment to O1 and O2 Atoms.....	Pg. 63
Figure 29: Na3 Six Coordinated Environment to O1, O2, O3 and O4 Atoms.....	Pg. 63
Figure 30: Overall Structure of 10 %-Vanadium-Paranatisite.....	Pg. 64
Figure 31: SEM Images of Vanadium-Paranatisite.....	Pg. 67
Figure 32: Overlay of XRF Spectra for 5 % and 10 %-Vanadium-Paranatisite.....	Pg. 70
Figure 33: Overlay of Phase A M1 5 %-Vanadium-Natisite XRD Pattern with known Ti-Natisite Literature.....	Pg. 73
Figure 34: Overlay of Phase B M2 5 %-Vanadium-Natisite XRD Pattern with known Ti-Natisite Literature.....	Pg. 75
Figure 35: Overlay of Phase C M2 10 %-Vanadium-Natisite XRD Pattern with known Ti-Natisite Literature.....	Pg. 77
Figure 36: Final Rietveld Fit of Phase C M2 10 %-Vanadium-Natisite.....	Pg. 82
Figure 37: Ti1 Coordinated in a Square Pyramidal Environment with O1 and O2 Atoms.....	Pg. 83
Figure 38: Si1 Coordinated in a Tetrahedral Environment to O1 Atoms.....	Pg. 83

Figure 39: Na1 Coordinated in an Octahedral Environment with O1 and O2 Atoms.....	Pg. 84
Figure 40: Overall Structure of 10 %-Vanadium-Natisite.....	Pg. 84
Figure 41: SEM Images of Vanadium-Natisite.....	Pg. 87
Figure 42: XRF Spectra for 5 and 10 %-Vanadium-Natisite Phases Aa, Ab, B and C.....	Pg. 91
Figure 43: Stack View of XRD Patterns of 5 %-Vanadium-Paranatisite, Cobalt and Cesium Ion Exchanged Materials.....	Pg. 102
Figure 44: Stack View of XRD Patterns of 10 %-Vanadium-Paranatisite, Strontium, Cobalt and Cesium Ion Exchanged Materials.....	Pg. 104
Figure 45: Stack View of XRD Patterns of 5 %-Vanadium-Paranatisite, Strontium, Cerium and Neodymium Ion Exchanged Materials.....	Pg. 107
Figure 46: Stack View of XRD Patterns of 10 %-Vanadium-Paranatisite, Cerium and Neodymium Ion Exchanged Materials.....	Pg. 108
Figure 47: SEM Images of 5 %-Vanadium-Paranatisite, Cesium, Cerium, Cobalt, Strontium and Neodymium Ion Exchanged Material.....	Pg. 114
Figure 48: SEM Images of 10 %-Vanadium-Paranatisite, Cesium, Cerium, Cobalt, Strontium and Neodymium Ion Exchanged Material.....	Pg. 115

Figure 49: EDX Spectrum of 10 %-Vanadium-Paranatisite-Cesium Ion Exchanged Material.	Pg. 116
Figure 50: EDX Spectrum of 10 %-Vanadium-Paranatisite-Cerium Ion Exchanged Material.....	Pg. 117
Figure 51: EDX Spectrum of 10 %-Vanadium-Paranatisite-Cobalt Ion Exchanged Material.....	Pg. 118
Figure 52: EDX Spectrum of 10 %-Vanadium-Paranatisite- Neodymium Ion Exchanged Material.....	Pg. 119
Figure 53: EDX Spectrum of 10 %-Vanadium-Paranatisite- Strontium Ion Exchanged Material.....	Pg. 120
Figure 54: Stack View of XRF Spectra of 10 %-Vanadium- Paranatisite, Cesium, Cerium, Cobalt, Strontium and Neodymium Ion Exchanged Material.....	Pg. 122
Figure 55: Stack View of XRD Patterns of 5 %-Vanadium-Natisite, Strontium-Cobalt and Cesium Ion Exchanged Material..	Pg. 128
Figure 56: Stack View of XRD Patterns of 10 %-Vanadium- Natisite, Strontium-Cobalt and Cesium Ion Exchanged Material.....	Pg. 130
Figure 57: Stack View of XRD Patterns of 5 %-Vanadium-Natisite, Cerium and Neodymium Ion Exchanged Material.....	Pg. 133
Figure 58: Stack View of XRD Patterns of 10 %-Vanadium- Natisite, Cerium and Neodymium Ion Exchanged Material.....	Pg. 134

Figure 59: SEM Images of 5 %-Vanadium-Natisite, Cesium, Cerium, Cobalt, Strontium and Neodymium Ion Exchanged Material.....	Pg. 140
Figure 60: SEM Images of 10 %-Vanadium-Natisite, Cesium, Cerium, Cobalt, Strontium and Neodymium Ion Exchanged Material.....	Pg. 141
Figure 61: EDX Spectrum of 10 %-Vanadium-Natisite-Cesium Ion Exchanged Material.....	Pg. 142
Figure 62: EDX Spectrum of 10 %-Vanadium-Natisite-Cerium Ion Exchanged Material.....	Pg. 143
Figure 63: EDX Spectrum of 10 %-Vanadium-Natisite-Cobalt Ion Exchanged Material.....	Pg. 144
Figure 64: EDX Spectrum of 10 %-Vanadium-Natisite-Neodymium Ion Exchanged Material.....	Pg. 145
Figure 65: EDX Spectrum of 10 %-Vanadium-Natisite-Strontium Ion Exchanged Material.....	Pg. 146
Figure 66: Stack View of XRF Spectra of 10 %-Vanadium-Natisite, Cesium, Cerium, Cobalt, Strontium and Neodymium Ion Exchanged Material.....	Pg. 148
Figure 67: Comparative Graph of 5 %-Vanadium-Paranatisite, 10 %-Vanadium-Paranatisite, 5 %-Vanadium-Natisite and 10 %-Vanadium-Natisite.....	Pg. 151

List of Tables

Table 1 : A List of Countries Operating on Open and Closed Fuel Cycles.....	Pg. 7
Table 2 : Typical Composition of the Spent Nuclear Fuel generated from Light Water Reactors.....	Pg. 11
Table 3 : Radioisotopes Present after 4.5 % Enrichment, with a Burn-Up of 45 GWd/t U after 8 Years of Cooling.....	Pg. 11
Table 4 : Characteristic Wavelengths of Cesium, Cerium, Cobalt, Neodymium and Strontium.....	Pg. 36
Table 5 : Synthesis Conditions and Products After Heating the Synthesis Gel for 3 - 12 Days.....	Pg. 43
Table 6 : Percentage Composition of Vanadium-Paranatisite and Vanadium-Natisite within Mix Phased Synthesised Batches.....	Pg. 49
Table 7 : Synthetic Conditions for the Vanadium-Paranatisite and Vanadium-Natisite Following the M1 and M2 Methods.....	Pg. 52
Table 8 : Refined Atomic Coordinates for 10 %-Vanadium-Paranatisite.....	Pg. 58
Table 9 : Refined Bond Lengths for 10 %-Vanadium-Paranatisite.....	Pg. 59
Table 10: Refined Bond Angles for 10 %-Vanadium-Paranatisite.....	Pg. 59
Table 11: Refined Lattice Parameters and Refinement Statistics for 10 %-Vanadium-Paranatisite.....	Pg. 60

Table 12: Bond Lengths of Ti-Paranatisite, 5 %-Vanadium-Paranatisite and 10 %-Vanadium-Paranatisite and the Difference in Lengths between 5 %-Vanadium-Paranatisite and 10 %-Vanadium-Paranatisite.....	Pg. 66
Table 13: Elemental Composition of 5 % and 10 %-Vanadium-Paranatisite.....	Pg. 68
Table 14: List of Characteristic XRF Emission Lines for Silicon, Titanium and Vanadium within 10 %-Vanadium-Paranatisite.....	Pg. 69
Table 15: Synthetic Conditions for Vanadium-Natisite Following the M1 and M2 Methods.....	Pg. 79
Table 16: Refined Atomic Coordinated for Phase C M2 10 %-Vanadium-Natisite.....	Pg. 80
Table 17: Refined Bond Lengths for Phase C M2 10 %-Vanadium-Natisite.....	Pg. 81
Table 18: Refined Bond Angles for Phase C M2 10 %-Vanadium-Natisite.....	Pg. 81
Table 19: Refined Lattice Parameters and Refinement Statistics for Phase C M2 10 %-Vanadium-Natisite.....	Pg. 82
Table 20: Elemental Composition of Phase Aa, Phase Ab, Phase B and Phase C.....	Pg. 89
Table 21: List of Characteristic XRF Emission Lines for Silicon, Titanium and Vanadium within Vanadium-Natisite.....	Pg. 90
Table 22: Refined Lattice Parameters for Phase Aa, Phase Ab, Phase B and Phase C.....	Pg. 95

Table 23:	Refined Bond Lengths for Phase Aa, Phase Ab, Phase B and Phase C.....	Pg. 95
Table 24:	Percentage Uptake from 24 Hour Ion Exchange for Vanadium-Paranatisite.....	Pg. 98
Table 25:	Peak Analysis of 5 %-Vanadium-Paranatisite-Cesium and Cobalt Ion Exchanged Material.....	Pg. 101
Table 26:	Peak Analysis of 10 %-Vanadium-Paranatisite-Cesium, Cobalt and Strontium Ion Exchanged Material.....	Pg. 103
Table 27:	Refined Lattice Parameters for 5 %-Vanadium-Paranatisite, Cesium, Cerium, Cobalt, Neodymium and Strontium.....	Pg. 110
Table 28:	Refined Lattice Parameters for 10 %-Vanadium-Paranatisite, Cesium, Cerium, Cobalt, Neodymium and Strontium.....	Pg. 112
Table 29:	Elemental Composition of Vanadium-Paranatisite-Cesium Ion Exchanged Material.....	Pg. 116
Table 30:	Elemental Composition of Vanadium-Paranatisite-Cerium Ion Exchanged Material.....	Pg. 117
Table 31:	Elemental Composition of Vanadium-Paranatisite-Cobalt Ion Exchanged Material.....	Pg. 118
Table 32:	Elemental Composition of Vanadium-Paranatisite-Neodymium Ion Exchanged Material.....	Pg. 119
Table 33:	Elemental Composition of Vanadium-Paranatisite-Strontium Ion Exchanged Material.....	Pg. 120

Table 34:	List of Characteristic XRF Emission Lines for 10 %-Vanadium-Paranatisite-Cesium, Cerium, Cobalt, Neodymium and Strontium Ion Exchanged Material.....	Pg. 121
Table 35:	Ion Percentage Uptake from 24 Hour Ion Exchange with Regards to Vanadium-Natisite.....	Pg. 125
Table 36:	Peak Analysis of 5 %-Vanadium-Natisite-Cesium, Cobalt and Strontium Ion Exchanged Material.....	Pg. 127
Table 37:	Peak Analysis of 10 %-Vanadium-Natisite-Cesium, Cobalt and Strontium Ion Exchanged Material.....	Pg. 129
Table 38:	Refined Lattice Parameters for 5 %-Vanadium-Natisite-Cesium, Cerium, Cobalt, Neodymium and Strontium.....	Pg. 136
Table 39:	Refined Lattice Parameters for 10 %-Vanadium-Natisite-Cesium, Cerium, Cobalt, Neodymium and Strontium.....	Pg. 138
Table 40:	Elemental Composition of Vanadium-Natisite-Cesium Ion Exchanged Material.....	Pg. 142
Table 41:	Elemental Composition of Vanadium-Natisite-Cerium Ion Exchanged Material.....	Pg. 143
Table 42:	Elemental Composition of Vanadium-Natisite-Cobalt Ion Exchanged Material.....	Pg. 144
Table 43:	Elemental Composition of Vanadium-Natisite-Neodymium Ion Exchanged Material.....	Pg. 145
Table 44:	Elemental Composition of Vanadium-Natisite-Strontium-Ion Exchanged Material.....	Pg. 146

Table 45: List of Characteristic XRF Emission Lines for 10 %-
Vanadium-Paranatisite-Cesium, Cerium, Cobalt,
Neodymium and Strontium Ion Exchanged Material..... Pg. 147

Contents Page

Student Declaration	I
Abstract	II
Acknowledgements	IV
List of Abbreviations	V
List of Equations	VIII
List of Figures	IX
List of Tables	XV

Chapter One- Introduction

1.0.0.0: Background.....	1
1.1.0.0: Radioactive Waste Material.....	2
1.2.0.0: Radioactivity.....	4
1.3.0.0: Open and Closed Fuel Cycles.....	6
1.4.0.0: Generation of Nuclear Waste.....	10
1.5.0.0: Treatment of Nuclear Waste.....	12

Chapter Two- Zeolites

2.0.0.0: Composition of Zeolites.....	13
2.1.0.0: Structure of Zeolites.....	14
2.2.0.0: Applications of Zeolites.....	16
2.2.1.0: Adsorption.....	16
2.2.2.0: Ion Exchange.....	17
2.2.3.0: Site Ion Exchange Plant (SIXEP) Process.....	18

2.3.0.0:	Zeotypes.....	20
	2.3.1.0: Titanium Silicates	20
2.4.0.0:	Titanium Silicates and their Use/Potential in Industry....	22
	2.4.1.0: The IONSIV Family.....	22
	2.4.2.0: Engelhard Titanium Silicate 10 (ETS-10).....	24
	2.4.3.0: Paranatisite.....	26
	2.4.4.0: Natisite.....	27
2.5.0.0:	Aims of Research.....	28

Chapter Three- Characterisation Techniques

3.1.0.0:	X-Ray Diffraction (XRD).....	29
3.2.0.0:	Powder Analysis.....	32
	3.2.1.0: Pawley Refinements.....	32
	3.2.2.0: Rietveld Refinements.....	33
3.3.0.0:	X-Ray Fluorescence (XRF).....	34
3.4.0.0:	Inductively Coupled Plasma-Mass Spectroscopy (ICP-MS).....	35
3.5.0.0:	Scanning Electron Microscopy (SEM).....	38

Chapter Four- Optimisation of Hydrothermal Synthesis

4.0.0.0:	Synthesis of Vanadium-Natisite.....	39
	4.0.1.0: Method 1 (M1): Synthesis Following 'Hydrothermal Synthesis and Successive	

Transformation of Paranatisite into Natisite,' Kostov-Kytin <i>et al.</i>	39
4.0.1.1: Method 2 (M2): Synthesis following 'Crystallization of Sodium Titanium Silicate with Sitinakite Topology: Evolution from the Sodium Nonatitante Phase,' Dimitri. G. Medvedev <i>et al.</i>	40
4.0.1.2: Results and Discussion of the Synthetic Methods.....	41
4.0.2.0: X-Ray Diffraction Analysis.....	42
4.0.3.0: Rietveld Refinements.....	48
4.0.4.0: SEM Analysis.....	49
4.0.5.0: Conclusion of Mix Phased Synthesis.....	51
4.1.0.0: Characterisation of Vanadium-Paranatisite.....	53
4.1.1.0: X-Ray Diffraction Analysis of Vanadium-Paranatisite....	53
4.1.1.1: 5 %-Vanadium-Paranatisite.....	53
4.1.1.2: 10 %-Vanadium-Paranatisite.....	55
4.1.1.3: Results and Discussion of the Synthetic Methods.....	57
4.1.2.0: Rietveld Refinements.....	58
4.1.3.0: Structural Determination.....	61
4.1.3.1: Titanium/Vanadium Environments.....	61
4.1.3.2: Silicon Environments.....	62
4.1.3.3: Sodium Environments.....	62
4.1.3.4: 10 %-Vanadium-Paranatisite Overall Structure.....	64

4.1.3.5:	Results and Discussion of Paranatisite, 5 %- Vanadium-Paranatisite and 10 %-Vanadium- Paranatisite.....	65
4.1.4.0:	Vanadium-Paranatisite Particle Morphology.....	67
4.1.5.0:	EDX Analysis.....	68
4.1.6.0:	XRF Analysis.....	69
4.1.7.0:	ICP-MS Analysis.....	71
4.1.8.0:	Conclusion of the Synthesis of Vanadium-Paranatisite.	71
4.2.0.0:	Characterisation of Vanadium-Natisite.....	72
4.2.1.0:	X-Ray Diffraction Analysis of Vanadium-Natisite.....	72
	4.2.1.1: Phase Aa M1 5 %-Vanadium-Natisite.....	72
	4.2.1.2: Phase B M2 5 %-Vanadium-Natisite.....	74
	4.2.1.3: Phase C M2 10 %-Vanadium-Natisite.....	76
	4.2.1.4: Results and Discussion of the Synthetic Methods.....	78
4.2.2.0:	Rietveld Refinements.....	80
4.2.3.0:	Structural Determination.....	83
	4.2.3.1: Titanium/Vanadium Environments.....	83
	4.2.3.2: Silicon Environments.....	83
	4.2.3.3: Sodium Environments.....	84
	4.2.3.4: Overall Structure of 10 %-Vanadium-Natisite...	84
4.2.4.0:	Vanadium-Natisite Morphology.....	85
4.2.5.0:	EDX Analysis.....	88
4.2.6.0:	XRF Analysis.....	90

4.2.7.0:	ICP-MS Analysis.....	92
4.2.8.0:	Conclusion of the Synthesis of Vanadium-Natisite.....	92

Chapter Five- Analysis of Vanadium-Paranatisite and Vanadium-Natisite Ion Exchange Capabilities

5.0.0.0:	Experimental Procedure.....	96
5.1.0.0:	Vanadium-Paranatisite Ion Exchange Analysis.....	97
5.1.1.0:	ICP-MS Analysis.....	97
5.1.2.0:	X-Ray Diffraction Analysis.....	99
5.1.3.0:	Lattice Refinement Analysis Via Pawley Fit.....	109
	5.1.3.1: 5 %-Vanadium-Paranatisite.....	109
	5.1.3.2: 10 %-Vanadium-Paranatisite.....	111
5.1.4.0:	SEM Analysis.....	113
5.1.5.0:	EDX Analysis.....	116
	5.1.5.1: Cesium Analysis.....	116
	5.1.5.2: Cerium Analysis.....	117
	5.1.5.3: Cobalt Analysis.....	118
	5.1.5.4: Neodymium Analysis.....	119
	5.1.5.5: Strontium Analysis.....	120
5.1.6.0:	XRF Analysis.....	121
5.1.7.0:	Conclusion of Vanadium-Paranatisite Ion Exchange Capabilities.....	123
5.2.0.0:	Vanadium-Natisite Ion Exchange Analysis.....	125

5.2.1.0:	ICP-MS Analysis.....	125
5.2.2.0:	XRD Analysis.....	126
5.2.3.0:	Lattice Refinements via Pawley Fits.....	135
	5.2.3.1: 5 %-Vanadium-Natisite.....	135
	5.2.3.2: 10 %-Vanadium-Natisite.....	137
5.2.4.0:	SEM Analysis.....	139
5.2.5.0:	EDX Analysis.....	142
	5.2.5.1: Cesium Analysis.....	142
	5.2.5.2: Cerium Analysis.....	143
	5.2.5.3: Cobalt Analysis.....	144
	5.2.5.4: Neodymium Analysis.....	145
	5.2.5.5: Strontium Analysis.....	146
5.2.6.0:	XRF Analysis.....	147
5.2.7.0:	Conclusion of Vanadium-Natisite Ion Exchange Capabilities.....	149
5.2.8.0:	Comparison of Vanadium-Paranatisite and Vanadium- Natisite Ion Exchange Capabilities.....	150
	Future Work.....	152
	References.....	154
	Appendix.....	167

Chapter One- Introduction

1.0.0.0: Background

With the need for a sustainable, reliable energy pathway that can meet the growing energy demands, nuclear power is becoming an increasingly viable option. With targets set to reduce greenhouse emissions within the United Kingdom (UK), the growing interest in the use of nuclear energy is becoming of paramount importance^[4].

The dependence upon nuclear energy can be seen in a relatively brief period across the world, in particularly from 1990 - 2015. During this period countries such as France, the Czech Republic and the United Kingdom increased their reliance upon nuclear fuel by 39.3 %, 113.3 % and 7.0 % respectively^[5]. With France relying upon nuclear energy to generate 76.3 % of the country's total energy demand, it is one of the countries with the highest percentages of energy generated by nuclear fission^[6].

Currently the UK generates 21.0 % of its electricity from the nuclear fuel cycle^[7], with plans to increase this due to the sustainability and low carbon impact that this energy exhibits^[1]. Plans to build new reactors within the UK are in place with eight new sites already being selected and the construction of Hinckley Point C to be completed by 2025^[8, 9].

Waste is generated during most energy pathways with nuclear power being no different. Various disposal methods within the nuclear industry need to be used to protect human health and the environment against adverse effects of radioactive waste. The method by which the waste is treated is dependent upon the nuclear cycle adopted by a given country.

1.1.0.0: Radioactive Waste Material

Radioactive waste is any waste that contains above the background level of radioactivity and has the potential to cause detrimental effects to the environment, human and animal health. Although radioactivity is present in many different forms from various sources, where it exceeds the defined background level, it needs to be subjected to special treatment and disposal.

In the UK, the way in which radioactive waste generated by nuclear plants in the public sector is dealt with is in accordance with regulations set by the Office of Nuclear Regulations (ONR), the Environmental Agency (EA), the Scottish Environmental Protection Agency (SEPA), Natural Resources Wales (NRW) and the Department for Transport (DFT). The agencies provide a policy framework for the National Decommissioning Authority (NDA) to follow^[10, 11]. An outline is shown in Figure 1.

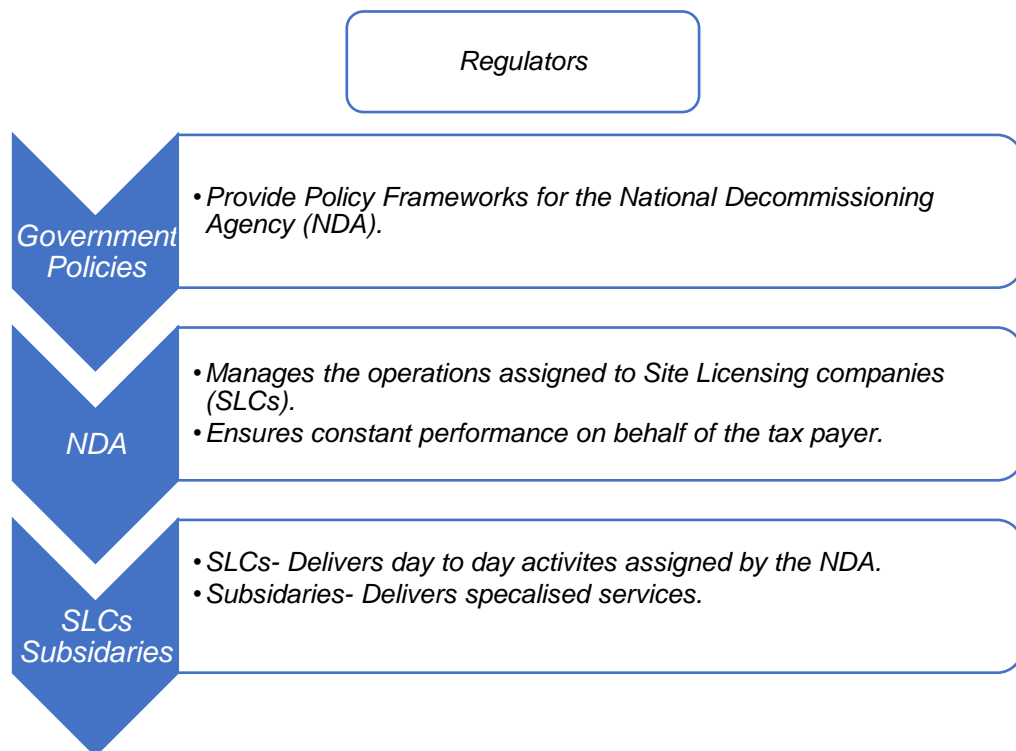


Figure 1 : Outline of the way in which radioactive waste generated from the nuclear industry, in the public sector, is dealt with^[12].

Materials which emit radiation can be classified as: alpha emitters, beta emitters or gamma emitters.

Alpha Emitters- Alpha emitters are the result of helium nuclei (containing 2 neutrons and 2 protons) being emitted from common materials used within the nuclear industry such as uranium, thorium and plutonium. Alpha particles are deemed the least detrimental to human health as penetration can be prevented by skin, paper and air, however adverse effects can happen if they are inhaled or are able to enter the bloodstream^[13, 14].

Beta Emitters- Beta emitters are charged particles that have comparable properties to electrons. Unlike alpha radiation, beta radiation is the result of emission from lighter elements such as strontium, a fission product. Beta particles tend to have a higher penetration capacity and will not be stopped by skin, paper or air; instead materials such as metal (Pb, steel) or wood are required to absorb the radiation^[13, 14].

Gamma Emitters-Gamma rays are electromagnetic waves that possess high ionisation capacities and therefore concrete or lead are required to completely stop the radiation^[14]. Gamma-rays are generally emitted from materials like cesium which is a fission product^[13]. Penetration capabilities of all emitters are shown in Figure 2.

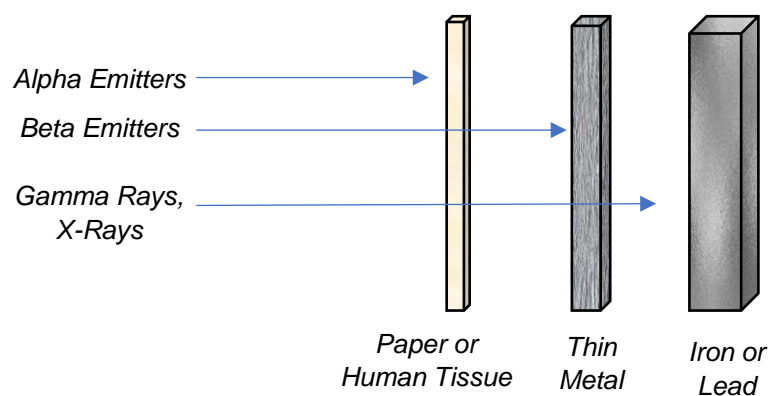


Figure 2: Diagram of alpha, beta and gamma penetration capabilities.

1.2.0.0: Radioactivity

To help deal with the way in which alpha, beta and gamma emitters are classified, several categories have been developed based upon the concentrations emitted and these categories are named: High-Level Waste, Intermediate-Level Waste and Low-Level Waste.

High-Level waste-High-Level Waste (HLW) is generated by the reprocessing of spent fuel and spent fuel that will not be reused. Generally, this comprises of fission products, actinides and transuranic elements. The radioactivity mainly arises initially due to fission product activity in which high-levels of heat are generated. To treat this category, waste must first be separated into long or short-lived radioactive components, cooled and shielded. HLW is said to constitute ~ 3 % of the amount of waste generated but ~ 95 % of the radioactivity associated with all nuclear wastes^[15]. The radioactivity within this category arises from relatively high concentrations of alpha, beta and gamma emitters^[14].

Intermediate-Level waste- Intermediate-Level waste (ILW) consists of fuel cladding, sludge, contaminated material and resins. ILW requires shielding but does not generate as much heat as HLW. To treat ILW, the waste is typically mixed with bitumen or concrete and solidified before disposal. In contrast to HLW, ILW constitutes ~ 7 % of the total waste and ~ 4 % of the total radioactivity^[15]. In intermediate waste, radioactivity arises from lower levels of beta and gamma radiation and sometimes alpha emitters^[14].

Low-Level Waste- Low-Level Waste (LLW) generated by the nuclear industry arises from the contamination of materials such as paper, clothing and filters. The radioactivity seen within this group does not require any shielding and can be buried in shallow land fill sites. Solid wastes fall into this category when < 4

GBq/te of alpha emitters and < 12GBq/te of beta/gamma emitters are present. Typically, LLW waste constitutes ~ 90 % of the total radwaste whilst only contributing ~ 1 % of the total radioactivity. Radioactivity within this category arises from low concentrations of beta and gamma decay and sometimes even low levels of alpha decay. To reduce the volume of LLW, it is often compacted before disposal in land fill sites^[14, 15]. A chart showing the composition of radioactive waste is shown in Figure 3.

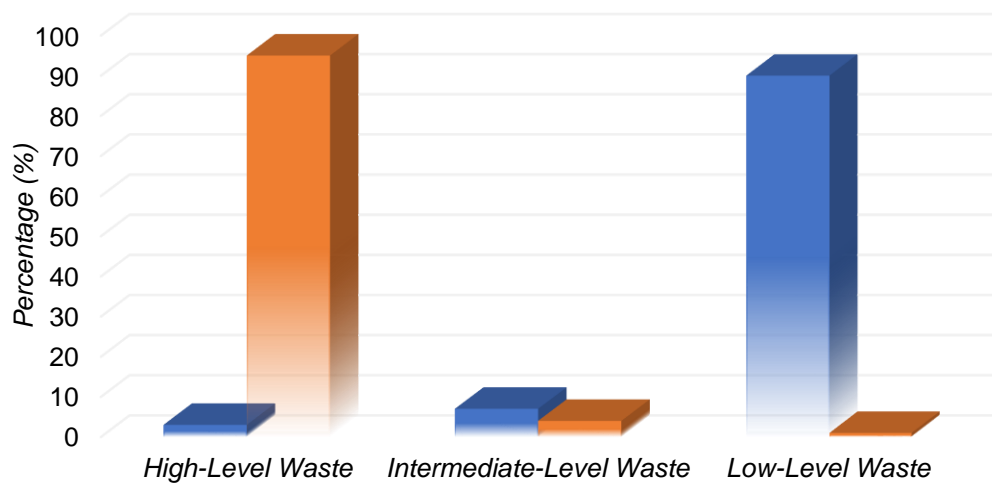


Figure 3: A chart to show the composition of radioactive waste.

A: Blue charts represent the volume of waste generated from each category.

B: Orange charts represents the total radioactivity generated from each category.

1.3.0.0: Open and Closed Fuel Cycles

Countries that are dependent on nuclear fuel typically opt for either an open or closed fuel cycle^[16], although there are some countries that are still undecided upon the best cycle to primarily adopt and therefore tend to use both.

Countries which have opted for the open fuel cycle work on a once through basis. This means any spent fuel that is generated through the cycle is stored intermittently in fuel rods ready for treatment at geological disposal facilities (GDF) ^[17]. Open fuel cycles focus upon 'Spent Fuel Management' which produces lower levels of ILW and LLW and higher levels of HLW due to waste not being pre-treated before disposal. To date, no country which has opted for the open fuel cycle has begun geological disposal^[18], although countries such as France, Finland and Sweden are expected to open their first GDF sites in 2025^[19].

Countries which have opted for the closed fuel cycle reprocess spent fuel to recuperate uranium and plutonium that can then be reused^[16]. This method also allows for the separation of radioactive cesium and strontium (the main constituents of heat generating radionuclides), other fission products and minor actinides. After being separated, they are kept in storage for a number of years to allow for the reduction in temperature and radioactivity. The waste is then vitrified, ready to be sent for disposal to underground repositories.

A schematic diagram of closed and open nuclear cycles is shown in Figure 4. A list of the countries operating on either an open or closed fuel cycle being shown in Table 1.

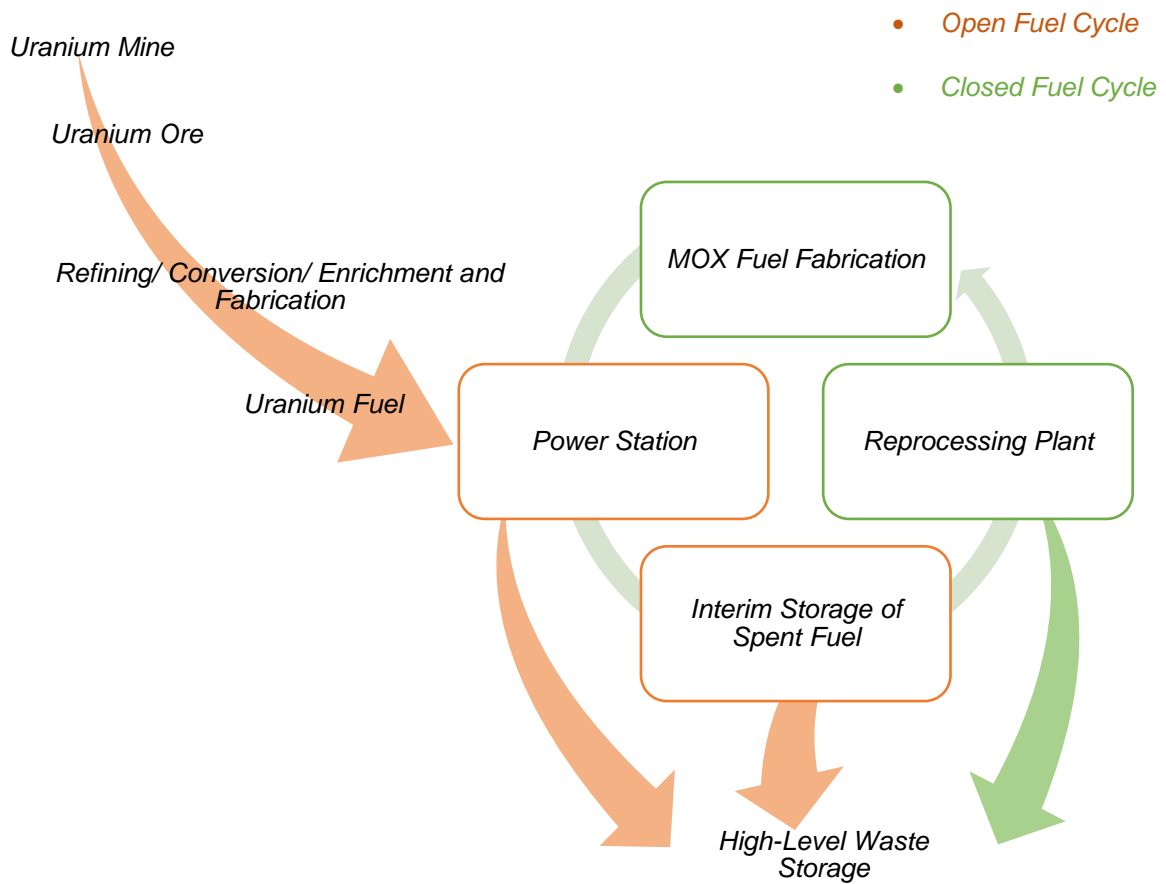


Figure 4: Simplistic schematic diagram of open and closed fuel cycles^[16].

Table 1: A list of countries operating on open and closed fuel cycles^[20].

Countries that have Adopted the Open Fuel Cycle	Countries that have Adopted the Close Fuel Cycle
Canada	China
Czech Republic	France
Finland	India
Republic of Korea	Japan
Romania	Netherlands
Sweden	Russian Federation
Switzerland	Switzerland
United Kingdom	United Kingdom
United States of America	

In the UK, most of the nuclear power stations or reactors operate within a closed fuel cycle. Spent fuel is reprocessed and fissile material is recovered and reused with a process called Plutonium Uranium Redox Extraction (PUREX)^[21]. However, many of the reprocessing plants in use within the UK are deemed to be out of date and are coming to an end of their usable life. Prime examples being the Thermal Oxide Reprocessing Plant (THORP) and the Magnox reprocessing plant at Sellafield which are scheduled to close by 2018 and 2020 respectively^[22].

Upon their closure, the UK will move to an open fuel cycle process, i.e. spent nuclear fuel may be stored on nuclear reactor site until a geological depository site is chosen, this is believed to be available for high active waste by 2075^[23].

Even though the UK is set to move to an open fuel cycle, three main scenarios are still in place regarding the continuation of the nuclear cycle, these scenarios are Baseline, Replacement or Expansion.

Baseline- upon the current generation of nuclear reactors, this scenario will allow for a phase out of nuclear energy^[24].

Replacement- currently the government has promised to support the build of nuclear reactors that have a 16 GW combined capacity^[24].

Expansion- increased reliance upon nuclear energy may lead the UK to introduce both 40 and 75 GW combined capacity^[24].

Currently the UK government has decided to shift emphasis towards open fuel cycle and implement the replacement scenario^[24]. All spent fuel generated following this change will be stored until a viable solution, such as a geological depository facility site is available^[23].

However, if the expansion scenario is adopted, the UK will most likely revert back to the closed fuel cycle to deal with the increasing amount of spent fuel that will require reprocessing^[24]. This will take advantage of advanced reprocessing technologies such as the PUREX process and a process known as Group Actinide Extraction Process (GANEX) which aims to completely remove all actinides^[25].

There are also questions being raised regarding the sustainability of uranium at a global level. The introduction of fast breed reactors as well as advanced reprocessing technologies will help preserve the Earth's uranium resources^[25].

Regardless of the cycle adopted the European Union (EU) suggests that the international accepted policy will be to dispose both low and intermediate waste in near surface facilities whilst HLW and spent fuel will be disposed deep in geological disposal facilities^[24, 26].

1.4.0.0: Generation of Nuclear Waste

Upon switching to the open fuel cycle, it is predicted that around 7,700 tonnes of used fuel from Advanced Gas Reactors (AGRs), Sizewell B Pressurised Water Reactors (PWRs) and legacy exotic fuels will be disposed of in an underground facility. A further 1,500 tonnes of material is predicted to be generated from the use of mixed oxide (MOX) fuel and from recycling the UK's Plutonium stock^[24].

Dealing with the increasing amount of waste produced and the waste already in storage is therefore of paramount importance. Currently, in the UK alone there is approximately 5 million tonnes of existing waste that needs to be treated^[15].

It has been reported that one light water reactor in the UK is responsible for producing around 200 - 350 m³ of both low and intermediate type waste per year and 20 m³ of used fuel. The composition of the spent nuclear fuel produced from light water reactors is noted in Table 2 and a list of radioisotopes present after 4.5 % enrichment, with a burn-up of 45 GWd/t U after 8 years cooling being shown in Table 3. Combined production of nuclear waste from all light water reactors has shown the total production of low and intermediate waste to be 200,000 m³ whilst 10,000 - 12,000 tonnes of high level waste is generated yearly^[15].

Table 2: Typical composition of the spent nuclear fuel generated from
LWR^[15].

Isotope	Percentage Composition (%)
Uranium ($< 1\%$ of which is U-235)	95.6
Plutonium	0.9
Stable fission products	2.9
Cesium and Strontium	0.3
Iodine and Technetium	0.1
Other long-lived fission products	0.1
Minor actinides (Americium, curium and neptunium)	0.1

Table 3: A list of radioisotopes present after 4.5 % enrichment, with a burn-up of 45 GWd/t U
after 8 years of cooling^[12].

Radioisotopes	TBq/t U	Heat Rating Factor (fW/Bq)	Heat Rating Contribution (WtU)
Y-90	3140	150	470
Sr-90	3140	31	98
Rh-106	89	260	23
Sb-125	47	85	4
Cs-134	502	275	138
Cs-137	4380	30	131
Ba-137m	4140	106	439
Ce-144	33	18	0.6
Pr-144	33	198	7
Eu-154	172	242	40
Am-241	77	904	69
Cm-242	0.01	995	0.01
Cm-244	121	946	114
		Total	1530

1.5.0.0: Treatment of Nuclear Waste

Whether open fuel cycles or closed fuel cycles are adopted by a country, both solvent extraction and ion exchange processes will play a significant role in the sustainability of the nuclear industry with ion exchange mediums being deployed for waste clean-up^[27].

The function in which the ion exchange medium (can be organic or inorganic base) generally depends upon the chemical composition of the medium^[28]. Compared to inorganic materials organic materials have higher mechanical strength and tend to have a higher exchange capacity^[2].

Organic and inorganic materials, are applied to roles such as the removal of radioactivity from decontamination liquors where the complete removal of these radionuclides is not necessary providing they are within the dose uptake limits to operators. A good example of the application of inorganic materials for liquor clean-up is the Site Ion Exchange Plant (SIXEP) which uses Clinoptilolite ^[29].

Inorganic materials are finding an array of applications as they can remove specific radionuclides efficiently even in the presence of highly concentrated competing ions^[29]. A prime example being the IONSIV materials which have high affinities towards cesium. Due to their high affinities towards cesium over other competing ions, the IONSIV family were utilised during the Fukushima, Chernobyl and Three Mile Island incidents^[30].

Inorganic materials can be separated into three main categories clays, oxides and zeolites. The function given to the material greatly depends upon the composition and structure of the materials^[2].

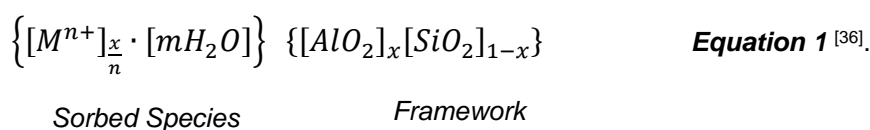
Chapter 2- Zeolites

2.0.0.0: Composition of Zeolites

Zeolites are a class of microporous aluminosilicates^[31] first discovered in the 18th century. Since then many natural and man-made zeolites have been discovered and to date there are over 231 different structures recognised by the International Zeolite Association (IZA)^[32].

By strict definition zeolites are materials which comprise of only aluminium, silicon and oxygen within the framework, where both silicon and aluminium must have tetrahedral coordination and all pore sizes must be less than 20 Å^[33].

Introduction of aluminium tetrahedra within the framework of the zeolite introduces a net negative charge^[34]. To maintain electrochemical neutrality, counterbalancing cations are loosely bound to the zeolite framework in the cages, cavities or channels^[35]. The size and shape of the cages or channels can influence the nature of the charge balancing cation preferred, with larger pore zeolites favouring larger cations. Typical cations found such as Na⁺, K⁺ or Ca²⁺ are in hydrated forms, introducing extra water species into the pores. The general zeolite formula is given in Equation 1^[36].



The replacement of silicon tetrahedra with aluminium tetrahedra can only happen to an extent within the zeolite framework, which is known as Lowenstein's rule^[37]. The rule states that the ratio of silicon to aluminium must be equal to or greater than one. A ratio of 1:1 implies that the aluminium and silicon tetrahedra alternate throughout the zeolite structure^[38]. If this condition is not met, it would imply that

Al-O-Al bonds would be present within the zeolite framework. To date, the presence of Al-O-Al bonds have not been observed experimentally^[39].

2.1.0.0: Structure of Zeolites

The primary building blocks within the zeolite structure compose of tetrahedrally bonded silicon and/or aluminium oxygen units^[33], $[SiO_4]^{4-}$ or $[AlO_4]^{5-}$ as shown in Figure 5.

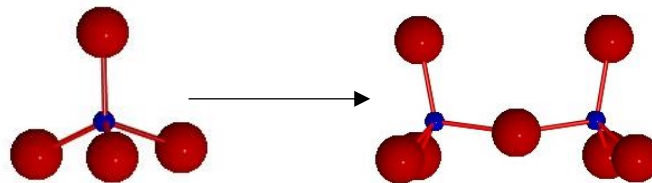


Figure 5: Illustration of primary building blocks of zeolites. (Oxygen atoms- red and silicon and aluminium atoms- blue).

It is these primary building blocks that can link together to form the secondary building blocks of the zeolite structure. The primary building blocks link through 2, 3 or 4 corners via oxygen bridges forming Si/Al-O-Si/Al bonds varying in bond angles of 120 - 180 °^[40]. The sharing oxygen atoms lead to either 4, 6, 8, 10 or 12 membered rings being produced with no unshared oxygen atoms within the framework, as shown in Figure 6^[41].

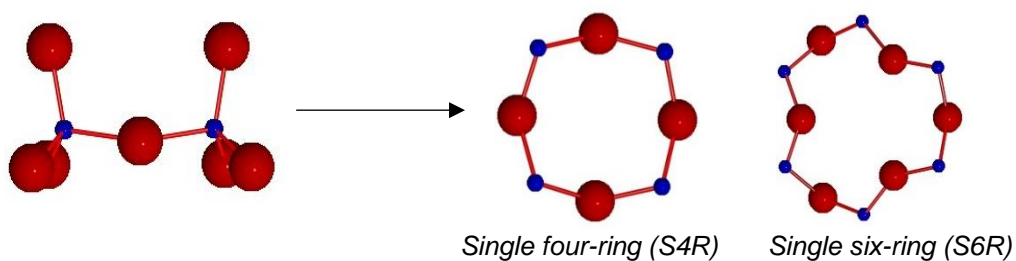


Figure 6: Illustration of secondary building blocks of zeolites forming single four ring (S4R) and single six ring (S6R) structures.

The manner in which the rings connect together gives rise to cages, cavities and/or channels, forming the tertiary building blocks and giving zeolites their physical and chemical properties^[42]. Channels extend throughout the whole structure of the zeolite and in doing so allows for the diffusion of any guest molecule along the entire pore. Cavities however, do not extend throughout the entire framework and instead allow for the passage of guest molecules in and out of the cavity^[43]. For example Zeolite A forms both beta (β) and alpha (α) cages. Beta cages are the result of 4 and 6 membered rings formed from alternating silicon and aluminium units, whilst alpha cages are larger in diameter having been formed from 4, 6 and 8 membered rings. The formation of β cages via four membered rings exhibit an internal pore size of $\sim 6.5 \text{ \AA}$ whilst α cages formed via six membered rings have an internal diameter of $\sim 11.5 \text{ \AA}$. Both cage types are shown in Figure 7.

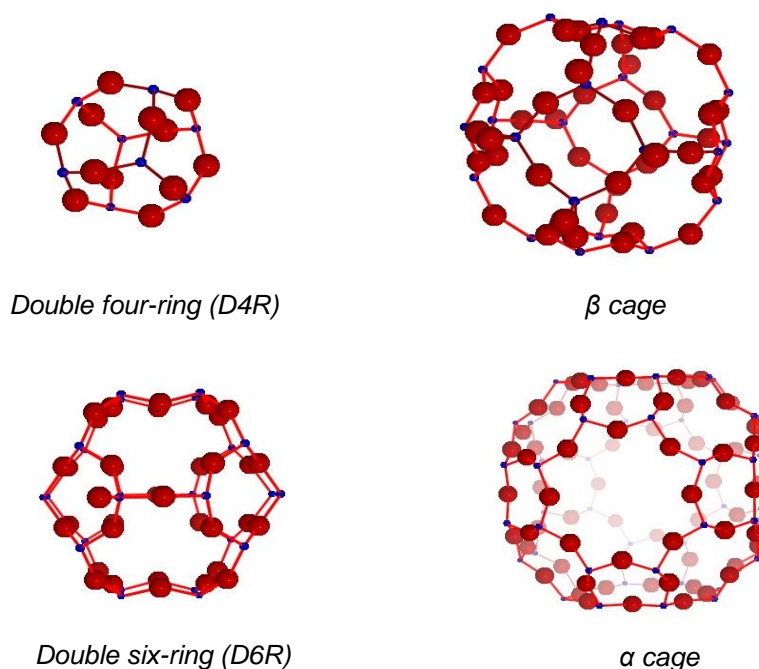


Figure 7: Illustration of double four ring (D4R) structures forming β cages and double six ring (D6R) structures forming α cages.

2.2.0.0: Applications of Zeolites

Since being discovered in 1756^[35], zeolites have shown to have a diverse range of applications due to their physical properties and chemical composition. To date zeolites are used in processes such as catalysis, separation, adsorption and ion exchange^[44].

2.2.1.0: Adsorption

The open porous structure that zeolites exhibit when dehydrated has meant that they have found applications in both the environmental and nuclear industry for the removal of carbon dioxide (CO₂)^[45] and radioactive xenon isotopes (such as Xe¹³³ and Xe¹³⁵)^[46].

With current aims to reduce carbon dioxide emissions, the environmental industry aims to separate CO₂ from hydrogen (H₂), nitrogen (N₂) and methane (CH₄) gas mixtures using zeolites such as Chabazite. Due to the location of counterbalancing cations within the ring system, Chabazite has shown to be able to act as a molecular sieve by adsorbing and separating CO₂ from CO₂/N₂ and CO₂/CH₄ mixtures^[45].

Zeolites such as Zeolite Socony Mobil-5 (ZSM-5) are finding applications within the nuclear industry as adsorption mediums too. Research of loaded silver ZSM-5 conducted by D. Farrusseng *et al.* has shown to be able to adsorb Xenon, a harmful radioactive contaminant of off-gas streams generated upon aqueous reprocessing of nuclear fuels^[46].

As shown from these examples, the ability to act as an adsorption medium is dictated by the size of the rings and the location of counterbalancing cations in a particular zeolite structure^[47]. Zeolites which have smaller ring sizes and internal surfaces tend to adsorb smaller molecules.

2.2.2.0: Ion Exchange

Counterbalancing ions that are present in aluminium containing zeolite frameworks are responsible for their ion exchange properties^[48]. These cations can be exchanged with other ions in aqueous solutions^[49]. As a result, zeolites have found applications in water treatment industries, in commercial detergents as water softeners and in the treatment of nuclear waste.

In the UK, before disposal or release back into the environment, spent fuel pond water generated by uranium fission, currently undergoes a pre-treatment process, such as ion exchange with zeolites. This allows for the removal of fission products such as strontium and cesium and allows for the recirculation of certain isotopes such as uranium and plutonium^[50]. Within the nuclear cycle, waste that is no longer deemed viable to the nuclear cycle is said to be 'spent nuclear fuel' and is placed within storage pools to cool and reduce radioactivity for several years^[51]. During this time the water in the ponds become contaminated through leakage of the cladding and particulates present upon fuel elements^[52]. The water is circulated through ion exchange mediums such as zeolites to remove radioactive ions.

Finally, nuclear disasters such as the Three Mile Island, Chernobyl and Fukushima, have resulted in the release of radioactive species into the environment. In all three incidents, zeolites have been used to remove any contaminants present in the environment such as strontium and cesium^[53].

The treatment of radioactive waste with ion exchange mediums therefore allows for recirculation of certain isotopes, the reduction in the amount of nuclear waste sent for long-term disposal, allows for water to be reintroduced into the environment as well as the reduction upon the burden of uranium resources^[2].

2.2.3.0: The Site Ion Exchange Plant (SIXEP) Process

Within the SIXEP process the naturally occurring zeolite Clinoptilolite is used to remove cesium (Cs-137) and strontium (Sr-90) from aqueous effluent in legacy pools found at Sellafield^[54]. Clinoptilolite used at Sellafield has the general formula of $\text{Na}_6\text{Al}_6\text{Si}_{30}\text{O}_{72}\cdot 24\text{H}_2\text{O}$ ^[55], the HEU typology with a space group of C2/m ^[56]. The structure of Clinoptilolite is shown in Figure 8.

The framework of Clinoptilolite consists of three channels which intersect and which are all located within the same plane. Both the *a* and *b* channels run parallel to the *c* axis and are formed by 10 and 8 membered rings respectively^[57]. The counterbalancing cations, mainly sodium and potassium predominately located in the intersections of A and C channels can be exchanged with Cs-137 and Sr-90^[54].

When the maximum exchange capacity i.e. the total capacity of Clinoptilolite to hold an exchangeable cation, has been reached (this generally takes a few months in the nuclear industry) Clinoptilolite is removed and stored in either bulk storage tanks or Medium Active Waste Export Plant (MASWEP) storage vessels. The spent Clinoptilolite and sand will be stored in these premises until packaging plants become fully operational in 2020.

Until this time elapses key issues with regards to the storage and the treatment of waste arising from the SIXEP process will need to be addressed. These issues include treating waste so that it can be stored in a passive manner, the way in which waste is immobilised pending long term disposal and reducing the concentration of fission products and alpha emitters emitted to long term storage. Reports suggest that 20 % of the cesium sent for deep disposal is from spent Clinoptilolite and sand following the treatment in the SIXEP process^[58].

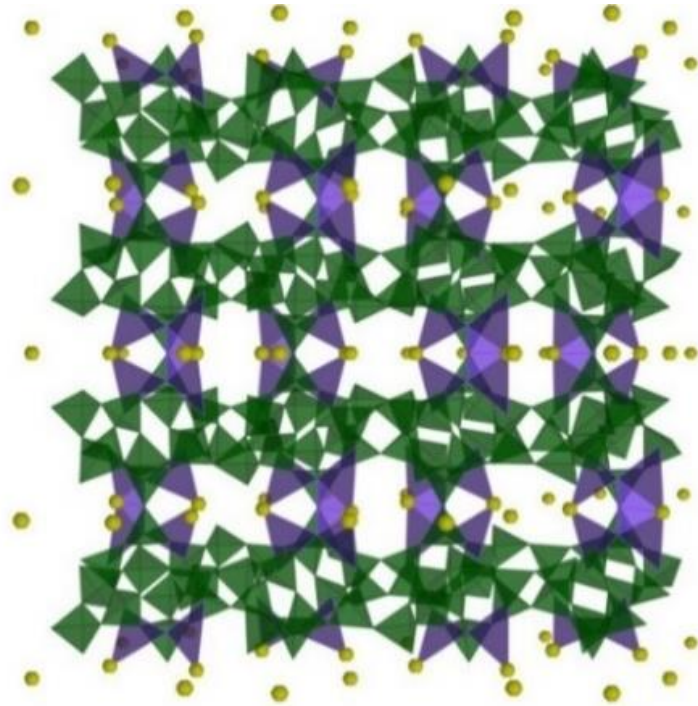


Figure 8: Structural representation of clinoptilolite. (Sodium atoms- yellow, oxygen atoms- purple and silicon atoms- green).

2.3.0.0: Zeotypes

Zeotypes are a family of synthetic materials based upon the zeolite structure. Unlike zeolites, zeotypes are 3 D crystalline frameworks which can exhibit micro-, meso- or nanopore structures^[59]. They do not adhere to the strict definition of a zeolite as both silicon (Si) and aluminium (Al) can be replaced by other heteroatoms. Further to this, Lowenstein's rule is not followed, so for example, where titanium (Ti) atoms have replaced Al atoms, Ti-O-Ti bonds can be formed^[60].

Due to the versatility of zeotypes several families have been formed such as gallophosphates^[59] and titanium silicates^[30]. In this study, titanium silicates have been the primary focus in the replacement of zeolites.

2.3.1.0: Titanium silicates

The increase of interest in titanium silicates over zeolites for certain applications is due to various characteristics that are seen within the titanium silicate family compared to zeolites.

Firstly, titanium silicates have shown to have higher selectivity towards common radionuclides such as strontium, cesium and actinides even in the presence of high levels of competing ions such as sodium and magnesium, common ions found within seawater^[61]. This would be advantageous in the event of another nuclear incident such as Fukushima. The nuclear disaster was the result of an earthquake followed by a tsunami. This caused the power supply to be cut and in turn the cooling operation systems failed^[62]. It is estimated that levels of highly radioactive material were released into the environment, namely, iodine-131, cesium-134 and cesium-137. Due to the soluble nature of cesium, the migration of the ions was vast. To this date, it has been reported that cesium-134, a

fingerprint ion for the incident, has been recorded off the west coast of the United States of America and low levels of the ion have been found in salmon in Canada^[63]. Implementing the use of titanium silicates could be used to remove undesired radionuclides from seawater^[64].

Unlike zeolites, titanium silicates do not contain aluminium within their structure and so have shown greater stability across a wide range of pH environments, especially environments that are acidic. The pH environment has previously had to be taken into account within the nuclear waste management programme^[65]. Within the SIXEP process, the liquor is too acidic for Clinoptilolite to be used and so it first must be neutralised by a carbonation process^[66]. It is therefore hoped that steps like these could be avoided by using a material that is more stable in extreme pH environments.

As mentioned previously, the versatility of the elements that can be introduced allows for the manipulation of the structure so that it can be tailored to the desired application allowing for changes within atomic size, bond length and ultimately the pore size in which cations can migrate into^[67]. The synthesis of titanium silicate structures is also deemed economically friendly and therefore large-scale syntheses are economically viable.

Finally, titanium silicates are also ideal for long-term disposal as they can be vitrified. Vitrification is a process used within the nuclear industry in order to produce a vitrified solid in which contaminants are securely immobilised^[68]. To produce the solid mass, the waste generated by industry is heated to 1000 °C and mixed with borosilicate glass, producing a melt. The melt is then poured into vessels and allowed to cool, entrapping HLW into the borosilicate glass. This process is known as vitrification. Research has shown that titanium silicates have

the potential to immobilise contaminants, forming part of the melt and vitrified mass^[69]. Following immobilisation, the vitrified mass can be stored within the environment.

2.4.0.0: Titanium Silicates and their Use/Potential in Industry

Throughout industry titanium silicates such as IONSIV IE-911 and ETS-10 are becoming more widely used in applications such as ion-exchange and catalysis.

2.4.1.0: The IONSIV Family

The IONSIV IE-910 series constitutes of IE-910, a zirconium bound crystalline sodium silicotitanate (CST)^[70], with the idealised CST formula of $\text{Na}_4\text{Ti}_9\text{O}_{20} \cdot n\text{H}_2\text{O}$ ^[71]. Manipulation of the IE-910 formula following the introduction of niobium into the framework forms IE-911 with the commercial formula of $\text{Na}_3\text{Si}_2(\text{Nb}_{0.3}\text{Ti}_{0.7})_4\text{O}_{13}(\text{OH}) \cdot 4\text{H}_2\text{O} + 0.93\text{Zr}(\text{OH})_4$ ^[72]. Both frameworks are said to exhibit a sitinakite like structure as shown in Figure 9.

The success of this family is due to the increased affinity towards cesium in the presence of extreme pH and competing non-radioactive ions compared to other exchange resins. This increased affinity is attributed to the comparable size of the unique tunnel system of the IONSIV material and the ionic radius of cesium. The comparable size allows for the cesium ion to occupy more favourable sites within the IONSIV framework when compared to other ionic species. In turn an increased exchange capability, or increased affinity, towards the ion is noted.

The increased affinity towards cesium can be especially seen within IE-911, which following niobium doping provides further lattice spacing apt for cesium sorption^[73]. Substituting Nb^{5+} for Ti^{4+} reduces the number of counterbalancing sodium ions present within the tunnel. The less crowded tunnel system therefore

facilitates the exchange for cesium hydrated ions and overall increasing the affinity to the cesium ion present within effluent.

IONSIV families have been incorporated into the removal of cesium and strontium from radioactive waste, alkaline supernatant, nuclear fuel storage pool water and during nuclear incidents such as Three Mile Island, Chernobyl and Fukushima^[73].

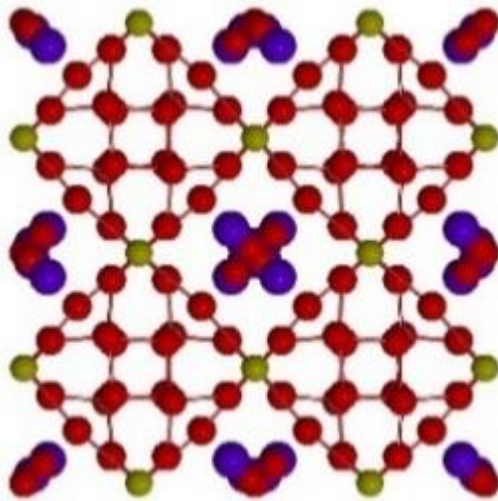


Figure 9: Structural representation of sitinakite. (Titanium atoms- purple, silicon atoms- light blue, oxygen atoms - red, sodium atoms- yellow and potassium atoms- purple).

2.4.2.0: Engelhard Titanium Silicate 10 (ETS-10)

ETS-10 is a titanium silicate with mixed coordination, with titanium being octahedrally coordinated and silicon being tetrahedrally coordinated^[36] exhibiting the general formula of $M_2\text{-TiSi}_5\text{O}_{13}\cdot n\text{H}_2\text{O}$ (where M can be K and Na). The octahedrally coordinated titanium shares four oxygen atoms with the tetrahedrally coordinated silicon^[74]. The connection in this way gives rise to a 12 ring pore structure forming channels of diameters of 8.6 by 9.2 Å^[75]. The structural representation is shown in Figure 10.

Research into ETS-10 has shown that when it is supported via hollow carbon nanotubes it has potential to act as an adsorption medium to capture radioactive iodine that is typically produced via off-gas emissions from aqueous reprocessing of nuclear fuels^[76].

Removing volatile radionuclides from the environment is a necessary precaution if nuclear fuel reprocessing facilities are to meet the conditions of licenses set by the Environmental Protection Agency (EPA) in the United States of America, which states that 99.4 % of the mass of iodine emissions must be captured and immobilised^[77].

Current research is suggesting that materials such as ETS-10 have a good affinity for adsorbing iodine (I_2) and krypton, common species emitted by the nuclear industry. In the future it is therefore hoped that these materials will be instrumental in the reduction of volatile radionuclides entering the environment.

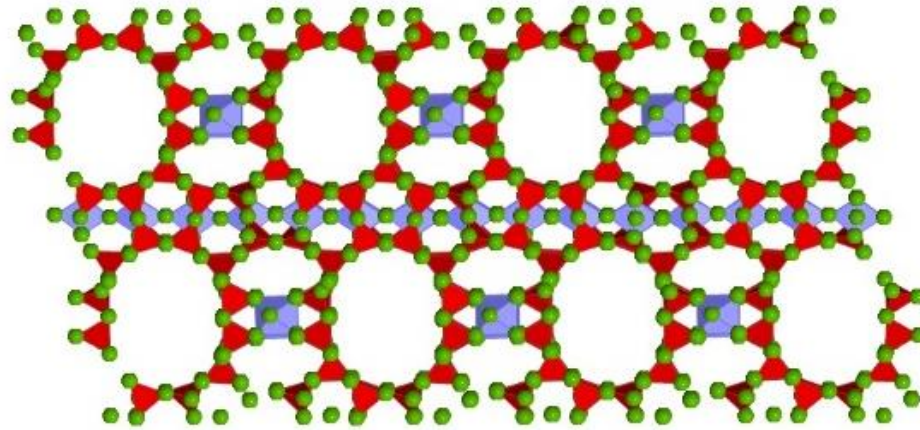


Figure 10: Structural representation of engelhard titanium silicate 10 (ETS-10). (Silicon atoms- red, oxygen atoms- green and titanium atoms- purple).

2.4.3.0: Paranatisite

Paranatisite, as shown in Figure 11, is a naturally occurring mineral which was first discovered as intergrowths within natisite in the Yukspor Mountain in Khibiny Massif, Russia^[78]. It adopts the empirical formula, $\text{Na}_2\text{TiO}(\text{SiO}_4)$, an orthorhombic crystal system (space group of $P m m a$) with unit cell parameters where $a = 9.82700 \text{ \AA}$, $b = 9.16700 \text{ \AA}$ and $c = 4.79900 \text{ \AA}$ with a unit cell volume of 432.3136 \AA^3 ^[79]. Research has shown that paranatisite can be synthesised using hydrothermal methods, appearing as a white powder.

Paranatisite is a titanium silicate which contains two distinct titanium (Ti) sites, one silicon (Si) site and three distinct sodium (Na) sites. The titanium sites, which are in square pyramidal and octahedral coordination, are connected through O-Si-O bonds, resulting in silicon being tetrahedrally coordinated. The framework is said to be fragmented by the three sodium sites, in which all sodium environments are octahedrally coordinated^[3].

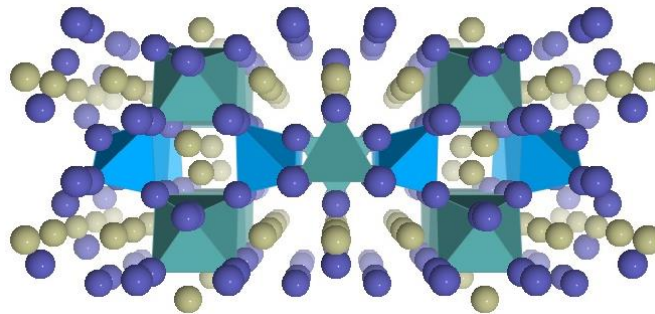


Figure 11: Structural representation of paranatisite. (Silicon atoms- blue, oxygen atoms- purple, titanium atoms- green and sodium atoms- yellow).

2.4.4.0: Natisite

Naturally occurring natisite has been found within a variety of locations such as the Yukspor Mountain in Khibiny Massif, Russia^[80]. Adopting the same empirical formula as paranatisite, $\text{Na}_2\text{TiO}(\text{SiO}_4)$, natisite forms crystals of yellow/green complexion, a tetragonal crystal system (space group of $P 4 / n m m$) and unit cell parameters of $a = b = 6.50 \text{ \AA}$ (1) and $c = 5.07 \text{ \AA}$ (1) and a cell volume of 214.444 \AA^3 ^[81].

Natisite, as shown in Figure 12, is a layered titanium silicate with corner sharing SiO_4 and TiO_5 units forming a layered structure. The introduction of titanium into the framework leads to an overall negative charge which must be counterbalanced. Counterbalancing cations, Na^+ ions, reinstate net neutrality and are located between the titanium silicate layers^[3]. These counterbalancing ions are weakly bound to the silicate layer of natisite and therefore can undergo exchange with other ions^[82].

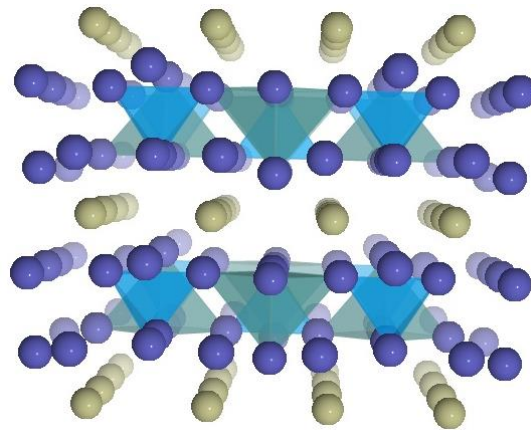


Figure 12: Structural representation of natisite. (Silicon atoms- blue, oxygen atoms- purple, titanium atoms- green and sodium atoms- yellow).

2.5.0.0: Aims of Research

Research has shown that titanium silicates may offer a promising alternative in the removal of radioactive waste from bulk solution. This project aims to investigate the potential of vanadium-paranatisite and vanadium-natisite, titanium silicates as ion exchange materials for use in the nuclear industry.

The first part of this project aimed to optimise the synthesis of the vanadium doped materials with doping levels of 5 and 10 %-vanadium. Vanadium was selected to dope the titanium silicate frameworks due to the versatility of the element. Vanadium has a variety of oxidation states, ranging from +2 to +5^[83], and has shown comparable properties to titanium regarding ionic radii and coordination behaviour. Further to this research into vanadium silicates such as VSH-1K has shown that vanadium silicates have increased adsorption abilities, ion exchange capabilities and improved stability in a variety of environments^[84]. Characterisation techniques such as powder X-ray Diffraction (XRD), X-ray Fluorescence (XRF), Inductively Coupled Plasma-Mass Spectroscopy (ICP-MS) and Scanning Electron Microscopy (SEM) coupled with Energy Dispersive X-Ray Spectroscopy (EDX).

The second part of the project focussed upon the ion-exchange capacity and selectivity of the materials synthesised. Ions commonly found in nuclear waste such as strontium (Sr), cesium (Cs) and cobalt (Co) were of interest, together with cerium (Ce) and neodymium (Nd) which are inactive surrogates for plutonium (Pu) and uranium (U).

Finally, the ion exchange capacity and selectivity will be compared to the parent Ti-natisite. The ion exchange results for the parent material was carried out by another student, R. Hall^[85].

Chapter 3-Characterisation Techniques

The main characterisation techniques used within this study were: X-ray Diffraction (XRD), X-ray Fluorescence (XRF), Inductively Coupled Plasma-Mass Spectroscopy (ICP-MS) and Scanning Electron Microscopy (SEM) coupled with Energy Dispersive X-Ray Spectroscopy (EDX).

3.1.0.0: X-Ray Diffraction (XRD)

X-ray diffraction (XRD) is the primary technique used in the characterisation of solid inorganic materials due to its ability to provide full structural determination, phase identification and phase purity information.

X-rays are generated by the interaction of an electron beam (generated from a tungsten wire) with a metal target such as copper. Upon contact of the electron beam and the metal target, core electrons from the inner K shell become ionised and leave the atom^[38]. To regain stability, electrons from higher energy shells such as the L and M shells drop to fill the vacancies created. Characteristic K_{α} radiation is the result of L shell electrons dropping to the K shells, whilst K_{β} radiation is the result of M shells dropping to the K shell energy level^[86].

Upon realising that crystalline solids could diffract X-rays, Bragg realised that crystals could be described in terms of layers and planes. Each layer/plane is treated as a semi-transparent mirror, in which some X-rays are reflected, whilst others, travel further into the crystal and are reflected off by a parallel layer/plane. Bragg reported the difference in length in terms of the incident angle and plane separation (d_{hkl}) in the form of Equation 2^[87]. In the equation CD and BD represent path lengths, θ represents the angle of incidence and d represents the lattice spacing.

$$CB + BD = 2d_{hkl} \sin \theta$$

Equation 2^[88].

To obtain a peak within the diffraction pattern, constructive interference must take place in order to cause amplification of two waves traveling in the same direction and at the same wavelength. Amplified waves are said to be in phase and therefore the path difference of two waves travelling in the same direction and of the same wavelength are said to be of an integer number, n . Conversely non-integer numbers result in destructive interference and thereby Bragg's Law is not satisfied and no peak is seen within the X-ray diffraction pattern^[89]. Bragg was able to combine these factors generating Equation 3, which is commonly known as Bragg's Law. In the equation λ represents wavelength, n represents the order of reflection, θ represents the angle of incidence and d represents the distance between lattice planes. An illustrative diagram of Bragg's Law is also shown in Figure 13.

$$n \lambda = 2d_{hkl} \sin\theta \quad \text{Equation 3}^{[88]}$$

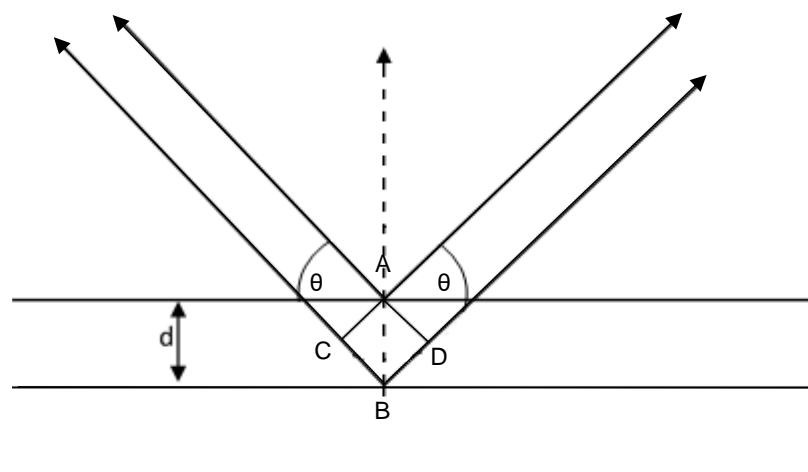


Figure 13: Illustration of Bragg's law^[90].

An X-ray diffraction pattern can provide a wealth of structural information. Firstly, the positions of the peaks on the pattern is determined by the unit cell size and symmetry of the material. Peak intensities, on the other hand, are determined by the position and nature of the atoms within the unit cell^[91]. To calculate intensities, Equation 4 is used. In the equation I represents the intensity factor, F_{hkl} represents the structure factor amplitude, LP represents the combined polarisation and geometry factor and A represents the absorption correction factor.

$$I_{hkl} = |F_{hkl}|^2 \cdot LP \cdot A \quad \text{Equation 4}^{[90]}$$

As shown in Equation 4, peak intensities are proportional to the square of the structure amplitude ($|F_{hkl}|^2$). To obtain peak intensities, the structure factor must first be calculated using Equation 5. In the equation F_{hkl} represents the structure factor, $f(j)$ represents the atomic scattering factor, $h k l$ represents the Miller indices, x, y, z represent the atomic positions and i represents the atom.

$$F_{(h,k,l)} = \sum_{j=1}^{atoms} f(j) \exp[2\pi \cdot i(hx_{(j)} + ky_{(j)} + lz_{(j)})] \quad \text{Equation 5}^{[90]}$$

The structure factor equation combines both amplitude and phase. In doing so, structure factors help to provide solutions and refinements of the crystal structures.

To allow for phase identification powdered samples were studied on a Bruker D2 Phaser powder diffractometer. The powder diffractometer was equipped with a Lynxeye solid state detector fitted with 1 mm solar slits, 6 mm slits and a 1 mm knife edge. A copper radiation ($\lambda = 1.5418 \text{ \AA}$) source was used in conjunction with a nickel K_{β} filter. The samples were rotated about the phi axis to improve powder averaging.

3.2.0.0: Powder Analysis

3.2.1.0: Pawley Fit Refinements

Initial analysis took place using Pawley fit refinements using the TOPAS^[92] software package with jEdit^[93]. Synthesised materials and ion exchanged materials that underwent Pawley Fit refinements were placed within the diffractometer for 30 minutes on a scan that ranged between 5 - 80 °. A step size of 0.020 ° and a scan time per step of 0.450 s. The parameters were refined were a Chebyshev background function and a Thompson-Cox-Hastings peak shape function. Unit cell parameters and zero point error were also refined.

Pawley fit refinements were initially conducted on powdered samples in order to provide an indication of the best possible fit that could be achieved via Rietveld refinements. Unlike, Rietveld refinements, Pawley fits do not use a structural model to compare observed data with known literature. Instead, peak fitting is conducted by constraining the observed peaks at 2θ values with known unit cell and space group dimensions. In doing so, Pawley refinements gives an indication of whether the observed data fits with known literature as well as indicating if impurities are present within the sample^[94].

3.2.2.0: Rietveld Refinements

Following Pawley fitting, synthesised materials underwent further structural analysis by Rietveld refinements. In this study Rietveld refinements were conducted upon samples which were placed in Bruker D2 Phaser power diffractometer on a 4-hour scan ranging between 5 - 80 °. A step size of 0.020 ° and a scan time per step of 3.65 s was adopted. Refinements took place using the TOPAS^[92] software package with jEdit^[93]. The parameters refined were a Chebyshev background function and a Thompson-Cox-Hastings peak shape function. In addition to the refinement of atomic positions, isotropic thermal parameters, lattice parameters and zero point error were also refined.

By minimising the differences between the calculated and observed data: atomic coordinates/ bond lengths, bond angles and phase quantities can all be obtained from the refinement. To improve the fit of the calculated and observed patterns manual refinements upon lattice parameters, intensities and background functions must all take place^[95, 96].

In doing so, the quality of the refinement i.e. the fit of the calculated and observed patterns is assessed. Both a visual and mathematical representation is provided from the refinement that takes place^[96]. When comparing a synthesised material to known literature an R_{wp} value (goodness of fit value) of 10 % or lower should be achieved. Within this study R_{wp} values for both vanadium-paranatisite and vanadium-natisite lied within the range of 5- 6 %. Therefore, the synthesised materials of vanadium-paranatisite and natisite were deemed to be true representations of the known literature structures.

3.3.0.0: X-Ray Fluorescence Spectroscopy (XRF)

X-ray Fluorescence Spectroscopy (XRF) is an elemental analysis technique that can be used for qualitative and quantitative determination of elements within a sample.

X-ray fluorescence occurs following the interactions of X-rays with matter. Upon interaction with the X-rays, which are also known as incident rays, inner shell electrons within the atoms become ionised^[97]. This can only occur when the incident X-ray is higher than the binding energy of the electrons within the atom. Following the formation of vacancies in the inner shell, the atom becomes unstable and electrons from higher energy levels fill the vacancy. As an electron from a higher energy level drops to the lower energy level, secondary X-rays equivalent to the energy between the two shells are emitted. This emission is known as X-ray fluorescence. Each emission is characteristic for each element and can therefore act as a fingerprint in order to allow for elemental detection^[98]. A schematic diagram is shown in Figure 14.

A Bruker Tracer VI handheld XRF was used in this work. Due to the handheld configuration, the XRF used was unable to provide quantitative results and was unable to detect elements that appeared below aluminium within the periodic table.

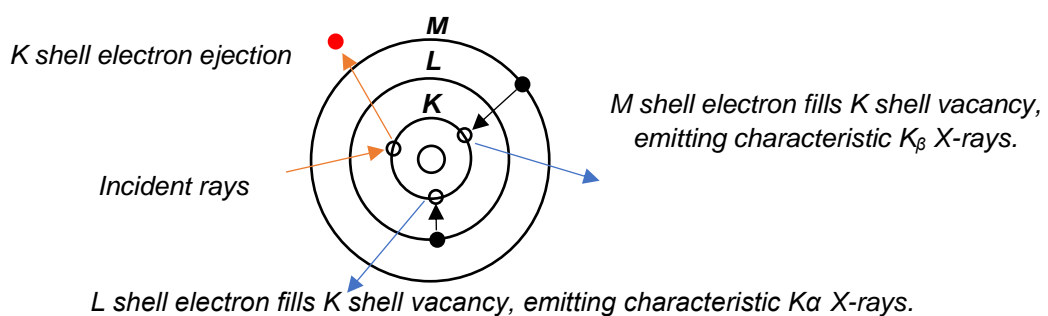


Figure 14: Illustration of the production of secondary X-rays from L and M shells^[97].

3.4.0.0: Inductively Coupled Plasma–Mass Spectroscopy (ICP-MS)

Inductively Coupled Plasma-Mass Spectrometry (ICP-MS), is an analytical technique which is able to detect most metals and certain non-metals within samples that have concentrations as low as part per trillion (ppt)^[99].

ICP-MS was the primary technique chosen for quantitative analysis to determine the percentage of titanium replacement with vanadium within the paranatisite and natisite frameworks as well as the ion exchange capacities of the materials.

ICP-MS analysis took place upon an ICP-MS Thermo Scientific Electron Corporation, X-Series and was chosen over other techniques such as flame ionisation and ICP-OES. The advantage of using plasma technology, over techniques such as flame ionisation is due to the inert environment it takes place in. By conducting analysis in an inert environment formation of oxide complexes is prevented. As well as preventing oxide formation, the torch within the ICP-MS is said to have a more uniform temperature profile, which reduces the self-absorption effects which are commonly seen with other ionisation techniques^[100].

ICP-MS analysis was chosen over ICP-OES analysis as it offers clear differentiation between elemental ions such as cesium, cerium, neodymium, strontium and cobalt. Unlike ICP-OES, which quantises elements based on the concentration of excited atoms and ions at a certain wavelength, ICP-MS quantises elements based upon their masses using mass spectroscopy^[101].

As referred to in Table 4, elemental characterisation using ICP-OES cannot always be relied upon due to spectral overlap of certain ions. The characteristic wavelengths of cesium, cerium, neodymium and strontium, as denoted in Table 4, have the tendency to overlap with each other and therefore if competitive ion

exchanged experiments are to be investigated then this technique would not be suitable for elemental analysis.

In saying this, ICP-MS suffers from spectroscopic interferences. Spectroscopic interferences are caused when atomic or molecular ions have the same mass-to-charge ratio. Nevertheless, ICP-MS software can correct any isobaric interferences or interferences caused by overlapping isotopes. As a result, for the scope of work investigated in this study, ICP-MS analysis will provide adequate quantisation of the elemental ions present within solution, without fear of spectroscopic interferences^[102].

Table 4: *Characteristic wavelengths of cesium, cerium, cobalt, neodymium and strontium used in ICP-OES analysis^[103].*

Element	Wavelength (nm)
Cesium	455.531
	672.239
Cerium	456.236
	404.076
Cobalt	228.616
	238.892
Neodymium	401.225
	406.109
	430.358
Strontium	407.771
	421.552

ICP-MS constitutes of two main features, an inductively coupled plasma, which is responsible for converting atoms into gaseous ions and a mass spectrometer, which is responsible for detecting and determining the concentration of specific ions and their isotopes.

For elemental detection, the sample is introduced into the plasma as an aerosol and travels to the ICP torch which converts the elements in the aerosol to

gaseous ions^[104]. Once ionised, the ions are directed to the mass spectrometer by interface cones. The mass spectrometer is where the ions are separated and identified due to their mass-to-charge ratio. An overview of the process of how the ICP-MS works is shown in Figure 15.

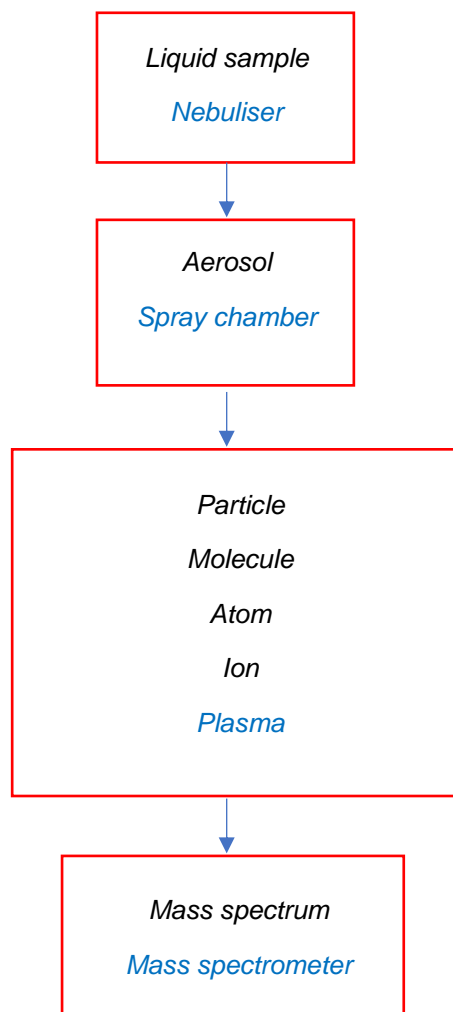


Figure 15: Schematic diagram of the inductively coupled plasma-mass spectroscopy technique^[104].

3.5.0.0: Scanning Electron Microscopy (SEM)

Scanning Electron Microscopy (SEM) linked to Energy Dispersive X-ray (EDX) analysis was used to determine particle morphology and elemental composition of the samples respectively. SEM uses electrons to view the surface of a sample and therefore, analysis must take place within a vacuum. A vacuum environment ensures that the electron beam can travel to the sample without any interference from dust or air particles^[105].

To produce a high-quality image, samples must have a conductive layer upon the surface. If samples are non-conductive, they must undergo pre-treatment before being placed within the SEM. To improve conductivity, which minimises specimen charging, a thin layer of sample must be sputtered with a gold coating under an argon environment to enhance the conductivity of the sample^[106].

EDX analysis is connected to the SEM and allows for elemental analysis of the sample. Similar to XRF spectroscopy, EDX takes place through electron excitation of the inner shell electrons. A high energy electron beam hits the sample, causing the ionisation of an inner shell electron forming vacancies. To regain stability an electron from a higher energy shell fills the vacancy, the energy difference between the shells is released in the form of characteristic X-rays. The areas of the peaks in the resulting spectra are proportional to the number of atoms of each element present^[107].

Within this study both a FEI Quanta 200 SEM with an EDX system attached and a SEM JCM-6000 PLUS were used to monitor changes to particle morphology during both the synthesis and ion exchange experiments. Approximately 0.0030g of synthesised or exchanged material was prepared on a stub and spluttered with a gold coating.

Chapter 4- Optimisation of Hydrothermal Synthesis

This section describes the synthesis of vanadium-natisite. Attempts to produce samples with doping levels of 5 and 10 %-vanadium-natisite were carried out. However, during the optimisation of the synthesis conditions it was found that paranatisite was first formed and transformed to natisite through prolonged heating.

4.0.0.0: Synthesis of Vanadium-Natisite

All chemicals used in this study were purchased from Sigma Aldrich, Fisher and used without further purification. Sodium hydroxide and tetraethyl orthosilicate were bought from Sigma Aldrich whilst vanadium acetylacetonate and titanium isopropoxide were bought from Fisher. Two methods were initially tested to determine the most efficient way to synthesise 5 %-vanadium-natisite. Method 1 (M1) followed the synthesis suggested by Kostov-Kytin *et al*^[3], whilst Method 2 (M2) followed the synthetic method suggested by Dimitri. G. Medvedev *et al*^[61].

4.0.1.0: Method 1 (M1): Synthesis Following 'Hydrothermal Synthesis and Successive Transformation of Paranatisite into Natisite,' Kostov-Kytin *et al*^[3].

5 %-vanadium-natisite was synthesised using the molar ratios of 0.15 VO₂: 2.85 TiO₂: 10 SiO₂: 20.00 Na₂O: 370 H₂O. In a typical reaction, 6.95 g of sodium hydroxide was added to 29 ml of deionised H₂O in a Teflon beaker and stirred at 300 rpm until the sodium hydroxide pellets fully dissolved, producing a clear solution. To this, 3.8 ml of titanium isopropoxide was added, causing the clear solution to turn a white precipitate, indicating the formation of Ti(OH)_x. Upon stirring, 0.175 g vanadium acetylacetonate was added to the beaker forming a dark orange/brown coloured solution, indicating dissolved vanadium in the

solution. Finally, 9.6 ml of tetraethyl orthosilicate is added and the mixture was stirred for an hour. It was found that 5 %-vanadium-natisite was synthesised in an oven at 200 °C for 5 days. Once cool, the resulting brown powder was washed with 1 litre of deionised water and left to dry.

4.0.1.1: Method 2 (M2): Synthesis following ‘Crystallization of Sodium Titanium Silicate with Sitinakite Topology: Evolution from the Sodium Nonatitane Phase,’ Dimitri. G. Medvedev *et al*^[61].

To synthesise 5 and 10 %-vanadium-natisite the reagents were added in the following molar ratios, 0.06 VO₂: 1.14 TiO₂: 0.88 SiO₂: 12.38 Na₂O: 208 H₂O and 0.24 VO₂: 1.08 TiO₂: 0.88 SiO₂: 12.38 Na₂O: 208 H₂O respectively. Typically, for the synthesis of 10 %-vanadium-natisite, 37.5 ml of deionised H₂O was added to a Teflon beaker. To which 4.95 g of sodium hydroxide was added and the mixture was left to stir until dissolved. Next, 3.07 g of titanium isopropoxide is added and the mixture was further stirred. Addition of titanium isopropoxide turns the colourless solution white following the appearance of a white precipitate. Following this, 0.319 g of vanadium acetylacetonate is added turning the solution dark orange/brown. Finally, 2.49 g of tetraethyl orthosilicate is added and the solution is left to stir for an hour. After an hour has elapsed, the solution appeared lighter in colour and was transferred to a hydrothermal autoclave. Optimisation of synthetic times as referred to in Table 5 saw that when the synthesis gel was placed in an oven at 200 °C for 12 days 10 %-vanadium-natisite was formed. Once cool, the brown powder was washed with 1 litre of deionised water and left to dry.

4.0.1.2: Results and Discussion of the Synthetic Methods

Both methods were carried out via hydrothermal synthesis. Hydrothermal synthesis allows for experimentation to take place at elevated pressures and temperatures by employing the use of autoclaves. Autoclaves are stainless steel vessels that are lined with a Teflon beaker which is corrosion resistant against acidic and alkaline solutions, can withstand elevated temperatures and pressures. Autoclaves can therefore mimic the natural environment for crystal formation, making them ideal apparatus for the synthesis of paranatisite and natisite.

Analysis of the experimental data collected following the M1 method suggested by Kostiv-Kytin *et al.* showed that pure phase 5 %-vanadium-natisite could be yielded after 5 days. Comparison to the M2 method, which is primarily used to synthesise sodium silicates with sitinakite typology, both pure phase 5 %-vanadium-paranatisite and natisite could be yielded at 7 and 72 hours of heating, respectively. The main difference in synthetic times between the M1 and M2 methods is believed to be attributed to the differences in molar ratios.

Due to time restraints, the M2 method was primarily adopted as the method yielded crystalline 5 % and 10 %-vanadium-paranatisite and natisite in a shorter period of time. To avoid repetition, unless stated otherwise analysis conducted will focus on the synthesis following the M2 method for 10 %-vanadium-natisite. Work conducted by Kostov-Kytin *et al.* suggested that the synthesis of Ti-natisite (un-doped natisite) took place after heating the synthesis gel for 6 days^[3]. However, during the synthesis of 10 %-vanadium-natisite it was seen that heating the synthesis gel between 4 - 11 days yielded mixed phases.

4.0.2.0: X-Ray Diffraction Analysis

X-ray diffraction patterns collected from synthesised materials showed that when compared to known Ti-paranatisite^[108] and Ti-natisite^[109] diffraction patterns, both vanadium-paranatisite and vanadium-natisite were present within samples that were placed in an oven for 4 - 11 days. When overlaid with known literature^[110] patterns it could be seen that no other impurities were within the sample and all peaks present were the result of either 10 %-vanadium-paranatisite or 10 %-vanadium-natisite. Synthesis times and products formed are given in Table 5. The X-ray diffraction pattern collected from 7 day synthesis is shown in Figure 16 with comparison to known literature of Ti-paranatisite^[108] and Ti-natisite^[109].

Table 5: Synthetic conditions and products after heating the 10 %-vanadium synthesis gel following the M2 method for 3 - 12 days.

10 %-Vanadium Transformation	Molar Ratios of Batch Synthesis (mol %)					Temperature (°C)
	Na ₂ O	TiO ₂	SiO ₂	VO ₂	H ₂ O	
	12.38	1.08	0.88	0.24	208.00	200.00

Synthesis Time (Days)	Product
3	10 %-vanadium-paranatisite
4	Mix phase
5	Mix phase
6	Mix phase
7	Mix phase
8	Mix phase
9	Mix phase
10	Mix phase
11	Mix phase
12	10 %-vanadium-natisite

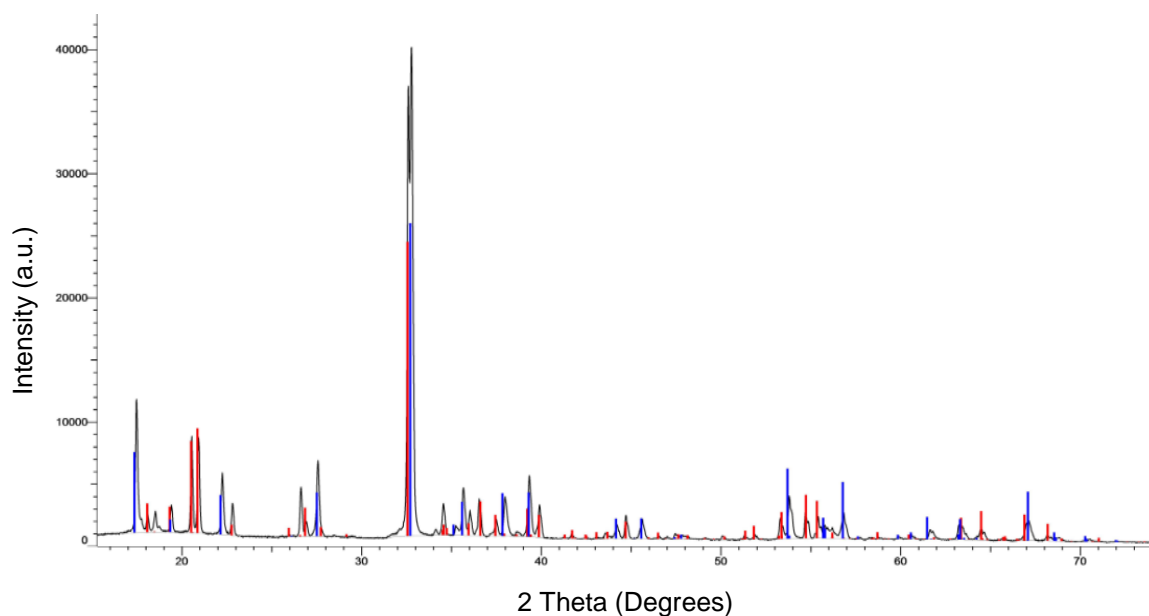


Figure 16: X-ray diffraction pattern of 10 %-vanadium doping following 7 day synthesis following the M2 method^[110]. (Ti-paranatisite- red overlay and Ti-natisite- blue overlay).

Analysis conducted on the samples showed the progressive transformation of vanadium-paranatisite to vanadium-natisite took place over a period of 12 days. In the X-ray diffraction patterns, characteristic paranatisite peaks such as those seen at 20.81 °, 20.95 °, 22.75 ° and 32.54 ° 2θ reduced in intensity over time until they were no longer present within the pattern. As these peaks continually reduced in intensity, characteristic natisite peaks were seen to appear and increase in intensity. Peaks seen at 17.45 °, 19.38 °, 22.27 °, 27.54 ° and 32.76 ° 2θ being prime examples.

Transformation of paranatisite to natisite is believed to take place through Ostwald ripening. Ostwald's rule states that the product formed first within the series is most like the parent structure and typically possesses the highest entropy and lowest thermodynamic stability. Through time a metastable form is produced allowing for the reaction to proceed to a product which possesses the lowest entropy and highest thermodynamic stability. Such transformation is believed to take place between paranatisite and natisite due to the super and undersaturated areas found around the titanium atom within the paranatisite structure. These areas allow for the influx of OH⁻ ions causing the structure to break apart and act as the secondary building blocks for the natisite structure.

Figures 17 and 18 shows the progressive transformation of vanadium-paranatisite to vanadium-natisite over the range of 12 days with Figure 17- 3 day synthesis representing pure phase vanadium-paranatisite and Figures 17- 4 - 11 day synthesis showing both phases and Figure 17- 12 day synthesis showing pure phase vanadium-natisite. (X-ray diffraction analysis for the successive transformation of 5 %-vanadium-paranatisite to 5 %-vanadium-natisite is shown in A1).

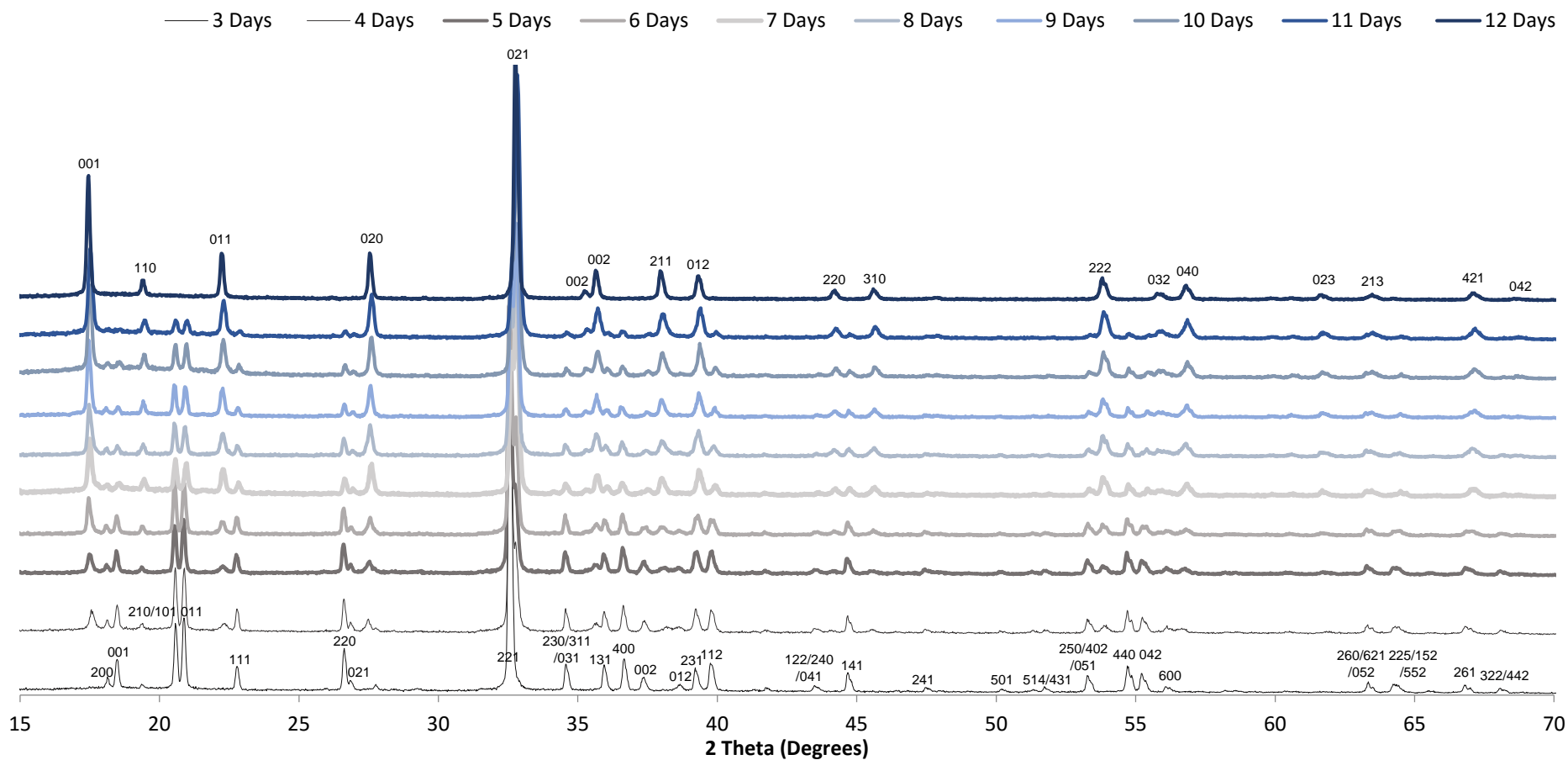


Figure 17: Stack view of X-ray diffraction patterns following the successive transformation of 10 %-vanadium-paranatisite to 10 %-vanadium-natisite.

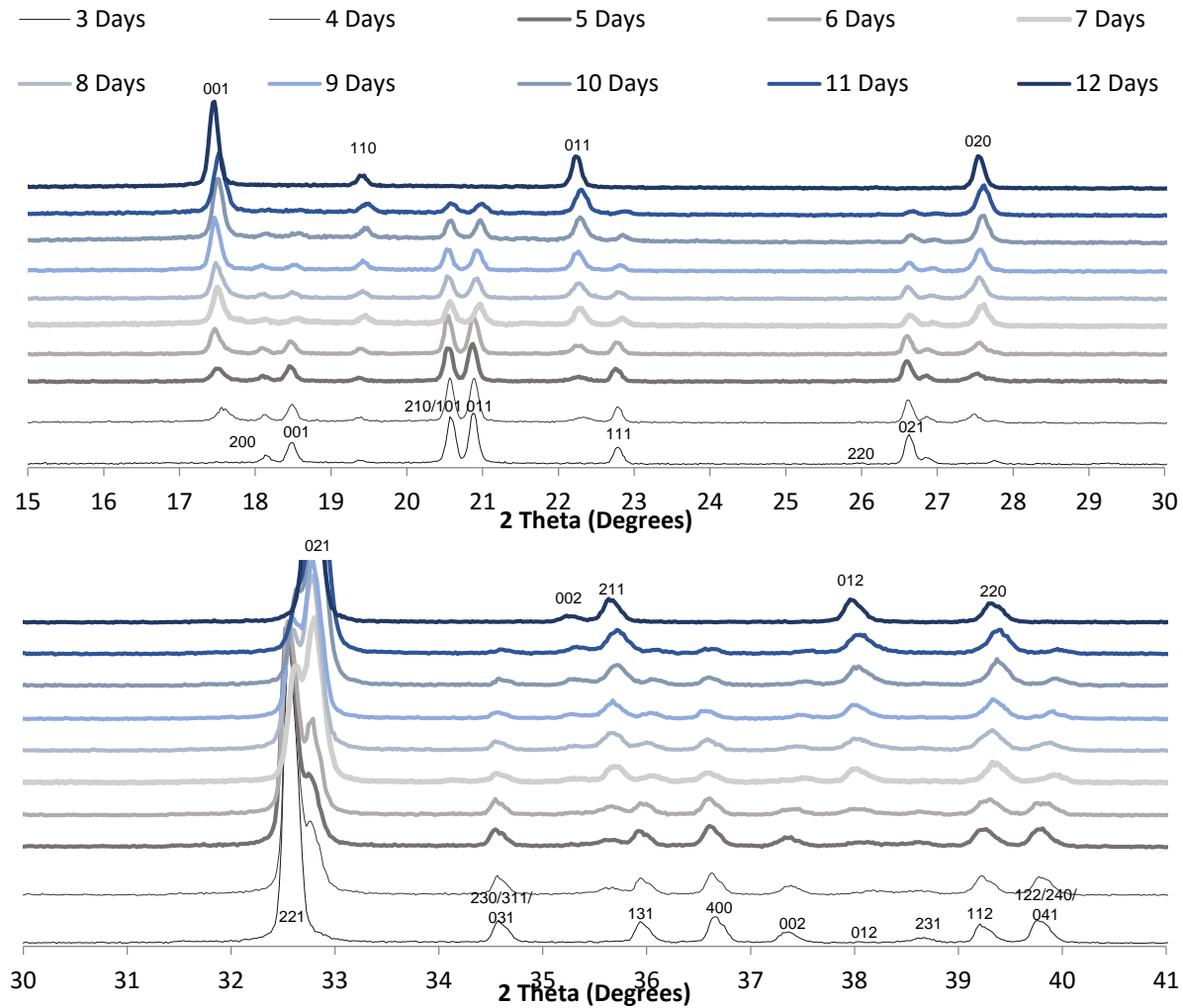


Figure 18: Close stack view of X-ray diffraction patterns following the successive transformation of 10 %-vanadium-paranatisite to 10 %-vanadium-natisite.

The peaks between 32.00° - 33.00° 2θ , as shown in Figure 19, clearly shows paranatisite to natisite phase transition. Samples which contained pure phase vanadium-paranatisite after heating for 3 days had a single peak at 32.54° 2θ . Prolonged heating brought about the transformation into vanadium-natisite. A shoulder appears at 32.76° 2θ after 4 days of heating which is characteristic of natisite. The peak increases in intensity with time, whilst the vanadium-paranatisite peak at 32.54° 2θ decreases in intensity until after 12 days of heating where only vanadium-natisite is present as shown in Figure 19.

In comparison to the synthetic times of Ti-paranatisite and Ti-natisite where Ti-paranatisite forms after heating for 28 hours and Ti-natisite forms after heating for 6 days^[3], introducing vanadium into the frameworks increases the synthetic times by 44 hours and 6 days respectively to Ti-paranatisite and Ti-natisite. One possible explanation for the increase in synthetic times could be due to vanadium stabilising the paranatisite phase by lowering the Gibbs Free energy value, as explained in Chapter 4.0.5.0.

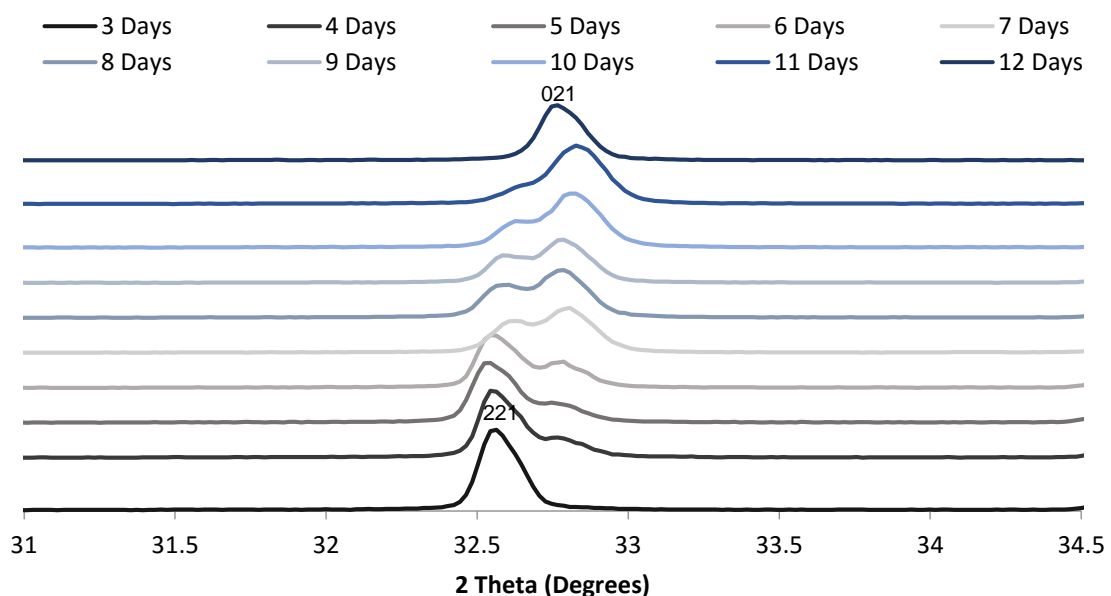


Figure 19: Peaks analysis at 32.00° - 33.00° 2θ following the successive transformation of 10 %-vanadium-paranatisite to 10 %-vanadium-natisite.

4.0.3.0: Rietveld Refinements

Rietveld refinements were used to monitor the phase transition of vanadium-paranatisite to vanadium-natisite through quantitative phase analysis. Atomic positions were analysed in order to determine any changes taking place during the progressive transformation.

Rietveld refinements upon the batch synthesised for 3 days showed the formation of 10 %-vanadium-paranatisite, whilst 4 - 7 days synthesis showed that 10 %-vanadium-paranatisite was the main phase within the samples, with natisite type impurities. Batches that were left for a synthesis time of 8 - 11 days showed that vanadium-natisite had become the main phase. After synthesis time of 12 days pure phase vanadium-natisite was present with no type of paranatisite impurities. Further analysis of the Rietveld results showed that there was little variation in lattice parameters and atomic coordinates indicating no distortion of the structures during the phase transition. Quantitative phase percentages are given in Table 6. (Bond lengths and angles are shown in A2 and A3. Refined lattice parameters, refinement statistics and final Rietveld fits for 3 - 12 day synthesis are shown in A4- A13).

Table 6: Percentage composition of vanadium-paranatisite and vanadium-natisite within mixed phased synthesised batches.

Synthetic Time (Days)	Vanadium-Paranatisite (%)	Vanadium-Natisite (%)
3	100.00	0.00
4	79.09	20.91
5	76.19	23.81
6	69.28	30.72
7	53.39	46.61
8	42.80	57.20
9	39.90	60.10
10	30.42	69.58
11	17.94	82.06
12	0.00	100.00

4.0.4.0: SEM Analysis

SEM analysis conducted upon all samples showed only one morphology was present during the phase transition even though two phases co-exist as shown in Figure 20. Between 3 - 6 days synthesis time the morphology showed a cross like particle. 7 - 8 days synthesised batches had equal distribution of both vanadium-paranatisite and vanadium-natisite whilst electron micrographs obtained from 9 - 12 days syntheses showed the spherical particles with a protruding cross typical of natisite^[82].

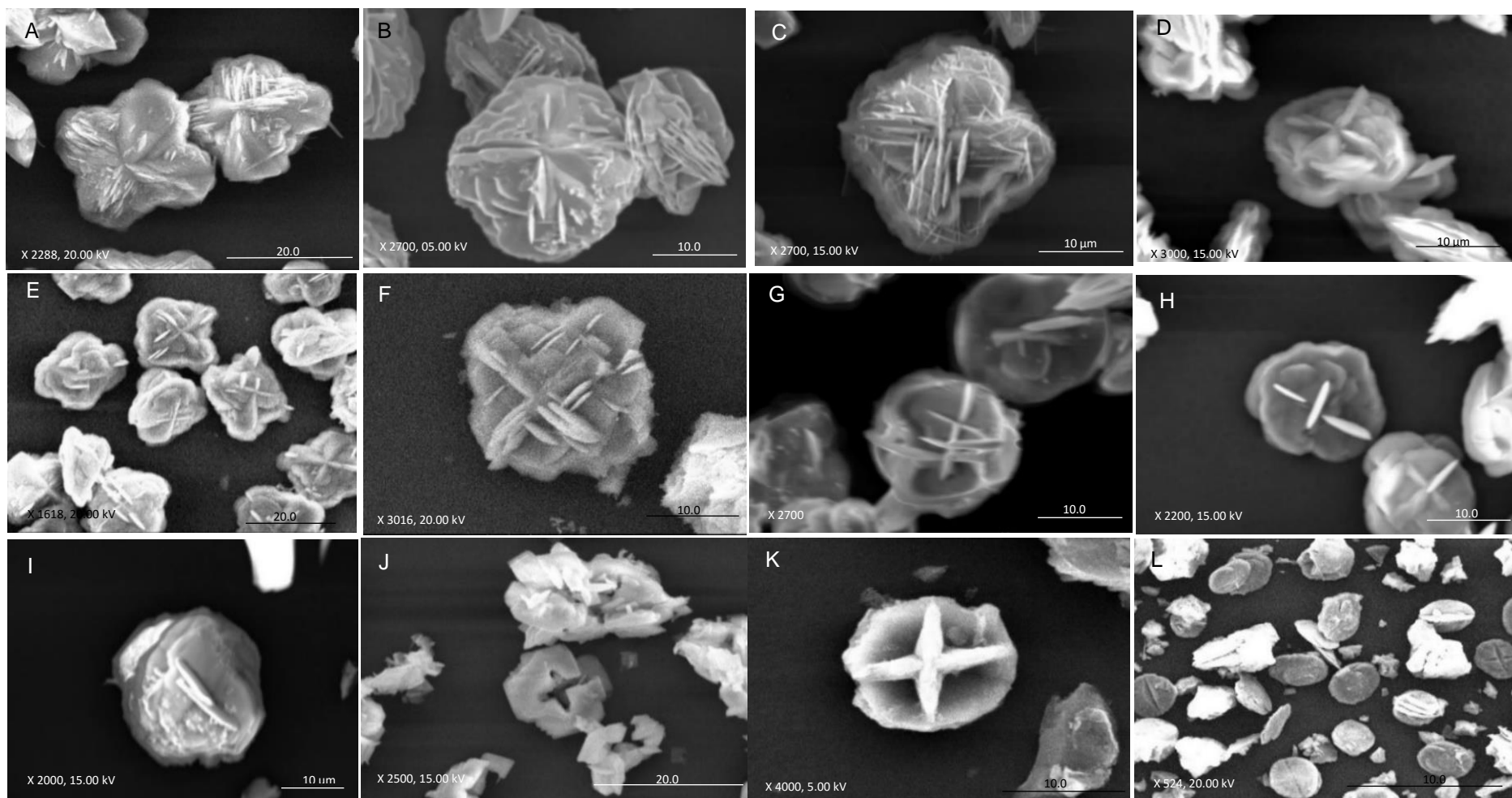


Figure 20: SEM images of synthesised material following 3-12 day synthesis. A: 3 day synthesis- paranatisite, B: 4 day synthesis- mix phase, C: 5 day synthesis- mix phase, D: 6 day synthesis- mix phase, E: 7 day synthesis- mix phase, F: 8 day synthesis- mix phase, G: 9 day synthesis- mix phase H: 10 day synthesis- mix phase, I: 11 day synthesis- mix phase, J, K and L: 12 day synthesis- vanadium- natisite.

4.0.5.0: Conclusion of Mixed Phased Synthesis

Comparison with the work conducted by Kostov-Kytin *et al*^[3]. showed that doping the Ti-frameworks with vanadium altered the synthesis times required for the synthesis of 5 % and 10 %-vanadium-natisite.

Introducing 5 %-vanadium into the synthesis gel, saw a decrease in synthesis times, producing vanadium-paranatisite after 7 hours of heating and vanadium-natisite formed after 3 days of heating.

Increasing the percentage of vanadium to 10 % within the synthesis gels showed an increase in synthesis times. Vanadium-paranatisite formed after 3 days of heating, whilst vanadium-natisite formed after heating the synthesis gel for 12 days. All synthetic conditions are referred to in Table 7.

Transformation of paranatisite to natisite occurs through Ostwald's rule of successive transformation with increase length in synthetic time favouring the formation of natisite. It can therefore be inferred that vanadium-paranatisite is the phase which exhibits highest entropy and lowest thermodynamic stability, when compared to vanadium-natisite^[3, 79, 111].

As stated by Ehrenfest, a first order phase transition occurs as both phases i.e. paranatisite (phase 1) and natisite (phase 2), can co-exist. According to Ehrenfest's rule, phase 1, paranatisite, has the highest Gibbs free energy value and lingers within a metastable phase when the synthetic batch has exceeded the critical temperature, T_c . Once the T_c has surpassed and conditions are no longer in equilibrium, the new phase, phase 2, can begin to form. Exceeding the T_c and equilibrium conditions allows phase 2 to dominate the crystal batch until phase 1 is no longer present. Phase 2, natisite, is known to be the more stable phase as the Gibbs free energy value is lower than that of phase 1, paranatisite^[112].

Table 7: Synthetic conditions for vanadium-natisite following the M1 and M2 methods.

Method	Molar Ratios of Batch Synthesis					Experimental Conditions	
	Na ₂ O	TiO ₂	SiO ₂	VO ₂	H ₂ O	Time (Hours)	Temperature (°C)
M1 5 %-Vanadium-Natisite	20.00	2.85	10.00	0.15	370.00	144.00	200.00
M2 5 %-Vanadium-Paranatisite	12.38	1.14	0.88	0.06	208.00	7.00	200.00
M2 5 %-Vanadium-Natisite	12.38	1.14	0.88	0.06	208.00	72.00	200.00
M2-10 %- Vanadium-Natisite	12.38	1.08	0.88	0.24	208.00	72.00	200.00
M2-10 %- Vanadium-Paranatisite	12.38	1.08	0.88	0.24	208.00	288.00	200.00

4.1.0.0: Characterisation of Vanadium-Paranatisite

4.1.1.0: X-Ray Diffraction Analysis of Vanadium-Paranatisite

4.1.1.1: 5 %-Vanadium-Paranatisite following the M2 Method

X-ray diffraction analysis showed that 5 %-vanadium-paranatisite had been synthesised. However, on most occasions a poorly crystalline phase with a degree of amorphous content was produced. Upon a few attempts (around 20 %), crystalline phases were achieved.

Refined cell parameters were $a = 9.8172 \text{ \AA} (2)$, $b = 9.2017 \text{ \AA} (2)$, and $c = 4.82602 \text{ \AA} (7)$, a cell volume of $435.96 \text{ \AA}^3 (1)$ and an R_{wp} value of 5.750 %. When compared to Ti-paranatisite^[108], 5 %-vanadium-paranatisite showed a reduction in the a axis by $-0.010 \text{ \AA} (3 \text{ d.p.})$ and an increase in both b and c axes by $0.035 \text{ \AA} (3 \text{ d.p.})$ and $0.035 \text{ \AA} (3 \text{ d.p.})$ respectively, with an overall increase in volume by $3.646 \text{ \AA}^3 (3 \text{ d.p.})$. Such changes to the unit cell dimensions when compared to known Ti-paranatisite literature could be attributed to several factors. These factors include the introduction of vanadium within the titanium silicate framework, the position of vanadium within the framework and the synthetic conditions used within the synthesis process such as aging of the synthesis gel, the rate of speed the gel was stirred at during the aging process and the molar ratio used to produce the synthetic gel.

Both amorphous and crystalline 5 %-vanadium-paranatisite materials were overlaid with Ti-paranatisite^[108] and shown in Figure 21.

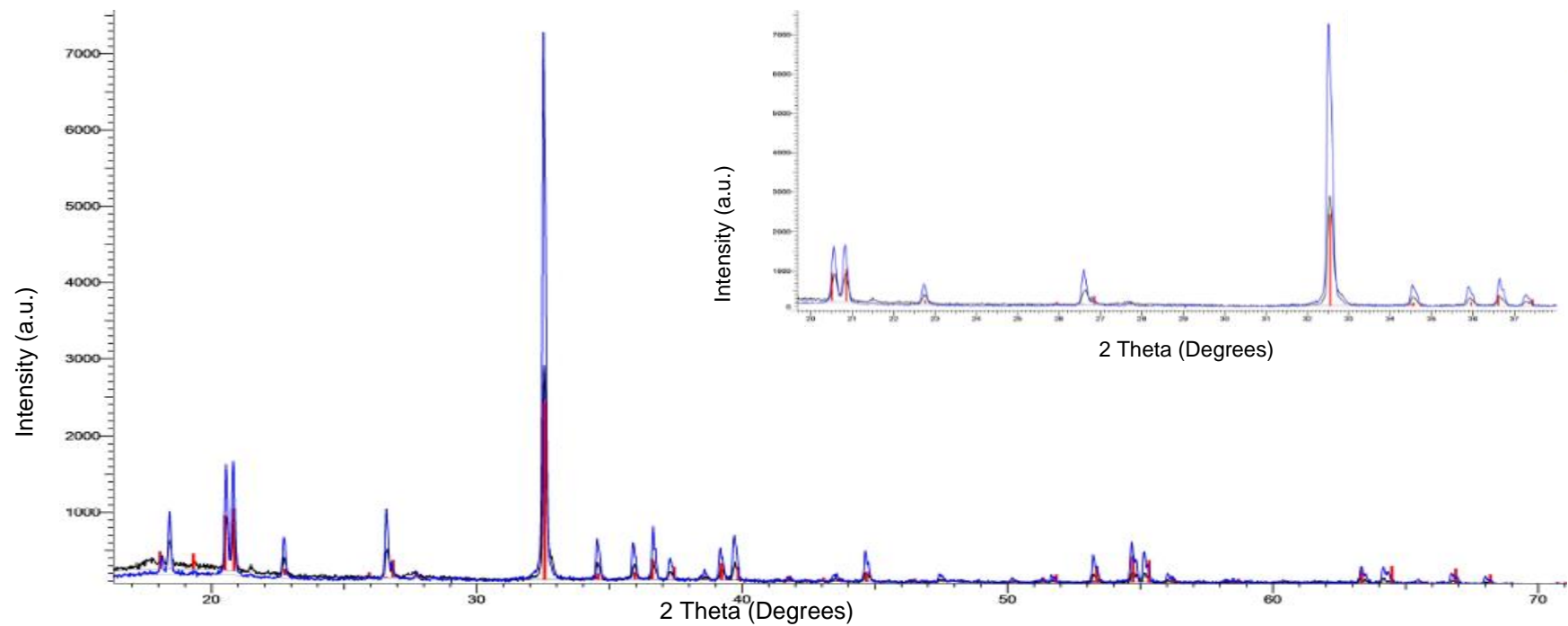


Figure 21: Overlay of amorphous and crystalline 5 %-vanadium-paranatisite XRD patterns with known Ti-paranatisite literature^[108]. (Amorphous 5 %-vanadium-paranatisite pattern- black, crystalline 5 %-vanadium-paranatisite pattern- blue and known Ti-paranatisite literature pattern- red^[108])

4.1.1.2: 10 %-Vanadium-Paranatisite following the M2 Method

In contrast, 10 %-vanadium-paranatisite was more crystalline with a high degree of purity, as shown in Figure 22. The refined lattice parameters were $a = 9.8282 \text{ \AA} (1)$, $b = 9.2060 \text{ \AA} (1)$ and $c = 4.82489 \text{ \AA} (7)$, a cell volume of $436.54 (1) \text{ \AA}^3$ and an R_{wp} of 5.408 %. Comparison of 10 %-vanadium-paranatisite with Ti-paranatisite^[108] showed an increase in all three axes with the a axis increasing by $0.0012 \text{ \AA} (3 \text{ d.p.})$, the b axis increasing by $0.039 \text{ \AA} (3 \text{ d.p.})$ and the c axis increasing by $0.026 \text{ \AA} (3 \text{ d.p.})$. The overall elongation of the cell parameters saw the unit cell volume increase by $4.226 \text{ \AA}^3 (3 \text{ d.p.})$. Such changes to the unit cell dimensions when compared to known Ti-paranatisite literature could be attributed to several factors. These factors include the introduction of vanadium within the titanium silicate framework, the position of vanadium within the framework and the synthetic conditions used within the synthesis process such as aging of the synthesis gel, the rate of speed the gel was stirred at during the aging process and the molar ratio used to produce the synthetic gel.

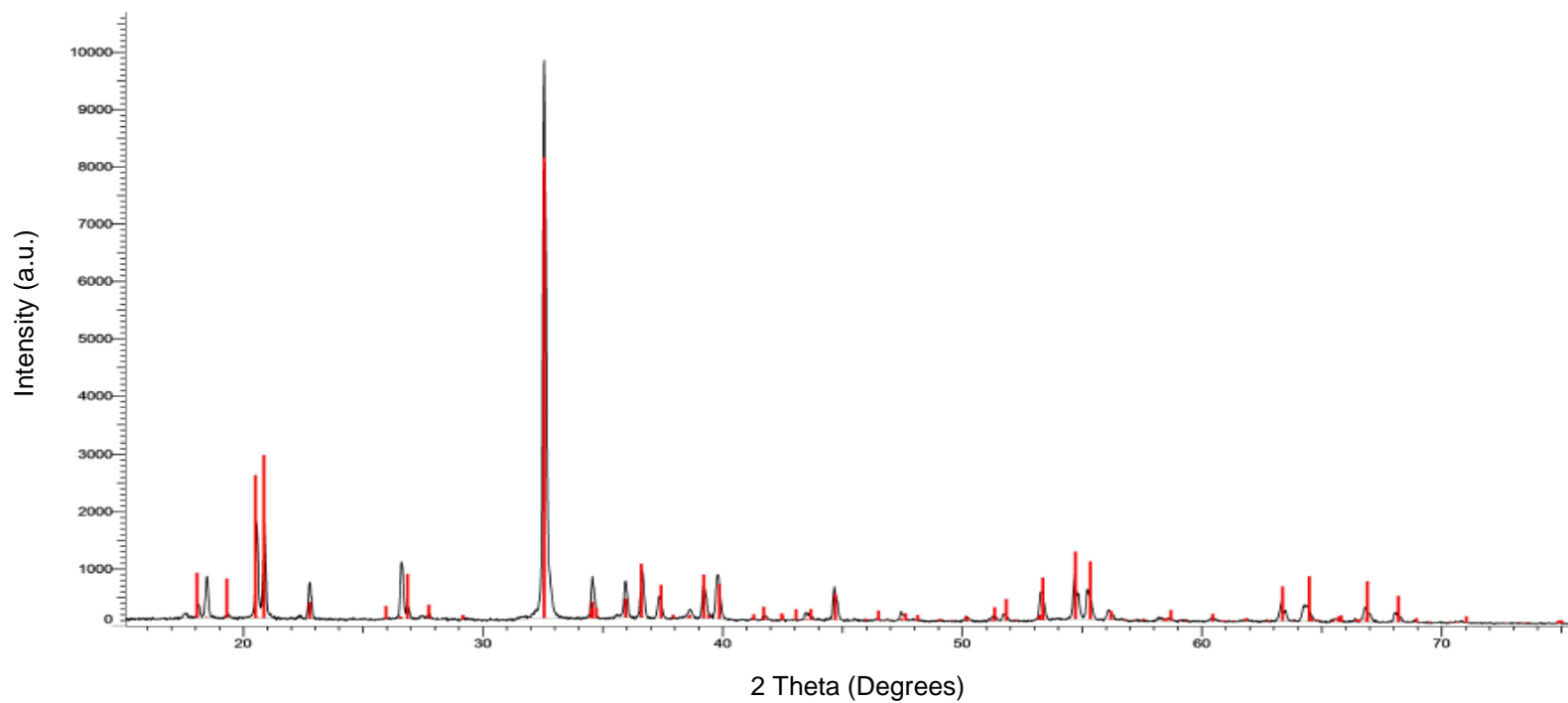


Figure 22: Overlay of 10 %-vanadium-paranatisite XRD pattern with known Ti-paranatisite literature^[108]. (10 %-vanadium-paranatisite pattern- black and known Ti-paranatisite literature pattern- red^[108]).

4.1.1.3: Results and Discussion of the Synthetic Methods

Following the method suggested by Dimitri. G. Medvedev *et al*^[61], several changes were made to the hydrothermal synthesis of vanadium-paranatisite in order to obtain a pure phase product.

The first factor affecting the successful synthesis of vanadium-paranatisite was the heating time. It was noted that increasing the percentages of vanadium within the framework increased the length of the heating stage needed for the synthesis of pure paranatisite. The optimum heating time for pure phase 5 %-vanadium-paranatisite was 7 hours whilst 10 %-vanadium-paranatisite was produced after 72 hours.

It was also noted that the age of the reagents used had a role to play in the successful synthesis of pure phases with titanium isopropoxide being the main factor. Using a bottle of titanium isopropoxide that had been opened for a longer period would favour formation of the two phases. However, unopened bottles of titanium isopropoxide favoured the formation of pure vanadium-paranatisite when using times reported in Table 7. Upon contact with moisture within the atmosphere titanium isopropoxide becomes hydrolysed to $Ti(OH)_x$. The increased age of the bottle therefore contains an increased concentration of $Ti(OH)_x$ due to increased exposure to the atmosphere. It is therefore postulated that hydrolysis of titanium isopropoxide to $Ti(OH)_x$ prevents the formation of crystalline phases such as paranatisite and natisite.

Furthermore, increasing the percentage of vanadium introduced into the synthesis gel increased the crystallinity of the material formed. Attempts following the methods given by Dimitir. G. Medvedev *et al*^[61], and Kostov-Kytin *et al*^[3], to synthesise Ti-paranatisite were not successful.

4.1.2.0: Rietveld Refinement

Rietveld refinement of the powder diffraction data was carried out to compare crystal structures to known literature. Vanadium was not included in the refinements due to the almost identical X-ray scattering power. The ability of an atom to cause X-ray scattering is dependent upon the electron density surrounding the nucleus of the atom. As titanium and vanadium both have 22 and 23 electrons respectively, their ability to scatter X-rays is almost identical and therefore both elements can be treated as Ti within the refinement.

To avoid repetition complete structural analysis via Rietveld refinements will solely focus upon 10 %-vanadium-paranatisite. Refined atomic coordinates of 10 %-vanadium-paranatisite are denoted in Table 8, selected bond distances are shown in Table 9 and bond angles are denoted in Table 10. Refined lattice parameters and refinement statistics for 10 %-vanadium-paranatisite are shown in Table 11 and the final Rietveld fit of 10 %-vanadium-paranatisite is shown in Figure 23. (Refined atomic coordinates, bond lengths. Refined lattice parameters, refinement statistics and final Rietveld fits for 5 %-vanadium-paranatisite are shown in A15).

Table 8: Refined atomic coordinates for 10 %-vanadium-paranatisite.

Site	X	Y	Z	Occ	beq
Ti1	0	0	0	0.75	9.1 (3)
Ti2	0.25	0.5	0.536 (1)	1	6.7 (2)
Si1	0	0.2486 (9)	0.5	1	5.9 (2)
Na1	0.25	0	0.417 (2)	1	8.8 (4)
Na2	0	0.5	0	1	5.1 (3)
Na3	0.25	0.2432 (8)	0.988 (2)	1	5.6 (2)
O1	0.6124 (5)	0.351 (1)	0.354 (1)	1	5.9 (2)
O2	0.4299 (5)	0.151 (1)	0.259 (1)	1	5.0 (2)
O3	0.312 (1)	0	0.839 (3)	0.5	2.9 (6)
O4	0.25	0.5	0.178 (2)	1	4.7 (5)

Table 9: Refined bond lengths of 10 %-vanadium-paranatisite.

Bond	Length (Å)	Bond	Length (Å)
Na1-O2	2.379 (5)	Na3-O4	2.516 (5)
Na1-O3	2.11 (1)	O1-Si1	1.607 (4)
Na1-O3	2.86 (1)	O2-Si1	1.634 (4)
Na2-O1	2.456 (4)	O2-Ti1	1.987 (4)
Na2-O4	2.600 (2)	O3-Ti1	2.029 (8)
Na3-O1	2.344 (6)	O1-Ti2	2.008 (4)
Na3-O3	2.444 (5)	O4-Ti2	1.741 (8)
Na3-O2	2.345 (5)		

Table 10: Refined bond angles of 10 %-vanadium-paranatisite.

Bond	Angle (°)	Bond	Angle (°)	Bond	Angle (°)
O3-Na1-O2	121.1 (3)	O1-Na3-O3	107.4 (3)	Na3-O3-Na1	69.4 (2)
O3-Na1-O2	95.8 (2)	O1-Na3-O4	82.1 (2)	Ti2-O4-Na3	110.6 (2)
O3-Na1-O3	175.7 (1)	O2-Na3-O2	98.0 (2)	Na3-O4-Na2	83.4 (1)
O3-Na1-O3	151.9 (4)	O2-Na3-O3	69.5 (2)	Na2-O4-Na2	141.8 (3)
O2-Na1-O2	96.2 (2)	O2-Na3-O3	90.8 (3)	O1-Si1-O1	110.8 (4)
O2-Na1-O2	71.6 (2)	O2-Na3-O4	98.6 (2)	O1-Si1-O2	106.6 (2)
O2-Na1-O3	62.1 (2)	O3-Na3-O4	165.9 (2)	O2-Si1-O2	112.4 (4)
O2-Na1-O3	80.7 (2)	Si1-O2-Ti1	133.8 (2)	O2-Ti1-O2	88.9 (2)
O2-Na1-O2	142.4 (4)	Si1-O2-Na3	120.3 (3)	O2-Ti1-O2	180.000
O2-Na1-O2	93.2 (2)	Si1-O2-Na1	114.0 (2)	O2-Ti1-O3	94.3 (2)
O1-Na2-O1	68.9 (2)	Ti1-O2-Na3	100.2 (2)	O2-Ti1-O3	85.7 (2)
O1-Na2-O1	111.1 (2)	Ti1-O2-Na1	92.8 (2)	O2-Ti1-O2	91.1 (2)
O1-Na2-O1	180.000	Na3-O2-Na1	80.0 (2)	O2-Ti1-O3	64.2 (3)
O1-Na2-O4	78.4 (1)	Ti1-O3-Na1	129.2 (2)	O3-Ti1-O3	180.000
O1-Na2-O4	101.6 (1)	Ti1-O3-Na3	95.8 (2)	O4-Ti2-O1	105.6 (1)
O1-Na3-O1	70.1 (2)	Ti1-O3-Na1	78.9 (3)	O1-Ti2-O1	84.2 (2)
O1-Na3-O2	95.8 (1)	Na1-O3-Na3	103.3 (3)	O1-Ti2-O1	148.8 (2)
O1-Na3-O2	165.8 (2)	Na1-O3-Na1	151.9 (4)	O1-Ti2-O1	87.5 (2)
O1-Na3-O3	91.3 (3)	Na3-O3-Na3	133.8 (4)		

Table 11: Refined lattice parameters and refinement statistics for 10%-vanadium-paranatisite

Parameter	Ti-Paranatisite ^[108]	10 %-Vanadium-Paranatisite
System	Orthorhombic	Orthorhombic
Space Group	P m m a	P m m a
<i>a</i> (Å)	9.827	9.8282 (1)
<i>b</i> (Å)	9.167	9.2060 (1)
<i>c</i> (Å)	4.799	4.82489 (7)
<i>V</i> (Å ³)	432.3136	436.54 (1)
R _{WP} (%)	-	5.408
R _P (%)	-	4.094
R _{exp} (%)	-	2.647

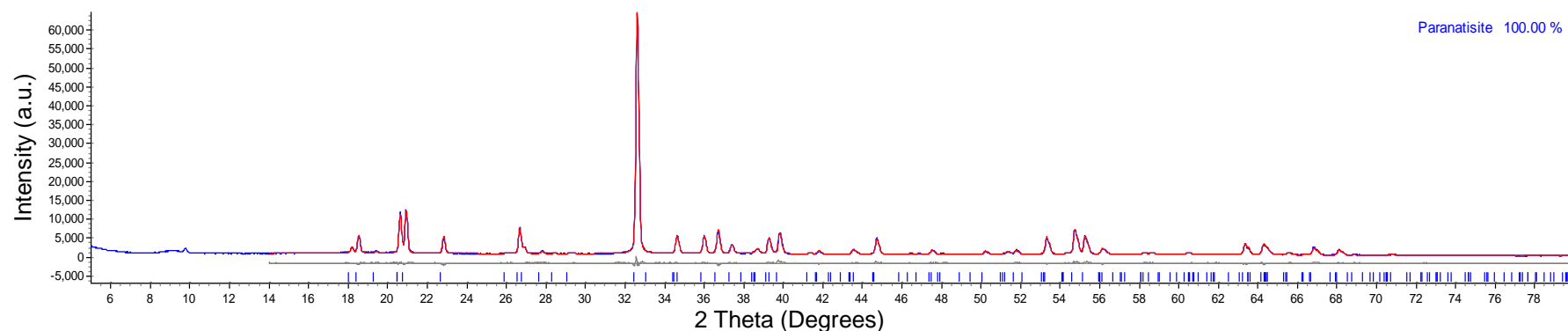


Figure 23: Final Rietveld fit of 10 %-vanadium-paranatisite. (Synthesised pattern –blue, known literature- red^[108] and difference plot ($I_{syn}-I_{known}$)-grey).

4.1.3.0: Structural Determination

4.1.3.1: Titanium/ Vanadium Environments

Titanium holds two crystallographic sites in the paranatisite structure. The first titanium site (Ti1) has a coordination number of six. Each octahedral environment has four Ti1-O2 bonds and two Ti1-O3 bonds which are of 1.987 (4) Å and 2.029 (8) Å respectively and has an overall -2 negative charge. As shown in Figure 24.

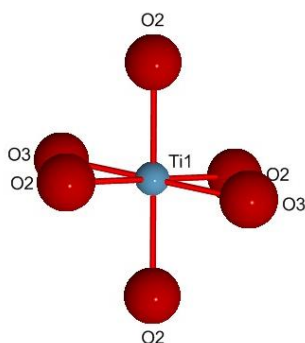


Figure 24: Ti1 octahedrally coordinated to O2 and O3 atoms. (Titanium atoms- light blue and oxygen atoms- red).

The second titanium site (Ti2) has square pyramidal coordination, as shown in Figure 25. With four Ti2-O1 bonds with a length of 2.008 (4) Å and a single Ti2-O4 bond of 1.741 (8) Å with an overall -1 charge.

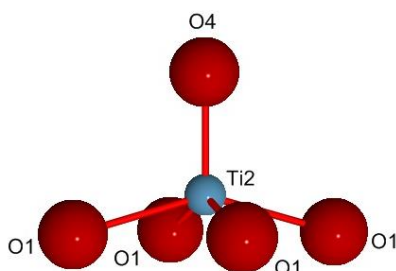


Figure 25: Ti2 coordinated in a square pyramidal environment to O1 and O4 atoms. (Titanium atoms- light blue and oxygen atoms- red).

4.1.3.2: Silicon Environment

There is only one silicon site in the structure denoted as Si1 which is tetrahedrally coordinated to two O1 and two O2 atoms, as shown in Figure 26. The lengths of the bonds shown as Si1-O1 are 1.607 (4) Å and the bonds shown as Si1-O2 are 1.634 (4) Å in length.

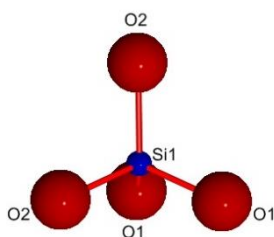


Figure 26: Si1 coordinated in a tetrahedrally coordinated environment to O1 and O2 atoms.
(Silicon atoms- dark blue and oxygen atoms- red).

4.1.3.3: Sodium Environments

In the paranatisite structure there are three crystallographic sites, Na1, Na2 and Na3. The first sodium environment (Na1), as shown in Figure 27, is coordinated to six different oxygen atoms, four of which have slightly longer bond distances. The oxygen atoms labelled O2, form four bonds at 2.379 (5) Å, whilst the oxygen atoms labelled O3 form two bonds. These bonds can be located at the positions labelled as O3 at a distance of 2.860 (1) Å (0.5 occupancy), forming a pseudo octahedral coordinated site.

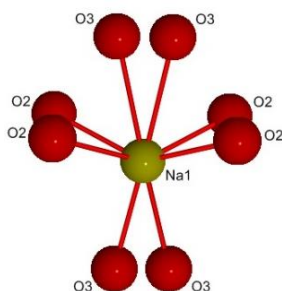


Figure 27: Na1 in a pseudo octahedral coordinated environment to O2 and O3 (0.5 occupancy) atoms. (Sodium atoms-yellow and oxygen atoms- red).

The second sodium site (Na2) has a coordination number of six, as shown in Figure 28. From Rietveld refinements, there are two Na2-O4 bonds of a distance of 2.600 (2) Å and four Na2-O1 bonds at 2.455 (4) Å. It is noted that this environment also forms layers. The Na2 atoms form layers between the silicate layers.

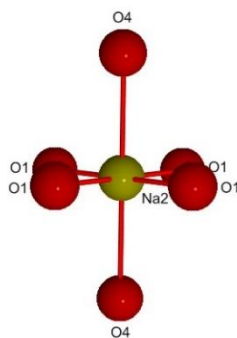


Figure 28: Na2 coordinated in an octahedral environment to O1 and O2 atoms. (Sodium atoms- yellow and oxygen atoms- red).

The third and final sodium site (Na3) is six coordinated as shown in Figure 29 and connects the other two sodium atoms through bridging oxygens. There are two Na3-O1 bonds at a distance of 2.344 (6) Å, two Na3-O2 bonds at a distance of 2.345 (5) Å, one Na3-O4 bond of a distance of 2.516(5) Å and one Na3-O3 bond of 2.444 (5) Å which can be located at either position labelled as O3 (0.5 occupancy), forming a distorted octahedron.

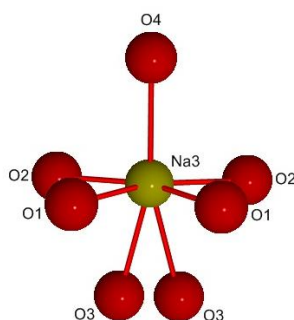


Figure 29: Na3 six coordinated (distorted octahedron) to O1, O2, O3 (0.5 occupancy) and O4. (Sodium atoms- yellow and oxygen atoms- red).

4.1.3.4: 10 %-Vanadium-Paranatisite Overall Structure.

The overall structure of the refined 10 %-vanadium-paranatisite structure is shown in Figure 30.

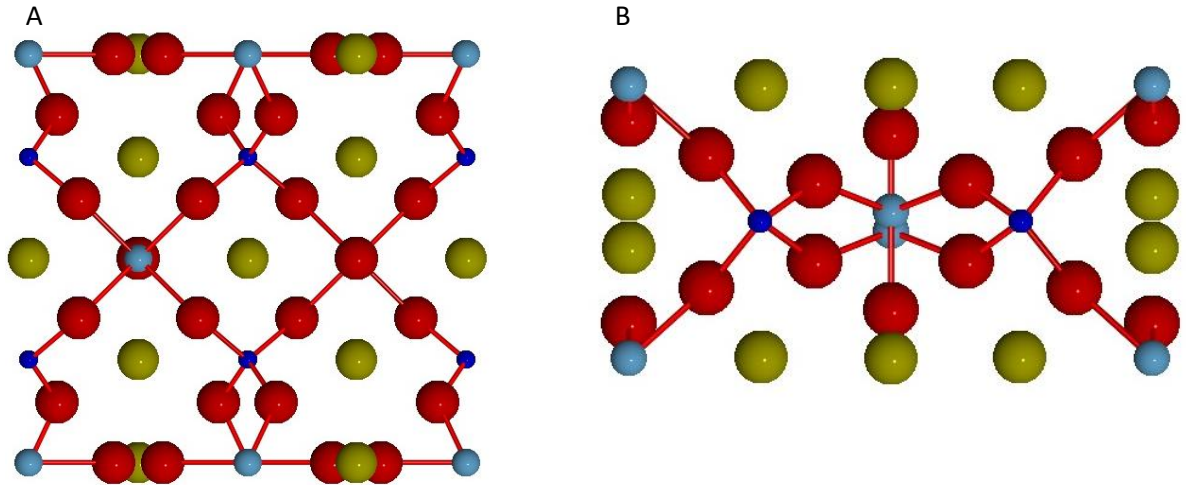


Figure 30: Overall structure of 10 %-vanadium-paranatisite. A- direction 001 and B- direction 100. (Titanium atoms- light blue, silicon atoms- dark blue, sodium atoms- yellow and oxygen atoms- red). (Labels were removed for clarity).

4.1.3.5: Results and Discussion of Paranatisite, 5 %-Vanadium-Paranatisite and 10 %-Vanadium-Paranatisite.

Rietveld refinements conducted upon 5 % and 10 %-vanadium-paranatisite materials showed that increasing the vanadium content from 5 % to 10 % caused a general increase in Ti-O bond distances, specifically the Ti2-O4 and Ti2-O1 bonds of the five-coordinate site. The bonds of the six-coordinate site showed an elongation of the Ti1-O3 bonds and contraction of the Ti1-O2 bonds.

It is believed that the increase in Ti-O bond lengths with regards to the five coordinated environments can be attributed to the slight increase of the vanadium ionic radius when compared to titanium. When titanium is in a +4-oxidation state and is five-coordinate the ionic radius is $\sim 0.51 \text{ \AA}$ whilst the ionic radius of vanadium in this coordination is $\sim 0.53 \text{ \AA}$ ^[113].

For the six-coordinate site there is a decrease in the length of the Ti-O bond. The literature states that the ionic radius of titanium in this coordination is $\sim 0.605 \text{ \AA}$ whilst vanadium has an ionic radius $\sim 0.58 \text{ \AA}$ ^[113].

It can be postulated that the increase of Ti-O bond lengths cause contraction of the Na-O and O2-Si1 bond lengths allowing for similar lattice parameters compared to the un-doped material. All bond lengths are depicted in Table 12.

It must be noted that the variation in both ionic radii and bond lengths is minimal and therefore may be the result of synthetic conditions. To verify that the differences in bond length are the result of vanadium doping, further research would have to be conducted.

Table 12: Bond lengths of Ti-paranatisite, 5 %-vanadium-paranatisite and 10 %-vanadium-paranatisite and the difference in lengths between 5 %-vanadium-paranatisite and 10 %-vanadium-paranatisite.

Bond	Paranatisite Length (Å)^[108]	5 %- Vanadium- Paranatisite Length (Å)	10 %- Vanadium- Paranatisite Length (Å)	Difference in length of bond between 10 % and 5 %-Vanadium Paranatisite (Å)
Na1-O2	2.3785	2.387 (6)	2.379 (5)	-0.0078
Na1-O3	2.3194	2.11 (1)	2.11 (1)	-0.001
Na1-O3	2.6091	2.88 (1)	2.86 (1)	-0.021
O3-O3	1.1203	1.26 (2)	1.18 (2)	-0.08
Na2-O1	2.4340	2.465 (5)	2.456 (4)	-0.0098
Na2-O4	2.6610	2.609 (3)	2.600 (2)	-0.0094
Na3-O1	2.3484	2.359 (7)	2.344 (6)	-0.0146
Na3-O2	2.3998	2.366 (6)	2.345 (5)	-0.0214
Na3-O3	2.4492	2.450 (7)	2.444 (5)	-0.006
Na3-O4	2.4354	2.523 (7)	2.516 (5)	-0.0067
O1-Si1	1.6273	1.614 (6)	1.607 (4)	-0.0062
O2-Si1	1.6377	1.618 (6)	1.634 (4)	0.0162
O2-Ti1	1.9355	1.997 (6)	1.987 (4)	-0.0102
O3-Ti1	1.9921	1.978 (9)	2.029 (8)	0.0503
O1-Ti2	1.9375	1.975 (5)	2.008 (4)	0.0337
O4-Ti2	1.7132	1.714 (9)	1.741 (8)	0.0268

4.1.4.0: Vanadium-Paranatisite Morphology

Although there has been some research into the structure of paranatisite, little information has been published upon the morphology of the particles. During this study, it was observed that changes to the percentage of vanadium had no real effect upon the particle morphology.

SEM images showed that vanadium-paranatisite typically adopts a cross like structure. Some of the units have a larger proportion of protruding rectangular shapes on the surface of the structure, whilst others, have only a few. Electron micrographs of vanadium-paranatisite is shown in Figure 31.

Particle size was measured from the images obtained for both 5 % and 10 %-vanadium-paranatisite and particle sizes ranging between 15 - 23 μm in diameter were recorded.

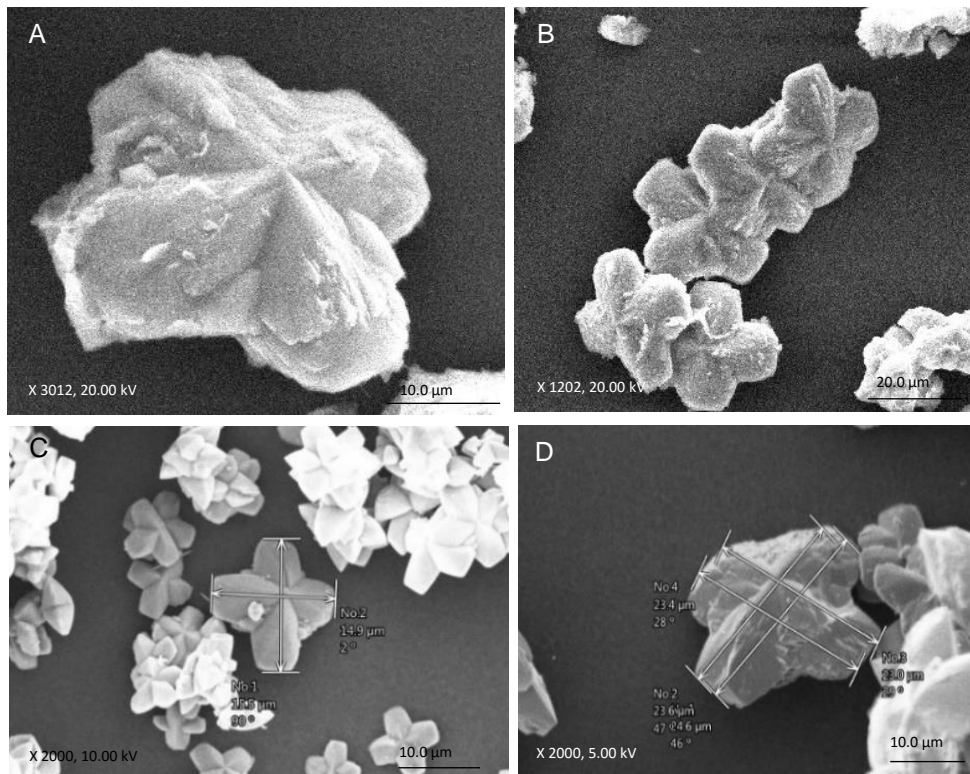


Figure 31: SEM images of vanadium-paranatisite. A: 10 %-vanadium-paranatisite, B: 5 %-vanadium-paranatisite, C: 5 %-vanadium-paranatisite and D: 10 %-vanadium-paranatisite.

4.1.5.0: EDX Analysis

The EDX results showed that the atomic percentage of vanadium had doubled from 5 % to 10 %-vanadium doping and the percentage of titanium had decreased from 5 % to 10 %-vanadium materials suggesting the successful replacement of titanium with vanadium.

However, the percentage of vanadium within the framework is lower than to be expected. One possible explanation for this is due to the overlap of titanium and vanadium emission lines. EDX analysis conducted was unable to differentiate the two elements and therefore quantitative analysis of the two elements was not possible. With regards to oxygen, sodium and silicon; between the two frameworks, the difference of atomic percentage was negligible. Average elemental compositions over a number of data points are recorded in Table 13. (EDX Spectra for 5 % and 10 %-vanadium-paranatisite are shown in A16 and A17 respectively).

Table 13: Elemental composition of 5 % and 10 %-vanadium-paranatisite.

Element	5 %-Vanadium-Paranatisite		10 %-Vanadium-Paranatisite	
	Weight (%)	Atomic (%)	Weight (%)	Atomic (%)
O K	38.77 (\pm 2.67)	55.74 (\pm 3.07)	39.05 (\pm 5.49)	54.72 (\pm 5.02)
Na K	19.75 (\pm 3.21)	19.76 (\pm 3.17)	22.63 (\pm 6.34)	22.05 (\pm 5.22)
Si K	13.55 (\pm 3.79)	11.10 (\pm 3.09)	16.01 (\pm 2.64)	12.80 (\pm 2.68)
Ti K	27.42 (\pm 3.07)	13.17 (\pm 1.50)	20.45 (\pm 5.69)	9.60 (\pm 2.96)
V K	0.51 (\pm 0.44)	00.23 (\pm 0.29)	1.87 (\pm 1.41)	0.83 (\pm 0.62)
Total	100.00	100.00	100.00	100.00

4.1.6.0: XRF Analysis

Analysis conducted via XRF indicated the presence of both silicon titanium and vanadium in the samples. Although quantitative data could not be provided by the model used, the intensities of the peaks could be used semi-quantitatively. A list of characteristic XRF emission lines for silicon, titanium and vanadium within 10 %-vanadium-paranatisite is shown in Table 14.

Table 14: List of characteristic XRF emission lines for silicon, titanium and vanadium within 10 %-vanadium-paranatisite.

Element	Energies (keV)	Emission
Silicon	1.73	$K_{\alpha 1}$, $K_{\alpha 2}$
Titanium	4.51	$K_{\alpha 1}$, $K_{\alpha 2}$
	4.95	$K_{\beta 1}$
Vanadium	4.95	$K_{\alpha 1}$, $K_{\alpha 2}$
	5.43	$K_{\beta 1}$

Analysis of both 5 % and 10 %-vanadium-paranatisite showed the $K_{\beta 1}$ peak appearing at 5.43 keV suggesting that vanadium was present within both materials. It can also be seen that the peak at 5.43 keV increases in intensity from 5 % to 10 %-vanadium doping which may be indicative of an increase of vanadium within the framework. The XRF spectra of 5 % and 10 %-vanadium-paranatisite are shown in Figure 32.

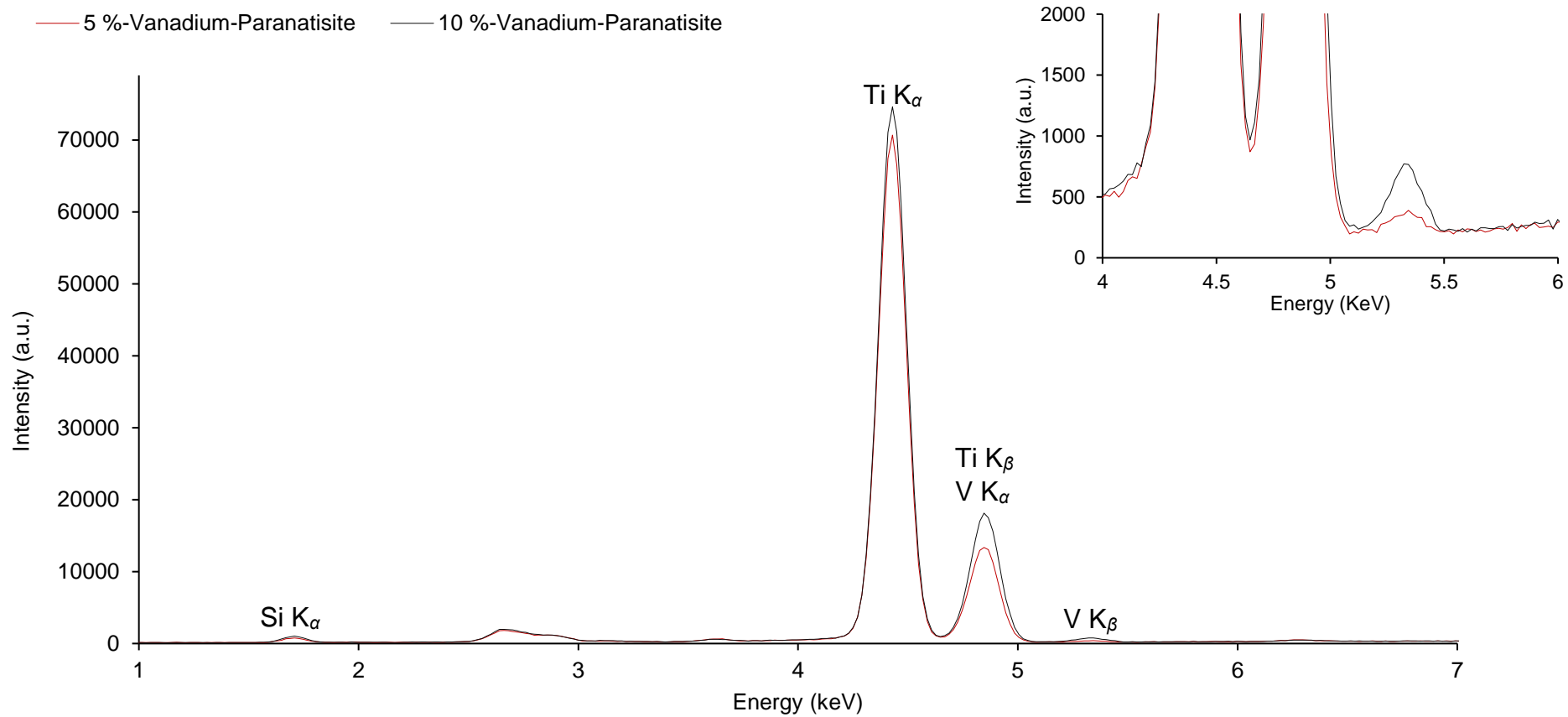


Figure 32: Overlay of XRF spectra for 5 and 10 %-vanadium-paranatisite.

4.1.7.0: ICP-MS Analysis

The filtrate was analysed and a percentage average was recorded for the vanadium-paranatisite frameworks. Assuming no vanadium was lost during sample preparation, on average, 5 %-vanadium-paranatisite contained 4.60 % (\pm 53) vanadium and 10 %-vanadium-paranatisite contained on average, 7.97 % (\pm 0.19) vanadium within the framework. (Vanadium percent doping levels of individual samples for 5 % and 10 %-vanadium-paranatisite are shown in A18).

4.1.8.0: Conclusion of the Synthesis of Vanadium-Paranatisite

Analysis conducted of the X-ray diffraction patterns showed that synthesis of 5 %-vanadium-paranatisite produced a phase which was poorly crystalline whilst 10 %-vanadium-paranatisite synthesis resulted in a more crystalline product. 10 %-vanadium-paranatisite showed high purity with X-ray diffraction patterns being overlaid with known Ti-paranatisite literature patterns^[108].

Refined lattice parameters showed that both materials varied little from the known literature values for un-doped materials. Changes were seen within unit cell axes with 5 %-vanadium-paranatisite showing contraction of the *a* axis and elongation within the *b* and *c* axes whilst 10 %-vanadium-paranatisite showed elongation of all three axes.

Replacement of titanium with vanadium was also confirmed with XRF and ICP-MS analysis, as well as visible changes to the powder. Upon introducing vanadium, the white powder turned brown and appeared darker in colour upon increased doping.

4.2.0.0: Characterisation of Vanadium-Natisite

4.2.1.0: X-Ray Diffraction Analysis of Vanadium-Natisite

4.2.1.1: Phase Aa M1 5 %-Vanadium-Natisite

X-ray diffraction showed that 5 %-vanadium-natisite had been synthesised following M1, as shown in Figure 33. Comparison with known pattern for Ti-natisite^[109] showed that the material produced here exhibited the same unit cell and space group. Refined lattice parameters obtained by Rietveld refinements were carried out using TOPAS^[92] with jEdit^[93]. The reported parameters were $a = b = 6.4836 \text{ \AA} (3)$ and $c = 5.1015 \text{ \AA} (3)$ with an overall cell unit of $214.450 \text{ \AA}^3 (2)$ and an R_{wp} value of 6.399 %. Compared to known literature of Ti-natisite^[109, 110], 5 %-vanadium-natisite showed contraction by $-0.016 \text{ \AA} (3.d.p.)$ in the $a = b$ axes and elongation within the c axis by $0.032 \text{ \AA} (3.d.p.)$ and an overall increase in volume by $0.076 \text{ \AA}^3 (3 d.p.)$. Such changes to the unit cell dimensions when compared to known Ti-paranatisite literature could be attributed to several factors. These factors include the introduction of vanadium within the titanium silicate framework, the position of vanadium within the framework and the synthetic conditions used within the synthesis process such as aging of the synthesis gel, the rate of speed the gel was stirred at during the aging process and the molar ratio used to produce the synthetic gel. It must be also noted that diffuse scattering can be seen at lower 2θ values indicating amorphicity in the sample that may have arisen from unreacted species such as SiO_2 within the synthetic batch.

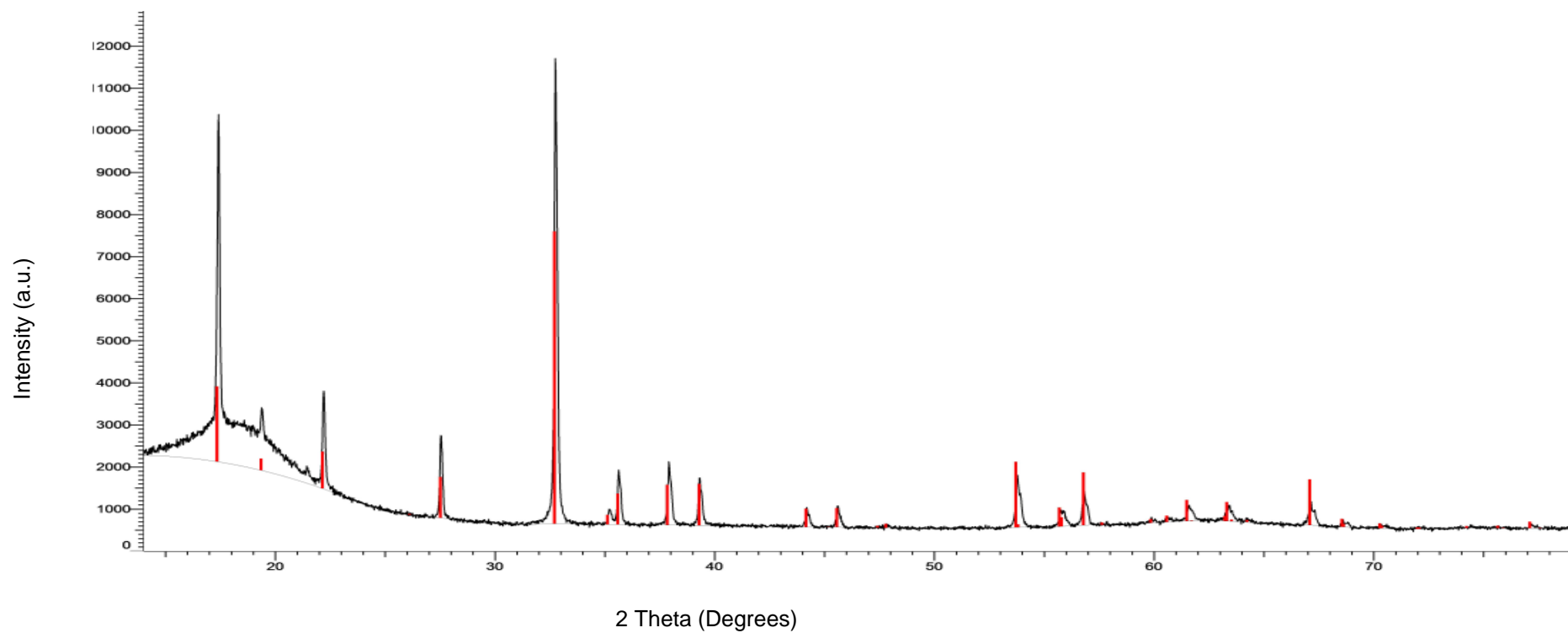


Figure 33: Overlay of phase A M1 5 %-vanadium-natisite XRD pattern with known Ti-natisite literature. (M1 5 %-vanadium-natisite pattern- black and known Ti-natisite literature pattern- red^[109])

4.2.1.2: Phase B M2 5 %-Vanadium-Natisite

X-ray diffraction showed that 5 %-vanadium-natisite had been synthesised by M2. Overlaying the known literature pattern of natisite^[109] with the synthesised material showed that there were no visible impurities. Therefore, it can be concluded that the synthesised material had the same unit cell and space group as Ti-natisite^[109]. Refined lattice parameters obtained by Rietveld refinements were $a = b = 6.48993 \text{ \AA}$ (7) and $c = 5.09595 \text{ \AA}$ (9) and a cell volume of 214.637 \AA^3 (6) were reported. In comparison to Ti-natisite^[109], 5 %-vanadium-natisite showed contraction by -0.010 \AA (3 d.p.) within the $a = b$ axes and elongation by 0.0260 \AA (3 d.p.) within the c axis with an overall increase in cell volume by 0.0193 \AA^3 (3 d.p.). with an R_{wp} value of 5.934 % Such changes to the unit cell dimensions when compared to known Ti-paranatisite literature could be attributed to several factors. These factors include the introduction of vanadium within the titanium silicate framework, the position of vanadium within the framework and the synthetic conditions used within the synthesis process such as aging of the synthesis gel, the rate of speed the gel was stirred at during the aging process and the molar ratio used to produce the synthetic gel. An overlay of 5 %-vanadium-natisite with Ti-natisite^[109] is shown in Figure 34.

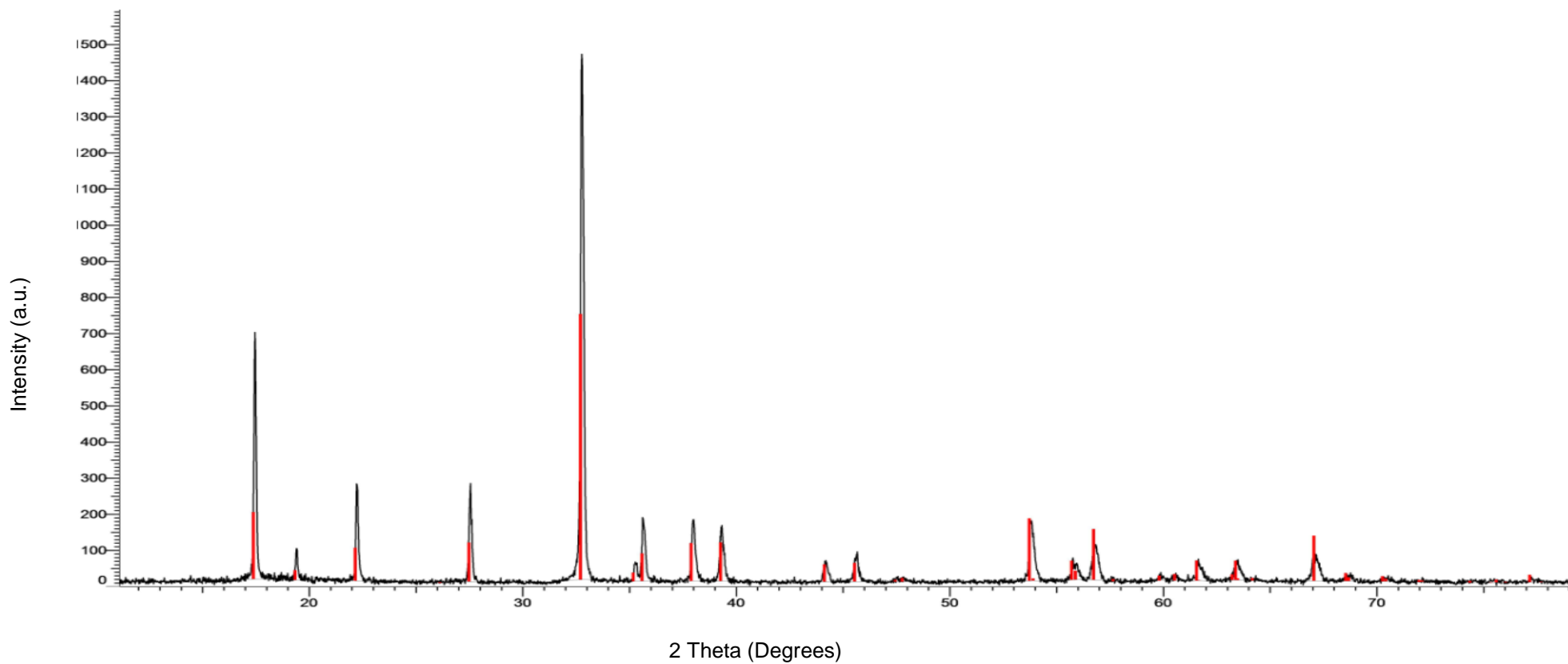


Figure 34: Overlay of phase B M2 5 %-vanadium-natisite XRD pattern with known Ti-natisite literature^[109]. (M2 5 %-vanadium-natisite pattern- black and known Ti-natisite literature pattern- red^[109]).

4.2.1.3: Phase C M2 10 %-Vanadium-Natisite

Synthesis of 10 %-vanadium-natisite was also synthesised by the M2 method and was analysed by comparison to Ti-natisite^[109]. The material that was synthesised was highly crystalline with the same unit cell and space group as Ti-natisite^[109]. Refined lattice parameters obtained by Rietveld refinement were of $a = b = 6.48729 \text{ \AA}(7)$ and $c = 5.0973 \text{ \AA} (1)$ and a unit cell volume of $214.520 \text{ \AA}^3 (6)$. In comparison to Ti-natisite, a contraction by $-0.013 \text{ \AA} (3 \text{ d.p.})$ in the $a = b$ parameter occurred whilst elongation by $0.027 \text{ \AA} (3 \text{ d.p.})$ occurred in the c parameter. Overall expansion was seen within the unit cell by $0.094 \text{ \AA}^3 (3 \text{ d.p.})$ with an R_{wp} value of 5.602 %. Such changes to the unit cell dimensions when compared to known Ti-paranatisite literature could be attributed to several factors. These factors include the introduction of vanadium within the titanium silicate framework, the position of vanadium within the framework and the synthetic conditions used within the synthesis process such as aging of the synthesis gel, the rate of speed the gel was stirred at during the aging process and the molar ratio used to produce the synthetic gel. Overlay of 10 %-vanadium-natisite with Ti-natisite^[109] is shown in Figure 35.

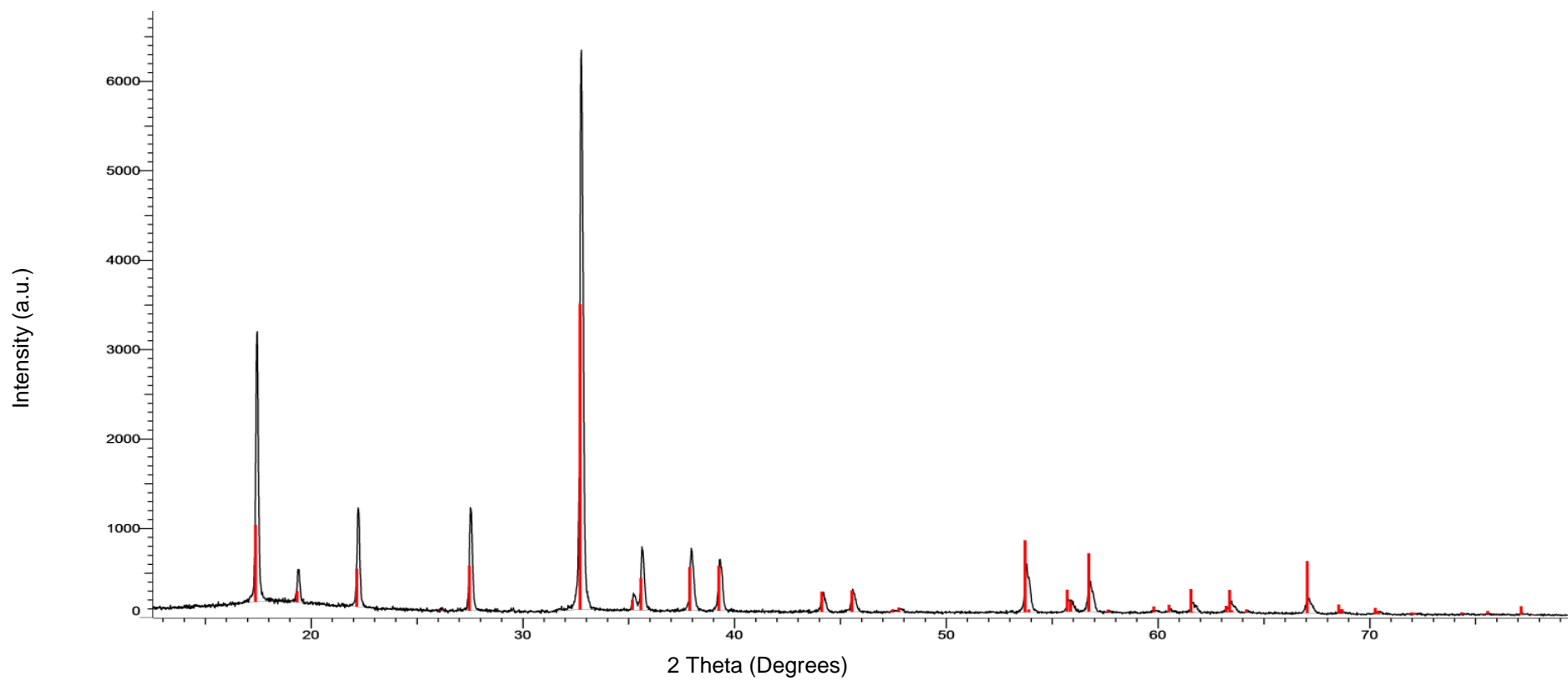


Figure 35: Overlay of phase C M2 10 %-vanadium-natisite XRD pattern with Ti-natisite. (M2 10 %-vanadium-natisite pattern- black and known Ti-natisite literature pattern- red^[109]).

4.2.1.4: Results and Discussion of the Synthetic Methods

The methods suggested by Kostov-Kytin *et al*^[3]. (M1) and Dimitir. G. Medvedev *et al*^[14]. (M2) yielded pure phase vanadium-natisite the majority of times the experimental procedure was attempted. However, it was noted that the age of titanium isopropoxide affected the purity and synthesis time. It was also observed that the increase percentage in vanadium increased the synthetic time length required to synthesise pure phase vanadium-natisite.

Comparison of the the M1 and M2 methods diffraction patterns showed that the M1 synthesised batch produced an XRD pattern which showed diffuse scattering at lower 2θ values indicating slight amorphicity within the sample. The background of the pattern produced from the M2 method was flat indicating the synthesised batch contained a higher degree of crystallinity. Synthesis of 5 %-vanadium-natisite following the M2 method also showed a reduction in synthesis time from 144 hours to 72 hours. Due to time restraints, synthesis of vanadium-natisite focused upon the M2 method and so here on in, any analysis conducted, unless referred to, will be the result of the material obtained from the M2 method. All synthetic conditions are referred to in Table 15.

Table 15: Synthetic conditions for vanadium-natisite following the M1 and M2 methods.

Method	Molar Ratios of Batch Synthesis					Experimental Conditions	
	Na ₂ O	TiO ₂	SiO ₂	VO ₂	H ₂ O	Time (Hours)	Temperature (°C)
Phase A M1 5 %-Vanadium-Natisite	20.00	2.85	10.00	0.15	370.00	144.00	200.00
Phase B M2 5 %-Vanadium-Natisite	12.38	1.14	0.88	0.06	208.00	72.00	200.00
Phase C M2-10 %-Vanadium- Natisite	12.38	1.08	0.88	0.24	208.00	288.00	200.00

4.2.2.0: Rietveld Refinement

Both 5 % and 10 %-vanadium-natisite underwent Rietveld refinements to investigate the structures of the materials. Vanadium was not included in the refinements due to the almost identical X-ray scattering power. The ability of an atom to cause X-ray scattering is dependent upon the electron density surrounding the nucleus of the atom. As titanium and vanadium both have 22 and 23 electrons respectively, their ability to scatter X-rays is almost identical and therefore both elements can be treated as one within the refinement.

To avoid repetition complete structural analysis via Rietveld refinements will solely focus upon 10 %-vanadium-natisite. Refined atomic coordinates of 10 %-vanadium-natisite are denoted in Table 16, selected bond distances are shown in Table 17 and bond angles are denoted in Table 18. Refined lattice parameters and refinement statistics for phase C M2 10 %-vanadium-natisite are shown in Table 19. Final Rietveld fit of phase C M2 10 %-vanadium-natisite is shown in Figure 36. (Refined atomic coordinates, bond lengths, bond angles, refined lattice parameters, refinement statistics and final Rietveld fits for phase Aa, phase Ab and phase B are shown in A19, A20 and A21 respectively to the phase).

Table 16: Refined atomic coordinates for phase C M2 10 %-vanadium-natisite.

Site	X	Y	Z	Occ	beq
Na1	0.75	0.2500	0.5000	1	4.65 (7)
O1	1.0000	0.7906 (2)	1.1785 (2)	1	2.40 (6)
O2	1.0000	0.5000	0.7402 (9)	1	3.5 (1)
Si1	0.5000	0.5000	1.0000	1	2.80 (8)
Ti1	1.0000	0.5000	1.0630 (3)	1	3.43 (5)

Table 17: Refined bond lengths for phase C M2 10 %-vanadium-natisite.

Bond	Length (Å)
Na1-O1	2.32 (1)
Na1-O2	2.60 (2)
O1-Si1	1.63 (2)
Ti1-O1	1.97 (2)
Ti1-O2	1.65 (5)

Table 18: Refined bond angles for phase C M2 10 %-vanadium-natisite.

Bond	Angle (°)	Bond	Angle (°)
O1-Na1-O1	70.11 (7)	Ti1-O2-Na1	118.07 (5)
O1-Na1-O1	180.00	Na1-O2-Na1	77.21 (9)
O1-Na1-O1	109.89 (7)	Na1-O2-Na1	123.86 (2)
O1-Na1-O2	91.88 (8)	O1-Si1-O1	112.39 (1)
O1-Na1-O2	88.12 (8)	O1-Si1-O1	108.03 (5)
Si1-O1-Ti1	128.9 (1)	O2-Ti1-O1	107.34 (6)
Si1-O1-Na1	119.16 (5)	O1-Ti1-O1	145.33 (1)
Ti1-O1-Na1	95.86 (6)	O1-Ti1-O1	84.91 (4)
Na1-O1-Na1	88.66 (8)		

Table 19: Refined lattice parameters and refinement statistics for phase C M2 10 %-vanadium-natisite

Parameter	Ti-Natisite ^[109]	10 %-Vanadium-Natisite
System	Tetragonal	Tetragonal
Space Group	P 4/n m m	P 4 / n m m
<i>a</i> (Å)	6.50000	6.48747 (7)
<i>b</i> (Å)	6.50000	6.48747 (7)
<i>c</i> (Å)	5.07000	5.0975 (1)
<i>V</i> (Å ³)	214.444	214.538 (6)
R _{wp} (%)	-	5.605
R _p (%)	-	4.534
R _{exp} (%)	-	2.697

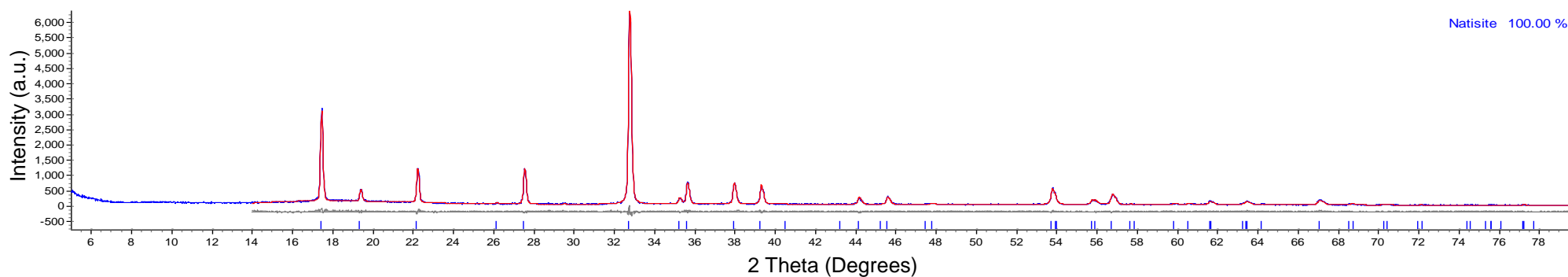


Figure 36: Final Rietveld fit of phase C M2 10 %-vanadium-natisite. (Synthesised pattern –blue, known literature- red and difference plot ($I_{syn}-I_{known}$)-grey).

4.2.3.0: Structural Determination

4.2.3.1: Titanium/ Vanadium Environment

Within the natisite structure, titanium holds one crystallographic site in which the titanium atoms have square pyramidal coordination. Four bonds are coordinated to O1, with a Ti1-O1 distance of 1.975 (2) Å, whilst the remaining bond is connected to O2 forming a Ti1-O2 bond of 1.647 (5) Å. The overall charge of this environment is -1. The titanium environment is depicted in Figure 37.

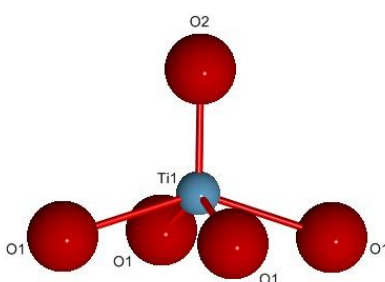


Figure 37: Ti1 coordinated in a square pyramidal environment with O1 and O2 atoms.

(Titanium atoms- light blue and oxygen atoms- red).

4.2.3.2: Silicon Environment

Within the layered structure there is one silicon site. Within the framework silicon forms four Si1-O1 bonds with each bond being of equal distance, 1.635 (2) Å. The coordination of this site is shown in Figure 38.

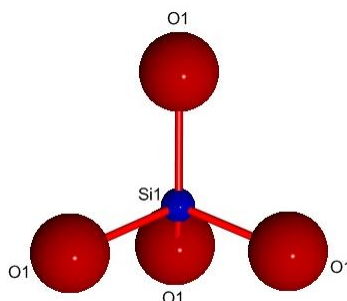


Figure 38: Si1 coordinated in a tetrahedral environment to O1 atoms. (Silicon atoms- dark blue and oxygen atoms- red).

4.2.3.3: Sodium Environment

Within the natisite structure sodium has only one crystallographic site, denoted as Na1. In this environment, sodium is octahedrally coordinated forming four Na1-O2 bonds and two Na1-O1 bonds. Na1-O2 bonds were at a distance of 2.600 (2) Å whilst Na1-O1 bonds were 2.321 (1) Å in length. The sodium environment is depicted in Figure 39.

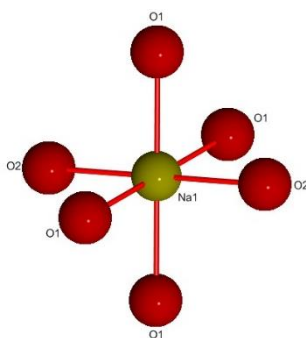


Figure 39: Na1 coordinated in an octahedral environment with O1 and O2 atoms. (Sodium atoms- yellow and oxygen atoms- red).

4.2.3.4: Overall Structure of 10 %-Vanadium-Natisite

The resulting structure of 10 %-vanadium-natisite is shown in Figure 40.

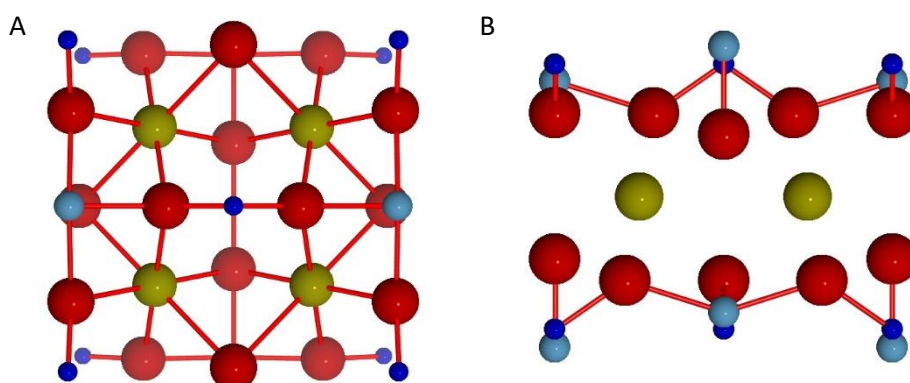


Figure 40: Overall structure of 10 %-vanadium-natisite. A- direction 001 and B- direction 010. (Titanium atoms- light blue, silicon atoms- dark blue, sodium atoms- yellow and oxygen atoms- red). (Labels removed for clarity).

4.2.4.0: Vanadium-Natisite Morphology

As previously reported natisite can adopt different morphologies as a result of varying synthetic conditions, such as altering the synthesis gel composition. Three different morphologies for vanadium-natisite were reported in this work; both pillow shaped particle morphology, phase Aa and phase Ab and, coin shaped particle morphology^[82], phase C, have been previously seen. One other morphology, phase B, was observed and is believed to be previously unseen. Changes to particle morphology is believed to be the result of changes to the gel composition during the experimental procedure.

SEM images of 5 % and 10 %-vanadium-natisite, synthesised using the molar ratios of 0.15 VO₂: 2.85 TiO₂: 10 SiO₂: 12.38 Na₂O: 370H₂O and 0.24 VO₂: 1.08 TiO₂: 0.88 SiO₂:12.38 Na₂O: 208.00 H₂O respectively, produced a particle morphology commonly known as pillow shaped (phase Aa and phase Ab). Phase Aa (the M1 method, 5 %-vanadium-natisite) showed particle diameters of around 6 µm whilst phase Ab (the M2 method, 10 %-vanadium-natisite) showed an increased size in particle morphology of ~ 15 µm diameter. This phase is shown within Figure 41- A, B and C, D respectively.

The second particle morphology observed, was a sphere with a protruding cross on the surface (phase B). This particle morphology resulted from a synthesis gel with the molar ratio of 0.06 VO₂: 1.14 TiO₂: 0.88 SiO₂: 12.38 Na₂O: 208 H₂O and had an diameter of 18 µm. This morphology was also seen when the doping level was increased to 10 %-vanadium with negligible effect to particle size. This phase is shown in Figure 41- E and F.

The third particle morphology, denoted as phase C, was synthesised with the molar ratio, 0.24 VO₂: 1.08 TiO₂: 0.88 SiO₂: 12.38 Na₂O: 208.00 H₂O. Electron micrographs taken of the powdered sample showed a disc like structure with a hole in the shape of a cross in the middle of the disc. This is typical of the coined shape morphology. Phase C had a diameter of 15 µm and was often present alongside the second morphology. This phase is shown in Figure 41- G and H.

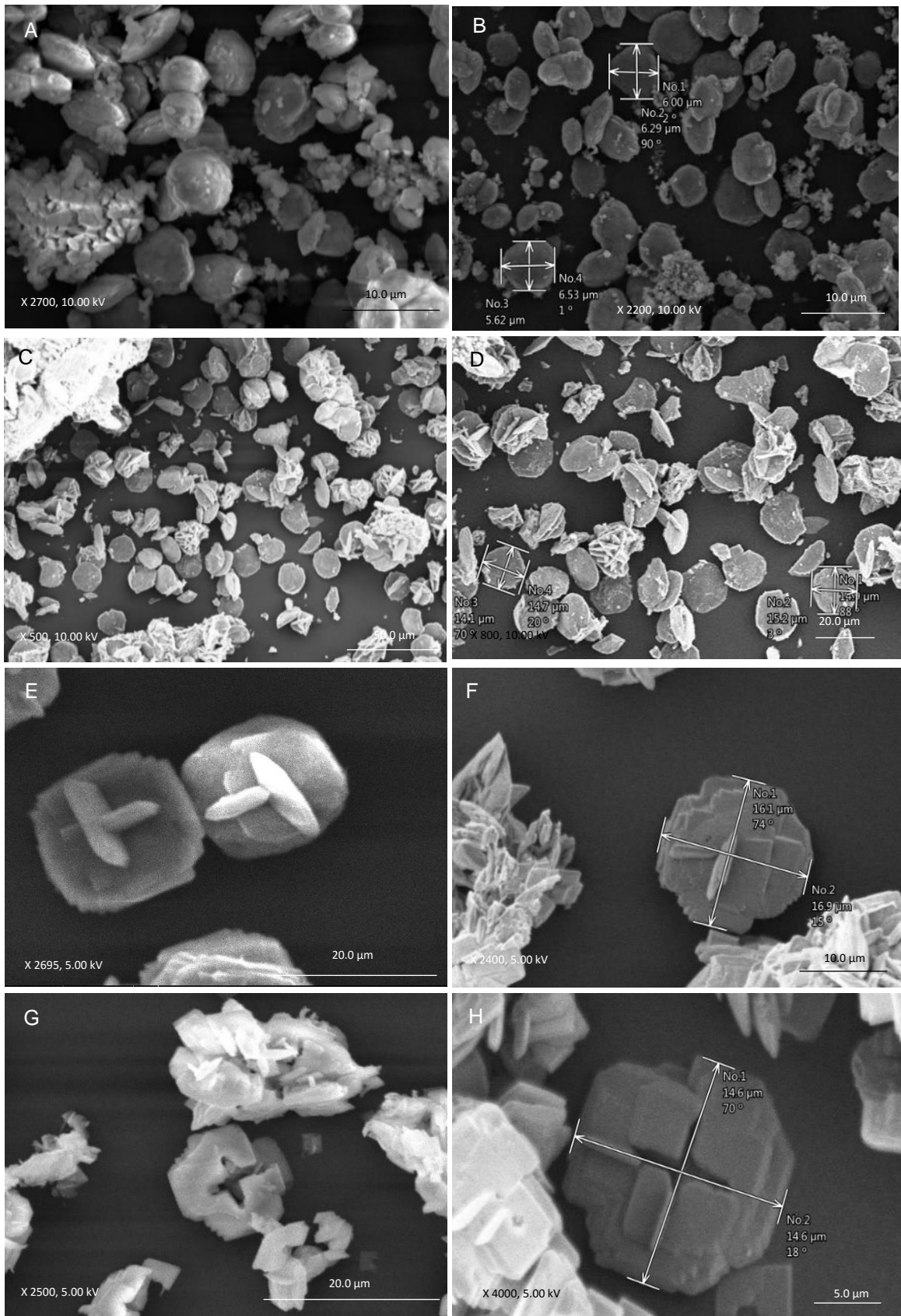


Figure 41: SEM images of vanadium-natisite. A and B-phase Aa, C and D- phase Ab, E and F-phase B and G and H-phase C.

4.2.5.0: EDX Analysis

EDX analysis was used to determine the elemental composition of the synthesised vanadium-natisite samples. The results showed that the atomic percentages for oxygen, sodium and silicon remained constant regardless of the morphology observed. This is to be expected as the molar ratios of these elements remained unchanged during each synthesis. With regards to vanadium, atomic percentages were lower than what was to be expected. The high degree of overlap between titanium and vanadium emission lines and the inability to distinguish between these two elements could be the possible explanation of the relatively low vanadium content recorded from EDX analysis.

Although there is a high degree of overlap between the titanium and vanadium emission lines, it is believed that the atomic percentage increase of vanadium from 5 % to 10 %-vanadium materials is indicative of the increased doping within the natisite framework with all average data points for EDX analysis being referred to in Table 20. (EDX Spectra for phase Aa, phase Ab, phase B and phase C are shown in A23, A24, A25 and A26 respectively).

Table 20: Elemental composition of phase Aa, Ab, B and C.

Element	Phase Aa M1 5 %- Vanadium-Natisite		Phase Ab M2 10 %- Vanadium-Natisite		Phase B M2 5 %-Vanadium- Natisite		Phase C M2 10 %- Vanadium-Natisite	
	Weight (%)	Atomic (%)	Weight (%)	Atomic (%)	Weight (%)	Atomic (%)	Weight (%)	Atomic (%)
O K	39.80 (± 17.20)	57.40 (± 28.48)	38.36 (± 02.27)	54.20 (± 02.55)	45.68 (± 12.60)	64.97 (± 16.63)	37.66 (± 11.01)	53.24 (± 00.45)
Na K	14.27 (± 05.25)	14.97 (± 02.81)	24.01 (± 01.99)	23.61 (± 01.74)	09.56 (± 00.12)	09.17 (± 00.14)	24.79 (± 0.22)	24.39 (± 0.12)
Si K	14.27 (± 01.34)	11.91 (± 01.03)	13.45 (± 03.22)	10.82 (± 02.81)	12.42 (± 01.97)	10.26 (± 02.49)	14.01 (± 00.14)	11.30 (± 03.10)
Ti K	30.62 (± 10.75)	15.23 (± 08.30)	22.65 (± 01.73)	10.69 (± 00.95)	31.31 (± 25.74)	15.25 (± 04.70)	22.03 (± 00.23)	10.41 (± 00.25)
V K	100.0 (± 00.41)	0.49 (± 00.31)	01.53 (± 00.93)	00.68 (± 00.40)	00.74 (± 00.24)	00.34 (± 00.17)	1.51 (± 00.89)	0.67 (± 00.51)
Total	100.0	100.0	100.0	100.0	100.0	100.0	100.0	100.0

4.2.6.0: XRF Analysis

XRF analysis was used in conjunction with EDX to confirm the presence of titanium, silicon and vanadium within each sample. Within the spectra, shown in Figure 42, it can be seen that all three elements of interest are present in each sample at the characteristic emission energies as referred to in Table 21.

Table 21: List of characteristic XRF emission lines for silicon, titanium and vanadium within vanadium-natisite.

Element	Energy (keV)	Emission
Silicon	1.73	$K_{\alpha 1}$, $K_{\alpha 2}$
Titanium	4.44	$K_{\alpha 1}$, $K_{\alpha 2}$
	4.88	$K_{\beta 1}$
Vanadium	4.88	$K_{\alpha 1}$, $K_{\alpha 2}$
	5.43	$K_{\beta 1}$

Although quantitative analysis cannot be carried out using the portable XRF used, comparison of the relative peaks intensities can give an indication of an increase in the amount of an element. The characteristic vanadium emission line, $K_{\beta 1}$, which occurs at 5.34 keV, shows an increase in intensity from 5 % to 10 %-vanadium samples. Due to no other overlap of the emission line it can be inferred that the vanadium percentage has increased.

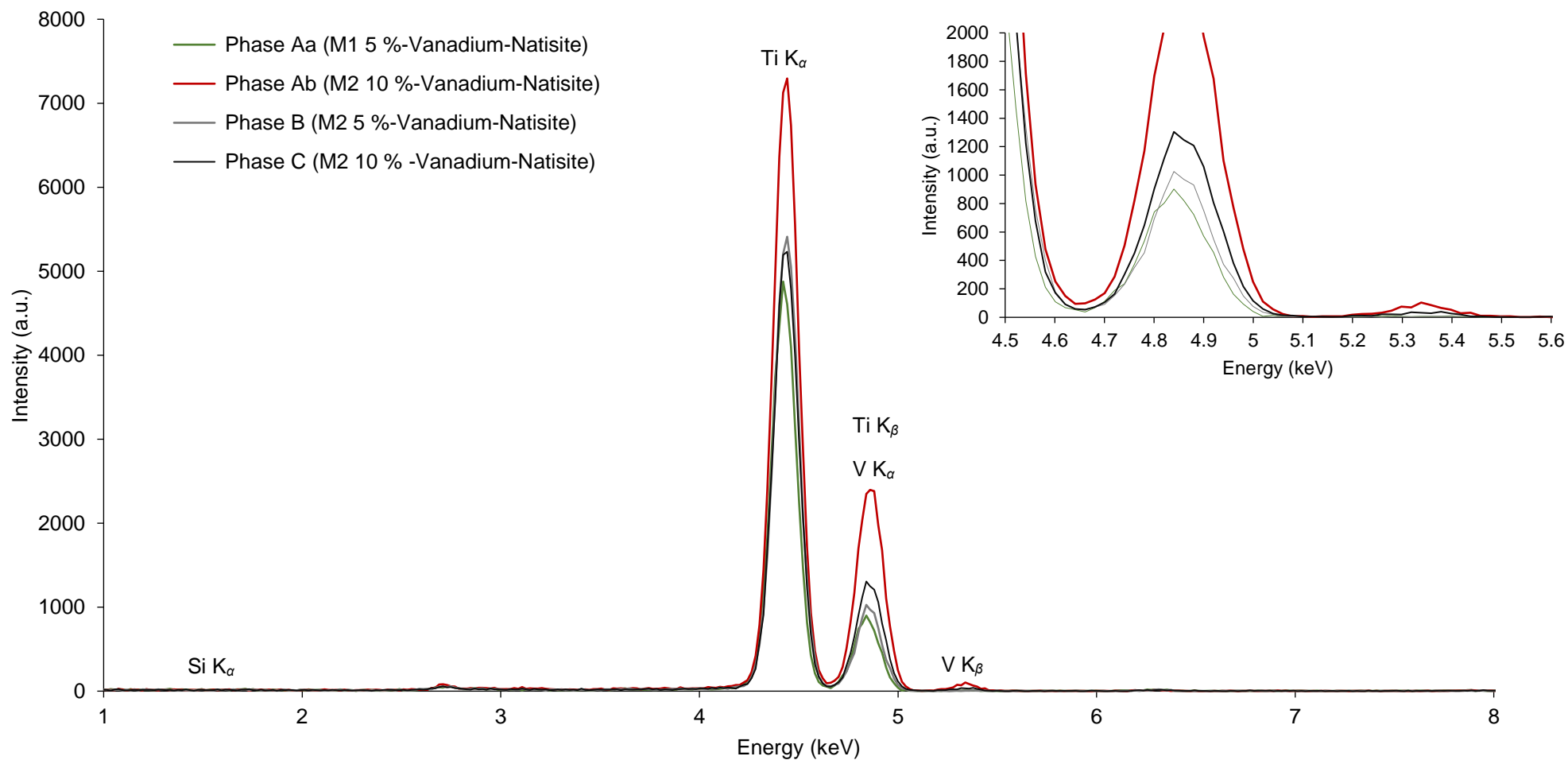


Figure 42: XRF spectra for 5 and 10 %-vanadium-natisite phases Aa, phase Ab, phase B and phase C.

4.2.7.0: ICP-MS Analysis

Due to the limitations of both EDX and XRF, ICP-MS analysis was conducted to provide quantitative analysis.

First attempts to obtain a solution suitable for ICP-MS analysis were to degrade the solid material in acidic conditions (1 M of nitric acid and the sample was left to stand for several weeks) to provide a solution of metal ions, however the sample did not dissolve completely.

Instead, analysis took place using the filtrate from the synthesis product and a percentage average was taken. To determine the percentage of successful doping, it was assumed that no vanadium was lost through transfer of material. As a result, it was determined that, on average, for samples labelled 5 %-vanadium-natisite, 4.61 % (± 0.71) of titanium had been replaced with vanadium whilst samples labelled as 10 %-vanadium-natisite, 7.97 % (± 0.38) of titanium had been replaced with vanadium. (Vanadium percent doping levels of individual samples for 5 and 10 %-vanadium-natisite are shown in A27).

4.2.8.0: Conclusion of the Synthesis of Vanadium-Natisite

X-ray diffraction analysis showed that vanadium-natisite could be synthesised by both the M1 and M2 methods with XRD patterns showing high purity and crystallinity of all materials.

Refined lattice parameters obtained from Rietveld refinements showed that the presence of vanadium within the Ti-natisite framework caused contraction in the *a* and *b* axes with elongation along the *c* axis by varying amounts. Phase Aa (5 %-vanadium-natisite) showed the largest contraction and elongation in the *a = b* and *c* axis when compared to all other phases, whilst phase Ab (10 %-vanadium-

natisite) showed the shortest contraction in the $a = b$ axes and elongation in the c axis. All lattice refinements are shown in Table 22.

Previous work by S. Fedrov conducted comparative analysis upon pillow (phase A) and coin (phase C) morphologies^[82]. It was reported that when compared to pillow morphology, coin morphology showed longer $a = b$ axes and a shorter c axis. The c axis within pillow morphology is believed to be longer in order to compensate for the shorter $a = b$ axis. This compensation is attributed to the increase in length of the axial (terminal) Ti1-O2 bond^[82].

However, analysis conducted on the samples produced in this work, namely phase Ab (10 %-vanadium-natisite, pillow morphology) and phase C (10 %-vanadium-natisite, coin morphology) showed that phase C exhibited shorter $a = b$ axes and a larger c axis when compared to Ab.

Further to this Rietveld refinements conducted upon all phases did not cohere to the reported findings of S.Fedrov^[82]. Instead phase Aa (5 %-vanadium-natisite, pillow morphology) and phase Ab (10 %-vanadium-natisite, pillow morphology) had shorter Ti1-O2 bonds compared to all the other phases. Comparison of all phases also showed that phase B (5 %-vanadium-natisite) exhibited an increase length of the Ti1-O2 bond with all bond lengths being depicted in Table 23.

To verify these results further analysis would need to be conducted. Synthesis of single crystals of vanadium-paranatisite and vanadium-natisite could be conducted to act as a better comparison with the results seen with S.Fedrov.

Further analysis upon the powdered framework samples could also be conducted. Firstly, more in-depth studies of the effect of synthetic conditions such as molar composition and the pH of solution could be undertaken to understand the true effect these conditions have upon particle morphology.

As well as this in depth structural analysis could be conducted using Extended X-ray Absorption Fine Structure Spectroscopy (EXAFS). EXAFS would provide greater information upon interatomic distances and near neighbour coordination numbers. This would allow for further indication of successful vanadium doping as well as the effect of vanadium upon the unit cell parameters.

Although the full extent of the effect of vanadium doping is not known, analysis from EDX showed that there is slight variation in the elemental composition between the two phases indicating that changes within the lattice parameters are the result of the variation of structural changes. As mentioned previously, due to time restraints and the ease of synthesis, all ion exchange material used was synthesised based upon the M2 method.

Table 22: Refined lattice parameters for phase Aa, phase Ab, phase B and phase C.

Compound	Phase Aa M1-5 %-Vanadium- Natisite	Phase Ab M2-10 %-Vanadium- Natisite	Phase B M2-5 %-Vanadium- Natisite	Phase C M2-10 %-Vanadium- Natisite
Molar Ratio	0.15 VO ₂ -2.85 TiO ₂ - 10.00 SiO ₂ -20.00 Na ₂ O-370.00 H ₂ O	0.24 VO ₂ -1.08 TiO ₂ - 0.88 SiO ₂ -12.38 Na ₂ O-208.00 H ₂ O	0.06 VO ₂ -1.14 TiO ₂ - 0.88 SiO ₂ -12.38 Na ₂ O -208 H ₂ O	0.24 VO ₂ -1.08 TiO ₂ - 0.88 SiO ₂ -12.38 Na ₂ O-208.00 H ₂ O
Crystal System	Tetragonal	Tetragonal	Tetragonal	Tetragonal
Space Group	P 4/ n m m	P 4/ n m m	P 4/ n m m	P 4/ n m m
Unit Cell	a = b = 6.4836(3)	a = b = 6.4942 (4)	a = b = 6.48993 (7)	a = b = 6.48729 (7)
Dimensions (Å)	and c = 5.1015 (3)	c = 5.0888 (5)	c = 5.09595 (9)	c = 5.0973 (1)
Volume (Å³)	214.450 (2)	214.62 (3)	214.637 (6)	214.538 (6)

Table 23: Refined bond lengths for phase Aa, phase Ab, phase B and phase C.

Compound	Phase Aa M1-5 %-Vanadium- Natisite	Phase Ab M2-10 %-Vanadium- Natisite	Phase B M2-5 %-Vanadium- Natisite	Phase C M2-10 %-Vanadium- Natisite
Na1-O1	2.354 (3)	2.355 (4)	2.295 (1)	2.321 (1)
Na1-O2	2.614 (9)	2.60 (1)	2.562 (2)	2.600 (2)
O1-Si1	1.644 (5)	1.601 (5)	1.635 (2)	1.635 (2)
Ti1-O1	1.92 (6)	1.987 (5)	2.0181(2)	1.975 (2)
Ti1-O2	1.60(2)	1.60 (2)	1.722 (5)	1.646 (5)

Chapter 5- Ion Exchange Analysis of Vanadium-Paranatisite and Vanadium-Natisite

5.0.0.0: Experimental Procedures

All ion exchanges that took place during this study were based upon the batch operation method and the ions of interest were in nitrate form. For each experiment, a 0.05 M, pH 7 solution of the ion of interest was made up in 250 ml of deionised water in a conical flask. Once the desired ion had fully dissolved, 0.5 g of the silicate material was added and stirred at 300 rpm for 24 hours. The conical flask was sealed with parafilm and left to stir at room temperature within a fume cupboard.

Following ion-exchange experiments 50 ml of the ion exchange solution was centrifuged at 1000 rpm for 2 minutes. Once 2 minutes had elapsed the filtrate was poured into a new conical flask, leaving the powder within the centrifuge tube. More ion exchange solution was then added, and the method repeated. This process continued until the powder was washed with 1 litre of deionised water. The powder sample was ground and the particle size within the powder were as those reported in Chapter 4. The powder was retained for XRD, SEM, EDX and XRF analysis whilst the filtrate was retained for ICP-MS analysis.

Upon drying both vanadium-paranatisite and natisite materials following cobalt ion exchange experiments, an uncharacteristic green powder was seen. As a result, cobalt chloride species were also investigated with 5 %-vanadium-natisite. Again, a similar green powder was recorded with comparable ion exchange properties, morphology and changes to unit cell parameters. (Pawley refinements, ion exchange percentages and morphologies of 5 %-vanadium-natisite-cobalt ion exchange are shown in A28).

5.1.0.0: Vanadium-Paranatisite Ion Exchange Analysis

5.1.1.0: ICP-MS Analysis

To determine the percentage uptake of each specific ion ICP-MS was conducted upon the filtrate collected post ion exchange.

The results shown in Table 24 indicate that when compared to 10 %-vanadium-paranatisite, 5 %-vanadium-paranatisite had a higher affinity to cerium, cobalt, strontium and neodymium whilst 10 %-vanadium-paranatisite had a slightly higher affinity towards cesium, by 1 %.

Both materials showed the same general trends with regards to the affinity towards particular ions. The trend seen for 5 %-vanadium-paranatisite was determined to be Ce<Nd<Cs<Co<Sr with strontium being the highest exchanged and cerium being the lowest. For 10 %-vanadium-paranatisite, the trend as reported in Table 24 is Ce<Nd<Cs<Co<Sr. Each ion exchange experiment was conducted separately and analysed as a cohort of samples.

Ion exchange materials commonly used within the nuclear industry such as Clinoptilolite and IONSIV materials show to have the highest affinities towards cesium and strontium removal. Similarly, to these materials both vanadium-paranatisite and natisite showed to have higher affinities towards strontium and cesium. However, unlike common industrial materials, both vanadium-paranatisite and natisite showed to have the highest affinity towards cobalt. To date, there is no ion exchange material which is used for the removal of ⁶⁰Co, a common radioactive containment following neutron absorption to the graphite moderator. Initial experiments may indicate that vanadium-paranatisite and

paranatisite could be primarily used for the removal of ^{60}Co , however, further tests such as competitive ion exchanges would need to be investigated.

Table 24: Ion percentage uptake from 24 hour ion exchange in pH 7 solution for vanadium-paranatisite.

	5 %-Vanadium-Paranatisite Ion Percentage Exchanged into Framework (%)	10 %-Vanadium-Paranatisite Ion Percentage Exchanged into Framework (%)
Cesium	24 (\pm 0.23)	25 (\pm 0.42)
Cerium	20 (\pm 0.23)	18 (\pm 0.29)
Cobalt	29 (\pm 0.82)	26 (\pm 0.61)
Strontium	32 (\pm 0.62)	28 (\pm 0.52)
Neodymium	23 (\pm 0.41)	22 (\pm 0.79)

5.1.2.0: X-Ray Diffraction Analysis

Analysis of 5 %-vanadium-paranatisite diffraction patterns following all ion exchanges saw that cobalt exchanged and cesium exchanged materials retained crystallinity with minimal changes in the patterns as shown in Figure 43. There was little variation in the position of the peaks and no new peaks were observed, suggesting minimal changes had occurred to space group and unit cell size.

Only slight variations in peak intensities took place with regards to the cobalt and cesium ion exchanged materials. The most prominent changes to peak intensities occurred at lower 2θ values in the range of 18.130° - 32.571° . Of the two exchanges, where the solid remained crystalline, cesium, showed greater variation from un-exchanged samples with peak positions at 20.570° , 20.878° and 22.786° 2θ showing changes of 6.1 %, 3.5 % and 4.2 peak positions at 20.570° , 20.878° and 22.786° 2θ showing changes of 6.1 %, 3.5 % and 4.2 %. Increased variation following cesium exchange could be indicative of the increased ionic radius of cesium when compared to the other ions investigated. The greater ionic size of cesium is believed to have caused greater structural changes to the atomic positions within the framework. As the framework tries to accommodate the cesium ions in place of the smaller sodium ions, the vanadium-titanium silicate framework distorts to a greater extent when compared to the exchange of sodium ions with the other smaller ions being investigated. As a result, increased variation of peak intensities of the cesium exchanged material were noted.

Peak by peak analysis of cobalt and cesium ion exchange materials can be seen in Table 25 and a stacked view of 5 %-vanadium-paranatisite, cobalt and cesium ion exchanged material shown in Figure 43.

Analysis of 10 %-vanadium-paranatisite following ion exchange experiments showed that crystallinity was retained during ion exchange experiments involving strontium, cobalt and cesium. Peak by Peak analysis, as shown in Table 26, shows that peak positioning and peak intensities were as to be expected with minimal changes. The greatest change in peak intensities were seen at lower 2θ values following cobalt ion exchange. Increased variation to intensity values may be indicative of the increased exchange to this particular ion. Peaks positioned at 18.485° , 20.570° , 20.878° and 22.786° 2θ saw peak intensities vary by 3.6 %, 4.6 %, 7.3 % and 1.4 %. Peak analysis is shown in Table 26 and a stack view of 10 %-vanadium-paranatisite, strontium, cobalt and cesium ion exchanged materials can be seen in Figure 44.

Table 25: Peak analysis of 5 %-vanadium-paranatisite-cesium and cobalt ion exchanged material.

hkl	2 Theta (Degrees)	5 %-Vanadium- Paranatisite (%)	Cobalt (%)	Cesium (%)
200	18.130	3.5	3.8	-
001	18.485	11.9	10.6	13.2
210/101	20.570	22.4	20.4	28.5
011	20.878	23.7	22.0	30.2
111	22.786	7.9	6.7	12.1
220	26.624	13.1	13.0	14.2
021	26.859	2.7	3.7	-
211	27.737	1.4	2.2	-
221	32.571	100.0	100.0	100.0
230/311/031	34.588	6.9	8.1	5.8
131	35.961	6.2	7.4	9.8
400	36.647	8.6	6.9	9.6
002	37.376	3.6	4.6	-
012	38.642	1.8	1.6	-
231	39.243	5.3	4.4	9.6
112	39.807	7.2	8.4	8.5
122/240/041	43.532	1.1	1.5	-
141	44.701	4.3	5.3	7.5
241	47.490	1.1	0.9	-
501	50.193	0.7	1.2	-
514/431	51.313	0.7	-	-
232/341	51.776	1.0	1.4	-
250/402/051	53.317	3.7	3.9	-
440	54.732	5.6	6.1	7.9
042	55.271	4.2	4.2	5.5
600	56.145	0.9	1.6	-
441/103/013	58.262	0.5	-	-
242	59.248	0.3	-	-
531/113	60.447	0.2	-	-
203	60.448	0.3	-	-
260/621/052	63.336	2.4	2.1	-
225/152/552	64.342	2.3	2.3	3.5
261	68.104	1.3	0.7	-
322/442	68.164	0.7	0.9	-

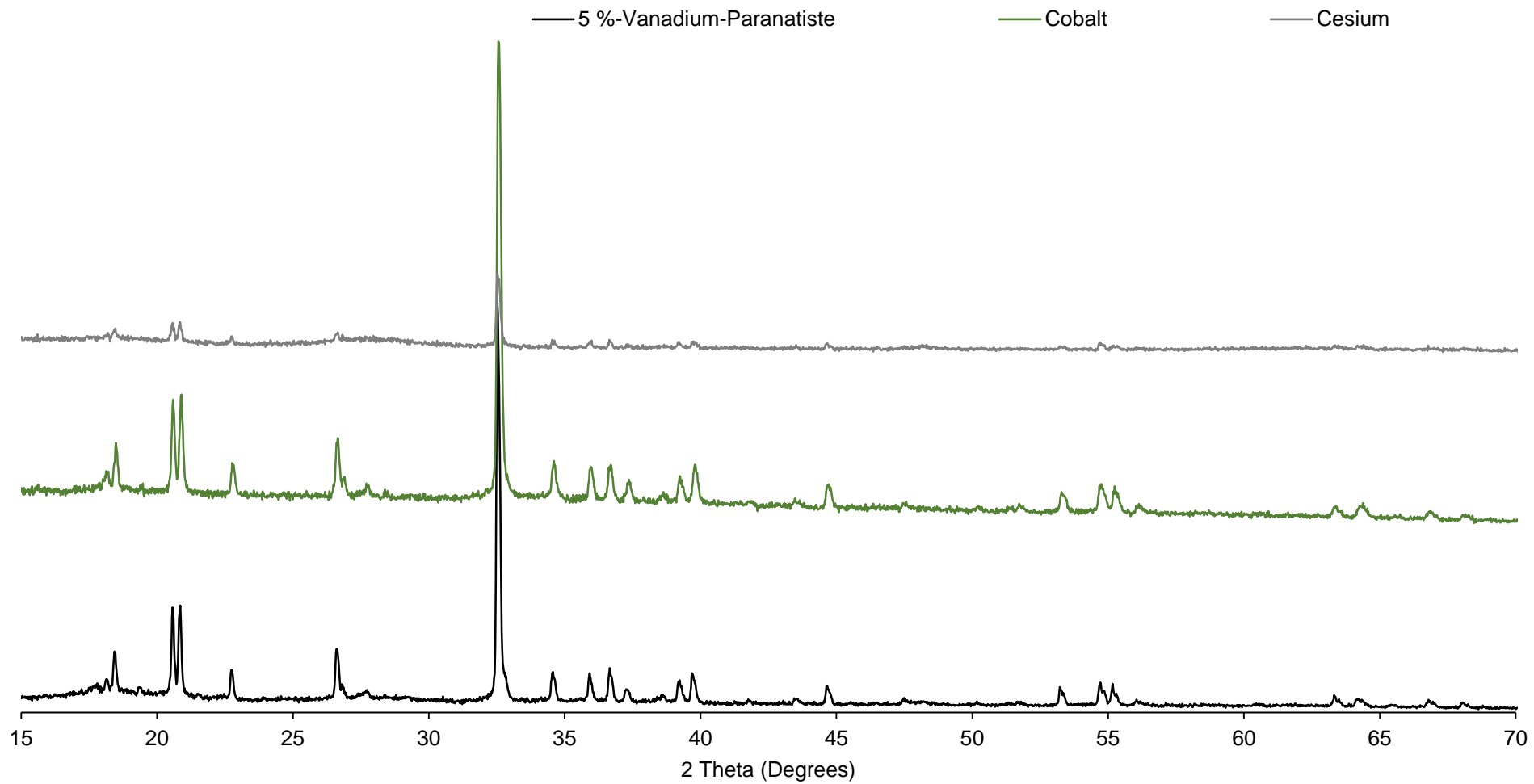


Figure 43: Stack view of XRD patterns of 5 %-vanadium-paranatisite, cobalt and cesium ion exchanged materials.

Table 26: Peak analysis of 10 %-vanadium-paranatisite-cesium, cobalt and strontium ion exchanged material.

hkl	2 Theta (Degrees)	10 %-Vanadium-Paranatisite (%)	Strontium (%)	Cobalt (%)	Cesium (%)
200	18.130	2.5	2.7	4.7	2.4
001	18.485	7.6	7.3	11.2	6.4
210/101	20.570	17.6	17.7	22.3	15.8
011	20.878	19.0	19.6	26.3	19.6
111	22.786	6.7	6.0	8.1	6.3
220	26.624	10.1	10.5	12.4	10.3
021	26.859	2.5	2.7	3.4	2.5
211	27.737	1.0	0.8	2.5	1.1
221	32.571	100.0	100.0	100.0	100.0
230/311/031	34.588	7.0	6.9	7.5	7.5
131	35.961	6.7	7.5	5.5	
400	36.647	8.7	9.3	7.2	9.3
002	37.376	3.6	3.6	4.0	4.1
012	38.642	1.7	1.7	1.0	1.9
231	39.243	6.1	7.4	5.3	6.7
112	39.807	8.2	8.4	7.6	10.5
122/240/041	43.532	1.0	1.0		0.9
141	44.701	5.2	5.5	4.8	6.2
241	47.490	1.3	1.3	1.2	1.4
501	50.193	0.9	0.8	-	1.2
514/431	51.313	1.0	1.2	-	1.2
232/341	51.776	1.1	1.4	1.0	1.4
250/402/051	53.317	5.0	5.2	1.2	6.1
440	54.732	6.9	7.5	3.7	8.5
042	55.271	4.7	5.7	5.6	6.6
600	56.145	1.5	1.7	3.7	1.8
441/103/013	58.262	0.5	0.5	1.0	0.9
242	59.248	0.4	-	-	-
531/113	60.447	0.4	-	-	-
203	60.448	0.4	0.6	-	0.7
260/621/052	63.336	3.1	3.2	2.2	2.9
225/152/552	64.342	2.8	3.1	2.1	3.6
261	68.104	1.8	1.6	1.0	1.8
322/442	68.164	11.1	-	-	1.7

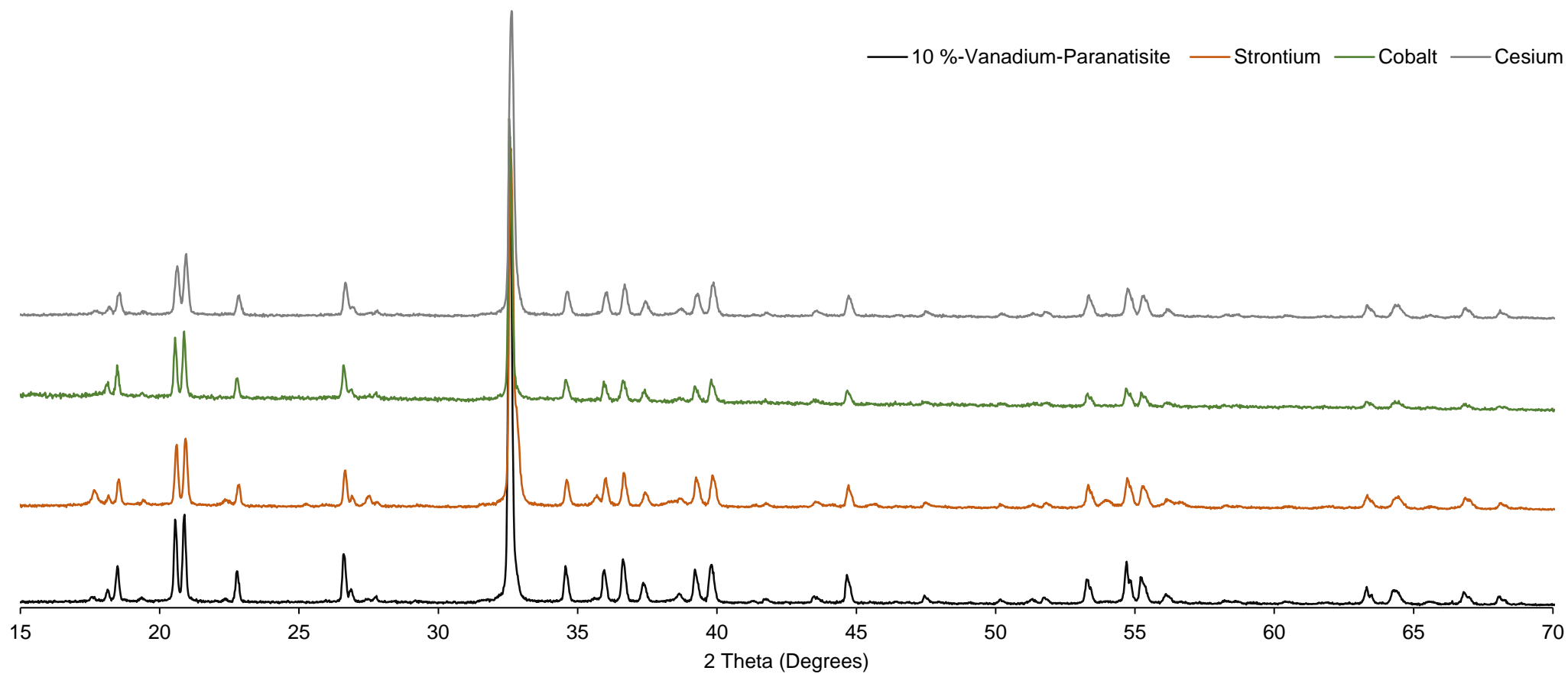


Figure 44: Stack view of XRD patterns of 10 %-vanadium-paranatisite, strontium, cobalt and cesium ion exchanged materials.

5 %-vanadium-paranatisite diffraction analysis showed that exchanges involving strontium, neodymium and cerium caused peak broadening and a reduction in peak intensities indicating a loss of long range order. Diffraction pattern analysis conducted upon cerium and neodymium showed the presence of the same three characteristic paranatisite peaks situated at 27.737° , 32.571° and $47.490^\circ 2\theta$. Strontium analysis however, showed the presence of four characteristic paranatisite peaks at 25.315° , 26.624° , 32.571° and $36.467^\circ 2\theta$. These changes to peak intensities and positioning is indicative that ion exchange experiments had caused structural damage to the framework or that new phases were forming. A stack view of X-ray diffraction patterns of 5 %-vanadium-paranatisite, strontium, cerium and neodymium ion exchanged material is shown within Figure 45.

Similarly, to 5 %-vanadium-paranatisite, 10 %-vanadium-paranatisite showed reduced crystallinity with respects to cerium and neodymium exchange but less structural damage when compared to 5 %-vanadium-paranatisite as shown in Figure 46. It can be seen within the analysis of neodymium that characteristic paranatisite peaks at lower 2θ values are present but at low intensities. After around $50.000^\circ 2\theta$, crystallinity and peak positioning is lost. With regards to cerium, three main peaks were present at 20.731° , 21.014° and $32.645^\circ 2\theta$, these peaks have the highest intensities within the un-exchanged materials. Again, it is postulated that such changes are the result of damage to the framework.

Previous work conducted by R. Hall^[115] showed that cerium dioxide and neodymium hydroxide formed during the ion exchange procedure. One possible reason for increased structural changes to the vanadium-titanium silicate

framework may be due to the fact both cerium dioxide and neodymium hydroxide are forming between vanadium-titanium silicate layers. Although the mechanism is not fully understood, when looking at Pourbaix diagrams both cerium dioxide^[116], and neodymium hydroxide^[117] are species that typically form within solution at pH 7. The increased size of the cerium dioxide and neodymium hydroxide species within the framework may be forcing the layers further apart and reducing the long range order in the materials resulting in increased variation in the unit cell parameters noted.

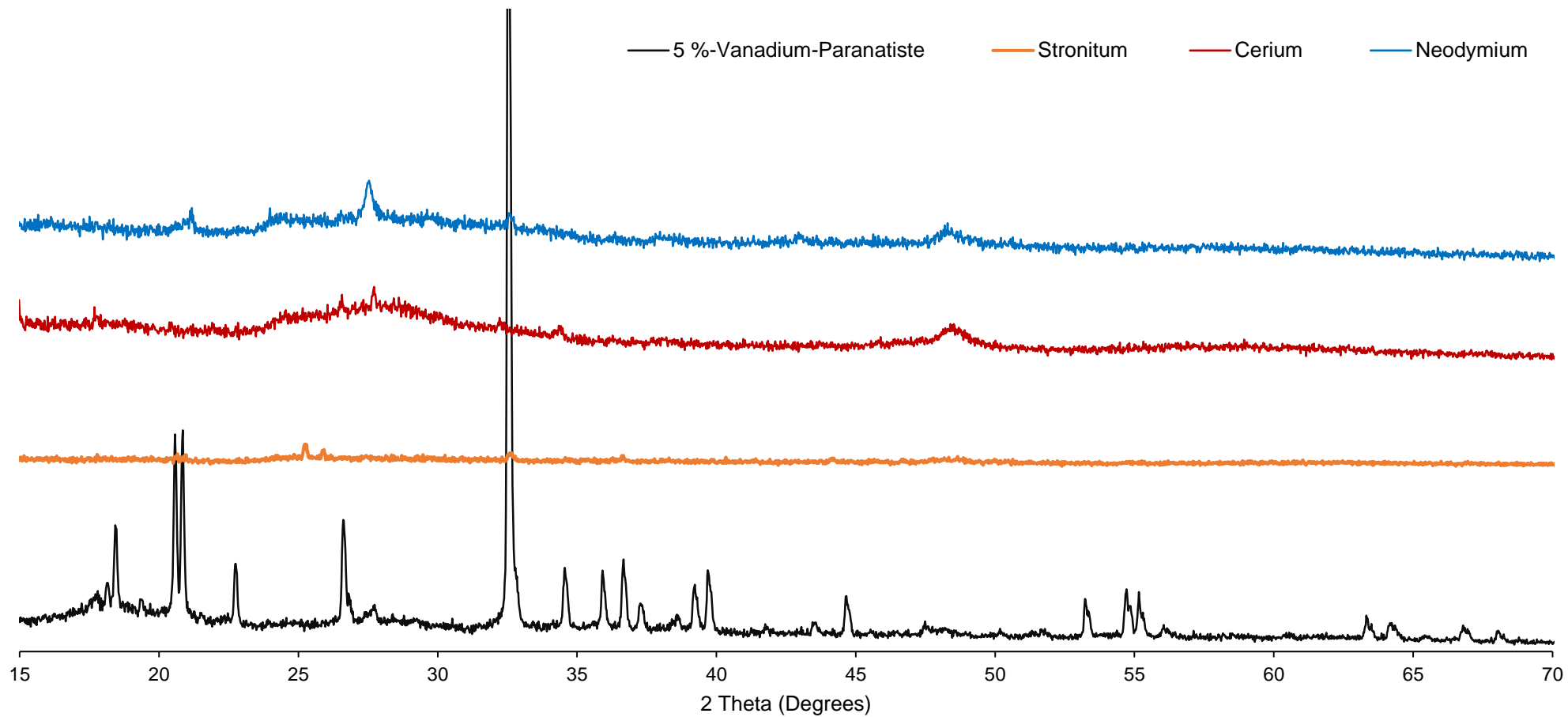


Figure 45: Stack view of XRD patterns of 5 %-vanadium-paranatisite, strontium, cerium and neodymium ion exchanged materials.

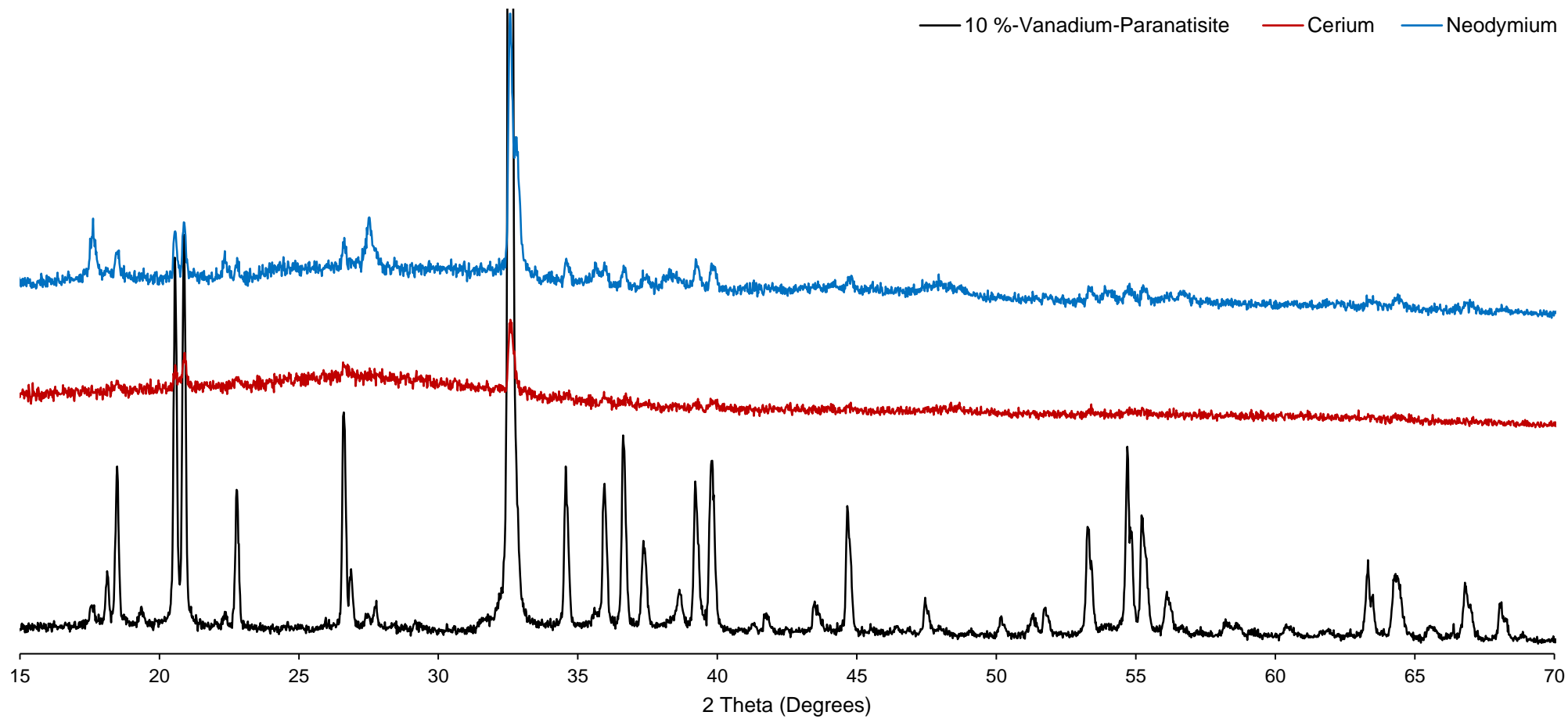


Figure 46: Stack view of XRD patterns of 10 %-vanadium-paranatisite, cerium and neodymium ion exchanged materials.

5.1.3.0: Lattice Refinements Analysis via Pawley Refinements

5.1.3.1: 5 %-Vanadium-Paranatisite

Unit cell parameters following ion exchanges were determined by using TOPAS^[92] with jEdit^[93].

All ion exchanges showed an increase in at least one of the lattice parameters. Strontium, cobalt and cerium showed elongation in only the *a* axis and contraction in the *b* and *c* axes. Cesium showed expansion in the *a* and *b* axes and contraction in the *c* axis, whilst neodymium showed expansion within the *a* and *c* axes but contraction in the *b* axis. Changes to lattice parameters may be indicative of the size of the exchanged ion. Cobalt and cerium possess the smallest ionic radii and so it was seen that only the *a* axes expanded, whilst cesium possesses the largest ionic radius and in turn it was observed that two of the axes had expanded upon ion exchange experiments. As the ionic radius increases it is believed that the vanadium-titanium silicate framework distorts to accommodate the larger sized ions. As a result, greater variations are shown in the axes of the unit cell parameters. It must be remembered that strontium, cerium and neodymium produced amorphous XRD patterns and so variation to the axes may be the result of the lack of crystallinity exhibited.

Both cobalt and cesium lattice refinements showed smaller variations from the original un-exchanged framework. ICP-MS analysis indicated that these two ions possessed some of the greatest exchange capacities with X-ray diffraction analysis showing minimal changes to crystallinity. It is therefore postulated that the frameworks were able to withstand the exchange of cobalt/cesium for sodium ions within the vanadium-paranatisite structure. All lattice parameters are shown in Table 27. (Refined lattice parameters, Rietveld statistics and final Pawley fits

for 5 %-vanadium-paranatisite-cesium, cerium, cobalt, strontium and neodymium ion exchanged material is shown in A29, A30, A31, A32 and A33).

Table 27: Refined lattice parameters for 5 %-vanadium-paranatisite, cesium, cerium, cobalt, neodymium and strontium.

	a (Å)	b (Å)	c (Å)	R_{WP} (%)
5 %- Vanadium- Paranatisite	9.8172 (2)	9.2017 (2)	4.8260 (1)	5.750
Cesium	9.820 (2)	9.202 (1)	4.8253 (8)	10.966
Cerium	10.0 (1)	9.2 (1)	4.75 (5)	7.539
Cobalt	9.8240 (7)	9.1999 (6)	4.8231 (3)	5.742
Strontium	9.83 (2)	9.13 (3)	4.819 (1)	18.911
Neodymium	10.18 (3)	9.15 (2)	4.84 (1)	6.616

5.1.3.2: 10 %-Vanadium-Paranatisite

Pawley refinements took place upon all ion exchange experiments. With regards to the ion exchange experiments involving strontium and cesium, the *a* axis of the unit cell parameter showed to expand whilst both the *b* and *c* axes contracted. With regards to cobalt, cerium and neodymium all three axes of the unit cell parameters, contracted. Changes to lattice parameters may be in accordance to size of the exchanged ion as both strontium and cesium possess larger ionic radii compared to the other exchange ions.

Comparison to the un-exchanged lattice parameters showed that both cerium and neodymium showed the greatest variation. Refinements upon neodymium exchanged material showed contraction by -0.0032 \AA , -0.086 \AA and -0.00689 \AA with respects to *a*, *b* and *c* whilst cerium showed contraction by -0.0182 \AA , -0.014 \AA and -0.1189 \AA with respects to *a*, *b* and *c*. It is believed that such variation is the result of damage to the structural framework following the exchange of sodium ions with cerium/neodymium.

Of the crystalline phases, cobalt showed the greatest variation from the un-exchanged lattice parameters with *a*, *b* and *c* varying by 0.00054 \AA , -0.00105 \AA and -0.00879 \AA , in accordance to the higher exchange capacity. Cesium exchanged material showed the lowest variation with contraction of the *a*, *b* and *c* axes as followed, -0.0046 \AA , -0.0032 \AA and -0.00379 \AA , in accordance with the lower exchange capacity. All refined lattice parameters are shown in Table 28. (Refined lattice parameters, Rietveld statistics and final Pawley fits for 10 %-vanadium-paranatisite-cesium, cerium, cobalt, strontium and neodymium ion exchanged material is shown in A34, A35, A36, A37 and A38).

Table 28: Refined lattice parameters for 10 %-vanadium-paranatisite, cesium, cerium, cobalt, neodymium and strontium.

	a (Å)	b (Å)	c (Å)	R_{WP} (%)
10 %- Vanadium- Paranatisite	9.8282 (1)	9.2060 (1)	4.82489 (7)	5.408
Cesium	9.8328 (4)	9.2028 (4)	4.8211 (2)	10.073
Cerium	9.810 (6)	9.192 (4)	4.813 (2)	8.379
Cobalt	9.8228 (5)	9.1955 (5)	4.8161 (2)	6.280
Strontium	9.8314 (5)	9.1972 (5)	4.8189 (4)	10.373
Neodymium	9.825 (4)	9.120 (3)	4.818 (2)	11.615

5.1.4.0: SEM Analysis

Electron micrographs were recorded to determine if any structural changes to particle morphology could be observed. As mentioned in Chapter 4 paranatisite adopts a cross like structure with varying amounts of protruding surfaces.

Electron micrographs obtained upon the ion exchanged material showed no real variation from the un-exchanged particle morphology. In all cases the characteristic cross shape of vanadium-paranatisite could be seen with 5 %-vanadium-paranatisite exchanged material, shown in Figure 46 and 10 %-vanadium-paranatisite being shown in Figure 47.

Although the characteristic cross shape structure could still be seen, all images obtained from analysis showed varying amounts of surface texture when compared to the un-exchanged material. Cerium showed the greatest changes, with particle morphology appearing to break apart following ion exchange, as shown in Figures 47 B and 48 B. The electron micrographs obtain from cerium exchange mirror the loss of crystallinity seen from X-ray diffraction patterns.

As mentioned previously, it is believed that the loss of crystallinity seen in X-ray diffraction patterns and SEM images is the result of neodymium hydroxide and cerium oxide formation.

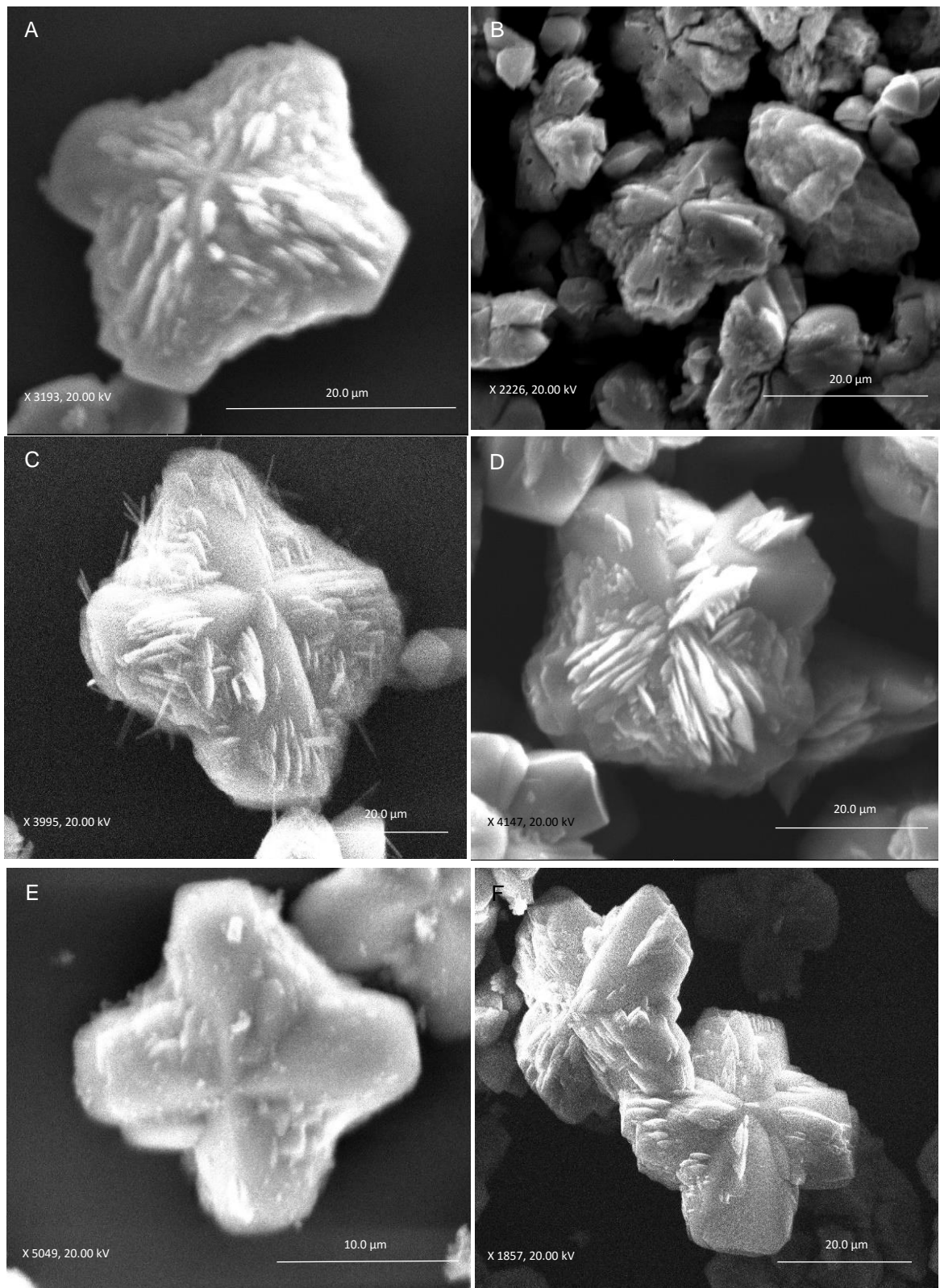


Figure 47: SEM images of 5 %-vanadium-paranatisite, cesium, cerium, cobalt, strontium and neodymium ion exchanged material. A- cesium ion exchange, B- cerium ion exchange, C-cobalt ion exchange, D- strontium ion exchange, E- neodymium ion exchange and F- 5 %-vanadium-paranatisite.

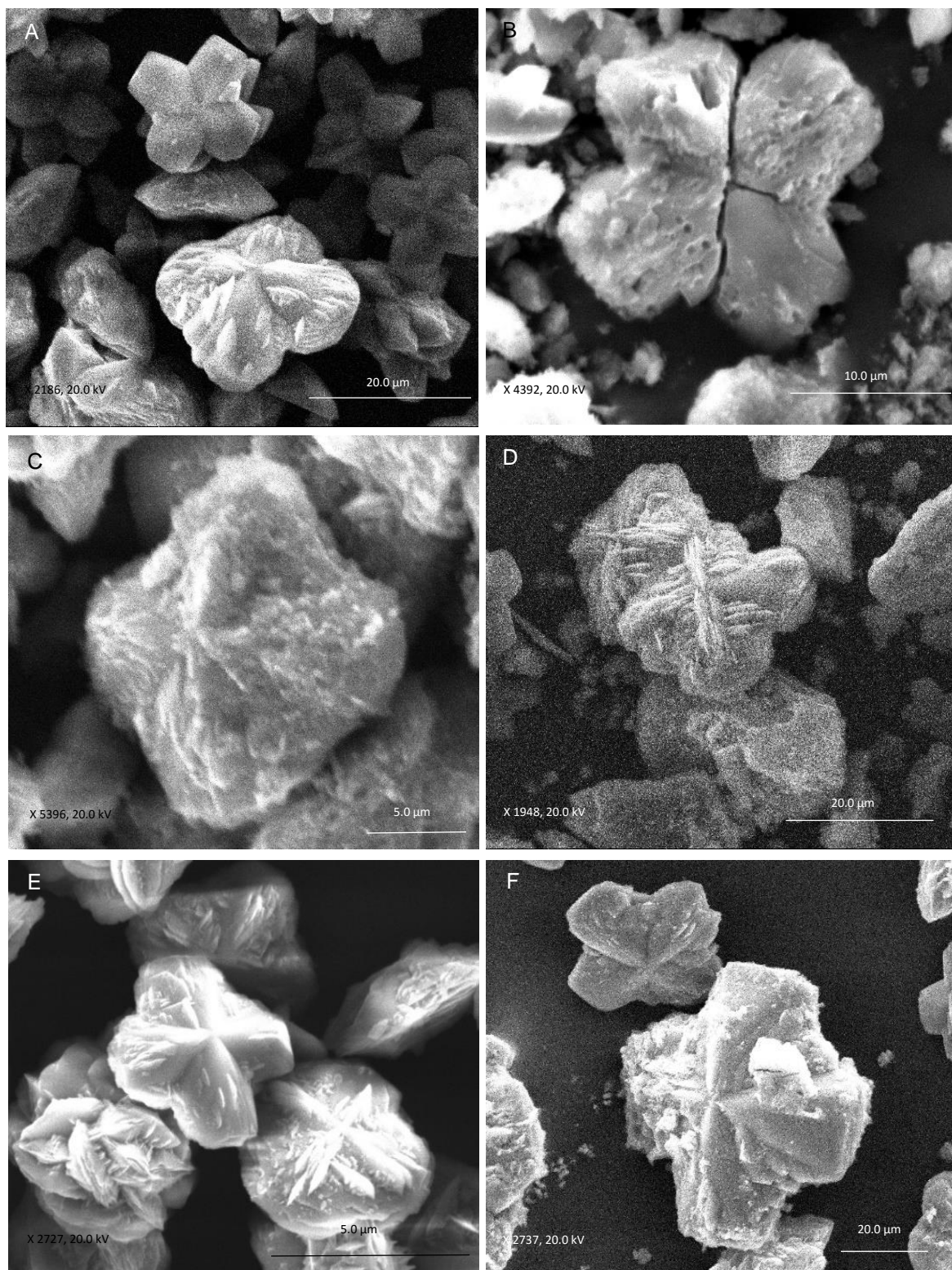


Figure 48: SEM images of 10 %-vanadium-paranatisite, cesium, cerium, cobalt, strontium and neodymium ion exchanged material. A- cesium ion exchange, B- cerium ion exchange, C-cobalt ion exchange, D- strontium ion exchange, E- neodymium ion exchange and F- 5 %-vanadium-paranatisite.

5.1.5.0: EDX Analysis

5.1.5.1: Cesium Analysis

Analysis for both vanadium doping levels saw that the percentage of cesium exchanged from 5 % to 10 %-vanadium-paranatisite had increased, as shown in Table 29. However, overlap of titanium and cesium, shown in Figure 49, saw cesium L emission lines present within the spectra at ~ 4.2 keV - 4.6 keV overlap with titanium K emission lines present at ~ 4.5 keV - 4.9 keV. As a result, the quantitative analysis upon the sample was deemed inaccurate and was solely used as a guide. (EDX Spectrum for 5 %-vanadium-paranatisite-cesium ion exchanged material shown in A39).

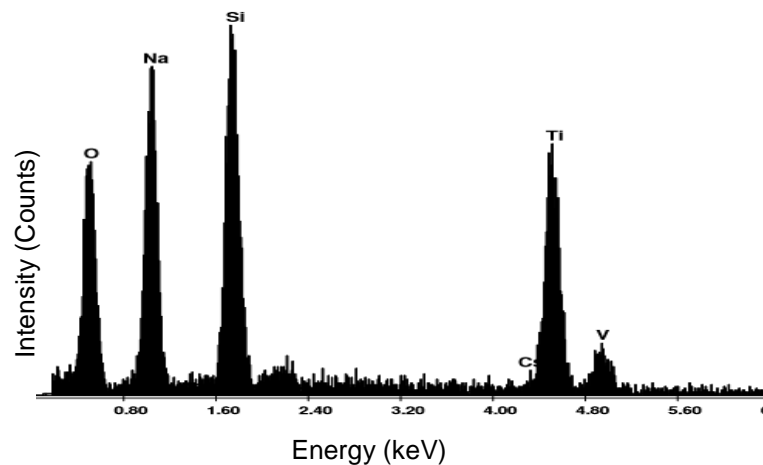


Figure 49: EDX spectrum of 10 %-vanadium-paranatisite-cesium ion exchanged material.

Table 29: Elemental composition of vanadium-paranatisite-cesium ion exchanged material.

	5 %-Vanadium-Paranatisite		10 %-Vanadium-Paranatisite	
	Weight (%)	Atomic (%)	Weight (%)	Atomic (%)
O K	33.33 (± 05.80)	59.28 (± 09.20)	39.00 (± 12.01)	53.84 (± 08.91)
Na K	10.39 (± 00.42)	12.86 (± 01.20)	26.14 (± 15.20)	25.11 (± 08.01)
Si K	05.60 (± 00.28)	5.67 (± 01.29)	16.84 (± 10.10)	13.24 (± 04.50)
Cs L	20.85 (± 12.10)	4.46 (± 02.03)	01.61 (± 0.60)	00.27 (± 00.09)
Ti K	29.84 (± 19.80)	17.73 (± 07.45)	15.57 (± 05.21)	07.18 (± 03.42)
V K	00.00	00.00	00.84 (± 00.12)	00.36 (± 00.10)
Total	100.00	100.00	100.00	100.00

5.1.5.2: Cerium Analysis

As seen in Figure 50, cerium L emission lines appear at ~ 4.84 keV causing overlap with titanium K emission lines present at ~ 4.94 keV, meaning that EDX analysis could only be used as a guide.

There was a greater percentage of cerium within the 5 %-vanadium-paranatisite framework. However, comparison of EDX analysis with other exchanged material, where no overlap (except for vanadium) takes place with titanium, shows the reported atomic weight percentage to be ~ 10 % of the total atomic percentage weight. Within Table 30, Ti K constitutes to 4.86 % and 7.69 % respectively to 5 % and 10 %-vanadium-paranatisite. It is therefore believed that the high atomic percentages reported for cerium are due to the overlap of cerium L emission lines with titanium K emission lines. (EDX Spectrum for 5 %-Vanadium-Paranatisite-Cesium ion exchanged material shown in A40).

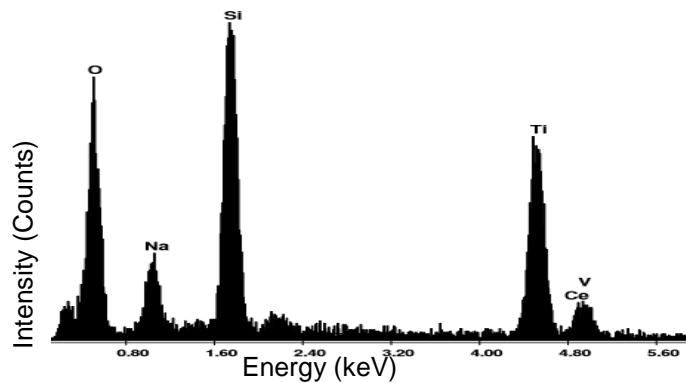


Figure 50: EDX spectrum of 10 %-vanadium-paranatisite-cerium ion exchanged material.

Table 30: Elemental composition of vanadium-paranatisite-cerium ion exchanged material.

	5 %-Vanadium- Paranatisite		10 %-Vanadium- Paranatisite	
	Weight (%)	Atomic (%)	Weight (%)	Atomic (%)
O K	35.47 (± 22.79)	65.96 (± 25.90)	51.58 (± 30.12)	68.78 (± 35.01)
Na K	01.59 (± 00.42)	02.05 (± 01.20)	09.56 (± 05.91)	08.87 (± 03.59)
Si K	05.18 (± 03.25)	05.49 (± 04.28)	18.30 (± 06.23)	13.90 (± 02.34)
Ce L	34.32 (± 25.12)	21.32 (± 17.24)	17.27 (± 05.27)	07.69 (± 02.43)
Ti K	22.89 (± 09.56)	04.86 (± 00.27)	02.34 (± 00.51)	00.36 (± 00.09)
V K	00.56 (± 00.12)	00.33 (± 00.07)	00.94 (± 00.19)	00.40 (± 00.03)
Total	100.00	100.00	100.00	100.00

5.1.5.3: Cobalt Analysis

EDX analysis shown in Figure 51, saw the presence of an extra peak at ~7.0 keV characteristic of the cobalt emission line. Elemental composition analysis suggested that 10 %-vanadium-paranatisite had higher levels of cobalt within the framework when compare to 5 %-vanadium-paranatisite as shown in Table 31. (EDX Spectrum for 5 %-vanadium-paranatisite-cobalt ion exchanged material shown in A41).

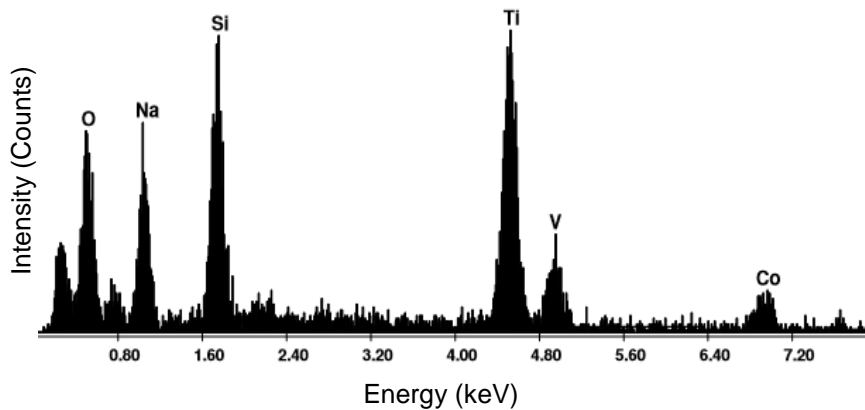


Figure 51: EDX spectrum of 10 %-vanadium-paranatisite-cobalt ion exchanged material.

Table 31: Elemental composition of vanadium-paranatisite-cobalt ion exchanged material.

	5 %-Vanadium-Paranatisite		10 %-Vanadium-Paranatisite	
	Weight (%)	Atomic (%)	Weight (%)	Atomic (%)
O K	48.52 (± 32.10)	65.71 (± 29.10)	39.88 (± 21.11)	57.43 (± 35.61)
Na K	12.80 (± 00.12)	12.07 (± 00.11)	18.62 (± 02.13)	18.66 (± 03.64)
Si K	15.98 (± 04.17)	12.32 (± 03.26)	13.26 (± 05.16)	10.88 (± 00.91)
Ti K	17.86 (± 06.20)	08.08 (± 05.12)	20.47 (± 10.12)	09.84 (± 00.12)
V K	00.79 (± 0.42)	00.34 (± 00.12)	02.46 (± 00.43)	01.11 (± 00.51)
Co K	04.05 (± 02.10)	01.49 (± 00.23)	05.30 (± 00.12)	02.07 (± 00.99)
Total	100.00	100.00	100.00	100.00

5.1.5.4: Neodymium Analysis

Characteristic neodymium emission lines can be clearly seen within the spectrum shown in Figure 52, confirming that successful ion exchange had taken place. Analysis collected from Table 32, indicated that 5 %-vanadium-paranatisite showed greater exchange capacity towards neodymium. Nevertheless, slight overlap of vanadium K emission lines with neodymium L emissions lines means that full quantitative data was unreliable. (EDX spectrum for 5 %-vanadium-paranatisite-neodymium ion exchanged material shown in A42).

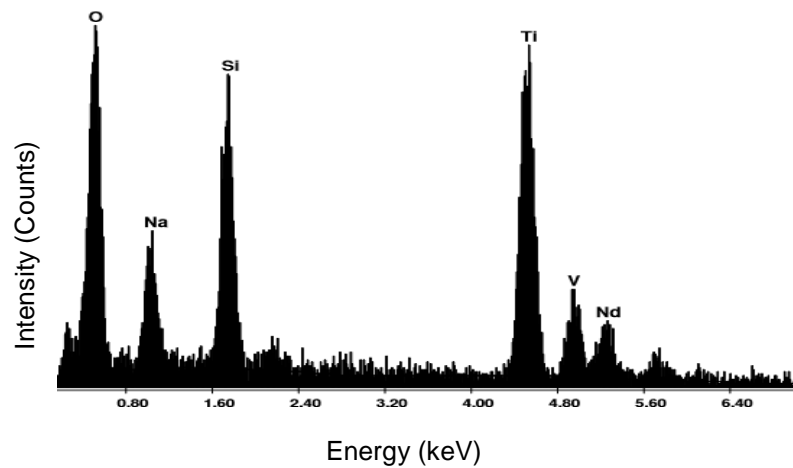


Figure 52: EDX spectrum of 10 %-vanadium-paranatisite-neodymium ion exchanged material.

Table 32: Elemental composition of vanadium-paranatisite-neodymium ion exchanged material.

	5 %-Vanadium-Paranatisite		10 %-Vanadium-Paranatisite	
	Weight (%)	Atomic (%)	Weight (%)	Atomic (%)
O K	41.62 (± 29.18)	59.97 (± 31.13)	49.41 (± 17.12)	69.95 (± 30.12)
Na K	15.21 (± 04.15)	15.25 (± 02.59)	10.86 (± 00.98)	10.70 (± 00.23)
Si K	13.78 (± 05.89)	11.31 (± 03.98)	11.09 (± 02.37)	08.95 (± 01.21)
Ti K	21.46 (± 11.59)	10.33 (± 02.14)	16.71 (± 05.17)	07.90 (± 02.99)
V K	00.78 (± 0.42)	00.35 (± 00.12)	02.19 (± 00.19)	00.97 (± 00.24)
Nd L	07.14 (± 05.21)	02.79 (± 00.71)	09.74 (± 00.42)	01.53 (± 00.24)
Total	100.00	100.00	100.00	100.00

5.1.5.5: Strontium Analysis

The overlap of characteristic strontium L emission lines with silicon K emission lines meant that full determination could not be conducted. Within Figure 53, it was observed that there was no presence of strontium K emission lines at ~ 14.00 keV indicating only a small amount of strontium had been exchanged during ion exchange experiments. This concurred with XRD patterns suggesting that minimal changes to the structure had occurred. Elemental composition analysis of the strontium ion exchanged material is shown in Table 33. (EDX spectrum for 5 %-vanadium-paranatisite-strontium ion exchanged material shown in A43).

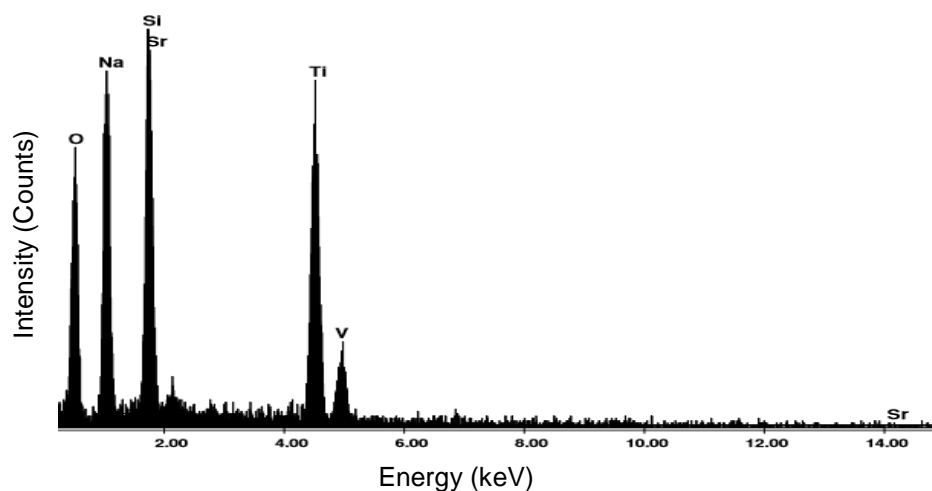


Figure 53: EDX spectrum of 10 %-vanadium-paranatisite-strontium ion exchanged material.

Table 33: elemental composition of vanadium-paranatisite-strontium ion exchanged material.

	5 %-Vanadium-Paranatisite		10 %-Vanadium-Paranatisite	
	Weight (%)	Atomic (%)	Weight (%)	Atomic (%)
O K	40.36 (± 30.12)	55.26 (± 25.01)	43.56 (± 20.12)	58.71 (± 28.10)
Na K	25.75 (± 11.12)	24.54 (± 10.13)	23.12 (± 09.13)	21.68 (± 08.13)
Si K	14.73 (± 10.87)	11.49 (± 09.87)	14.60 (± 04.99)	11.21 (± 02.37)
Sr L	00.00	00.00	00.00	00.00
Ti K	17.40 (± 07.55)	07.96 (± 05.39)	17.46 (± 04.78)	07.86 (± 02.31)
V K	01.75 (± 00.23)	00.75 (± 00.35)	01.25 (± 00.14)	00.53 (± 00.21)
Total	100.00	100.00	100.00	100.00

5.1.6.0: XRF Analysis

XRF analysis upon all vanadium-paranatisite exchanged materials was carried out to confirm the presence of all target ions. A list of energy values in which the peaks occurred are shown in Table 34, whilst a stack view of XRF data for 10 %-vanadium-paranatisite, cesium, cerium, cobalt, neodymium and strontium ion exchanged material is shown in Figure 54. (List of characteristic XRF emission lines for 5 %-vanadium-paranatisite-cesium, cerium, cobalt, neodymium and strontium ion exchanged material and the stack view of XRF spectra is shown in A44).

Table 34: List of characteristic XRF emission lines for 10 %-vanadium-paranatisite-cesium, cerium, cobalt, neodymium and strontium ion exchanged material.

Element	Energy (keV)	Emission
Cesium	4.86	L _{α1} , L _{α2}
	5.33	L _{β1}
Cerium	4.22	L _{α1} , L _{α2}
	5.59	L _{β2}
	5.23	L _{β1}
Cobalt	6.83	K _{α1} , K _{α2}
	7.54	K _{β1}
Neodymium	4.88	L _{α2}
	5.65	L _{α1}
	5.99	L _{β1}
	6.49	L _{β2}
	6.83	L _{γ1}
Strontium	13.98	K _{α1} , K _{α2}

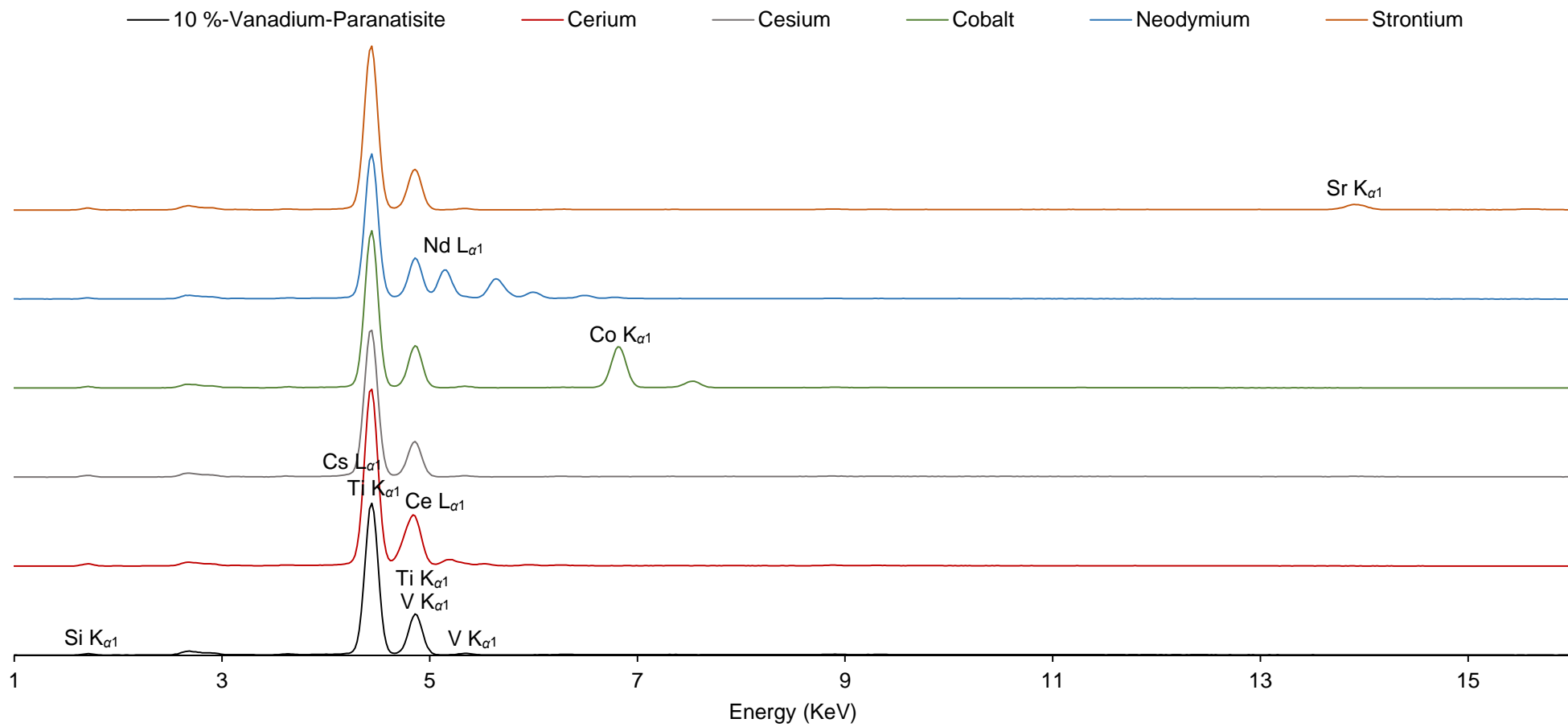


Figure 54: Stack view of XRF spectra of 10 %-vanadium-paranatisite, cesium, cerium, cobalt, strontium and neodymium ion exchanged material.

5.1.7.0: Conclusion of Vanadium-Paranatisite Ion Exchange Capabilities

Analysis conducted via ICP-MS, refined lattice parameters via Pawley refinements, EDX and XRF provided information regarding ion exchange capacity and affinity for 5 %-vanadium-paranatisite and 10 %-vanadium-paranatisite ion exchange behaviours.

ICP-MS analysis concluded that 5 %-vanadium-paranatisite when compared to 10 %-vanadium-paranatisite had higher affinities towards strontium, cobalt, neodymium and cerium, whilst 10 %-vanadium-paranatisite showed to possess higher affinities towards cesium.

XRD analysis conducted upon 5 %-vanadium-paranatisite concurred with the results obtained through ICP-MS analysis. XRD analysis showed that 5 %-vanadium-paranatisite lost crystallinity during exchanges involving strontium, cesium and neodymium with refined lattice parameters showing the greatest variations for cerium and neodymium ion exchanges. EDX analysis suggested that when compared to 10 %-vanadium-paranatisite, 5 %-vanadium-paranatisite contained higher percentages of cerium and neodymium. Finally, XRF analysis confirmed the presence of all ions within the exchanged materials.

Analysis conducted on the 10 %-vanadium-paranatisite ion exchanged materials showed that both cerium and neodymium exchanges showed the greatest variation of the lattice parameters compared to the un-exchanged lattice parameters. Of the crystalline phases, cobalt showed the greatest variation of peak intensities and refined lattice parameters, indicating the increased uptake of the ion in comparison to the other ions used in exchange experiments. EDX analysis did not concur with ICP-MS results with regards to cesium, however the increased overlap of emission lines could have caused inaccuracies within the

analysis yielded from this technique. Finally, XRF analysis conducted also concluded that all appropriate ions were present within the exchanged materials.

5.2.0.0: Vanadium-Natisite Ion Exchange Analysis

5.2.1.0: ICP-MS Analysis

To determine the percentage uptake of each specific ion, ICP-MS was used and analysis was conducted on the filtrate collected post the ion exchange experiment.

ICP-MS analysis showed that 5 %-vanadium-natisite had higher affinity towards strontium, cobalt, neodymium and cerium when compared to 10 %-vanadium-natisite. 10 %-vanadium-natisite showed the highest affinity towards cesium in comparison to 5 %-vanadium-natisite.

Both materials showed similar trends with respect to ions which had the highest and lowest exchange affinity. The trend seen for 5 %-vanadium-natisite was $Ce < Nd < Cs < Co < Sr$ with strontium having the highest exchange affinity and cerium being the lowest. However, with 10 %-vanadium-natisite, the trend as reported in Table 35 is $Ce < Nd < Cs < Sr < Co$.

Table 35: Ion percentage uptake from 24 hour ion exchange for vanadium-natisite.

	5 %-Vanadium-Natisite Ion Percentage Exchanged into Framework (%)	10 %-Vanadium-Natisite Ion Percentage Exchanged into Framework (%)
Cesium	19 (\pm 0.28)	21 (\pm 0.71)
Cerium	16 (\pm 0.42)	14 (\pm 0.62)
Cobalt	28 (\pm 0.26)	24 (\pm 0.23)
Strontium	30 (\pm 0.53)	23 (\pm 0.61)
Neodymium	19 (\pm 0.90)	17 (\pm 0.37)

5.2.2.0: XRD Analysis

Analysis of the 5 % and 10 %-vanadium-natisite diffraction patterns following exchange with strontium, cobalt and cesium showed minimal changes, suggesting little/no damage had occurred to both frameworks.

There was little change in the position of the peaks compared to the un-exchanged materials implying there was no change in the space group upon exchange.

Changes to peak intensities varied with the nature of the exchanged cation, with the greatest variation to peak intensities within all patterns being seen at lower 2θ values ranging from 17.47° - 32.79° 2θ . Both levels of vanadium doping showed the greatest changes to intensities after strontium exchange. Peak intensities at 17.46° , 19.42° and 22.25° 2θ showed an increase following strontium exchange by 31.3 %, 2.8 % and 2.3 % and 20.9 %, 1.8 % and 3.5 % for 5 % and 10 %-vanadium-natisite respectively.

The diffraction patterns for the cesium exchanged materials showed the fewest changes to the peak intensities for both vanadium-natisite frameworks. Monitoring the same peak positions at 17.46° , 19.42° and 22.25° 2θ showed a decrease in intensities for 5 %-vanadium-natisite by -3.9 %, -0.7 % and -0.8 %, whilst 10 %-vanadium-natisite saw variations by 8.7 %, -0.1 % and 1.6 %.

Comparison of the two frameworks following strontium and cobalt ion exchanges showed that there were greater variations in intensities for 5 %-vanadium-natisite when compared to the original un-exchanged patterns. This tied in with ICP-MS results that showed both strontium and cobalt showed the greatest exchange capacities with 5 %-vanadium-natisite. However, for cesium, 10 %-vanadium-natisite showed greater variation to peak intensities at lower 2θ values between

17.47 °- 32.79 ° 2 θ , tying in with ICP-MS results that showed 10 %-vanadium-natisite had higher capacity towards the cesium ion.

The diffraction peak relative intensities for 5 %-vanadium-natisite after strontium, cobalt and cesium ion exchange are shown in Table 36 with a stack view of the X-ray diffraction patterns shown in Figure 55. 10 %-vanadium-natisite peak analysis of cesium, cobalt and strontium ion exchanged material is shown in Table 37 with a stack view of the X-ray diffraction patterns shown in Figure 56.

Table 36: Peak analysis of 5 %-vanadium-natisite-cesium, cobalt and strontium ion exchanged material.

hkl	2 Theta (°)	5 %-Vanadium-Natisite (%)	Strontium (%)	Cobalt (%)	Cesium (%)
001	17.466	39.6	70.7	43.9	35.7
110	19.42	5.2	8.0	6.1	4.5
011	22.249	16.8	19.1	18.7	16.0
020	27.560	16.8	18.6	28.0	16.5
021	32.791	100.0	100.0	100.0	100.0
002	35.288	3.2	3.7	3.8	3.1
211	35.671	11.4	11.1	12.3	11.2
012	38.002	12.0	13.8	12.3	12.7
220	39.344	9.5	9.6	10.8	9.8
310	44.204	3.6	4.6	4.9	3.6
031	45.623	4.3	4.3	5.1	4.9
222	53.833	9.8	9.1	9.3	10.4
032	55.859	2.5	2.9	2.3	2.9
040	56.814	6.3	5.9	5.8	6.9
312	57.726	0.4	-	-	-
041	59.887	0.3	-	-	0.4
330	60.602	0.5	-	-	0.7
023	61.688	2.3	2.3	2.2	2.7
213	63.497	2.0	1.9	2.3	2.5
421	67.01807	3.7	3.2	2.4	3.8
042	68.7074	0.7	-	-	0.9

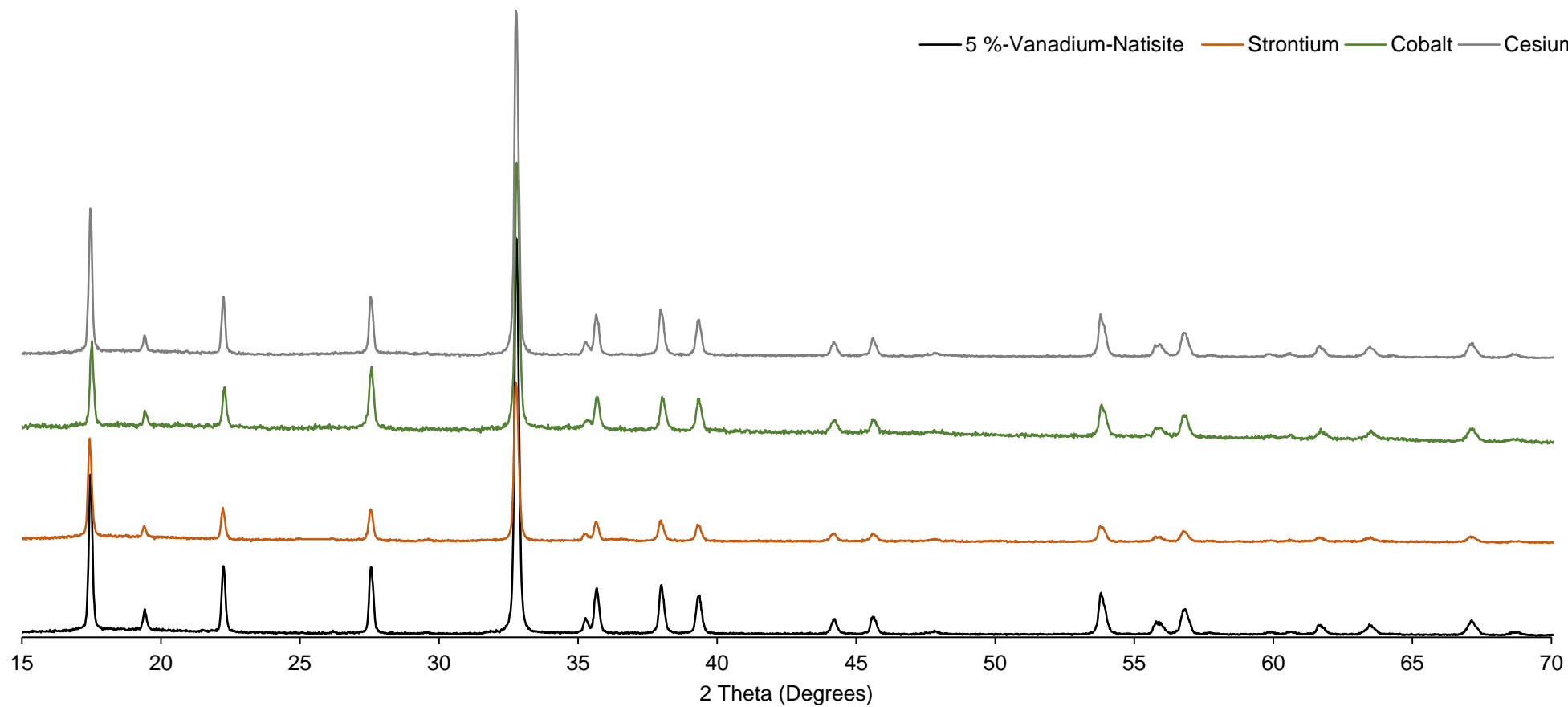


Figure 55: Stack view of XRD patterns of 5 %-vanadium-natisite, strontium, cobalt and cesium ion exchanged material.

Table 37: Peak analysis of 10 %-vanadium-natisite-cesium, cobalt and strontium ion exchanged material.

hkl	2θ ($^{\circ}$)	10 %- Vanadium- Natisite (%)	Strontium (%)	Cobalt (%)	Cesium (%)
001	17.500	32.2	53.1	43.9	40.9
110	19.436	4.7	6.5	6.1	4.6
001	22.272	13.6	17.1	18.7	15.2
020	27.582	16.4	19.7	28.0	16.5
021	32.810	100.0	100.0	100.0	100.0
002	35.348	2.5	2.1	3.8	2.2
211	35.690	11.8	10.5	12.3	10.5
012	38.028	9.5	8.1	12.3	7.9
220	39.362	10.3	9.3	10.8	9.7
310	44.222	3.4	3.5	4.9	3.5
031	45.647	4.6	3.2	5.1	4.0
311	47.901	1.4	-	-	0.6
222	53.857	10.9	8.3	9.3	8.6
032/013	55.817	2.6	1.8	2.3	1.8
040	56.847	6.7	5.5	5.8	6.5
023	61.735	2.3	1.1	2.2	1.8
213	63.503	2.4	2.0	2.3	2.0
421	67.162	3.9	3.0	2.4	3.7
042	68.721	0.8	-	-	0.4

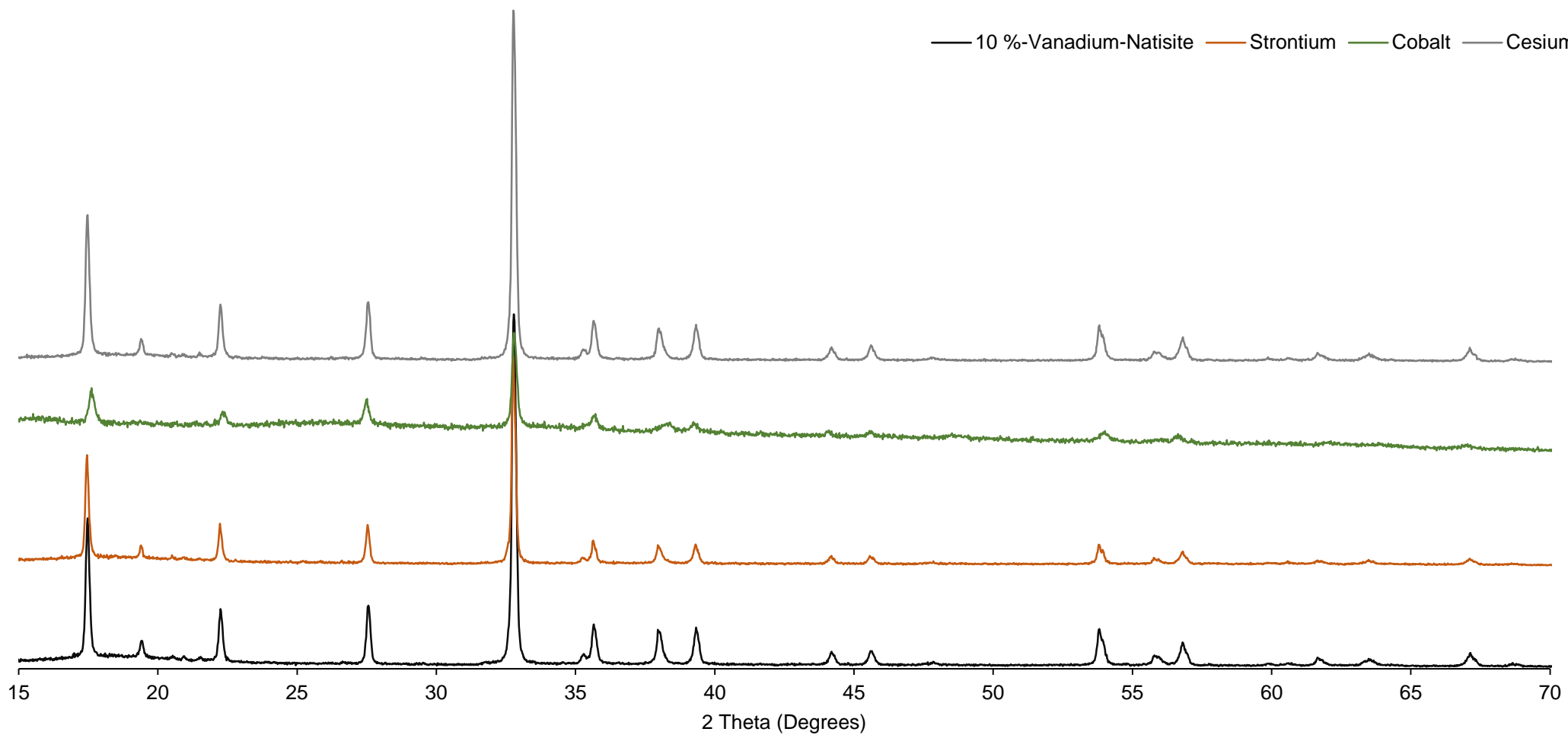


Figure 56: Stack view of XRD patterns of 10 %-vanadium-natisite, strontium, cobalt and cesium ion exchanged material.

5 % and 10 %-vanadium-natisite diffraction patterns following cerium and neodymium ion exchanges showed a loss of crystallinity and broadening of the diffraction peaks.

The X-ray diffraction patterns collected after cerium ion exchange saw the presence of peaks at 19.436° , 27.582° and 32.810° 2θ . These three peaks were some of the most intense peaks within the un-exchanged material's X-ray diffraction patterns. Following the lost in crystallinity it is noted that no other peaks can be easily distinguished within the pattern.

X-ray diffraction patterns collected following ion exchanges with neodymium saw peak broadening and the reduction of peak intensities. With regards to 5 %-vanadium-natisite extra peaks can be seen within the diffraction pattern at 16.834° and 29.273° 2θ . When compared to known literature the extra peaks were due to neodymium hydroxide^[118]. It is therefore believed that neodymium hydroxide was formed during the exchange experiments, although the mechanism is not known.

Following the exchange of cerium and neodymium, typical peaks within the diffraction patterns where $h k l$ values of $h k 0$ (such as $0 2 0$ and $1 1 0$) were primarily seen. This indicates that although the layers themselves remained intact, the way in which they became stacked altered. Increasing the percentage of vanadium within the material used for exchange saw the addition of characteristic natisite peaks within the pattern. The peaks that were noted in addition held an $h k l$ value (such as $1 1 1$ and $0 2 1$), indicating that disruption of the stacking of layers decreased following the increase of vanadium doping. The decrease in disorder validates results shown from ICP-MS analysis that a lower percentage of cerium and neodymium were exchanged with 10 %-vanadium-

natisite. Diffraction patterns of 5 %-vanadium-natisite, cerium and neodymium ion exchanged material is shown in Figure 57. Diffraction patterns of 10 %-vanadium-natisite, cerium and neodymium exchanged diffraction patterns are shown in Figure 58.

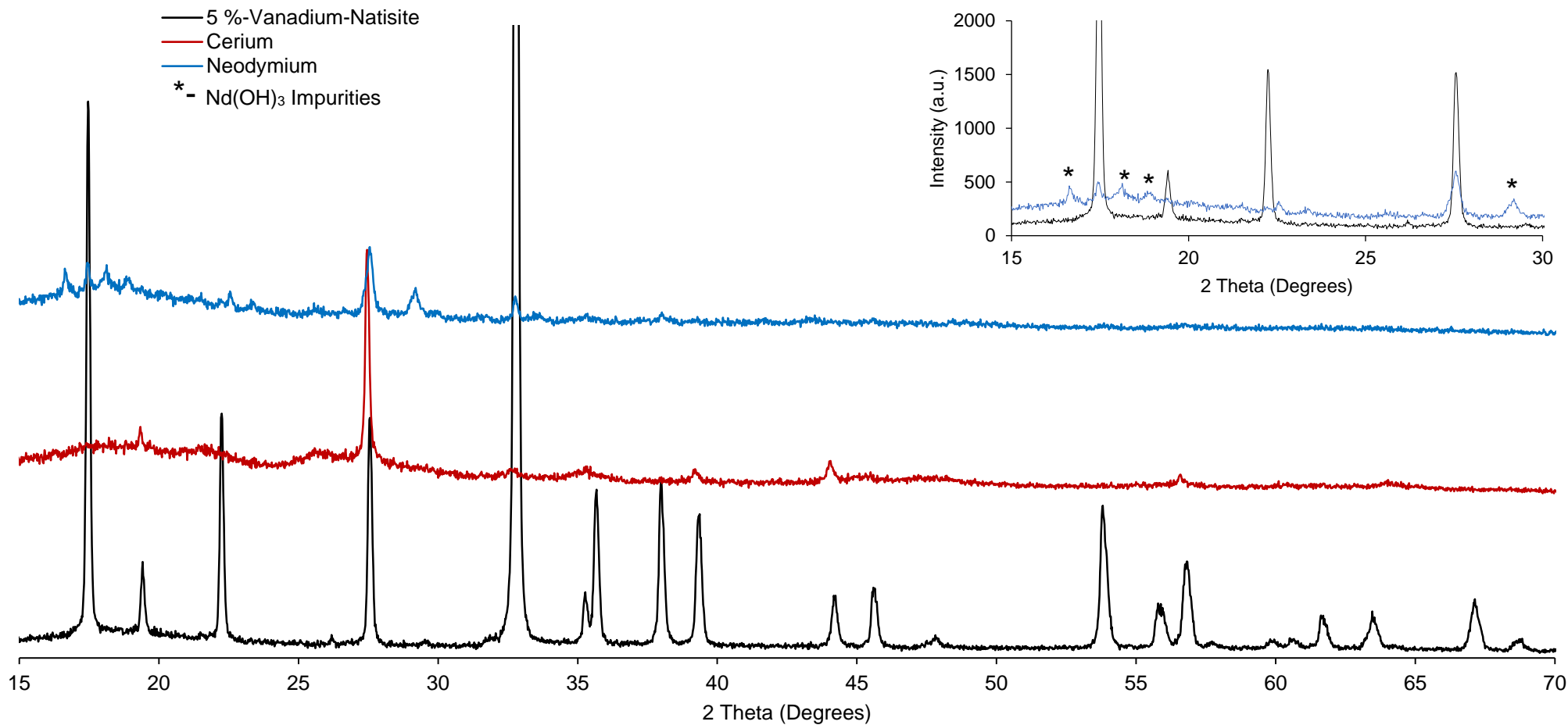


Figure 57: Stack view of XRD patterns of 5 %-vanadium-natisite, cerium and neodymium ion exchanged material.

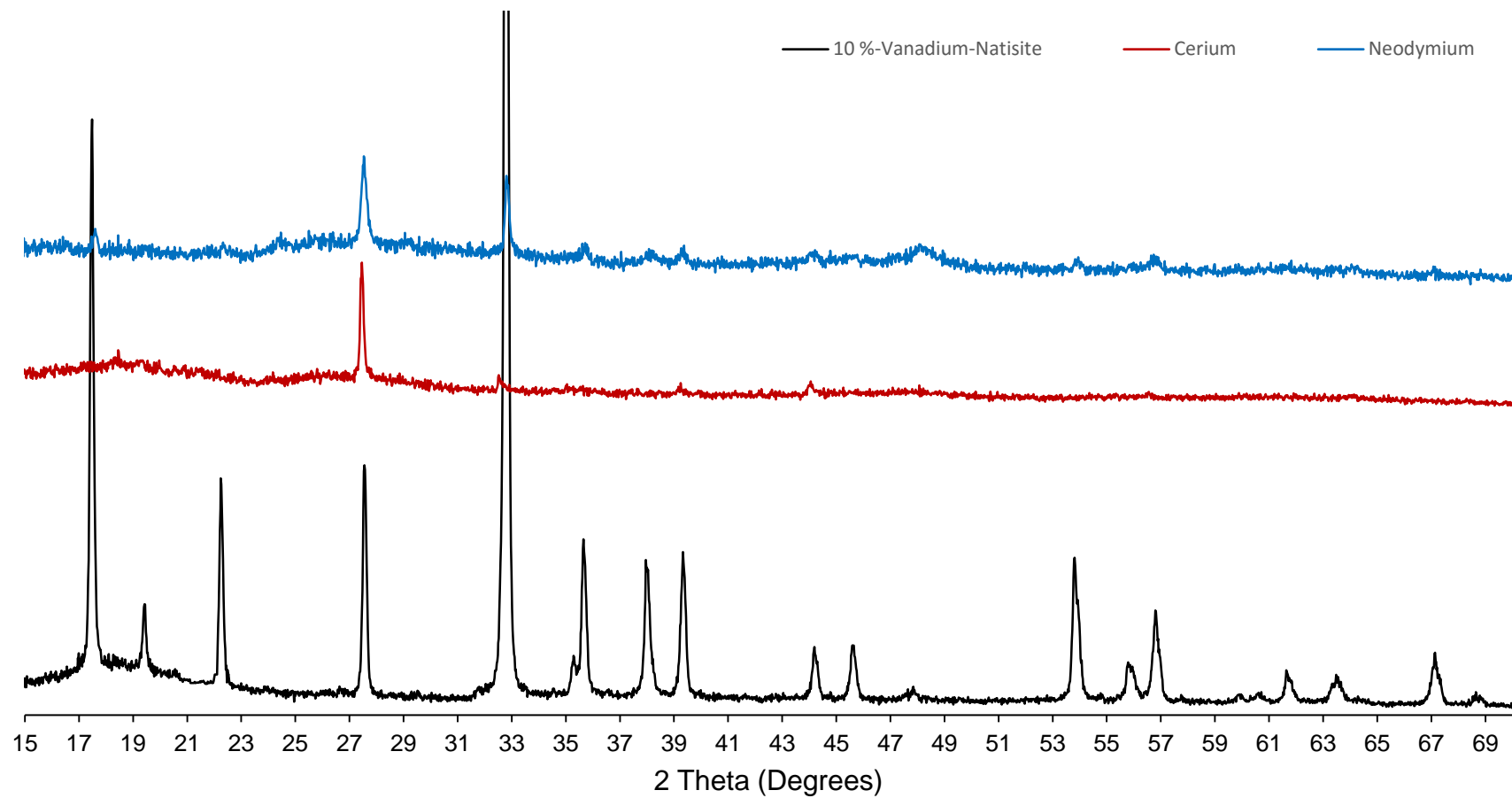


Figure 58: Stack view of XRD patterns of 10 %-vanadium-natisite, cerium and neodymium ion exchanged material.

5.2.3.0: Lattice Refinements via Pawley Fits

5.2.3.1: 5 %-Vanadium-Natisite

Unit cell parameters following ion exchanges were determined using Pawley fits. All ion exchanges, except for neodymium showed an increase in at least two of the lattice parameters. Cesium and cerium showed elongation of all three lattice parameters a , b and c , whilst cobalt and strontium showed increases in a and b and contraction in c when compared to un-exchanged 5 %-vanadium-natisite.

Of the crystalline phases, strontium, cobalt and cesium; strontium showed the greatest variation from the lattice parameters, showing elongation in the $a = b$ axes by 0.005 Å (3 d.p.) and contraction by -0.008 Å (3 d.p.) followed by cobalt which showed elongation in the $a = b$ axes by 0.003 Å (3 d.p.) and contraction by -0.003 Å (3 d.p.). Cesium showed the lowest variation of elongation in $a = b$ axes by 0.0007 Å (3 d.p.) and in the c axis by 0.0017 Å (3 d.p.).

The errors reported in Table 38 for cerium and neodymium, were of an order of magnitude bigger than the other exchanged material. Such variation could be attributed to the possible formation of cerium dioxide/ carbonate and neodymium hydroxide/ carbonate. As specified by Pourbaix diagrams these species typically form within solutions varying from pH 6-8^[117]. Another explanation for such variation in lattice parameters is the degradation of the natisite framework upon contact with both cerium and neodymium. Further research utilising EXAFS analysis should be carried out to clarify the coordination environments of both cerium and neodymium. (Refined lattice parameters, Rietveld statistics and final Pawley fits for 10 %-vanadium-natisite-cesium, cerium, cobalt, strontium and neodymium ion exchanged material is shown in A45, A46, A47, A48 and A49).

Table 38: Refined lattice parameters for 5 %-vanadium-natisite-cesium, cerium, cobalt, neodymium and strontium.

	<i>a</i> (Å)	<i>b</i> (Å)	<i>c</i> (Å)	α (°)	β (°)	γ (°)	<i>R</i>_{WP} (%)
5 %-Vanadium-Natisite	6.48993 (7)	6.48993 (7)	5.09595 (9)	90	90	90	5.595
Cesium	6.491 (1)	6.491 (1)	5.098 (2)	90	90	90	9.440
Cerium	6.51 (2)	6.51 (2)	5.13 (3)	90	90	90	10.467
Cobalt	6.493 (4)	6.493 (4)	5.093 (4)	90	90	90	5.383
Strontium	6.495 (4)	6.495 (4)	5.088 (5)	90	90	90	10.274
Neodymium	6.49 (4)	6.49 (4)	5.09 (4)	90	90	90	11.923

5.2.3.2: 10 %-Vanadium-Natisite

Lattice refinements conducted following ion exchange experiments on the 10 %-vanadium-natisite frameworks showed elongation in the $a = b$ axes and contraction in the c axis with regards to strontium, cobalt, cesium and neodymium. Within each refinement contraction of the c axis was nearly double that of the elongation of the $a = b$ axes, for example, in the refinement conducted upon the cobalt ion exchanged material the $a = b$ axis expanded by 0.022 Å (3 d.p.) whilst the c axis contracted by -0.041 Å (3 d.p.). Unlike the other ion exchanged materials, lattice refinements collected following cerium and neodymium, ion exchanges showed that all three lattice parameters expanded. It must however, be noted that the errors within this refinements for cerium and neodymium are substantial. Such variation could be attributed to the possible formation of cerium dioxide/ carbonate and neodymium hydroxide/ carbonate. As specified by Pourbaix diagrams these species typically form within solutions varying from pH 6-8^[117]. Another explanation for such variation in lattice parameters is the degradation of the natisite framework upon contact with both cerium and neodymium. Further research utilising EXAFS analysis should be carried out to clarify the coordination environments of both cerium and neodymium. All lattice parameters obtained from refinements were obtained from XRD patterns conducted within 7 days of experimental procedures. Similarly, XRF, SEM and ICP-MS data was collected in the same period. All lattice parameters obtained from refinements are shown in Table 39. (Refined lattice parameters, Rietveld statistics and final Pawley fits for 10 %-vanadium-natisite-cesium, cerium, cobalt, strontium and neodymium ion exchanged material is shown in A50, A51, A52, A53 and A54).

Table 39: Refined lattice parameters for 10 %-vanadium-natisite-cesium, cerium, cobalt, neodymium and strontium.

	a (Å)	b (Å)	c (Å)	α (°)	β (°)	γ (°)	R_{WP} (%)
10 %- Vanadium- Natisite	6.48747 (7)	6.48747 (7)	5.097 (1)	90	90	90	5.605
Cesium	6.489 (3)	6.489 (3)	5.093 (3)	90	90	90	10.615
Cerium	6.51 (4)	6.51 (4)	5.13 (4)	90	90	90	10.948
Cobalt	6.51 (2)	6.51(2)	5.07 (1)	90	90	90	4.477
Strontium	6.490 (3)	6.490 (3)	5.093 (4)	90	90	90	10.927
Neodymium	6.49 (3)	6.49 (3)	5.06 (3)	90	90	90	7.119

5.2.4.0: SEM Analysis

SEM microscopy was used to examine the particle morphology of 5 % and 10 %-vanadium-natisite after the ion exchange. As discussed previously, in Chapter 4, vanadium-natisite can adopt a variety of morphologies. The majority of samples had the phase B morphology. On a few occasions, mixed morphology, with phase A was seen within the samples.

The resulting images show minor changes took place to morphology upon ion exchange with all ions of interest. In all cases the characteristic cross could still be observed upon the surface of the natisite particle. The greatest change to particle morphology was seen during 5 %-vanadium-natisite-cerium and neodymium ion exchanges. The electron micrographs shown in Figure 59 B and 59 E shows that changes to the morphology can be seen with some particles retaining morphology, whilst others lost morphology. The changes to particle morphology mirrors the loss of crystallinity seen in X-ray diffraction patterns. To determine whether such changes were due to the reduction in particle size, the formation of oxide and hydroxide species or the degradation of the titanium silicate framework, extra analysis such as EXAFS and PDF should be conducted. 5 %-vanadium-natisite exchanges are shown in Figure 59, whilst 10 %-vanadium-natisite ion exchanges are shown in Figure 60.

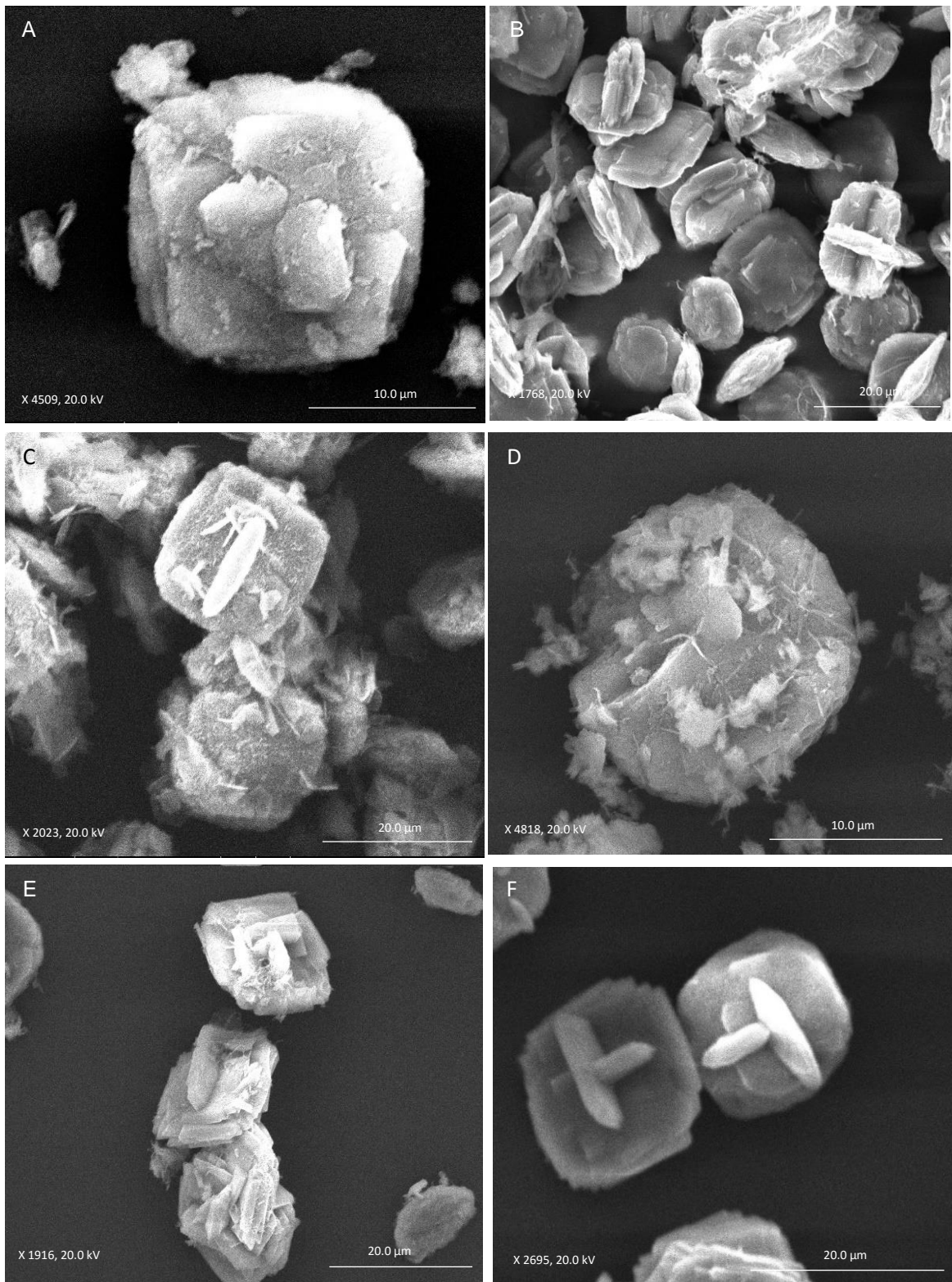


Figure 59: SEM images of 5 %-vanadium-natisite, cesium, cerium, cobalt, strontium and neodymium ion exchanged material. A- cesium ion exchange, B- cerium ion exchange, C- cobalt ion exchange, D- strontium ion exchange, E- neodymium ion exchange and F- 5 %-vanadium-natisite. 2695x magnification and 20.00 kV.

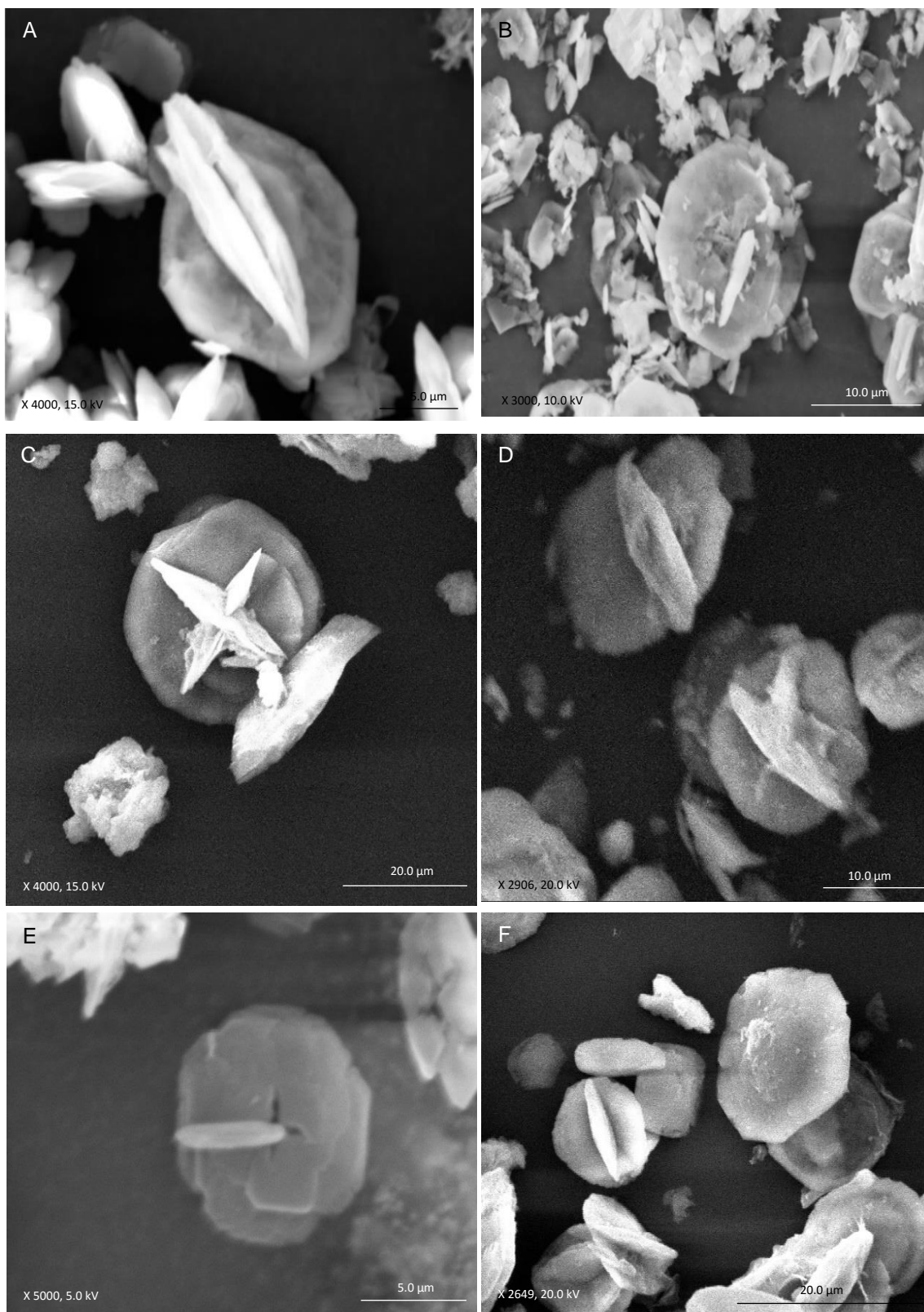


Figure 60: SEM images of 10 %-vanadium-natisite, cesium, cerium, cobalt, strontium and neodymium ion exchanged material. A- cesium ion exchange, B- cerium ion exchange, C-cobalt ion exchange, D- strontium ion exchange, E- neodymium ion exchange and F- 10 %-vanadium-natisite.

5.2.5.0: EDX Analysis

EDX analysis was carried out to determine the elemental composition of each ion exchanged material. However, due to overlap of the peaks from the exchanged ions and framework atoms, the reliability and accuracy of the results is questionable.

5.2.5.1: Cesium Analysis

In the spectrum, shown in Figure 61, cesium L emission lines, which appear ~ 4.23- 5.28 keV overlap with titanium and vanadium K emission lines. Elemental composition analysis indicated that 10 %-vanadium-natisite showed greater exchange capacity towards cesium compared to 5 %-vanadium-natisite. Nevertheless, due to the overlap of emission lines EDX analysis can only act as a guide. Atomic weight percentages are referred to in Table 40. (EDX spectrum for 5 %-vanadium-natisite-cesium ion exchanged material shown in A55).

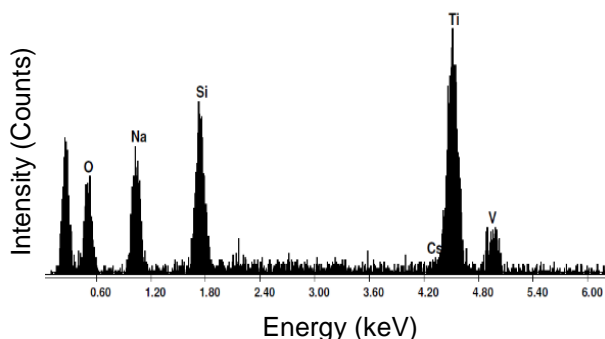


Figure 61: EDX spectrum of 10 %-vanadium-natisite-cesium ion exchanged material.

Table 40: Elemental composition of vanadium-natisite-cesium ion exchanged material.

	5 %-Vanadium-Natisite		10 %-Vanadium-Natisite	
	Weight (%)	Atomic (%)	Weight (%)	Atomic (%)
O K	47.64 (± 27.80)	62.39 (± 30.12)	32.95 (± 19.99)	50.26 (± 26.01)
Na K	24.10 (± 14.10)	21.97 (± 04.78)	21.08 (± 02.53)	22.37 (± 04.50)
Si K	10.64 (± 02.13)	07.94 (± 05.61)	13.58 (± 01.14)	11.80 (± 01.14)
Cs L	00.00	00.00	02.74 (± 00.74)	00.50 (± 00.23)
Ti K	17.35 (± 05.41)	07.59 (± 02.37)	28.20 (± 12.21)	14.37 (± 04.75)
V K	00.27 (± 00.05)	00.11 (± 00.21)	01.45 (± 00.47)	00.70 (± 00.24)
Total	100.00	100.00	100.00	100.00

5.2.5.2: Cerium Analysis

As shown in Figure 62, cerium L emission lines overlap with titanium and vanadium K emission lines. From Table 41, the atomic percentage of titanium is relatively low when compared to other samples where no overlap (except for vanadium) occurs. Typically, titanium has an atomic percentage weight of ~ 10.00 %, however, within the samples, where titanium overlaps with cerium, the atomic weight is reported to be ~ 0.78 %.

It is therefore believed that the atomic percentage of cerium within the samples are not accurate and the atomic percentage weight is the combination of cerium L and titanium K emission lines. (EDX Spectrum for 5 %-vanadium-natisite-cerium ion exchanged material shown in A56).

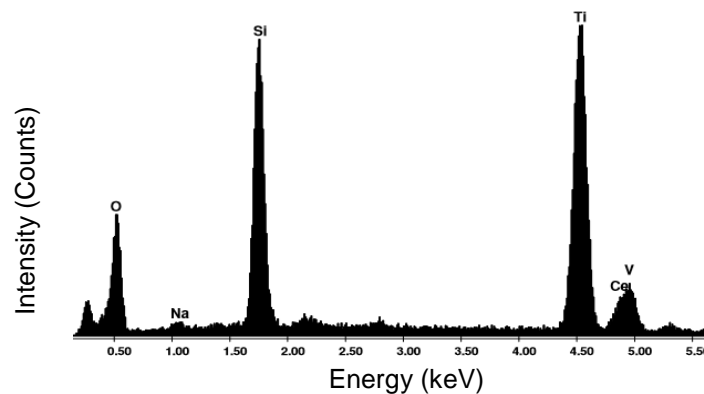


Figure 62: EDX spectrum of 10 %-vanadium-natisite-cerium ion exchanged material.

Table 41: Elemental composition of vanadium-natisite-cerium ion exchanged material.

	5 %-Vanadium-Natisite		10 %-Vanadium-Natisite	
	Weight (%)	Atomic (%)	Weight (%)	Atomic (%)
O K	37.40 (± 17.20)	60.31 (± 14.10)	37.40 (± 11.10)	60.31 (± 15.21)
Na K	01.13 (± 00.13)	01.27 (± 00.07)	01.13 (± 00.10)	01.27 (± 00.20)
Si K	18.00 (± 05.01)	16.53 (± 02.31)	18.00 (± 04.51)	16.53 (± 02.31)
Ce L	38.42 (± 22.58)	20.70 (± 10.01)	38.42 (± 10.25)	20.70 (± 09.78)
Ti K	04.25 (± 00.15)	00.78 (± 00.20)	04.25 (± 00.96)	00.78 (± 00.09)
V K	00.81 (± 00.20)	00.41 (± 00.10)	00.81 (± 00.29)	00.41 (± 00.13)
Total	100.00	100.00	100.00	100.00

5.2.5.3: Cobalt Analysis

EDX analysis showed the presence of two extra peaks at ~0.8 keV and ~7.0 keV, these peaks are said to be characteristic of cobalt L and K emission lines respectively, as shown in Figure 63. The elemental composition as shown in Table 42 further suggests that 5 %-vanadium-natisite had a higher affinity towards cobalt compared to the 10 % doped material. (EDX Spectrum for 5 %-vanadium-natisite-cobalt ion exchanged material shown in A57).

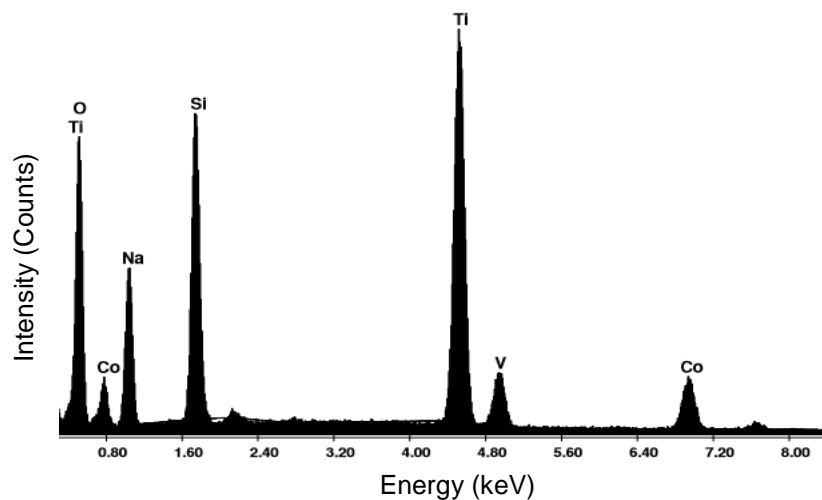


Figure 63: EDX spectrum of 10 %-vanadium-natisite-cobalt ion exchanged material.

Table 42: Elemental composition of vanadium-natisite-cobalt ion exchanged material.

	5 %-Vanadium-Natisite		10 %-Vanadium-Natisite	
	Weight (%)	Atomic (%)	Weight (%)	Atomic (%)
O K	44.85 (± 29.91)	63.33 (± 30.01)	44.44 (± 27.88)	61.10 (± 29.97)
Na K	13.96 (± 05.21)	13.72 (± 04.12)	16.20 (± 03.39)	15.49 (± 04.17)
Si K	12.31 (± 05.29)	09.90 (± 03.99)	17.30 (± 08.71)	13.55 (± 03.56)
Ti K	22.25 (± 07.77)	10.49 (± 02.31)	17.85 (± 05.78)	08.20 (± 01.12)
V K	00.38 (± 01.21)	00.17 (± 00.08)	01.52 (± 00.42)	00.66 (± 02.31)
Co K	06.25 (± 00.25)	02.40 (± 01.40)	02.69 (± 00.45)	01.00 (± 00.06)
Total	100.00	100.00	100.00	100.00

5.2.5.4: Neodymium Analysis

EDX analysis conclusively showed the presence of neodymium within the sample, as shown in Figure 64. The elemental composition shown in Table 43, suggested that 5 %-vanadium-natisite had a higher capacity of exchange for neodymium. However, quantitative analysis cannot be fully trusted using this technique due to the overlap of neodymium L lines with vanadium K emission lines. (EDX Spectrum for 5 %-vanadium-natisite-neodymium ion exchanged material shown in A58).

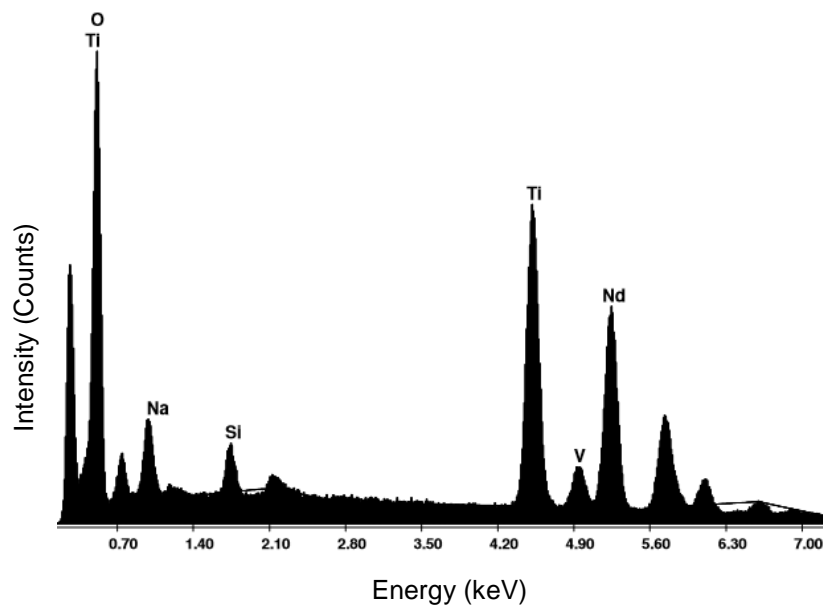


Figure 64: EDX spectrum of 10 %-vanadium-natisite-neodymium ion exchanged material.

Table 43: Elemental composition of vanadium-natisite-neodymium ion exchanged material.

	5 %-Vanadium-Natisite		10 %-Vanadium-Natisite	
	Weight (%)	Atomic (%)	Weight (%)	Atomic (%)
O K	44.64 (± 10.01)	76.93 (± 29.99)	32.71 (± 28.71)	58.93 (± 29.97)
Na K	05.16 (± 02.31)	06.19 (± 02.17)	10.01 (± 01.71)	12.55 (± 02.67)
Si K	02.21 (± 01.17)	02.17 (± 01.17)	08.67 (± 02.99)	08.89 (± 01.99)
Ti K	13.93 (± 03.25)	08.02 (± 00.21)	22.29 (± 04.59)	13.42 (± 02.17)
V K	00.51 (± 00.10)	00.28 (± 00.04)	02.59 (± 0.09)	01.47 (± 00.07)
Nd L	33.55 (± 12.97)	06.41 (± 01.49)	23.73 (± 12.79)	04.74 (± 01.28)
Total	100.00	100.00	100.00	100.00

5.2.5.5: Strontium Analysis

Figure 65 shows the overlap of strontium L emission lines with silicon K emission lines. Nevertheless, the atomic percentage weight of silicon close to the expected value and so as a result, other analysis techniques were also used to confirm the presence of strontium. Table 44 shows the elemental composition of vanadium-natisite-strontium ion exchanged material. (EDX spectrum for 5 %-vanadium-natisite-neodymium ion exchanged material shown in A59).

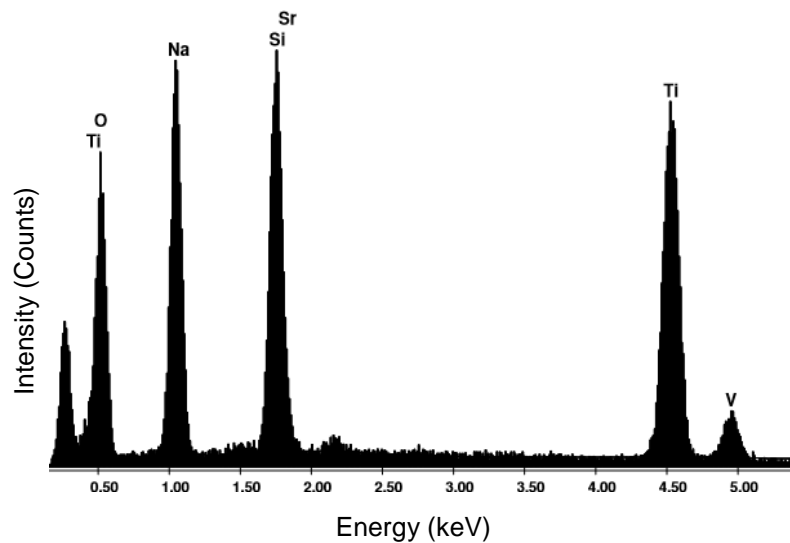


Figure 65: EDX spectrum of 10 %-vanadium-natisite-strontium ion exchanged material.

Table 44: Elemental composition of vanadium-natisite-strontium-ion exchanged material.

	5 %-Vanadium-Natisite		10 %-Vanadium-Natisite	
	Weight (%)	Atomic (%)	Weight (%)	Atomic (%)
O K	36.22 (± 16.21)	53.54 (± 18.87)	41.74 (± 12.21)	57.22 (± 17.17)
Na K	21.46 (± 09.97)	22.08 (± 08.79)	23.77 (± 13.01)	22.67 (± 11.07)
Si K	13.34 (± 03.34)	11.24 (± 00.87)	13.45 (± 00.14)	10.50 (± 00.57)
Sr L	05.22 (± 01.23)	01.41 (± 00.21)	19.96 (± 10.01)	09.14 (± 02.59)
Ti K	23.76 (± 12.01)	11.73 (± 09.97)	01.08 (± 00.81)	00.47 (± 00.21)
V K	00.00	00.00	00.00	00.00
Total	100.00	100.00	100.00	100.00

5.2.6.0: XRF Analysis

XRF analysis was conducted upon all the ion exchanged materials to determine the presence of the exchanged ions, as mentioned previously quantitative analysis could not be obtained.

The XRF data has been collated into one stack plot to give an overview of each exchange experiment, this can be seen in Figure 66. Characteristic emission lines with the Energy (keV) values they occurred at are given in Table 45. (List of Characteristic XRF Emission Lines for 5 %-vanadium-paranatisite-cesium, Cerium, Cobalt, Neodymium and Strontium Ion Exchanged Material and the stack view of XRF spectra is shown in A60).

Table 45: List of characteristic XRF emission lines for 10 %-vanadium-paranatisite-cesium, cerium, cobalt, neodymium and strontium ion exchanged material.

Element	Energy (keV)	Emission
Cesium	4.84	L _{α1} , L _{α2}
	5.57	L _{β2}
	5.24	L _{β1}
Cerium	4.22	L _{α1} , L _{α2}
	5.58	L _{β2}
	5.26	L _{β1}
Cobalt	6.87	K _{α1} , K _{α2}
	7.63	K _{β1}
Neodymium	4.92	L _{α2}
	5.20	L _{α1}
	5.72	L _{β1}
	6.06	L _{β2}
	6.57	L _{γ1}
Strontium	13.98	K _{α1} , K _{α2}
	15.62	K _{β1}

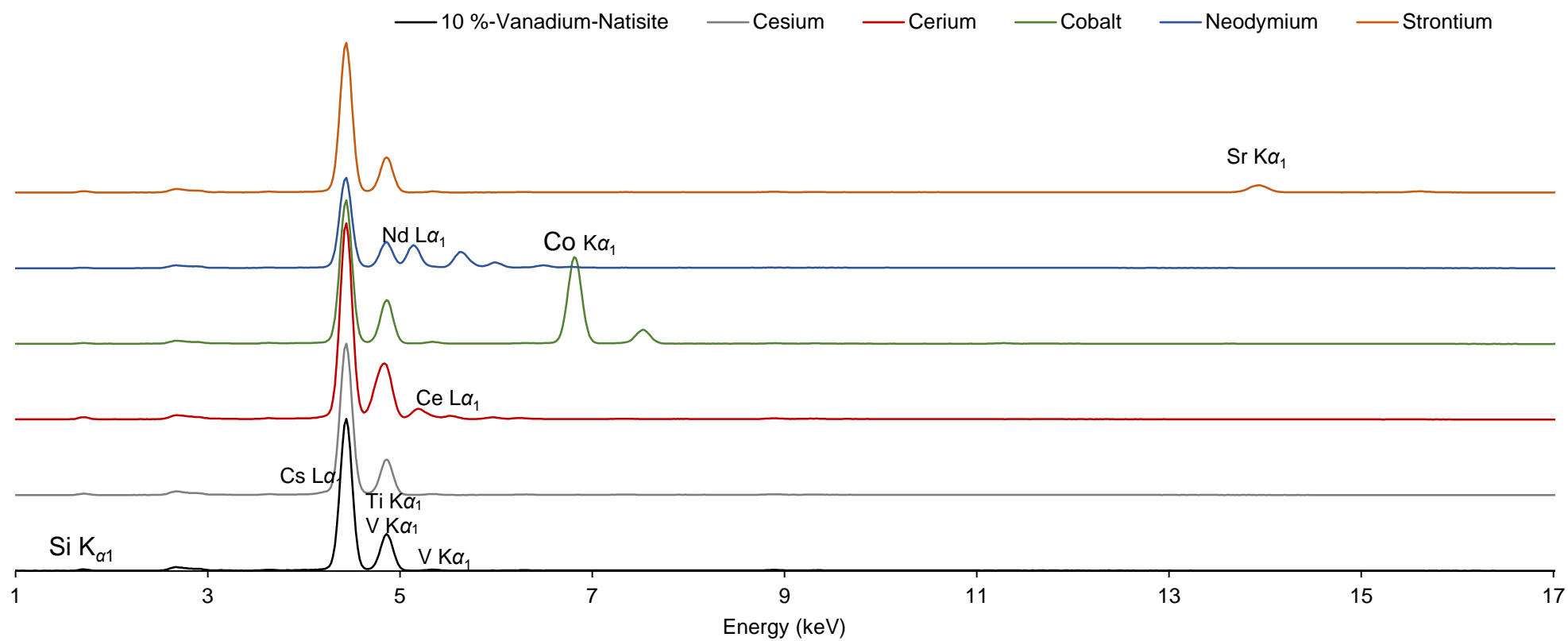


Figure 66: Stack view of XRF spectra of 10 %-vanadium-natisite, cesium, cerium, cobalt, strontium and neodymium ion exchanged material.

5.2.7.0: Conclusion of Vanadium-Natisite Ion Exchange Capabilities

Analysis via XRD, refined lattice parameters using TOPAS with jEdit, EDX, XRF and ICP-MS provided confirmation of one another, that strontium and cobalt underwent the greatest degree of exchange with the materials and cerium and neodymium underwent the least whilst causing possible structural damage to the frameworks.

Analysis via XRD and refined lattice parameters showed the greatest variation from the un-exchanged materials was the result of ion exchanges with strontium and cobalt. Further to this it showed that the greatest variation occurred with 5 %-vanadium-natisite in agreement with ICP-MS analysis that both strontium and cobalt exchange capacities were highest when 5 %-vanadium-natisite was used. Further to this XRD analysis showed that changes upon the exchange of cesium varied the greatest with regards to 10 %-vanadium-natisite, in alliance with ICP-MS analysis that cesium underwent greatest exchange upon contact with 10 %-vanadium-natisite.

EDX analysis also acted as a guide, indicating that 10 %-vanadium-natisite allowed for the greater exchange of cesium, whilst 5 %-vanadium-natisite allowed for greater exchange of cobalt and neodymium, acting in accordance with ICP-MS and XRD analysis.

Finally, XRF analysis showed the presence of all ions within each material, further indicating that although cerium and neodymium caused structural damage, ion exchange could take place with all ions.

5.2.8.0: Comparison of Vanadium-Paranatisite and Vanadium-Natisite Ion Exchange Capacities

Comparison undertaken on all materials showed that altering the percentage of vanadium within the framework altered both the overall capacity and affinities to certain ions.

For example, 5 %-vanadium-paranatisite exhibited the highest affinity towards strontium, cobalt and neodymium whilst 10 %-vanadium-paranatisite showed the highest affinity towards cesium and cerium when compared to one another and vanadium-natisite.

Vanadium-natisite showed similar general trends to vanadium-paranatisite, with 5 %-vanadium-natisite showing increased affinity to strontium, cobalt, cerium and neodymium. From the data presented in Table 24, Table 35 and Figure 67, the ion exchange capabilities of vanadium-paranatisite and vanadium-natisite are comparable, with 5 %-vanadium frameworks differing between 5-1 % exchange capabilities and 10 %-vanadium frameworks differing between 5 and 2 % exchange capabilities. Although the capabilities of both frameworks are similar, vanadium-paranatisite structures showed greater levels of exchange towards the ions when compared to vanadium-natisite materials.

The increased affinity of paranatisite to all ions when compared to natisite may be attributed to the overall structure of both frameworks. Paranatisite exhibits a less ordered structure, with the sodium ions adopting three unique environments. Natisite however, is more structured and the sodium ions adopt only one unique environment. The increase variation in sodium environments means there may be an increase likelihood that the ions under investigation can find a position within the framework that is more favourable. It therefore can be postulated that

the increased variation of sodium environments within the paranatisite framework as well as the possible increase access to the structure, enhances the ion exchange abilities of paranatisite.

Finally, the work conducted during this study were compared to the results obtained from another student following Ti-natisite^[85] ion exchange experiments. It was seen that doping the frameworks of Ti-natisite and Ti-paranatisite with varying amounts of vanadium showed an overall increase in the exchange capacities of both frameworks with regards to cesium, cobalt and strontium.

The increase in exchange capabilities following vanadium doping may be explained via other research. Previous research conducted has shown that vanadium doped/ vanadium silicate frameworks have shown increased affinity towards such ions^[84]. Although the mechanism to why the affinity increases is not fully understood, it can be assumed that altering the bond lengths of the unit cell alters the ion exchange environment available. This therefore changes the affinities towards certain ions, and in this way, the framework can be manipulated to suit the needs of the end user. An overview of the exchange capacities of each material and Ti-natisite are shown in Figure 67.

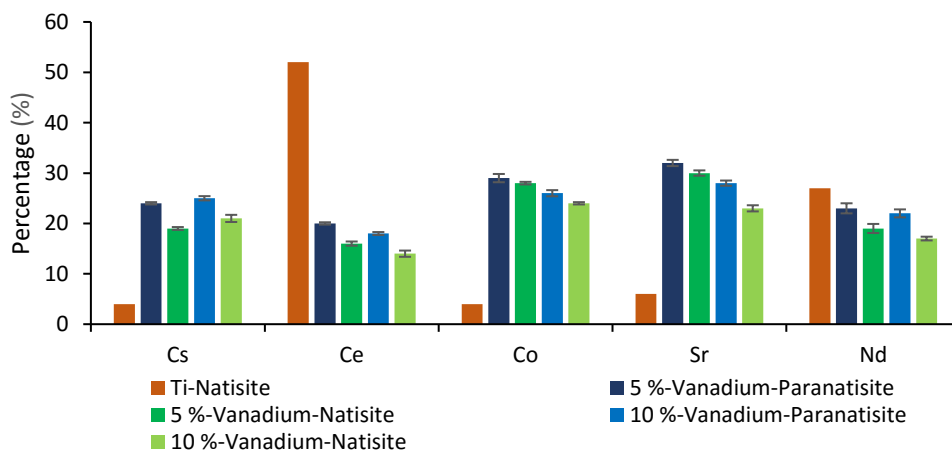


Figure 67: Comparison graph of Ti- natisite^[85], 5 %-vanadium-paranatisite, 10 %-vanadium-paranatisite, 5 %-vanadium-natisite and 10 %-vanadium-natisite ion exchange capabilities.

Future work

Continuation of the work presented in this thesis could be conducted in a number of areas, such as further research into ion exchange experiments.

Further ion exchange experiments could be conducted in order to determine the optimum capacity of both titanium silicate frameworks, the rate of exchange, their ability to undergo ion exchange in acidic conditions, common environments within the nuclear industry^[2]. Their ability to exchange with the desired radioactive ions in the presence of highly competing non-radioactive ions such as sodium and magnesium, environments seen during the Fukushima, Three Mile Long and Chernobyl incidents could be investigated.^[30, 70] Also the ability to regenerate and reuse both vanadium-paranatisite and vanadium-natisite following ion exchange experiments, as seen with Clinoptilolite in the SIXEP process^[58] could be studied. Leach testing could also be undertaken to determine the mobility of the ions in the structures. It would be undesirable for the ions to exchange back out of the materials during long term storage. Comparison of ion exchange capabilities could then be compared to other materials in use in industry today.

Further quantitative analysis could also be conducted. In addition to ICP-MS analysis, other techniques such as Wavelength Dispersive X-ray Fluorescence (WDXRF) could be used in to provide complementary quantitative analysis of the ion exchange percentages.

As well as conducting research into the exchange capacities of each framework, radiation tests at the Dalton Cumbrian Facility (DCF) at the University of Manchester could be undertaken. The facility uses Co-60, a gamma irradiator, to provide information upon the structural integrity of the materials. Following exposure to gamma radiation, the material would undergo X-ray diffraction

analysis to investigate the structure and then do further leach testing. As a result, both vanadium-paranatisite and vanadium-natisite could be tested to determine their capabilities in withstanding such radiation.

Finally, in depth structural analysis of both vanadium-paranatisite and vanadium-natisite could be conducted. Due to the similar X-ray scattering powers of vanadium and titanium, techniques such as V^{51} MAS NMR could be used in order to determine the environments in which vanadium is in. In doing so, it may be possible to obtain information upon the environment in which vanadium is within. Further analysis such as X-ray absorption spectroscopy (XAS) could be conducted at Diamond Light Source, Didcot. XAS would allow for obtaining local geometries and electronic structures, giving information such as the valency and coordination numbers of specific atoms. Running at energies between 2.05 – 20 keV would provide you with characteristic knife edges of individual atoms providing information on the oxidation states of specific atoms. It could therefore be used to obtain information upon the positioning of the cations within the frameworks. Gaining a greater understanding of how the frameworks behave following exchange experiments could mean that adaptations to the framework, i.e. the percentage of vanadium used to dope the framework, could be used in order to tailor to the needs of the nuclear industry.

References

1. World Nuclear Association. *Nuclear Power in the United Kingdom*. 2016 Available from: <http://www.world-nuclear.org/information-library/country-profiles/countries-t-z/united-kingdom.aspx> [17th December 2016].
2. International Atomic Energy Agency, *Application Of Ion Exchange Processes For The Treatment Of Radioactive Waste And Management Of Spent Ion Exchangers*. 2002: Vienna. p. 27-28.
3. V. Kostov-Kytin *et al*, *Hydrothermal Synthesis and Successive Transformation of Paranatisite into Natisite*. *Mineralogie*, 2002. **55**(2): p. 61-64.
4. G. Erbach, *The Paris Agreement: A New Framework for Global Climate Action*. 2016.
5. United Nations. *Atomic Energy*. Available from: <http://www.un.org/en/sections/issues-depth/atomic-energy/index.html> [13th December 2016].
6. World Nuclear Association. *Nuclear Power in France*. 2016 Available from: <http://www.world-nuclear.org/information-library/country-profiles/countries-a-f/france.aspx> [18th December 2016].
7. World Nuclear Association. *Nuclear Power in the United Kingdom*. 2017 Available from: <http://www.world-nuclear.org/information-library/country-profiles/countries-t-z/united-kingdom.aspx> [3rd January 2017].
8. Energy UK. *Nuclear Generation*. 2015 Available from: <http://www.energy-uk.org.uk/energy-industry/nuclear-generation.html> [8th January 2017].
9. Department for Business Energy and Industrial Strategy. *Hinkley Point C*. 2017 Department for Business, Energy and Industrial Strategy Available

from: <https://www.gov.uk/government/collections/hinkley-point-c> [5th January 2017].

10. Department of Energy & Climate Change, *Strategy for the Management of Solid Low Level Radioactive Waste from the Non-Nuclear Industry in the United Kingdom*. 2012, UK Government. p. 18-19.
11. Office for Nuclear Regulation. *Joint Regulatory Guide on Radioactive Waste Management*. 2017 Available from: <http://www.onr.org.uk/wastemanage.htm> [9th January 2017].
12. Nuclear Decommissioning Authority, *Annual Report and Accounts 2016/2017*. 2016/2017: United Kingdom.
13. United States Nuclear Regulatory Commission. *NRC: Radiation Basics*. 2014 United States Nuclear Regulatory Commission Available from: <https://www.nrc.gov/about-nrc/radiation/health-effects/radiation-basics.html> [18th January 2017].
14. EDF Energy, *Spent Fuel and Radioactive Waste Management*, in *Hinkley Point C Pre-Application Consultation*. United Kingdom. p. 42.
15. World Nuclear Association. *Radioactive Waste Management*. 2016.
16. International Atomic Energy Agency, *The Nuclear Fuel Cycle*. 2011: Austria. p. 2522.
17. S. Cornet, *Radiochemistry Webinars*, in *Nuclear Fuel Cycle Series*. 2014: United States of America.
18. International Atomic Energy Association, *Storage and Disposal of Spent Fuel and High Level Radioactive Waste*. 2005. p. 11.
19. European Nuclear Society. *The Forsmarl NPP, in Sweden, will be First to House a Deep Geological Repository for its High Level Radioactive Waste*

- (HLW). 2009 European Nuclear Society Available from: <https://www.euronuclear.org/e-news/e-news-25/editorial.htm> [20th January].
20. International Atomic Energy Agency, *Country Nuclear Fuel Cycle Profile*. 2005: Vienna
 21. K. Nash and G. Choppin, *Separations Chemistry for Actinide Elements: Recent Developments and Historical Perspective*. Nuclear Energy, 1997. **32**(1-4): p. 255-274.
 22. M. Leafe. *Dealing with the Past, Protecting the Future*. 2017 UK Gov Available from: <https://nda.blog.gov.uk/2017/01/24/end-in-sight-for-reprocessing-nuclear-fuel-at-sellafield/> [22nd January 2017].
 23. Nuclear Decommissioning Authority, *Review of Options for Accelerating Implementation of the Geological Disposal Programme*. 2011.
 24. National Nuclear Laboratory, *Advanced Reprocessing Research and Development Needs*. 2014.
 25. International Atomic Energy Agency, *Development of Advanced Reprocessing Technologies*. p. 11.
 26. World Nuclear Association. *Storage and Disposal of Radioactive Waste*. 2007 Available from: <http://www.world-nuclear.org/information-library/nuclear-fuel-cycle/nuclear-wastes/storage-and-disposal-of-radioactive-waste.aspx> [23rd January 2017].
 27. F. Mumpton, *La Roca Magica: Uses of Natural Zeolites in Agriculture and Industry*. National Academy of Sciences Colloquium, 1999. **96**: p. 3463-3470.

28. International Atomic Energy Agency, *Treatment of Spent Ion-Exchange Resins for Storage and Disposal*. 1985: Austria.
29. International Atomic Energy Agency, *Application Of Ion Exchange Processes For the Treatment Of Radioactive Waste and Management fo Spent Ion Exchangers*. 2002: Vienna. p. 29-31.
30. A Honeywell Company, *UOP IONSIV Ion Exchangers*. 2012: United States of America.
31. V. Kaucic, *The Structure of Zeolite and Aluminophosphate Molecular Sieves*. National Institute of Chemistry, 1994. **67**: p. 241-261.
32. J. Lu *et al*, *Screening Out Unfeasible Hypothetical Zeolite Structures via the Closest Non-Adjacent O...O Pairs*. Physical Chemistry Chemical Physics, 2017. **19**(2): p. 1276-1280.
33. B. Jha and D. Signh, *Fly Ash Zeolites, Innovations, Applications and Directions*. 2016: Springer.
34. E. Derouane *et al*, *The Acidity of Zeolites: Concepts, Measurements and Relation to Catalysis: A Review on Experimental and Theoretical Methods for the Study of Zeolite Acidity*. Catalysis Reviews- Science and Engineering, 2012. **55**(4): p. 454-515.
35. C. Harland, *Ion Exchange: Theory and Practise*. 2007: Royal Society of Chemistry.
36. P. Wright, *Microporous Framework Solids*. 2008, Cambridge: Royal Society of Chemistry.
37. R. Szostak, *Molecular Sieves: Principles of Synthesis and Identification*. second ed. 1998, United States of America: Springer Science and Buisness Media. 359.

38. L. Smart and E. Moore, *Solid State Chemistry: An Introduction*. Vol. 4. 2012, United States of America: CRC Press Taylor and Francis Group.
39. F. Riberio, *Zeolites: Science and Technology*. 2012: Springer Science and Business Media.
40. M. Weller, *Inorganic Materials Chemistry*. 2001, United States of America: Oxford University Press.
41. R. Stanten and M. Neurock, *Molecular Heterogeneous Catalysis: A Conceptual and Computational Approach*. 2009: John Wiley and Sons. 488.
42. W. Mozgawa *et al*, *FT-IR Studies of Zeolites from Different Structural Groups*. 65, 2011. **7**: p. 667-674.
43. S. Auerbach *et al*, *Handbook of Zeolite Science and Technology*. Technology and Engineering. 2003: CRC Press.
44. J. Ramsay and S. Kallus, *Zeolite Membranes*. Membrane Science and Technology, 2000. **6**: p. 373-395.
45. T. Pham *et al*, *Molecular Basis for the High CO₂ Adsorption Capacity of Chabazite Zeolites*. Chemistry and Sustainability Energy and Materials, 2014. **7**(11).
46. D. Farrusseng *et al*, *Xenon Capture on Silver-Loaded Zeolites: Characterisation of Very Strong Adsorption Sites*. J. Phys. Chem, 2013. **117**(29): p. 15122-15129.
47. S. Wang and Y. Peng, *Natural Zeolites as Effective Adsorbents in Water and Wastewater Treatment*. Chemical Engineering Journal, 2010. **156**(1): p. 11-24.

48. A. Dyer, *An Introduction to Zeolite Molecular Sieves*. 1988, United Kingdom: John Wiley and Sons.
49. C. Rhodes, *The Properties and Applications of Zeolites*. Science Progress, 2010: p. 1-63.
50. International Atomic Energy Agency, *Application of Ion Exchange Processes for the Treatment of Radioactive Waste and Management of Spent Ion Exchangers*. 2002, Vienna. 115.
51. Union of Concerned Scientists. *Safer Storage of Spent Nuclear Fuel*. 2016 Union of Concerned Scientists Available from: <http://www.ucsusa.org/nuclear-power/nuclear-waste/safer-storage-of-spent-fuel#.WafUT9HavIU> [27th January 2017].
52. Office for Nuclear Regulation, *Chemistry of Operating Civil Nuclear Reactors*. 2007, Office for Nuclear Regulation. p. 1-40.
53. M. Heley, *Fukushima: What You Need to Know*. 2014: North Atlantic Books.
54. S. Handley-Sidhu, *Influence of pH, Competing Ions, and Salinity on the Sorption of Strontium and Cobalt onto Biogenic Hydroxyapatite*. Scientific Reports, 2016. **6**: p. 23361.
55. K. Matlack *et al*, *Sellafield Thermal Treatment Trials Using Advanced Joule Heated Ceramic Melter Technology*, in *Annual Radioactive Waste Management Symposium*. 2010: United States of America. p. 1524-1537.
56. International Zeolite Association. *Clinoptilolite*. 2005 International Zeolite Association.
57. International Zeolite Association- Commission on Natural Zeolites. *Clinoptilolite*. IZA Commission on Natural Zeolites Available from:

<http://www.iza->

[online.org/natural/Datasheets/Clinoptilolite/clinoptilolite.htm](http://www.iza-online.org/natural/Datasheets/Clinoptilolite/clinoptilolite.htm)

[11th

February 2017].

58. Nuclear Decommissioning Authority, *Packaging Options for Sellafield SIXEP Sand, Clino and Sludge*, in *Guide to the Nirex Letter of Compliance Process*. 2008.
59. J. Cejka, *Zeolites and Ordered Mesoporous Materials: Progress and Prospects*. 2005, Czech Republic: Gulf Professional Publishing.
60. R. Lobo *et al*, *Modular Organic Structure-Directing Agents for the Synthesis of Zeolites*, in *Science*. 1995. p. 47.
61. A. Tripathi *et al*, *Crystallization of Sodium Titanium Silicate with Sittinakite Topology: Evolution from the Sodium Nonatitanate Phase*. *Chemistry of Materials*, 2004. **16**: p. 3659-3666.
62. World Nuclear Association. *Fukushima Accident*. 2017 Available from: <http://www.world-nuclear.org/information-library/safety-and-security/safety-of-plants/fukushima-accident.aspx> [10th February 2017].
63. K. Buesseler. *Radiation from Fukushima*. 2016 Woods Hole Oceanographic Available from: <http://www.whoi.edu/main/topic/fukushima-radiation> [12th February 2017].
64. World Nuclear Association. *Fukushima Accident*. 2016 Available from: <http://www.world-nuclear.org/information-library/safety-and-security/safety-of-plants/fukushima-accident.aspx> [13th February 2017].
65. K. Byrappa *et al*, *Handbook of Hydrothermal Technology*. Vol. 2. 2013, United States of America. 388.

66. M. Howden, *Radioactive effluent treatment plant- Sellafield reprocessing factory*. Proceedings of the Institution of Mechanical Engineers Part A, 1987(201): p. 1-15.
67. J. Cejka, *Zeolites and Ordered Mesoporous Materials: Progress and Prospects*, ed. G. Centi. Vol. 157. 2005: Elsevier B.V.
68. World Nuclear Association. *Treatment and Conditioning of Nuclear Waste*. 2017 Available from: <http://www.world-nuclear.org/information-library/nuclear-fuel-cycle/nuclear-wastes/treatment-and-conditioning-of-nuclear-wastes.aspx> [15th February 2017].
69. A. Maglio and D. Durocher, *Strontium and Cesium Specific Ion-Exchange Media*. 2014, BASF Corporation United States of America. p. 1.
70. F. Fondeur *et al*, *Measurements of the Effective Cesium-Sodium Ion Exchange Rate in IONSIV IE-910 and IE-911*. 2001, Westinghouse Savannah River Company: United States of America.
71. C. Philip and R. Anthony, *Crystalline Silicotitanate Ion Exchange Support for Salt Alternatives*, U.S.D.o. Energy, Editor. 2001, U.S. Department of Energy: United States of America.
72. T. Tood and V. Romanovskiy, *A Comparison of Crystalline Silicotitanate and Ammonium Molybdophosphate-Polyacrylonitrile Composite Sorbent for the Separation of Cesium from Acidic Waste*. Radiochemistry, 2005. **47**(4): p. 398-402.
73. A Honeywell Company, *Efficient Treatment of Liquid Nuclear Wastes*. 2012: p. 1-4.
74. M. Anderson *et al*, *Microporous Titanosilicate ETS-10: A Structural Survey*. Philosophical Magazine Part B, 1994. **71**(5): p. 813-841.

75. C. Claeys, *Recent Advances in the Science and Technology of Zeolites and Related Materials*. 2004, 2004: Gulf Professional Publishing.
76. S. Nandanwar *et al*, *Activity of Nanostructured C@ETS-10 Sorbent for Capture of Volatile Radioactive Iodine from Gas Stream*. *Chemical Engineering Journal*, 2015(287): p. 593-601.
77. N. Soelberg *et al*, *Radioactive Iodine and Krypton Control for Nuclear Fuel Reprocessing Facilities*. *Science and Technology of Nuclear Installations* 2013.
78. E. Sokolova and F. Hawthorne, *Reconsideration of the Crystal Structure of Paranatisite and the Crystal*. *The Canadian Mineralogist*, 2002. **40**.
79. S. Ferdov *et al*, *Improved Powder Diffraction Patterns for Synthetic Paranatisite and Natisite*. *Central Laboratory of Mineralogy and Crystallography*, 2002: p. 234-237.
80. A. Arzamastsev *et al*, *The Khibina and Lovozero Alkaline Massifs: Geology and Unique Mineralization*. 47, 2008: p. 53-54.
81. Web Mineral. *Natisite Mineral Data*. 2012 Available from: <http://webmineral.com/data/Natisite.shtml#WY2oZNHavIV> [16th February 2017].
82. S. Ferdov, *A Comparative Rietveld Refinement Study of Natisite Prepared in Different Morphology*. *J Chem Crystallogr*, 2013. **43**: p. 443–447.
83. J. Livage, *Hydrothermal synthesis of Nanostructured Vanadium Oxide*. *Materials*, 2010. **3**: p. 4175-4195.
84. M. Islam, T. Bredow, and A. Gerson, *Electronic Properties of Vanadium-Doped TiO₂*. *ChemPhysChem*, 2011. **12**: p. 3467 – 3473.

85. R. Hall, in *School of Physical Sciences and Computing*. 2017, University of Central Lancashire: United Kingdom.
86. L. Dutrow and C. Clark. *X-ray Powder Diffraction*. 2017 Geochemical Instrumentation and Analysis.
87. D. Henry and et al. *X-ray Reflection in Accordance with Bragg's Law*. Geochemical Instrumentation and Analysis Available from: https://serc.carleton.edu/research_education/geochemsheets/BraggsLaw.html [1st March 2017].
88. B. Fultz and J. Howe, *Transmission Electron Microscopy and Diffractometry of Materials*. 2013, Berlin: Springer.
89. P. Ewald, *Fifty Years of X-Ray Diffraction*. 1962: Springer US.
90. S. Wallwork, *Introduction to the Calculation of Structure Factors* 2001, Cardiff: University College Cardiff Press.
91. K. Cheetham and P. Day, *Solid State Chemistry: Techniques*. Vol. 1. 1990: Oxford University Press, Incorporated.
92. A. Coelho, *TOPAS Academic Version 4.1*. 2007.
93. *jEdit- Programmer's Text Editor*.
94. A. Blake, *Crystal Structure Analysis: Principles and Practice*. second ed. Structure Solution from Powder Diffraction Data 2009: Oxford University Press.
95. E. Kisi and C. Howard, *Applications of Neutron Powder Diffraction*. 2008: Oxford Science Publications 485.
96. L. McCusker and et al, *Reitveld Refinement Guidelines*. J. Appl. Cryst 1999. **32**: p. 36-50.

97. Bruker. *X-ray Diffraction and Elemental Analysis*. Bruker Available from: <https://www.bruker.com/products/x-ray-diffraction-and-elemental-analysis/handheld-xrf/how-xrf-works.html> [20th March 2017].
98. Oxford Instruments. *XRF-X-ray Fluorescence Analysis Explained*. 2017 Oxford Instruments Available from: <http://www.the-experts.com/x-ray-fluorescence-xrf-explained> [2nd March 2017].
99. M. Batsala et al, *Inductively Coupled Plasma Mass Spectrometry (ICP-MS)*. International Journal of Research in Pharmacy and Chemistry, 2012: p. 671-677.
100. D. Skoog et al, *Principles of Instrumental Analysis*. sixth ed. 2007, Belmont: Thomson Higher Education.
101. R. Wolf. *What is ICP-MS?... and More Importantly, What Can it Do?* 2005 Crustal Geophysics and Geochemistry Science Center Available from: <https://crustal.usgs.gov/laboratories/icpms/intro.html> [21st March 2017].
102. A. Bazilio and J. Weinrich, *An Easy Guide to Inductively Coupled Plasma-Mass Spectrometry (ICP-MS)*. 2007.
103. Thermo Scientific, *Thermo Scientific, ICAP 7000 PLUS Series, Periodic Table of Elements*. Thermo Scientific.
104. Agilent Technologies, *ICP-MS, Inductively Coupled Plasma-Mass Spectrometry*. 2005: Agilent Technologies. 80.
105. D. Leonard et al, *Scanning Electron Microscopy*. second ed. 2012: John Wiley and Sons, Inc. All.
106. Purdue University. *Scanning Electron Microscope*. 2014 Purdue University Available from: <https://www.purdue.edu/ehps/rem/rs/sem.htm>.

107. *Energy Dispersive X-Ray Microanalysis (EDX/EDS)*. 2017 Anderson Materials Evaluation, Inc [20th April 2017].
108. V. Sokolova *et al*, *Crystal structure of a New Mineral $\text{Na}_8 \text{Ti}_{3.5} \text{O}_2 (\text{O H})_2 (\text{Si O}_4)_4$ - A Polymorphous Modification of Natisite*. Doklady Akademii Nauk SSSR, 1985: p. 1136-1142.
109. H. Nyman *et al*, *Sodium Titanium Silicate, $\text{Na}_2\text{TiSiO}_5$* . Acta Crystallographica Section B, 1977. **B34**: p. 905-906.
110. ICDD., *Chemical Database*. 2013, PDF4.
111. J. Bernstein, *Polymorphism in Molecular Crystals*. Business and Economics 2007: OUP Oxford. 430.
112. M. Ulrich, *Symmetry Relationships Between Crystal Structures*. Vol. 18. 2013: Oxford Science Publications.
113. R. Shannon, *Revised Effective Ionic Radii and Systematic Studies of Interatomic distances in Halides and Chalcogenides*. Acta Crystallographica, 1976(A32): p. 751-767.
114. A. Tripathi *et al*, *Selectivity for Cs and Sr in Nb-substituted titanosilicate with sitinakite topology*. Journal of Solid State Chemistry, 2003. **175**: p. 72-83.
115. R. Hall, *A study of synthesis of natisite and it's zirconium doped analogues as spoke ion-exchangers for the remediation of nuclear waste*, in *School of Physical Sciences and Computing*. 2017, University of Central Lancashire: United Kingdom.
116. P. Yu and *et al*, *The Phase Stability of Cerium Species in Aqueous Systems II. The $\text{Ce}_{\text{III/IV}}\text{---H}_2\text{O-H}_2\text{O}_2/\text{O}_2$ Systems. Equilibrium Considerations and Pourbaix Diagram Calculations*. America. p. 153.

117. K. Eunyong and K. Osseo-Asare, *Aqueous stability of thorium and rare earth metals in monazite hydrometallurgy: Eh-pH diagrams for the systems Th-, Ce-, La, Nd- (PO₄)- (SO₄)- H₂O at 25 °C*. *Hydrometallurgy*, 2012. **113-114**: p. 67-78.
118. G. Beall *et al*, *Refinement of Neodymium Trihydroxide*. *Acta Crystallographica*, 1976. **B32**: p. 2227-2229.

Appendix

A1: stack view of XRD patterns following the transformation of 5 %-vanadium-paranatisite to 5 %-vanadium-natisite

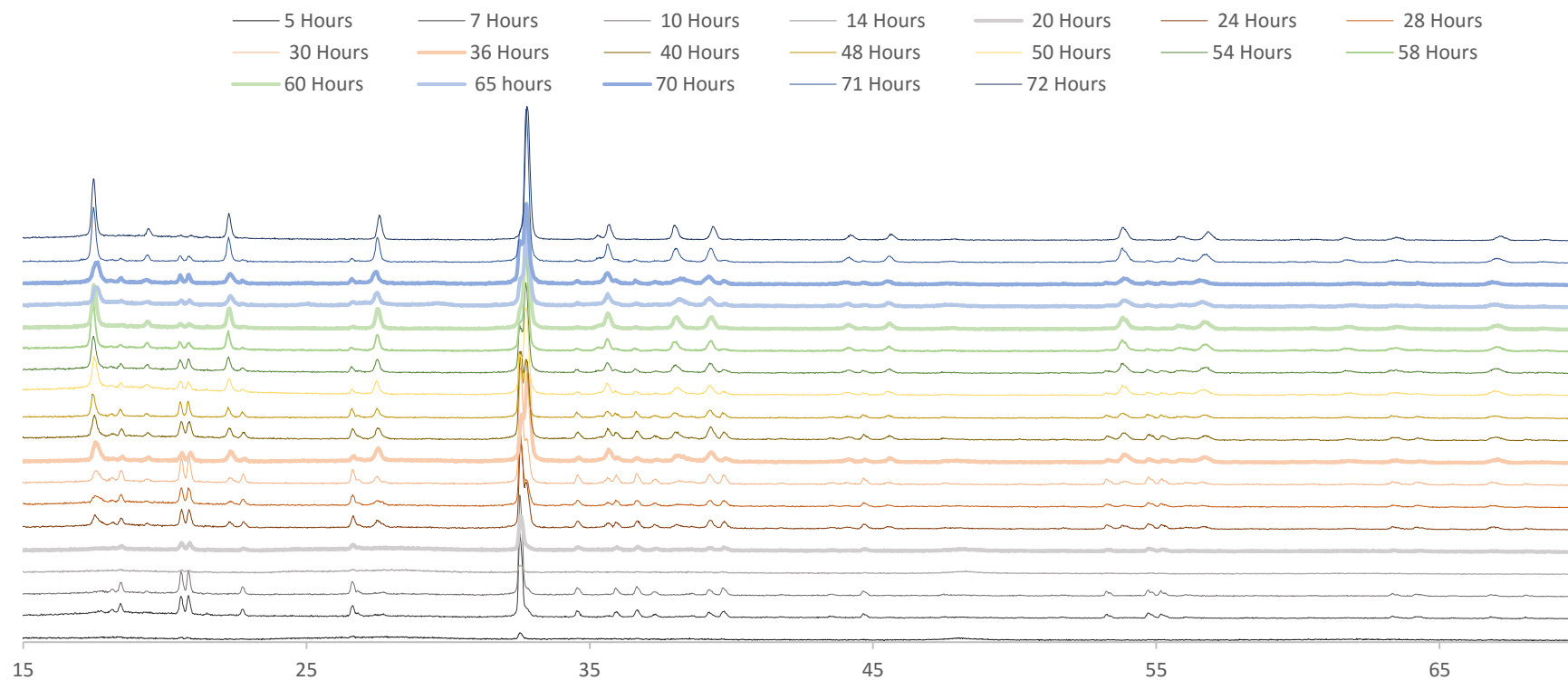
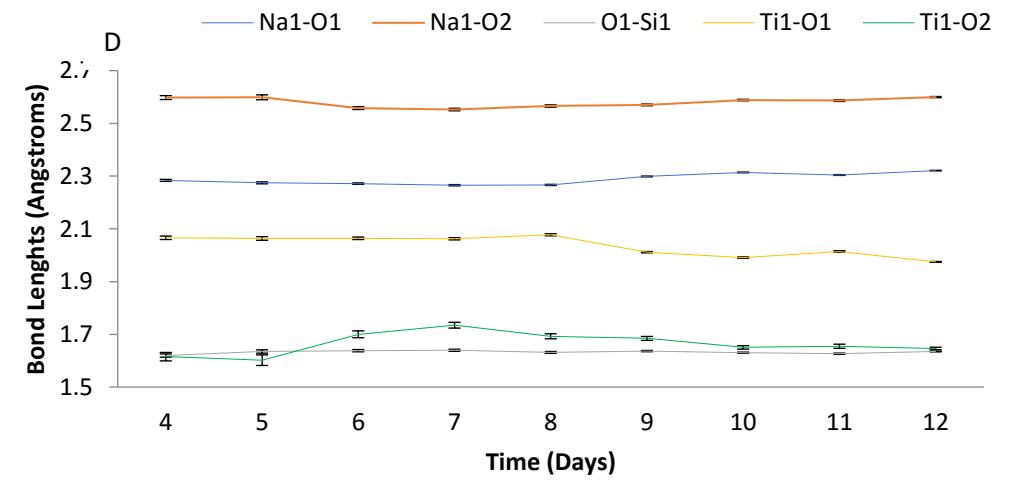
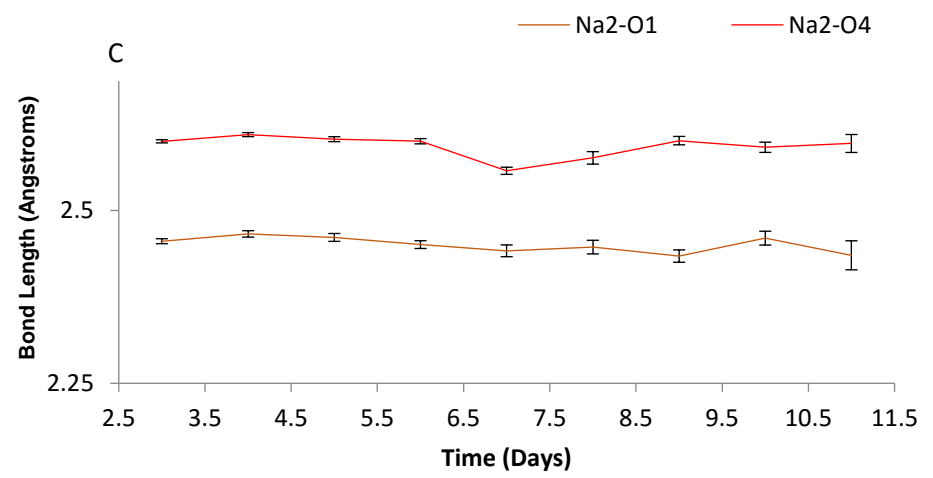
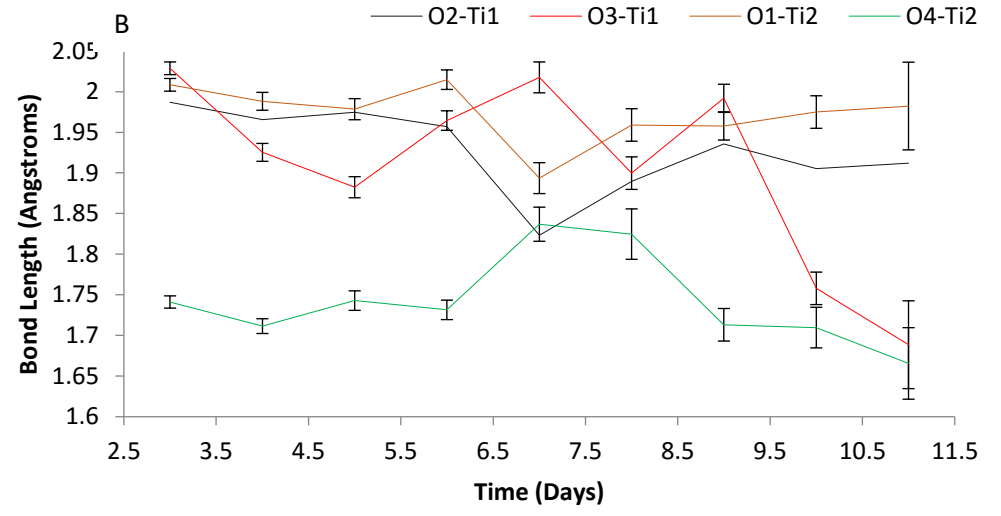
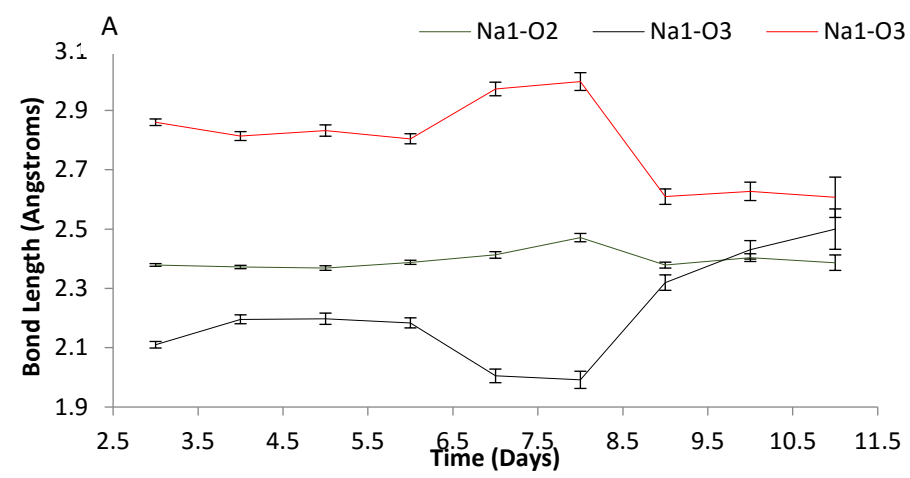


Figure A: Stack view of XRD patterns following the successive transformation of 5 %-vanadium-paranatisite to 5 %-vanadium-natisite.

A2: Paranasite rietveld refinements of bond length and angles variation from 10 %-vanadium-paranasite to 10 %-vanadium-natisite



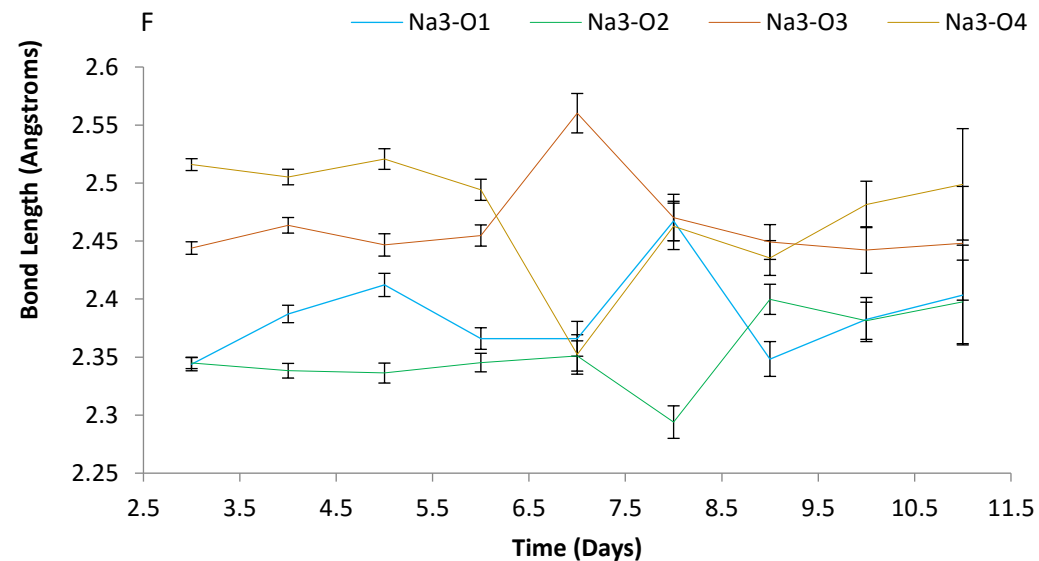
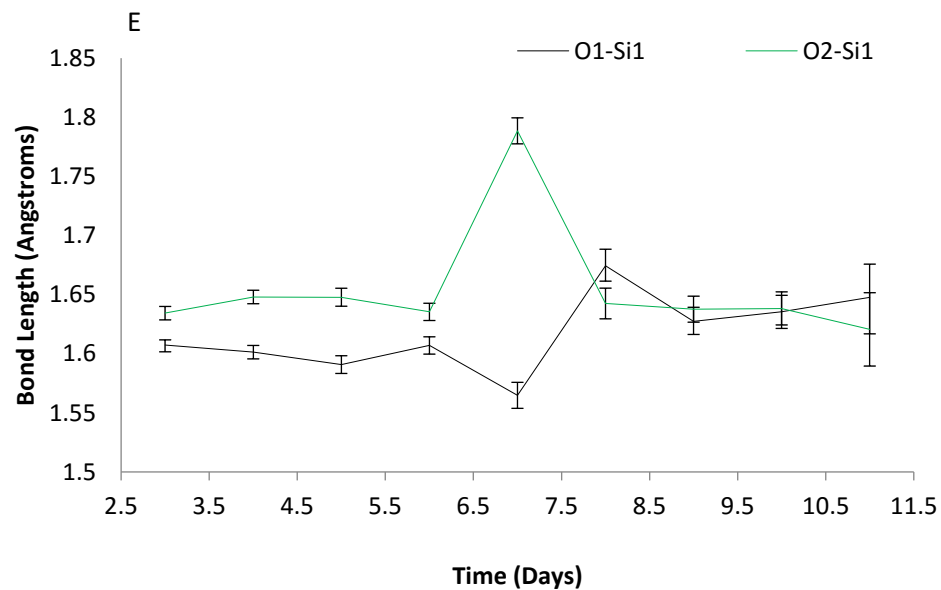
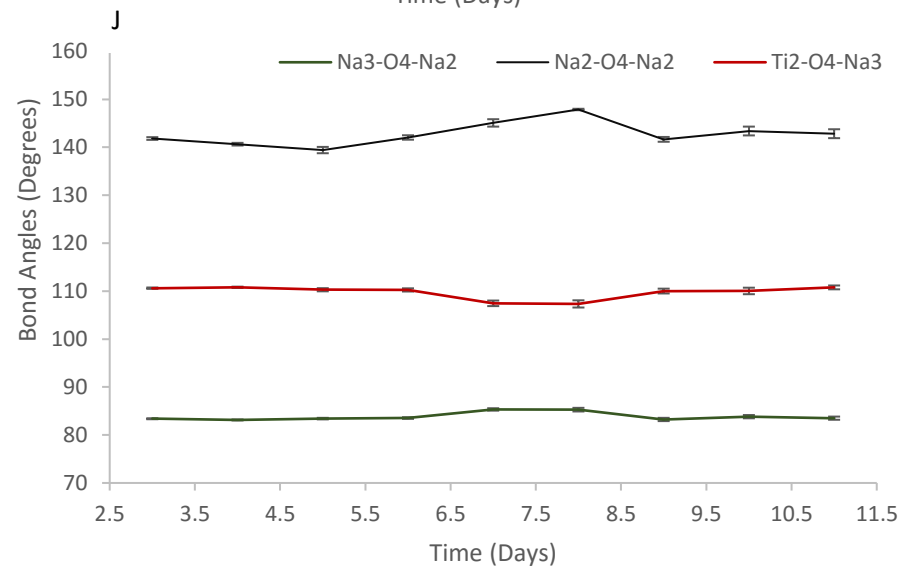
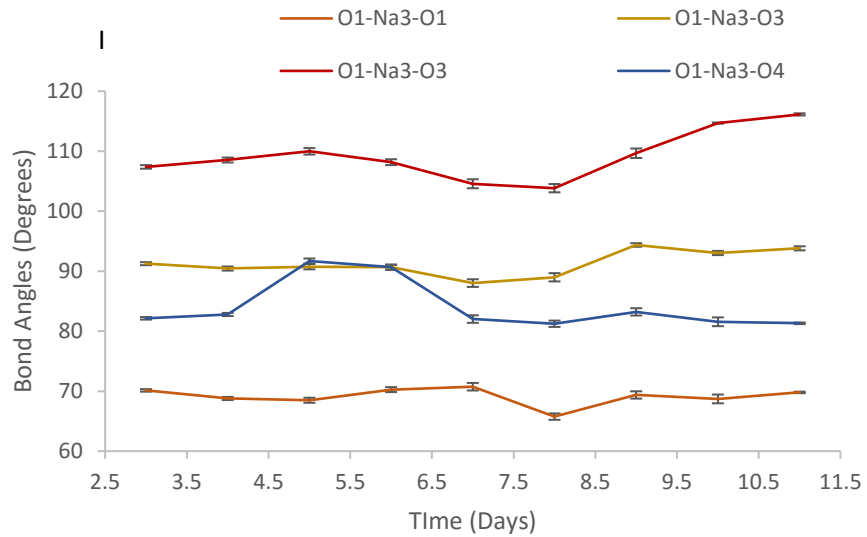
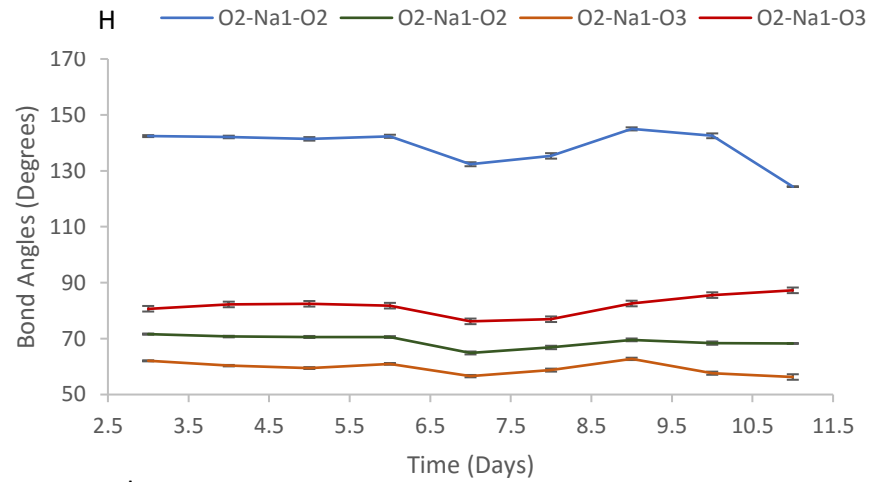
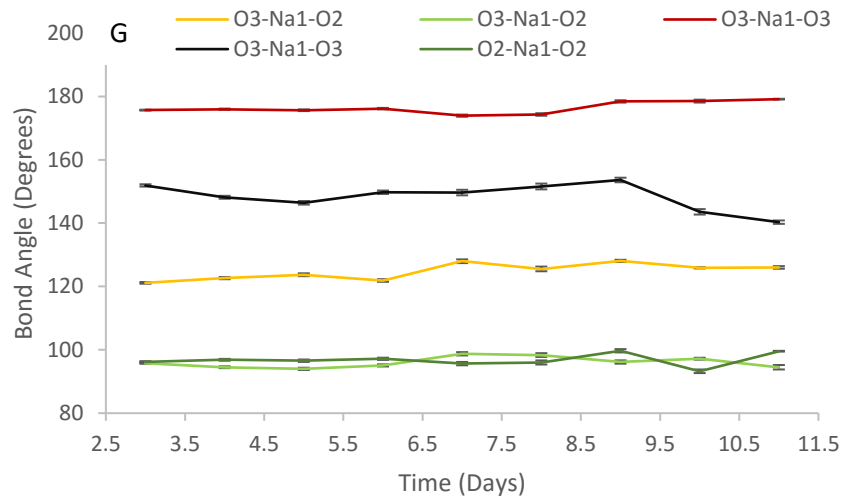


Figure A2.a: 10 %-vanadium-paranatisite rietveld refinements of bond lengths from 3-11 Days. A: Na1-O2, Na1-O3 and Na1-O3, B: Ti1-O3, Ti1-O2, Ti2-O2 and Ti2-O4, C: O3-O3, Na2-O1 and Na2-O4, D: Na1-O1, Na1-O2, O1-Si1, Ti1-O1 and Ti1-O2, E: O1-Si1 and O2-Si1 and F: Na3-O1, Na3-O2, Na3-O3-Na3-O4.



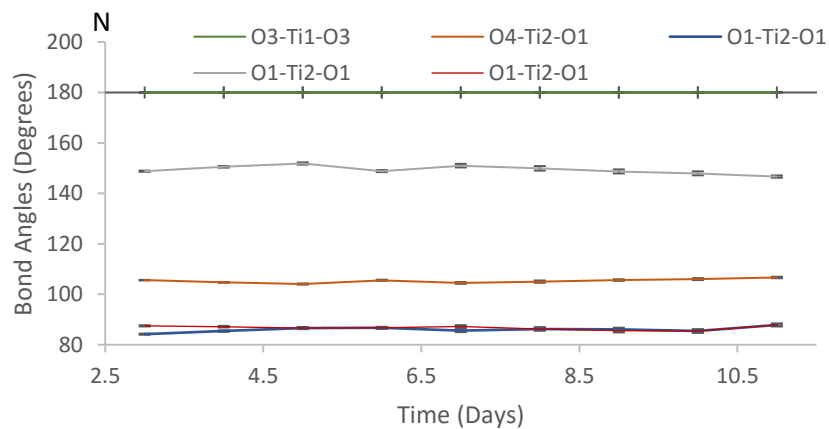
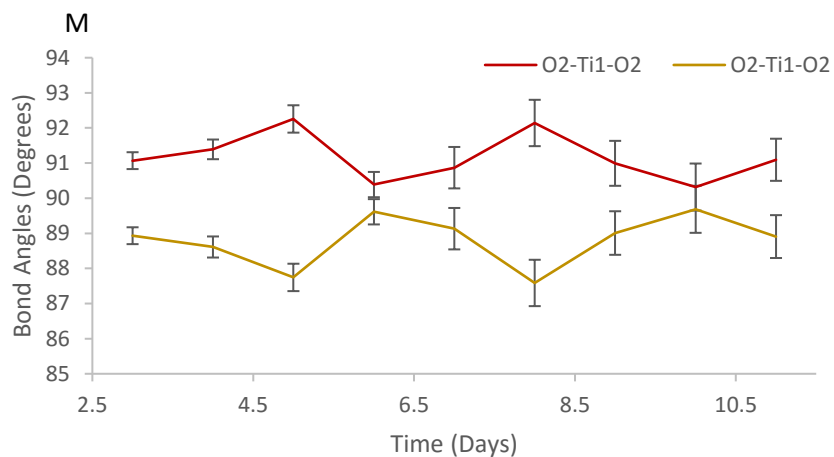
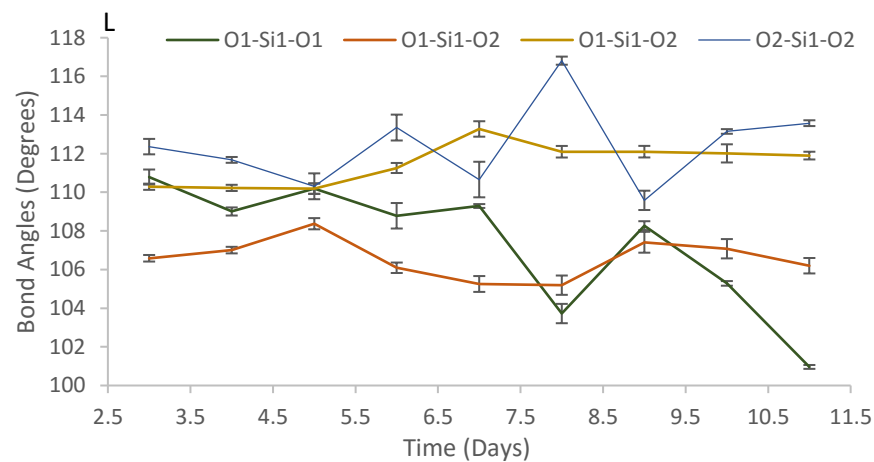
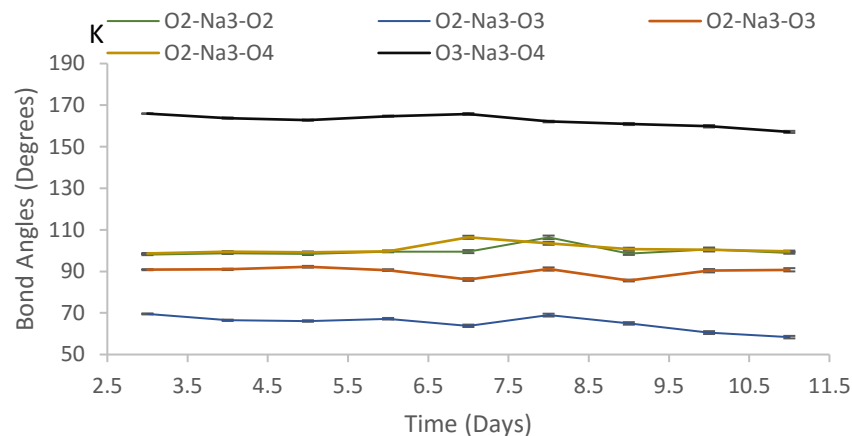


Figure A2.b: 10 %-vanadium paranatisite rietveld refinements of bond angles from 3-11 Days: G: O3-Na1-O3, O3-Na1-O2, O3-Na1-O2, O3-Na1-O3, O3-Na1-O3 and O2-Na1-O2, H: O2-Na1-O2, O2-Na1-O2, O2-Na1-O3, O2-Na1-O3 and O3-Na1-O3, I: O1-Na3-O1, O1-Na3-O3, O1-Na3-O3 and O1-Na3-O4, J: Na3-O4-Na2, Na2-O4-Na2 and Ti2-O4-Na3, K: O2-Na3-O2, O2-Na3-O3, O2-Na3-O3, O2-Na3-O4, O3-Na3-O3 and O3-Na3-O4, L: O1-Si1-O1, O1-Si1-O2 and O2-Si1-O2, M: O2-Ti1-O2 and O2-Ti1-O2 and N: O3-Ti1-O3, O4-Ti2-O1-O1-Ti2-O1, O1-Ti2-O1 and O1-Ti2-O1.

A3: Natisite rietveld refinements bond length and angles variation from 10 %-vanadium-paranatisite to 10 %-vanadium-natisite

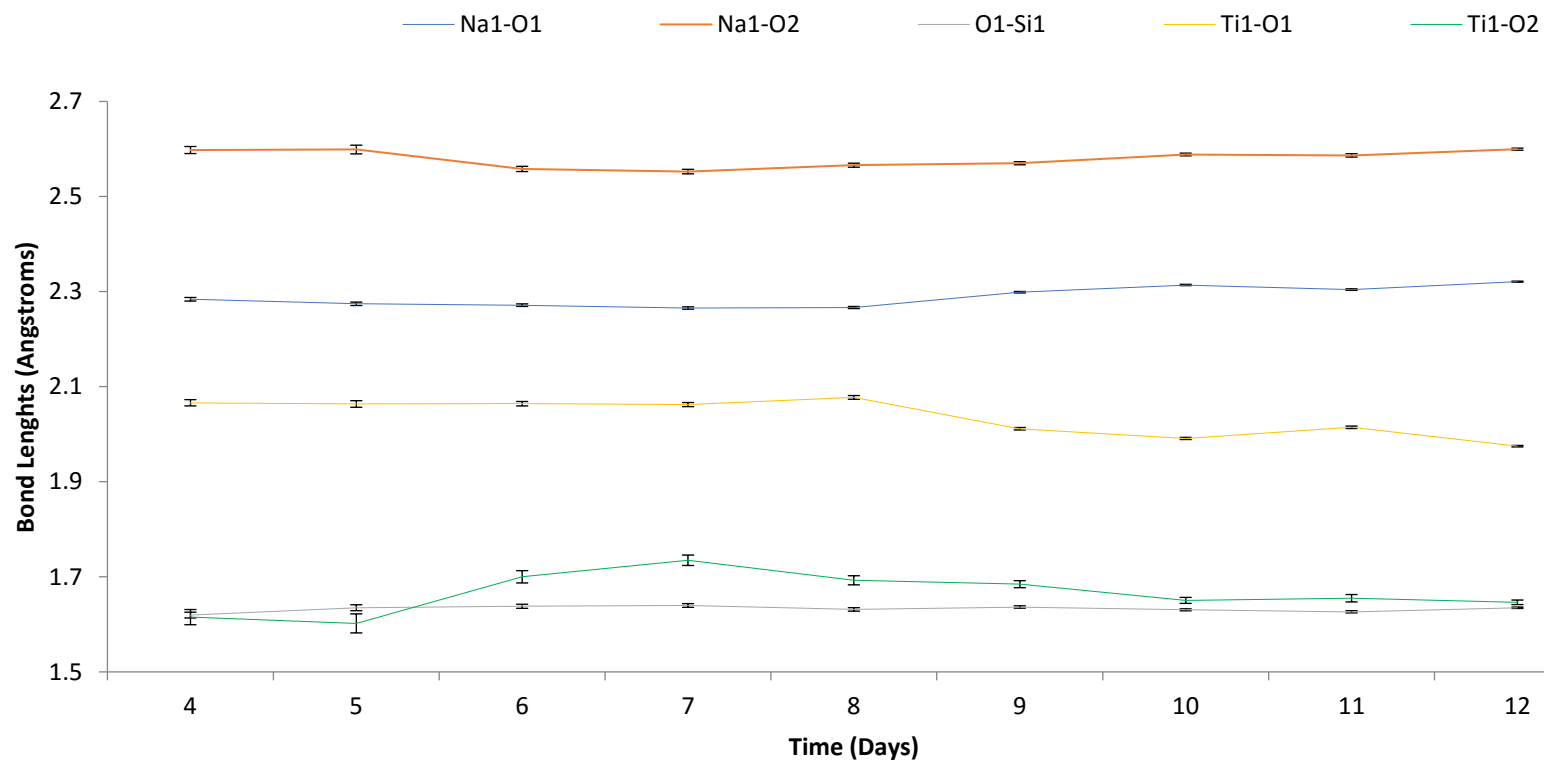
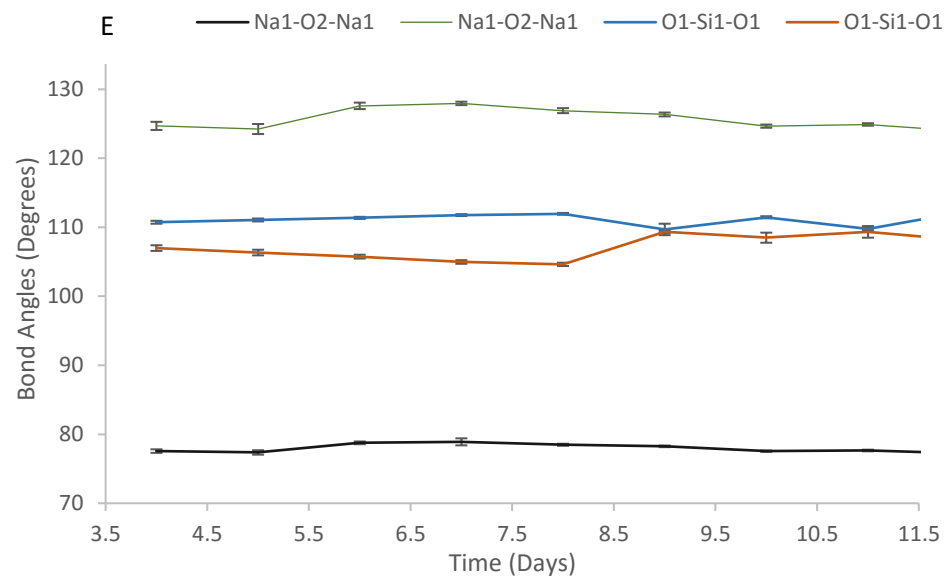
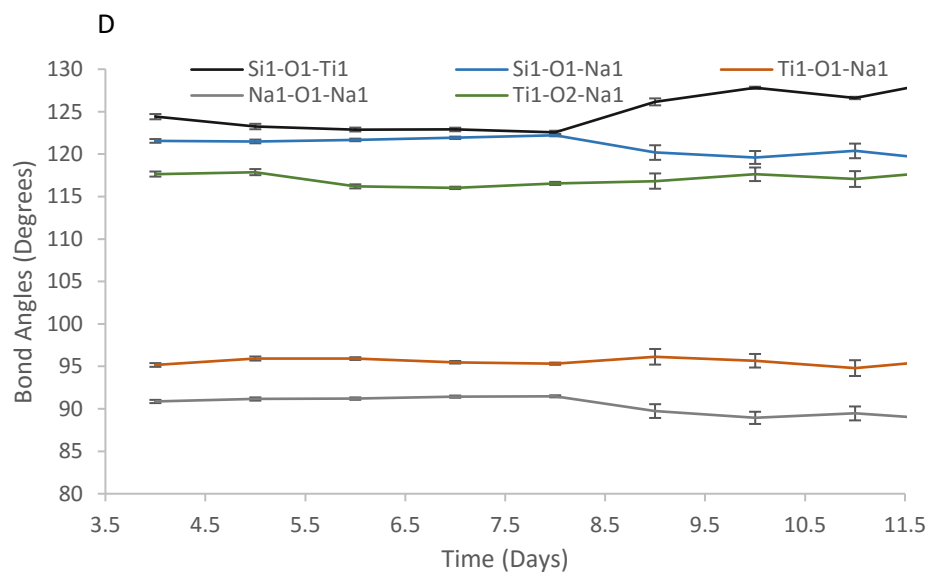
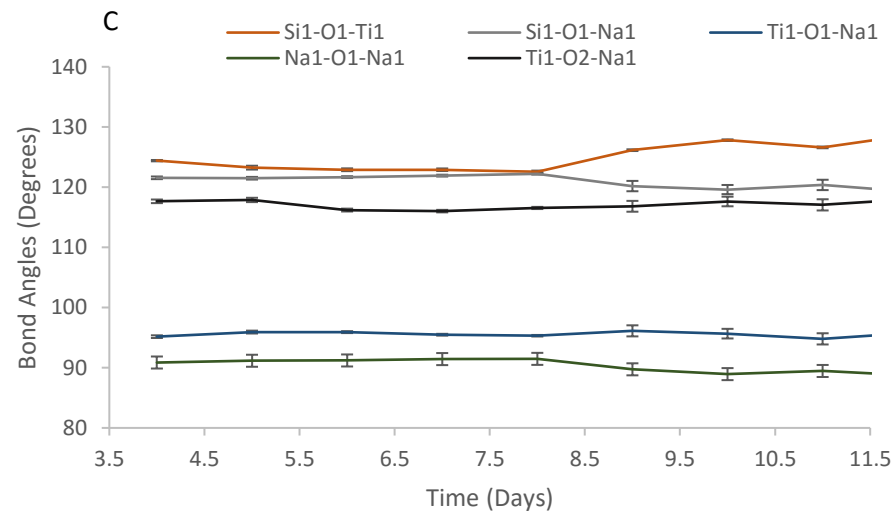
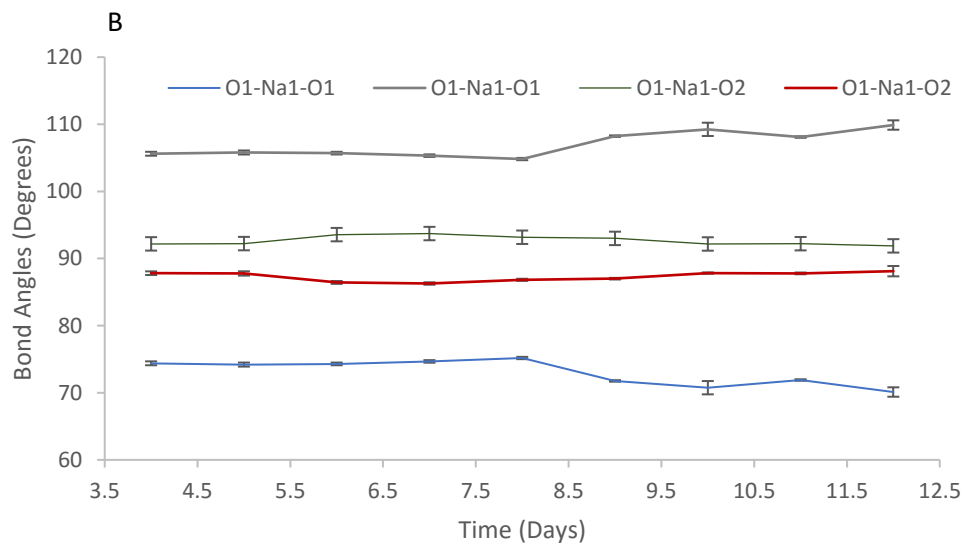


Figure A3.a: 10 %-vanadium-natisite rietveld refinements of bond lengths from 4-12 Days A: Na1-O1, Na1-O2, O1-Si1, Ti1-O1 and Ti1-O2



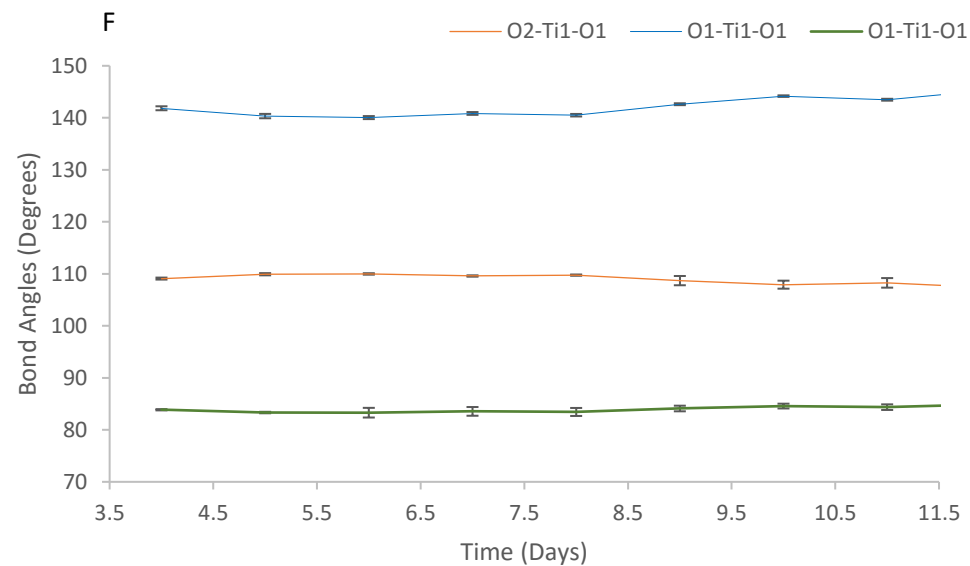


Figure A3.b: 10 %-vanadium-natisite rietveld refinements of bond angles from 4-12 Days: B: O1Na1-O1, O1-Na1-O1 and O1-Na1-O2, C: Si-O1-Tio1, Si1-O1-Na1, Ti1-O1-Na1, Na1-O1-Na1 and Ti1-O2-Na1, D: Si1-O1-Ti1, Si1-O1-Na1, Ti1-O1-Na1, Na1-O1-Na1 and To1-O2-Na1, E: Na1-O2-Na1, Na1-O2-Na1, O1-Si1-O1 and O1-Si1-O1 and F: O2-Ti1-O1, O1-Ti1-O1 and O1-Ti1-O1

A4: Crystallographic Data of 3 Day Synthesis

Table A4.a: Refined lattice parameters and refinement statistics for 3 day synthesis

Parameter	10 %-Vanadium-Paranatisite
System	Orthorhombic
Space Group	P m m a
<i>a</i> (Å)	9.8282 (1)
<i>b</i> (Å)	9.2060 (1)
<i>c</i> (Å)	4.82489 (7)
<i>V</i> (Å ³)	436.54 (1)
R _{WP} (%)	5.408
R _P (%)	4.094
R _{exp} (%)	2.647

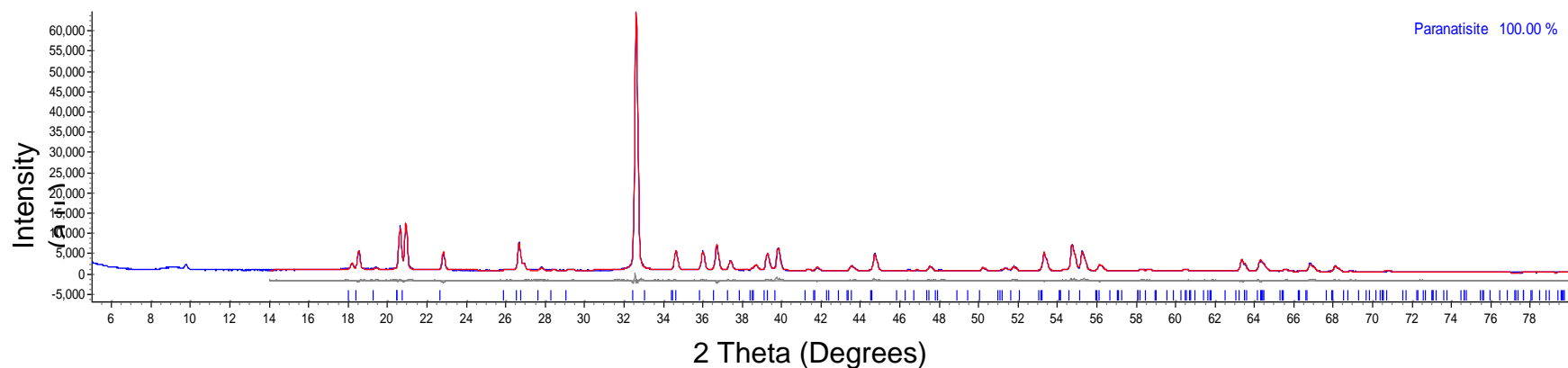


Figure A4.b: Final rietveld fit of 3 day synthesis

A5: Crystallographic Data of 4 Day Synthesis

Table A5.a: Refined lattice parameters and refinement statistics for 4 day synthesis

Parameter	10 %-Vanadium-Paranatisite	10 %-Vanadium-Natisite
System	Orthorhombic	Tetragonal
Space Group	P m m a	P 4 / n m m
a (Å)	9.8292 (2)	6.5084 (2)
b (Å)	9.1976 (2)	6.5084 (2)
c (Å)	4.82003 (8)	5.0656 (3)
V (Å³)	435.75 (1)	214.57 (2)
R_{WP} (%)	5.547	5.547
R_P (%)	4.180	4.180
R_{exp} (%)	2.363	2.363

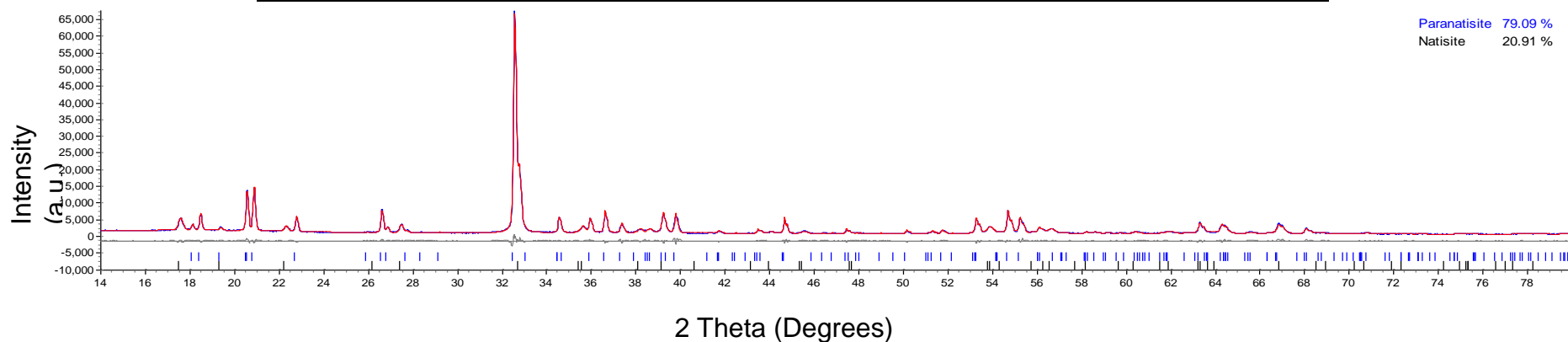


Figure A5.b: Final rietveld fit of 4 day synthesis

A6: Crystallographic Data of 5 Day Synthesis

Table A6.a: Refined lattice parameters and refinement statistics for 5 day synthesis

Parameter	10 %-Vanadium-Paranatisite	10 %-Vanadium-Natisite
System	Orthorhombic	Tetragonal
Space Group	P m m a	P 4 / n m m
a (Å)	9.8269 (2)	6.4973 (2)
b (Å)	9.1948 (2)	6.4973 (2)
c (Å)	4.81871 (9)	5.0805 (3)
V (Å³)	435.40 (1)	214.47 (2)
R_{WP} (%)	6.025	6.025
R_P (%)	3.020	3.020
R_{exp} (%)	4.567	4.567

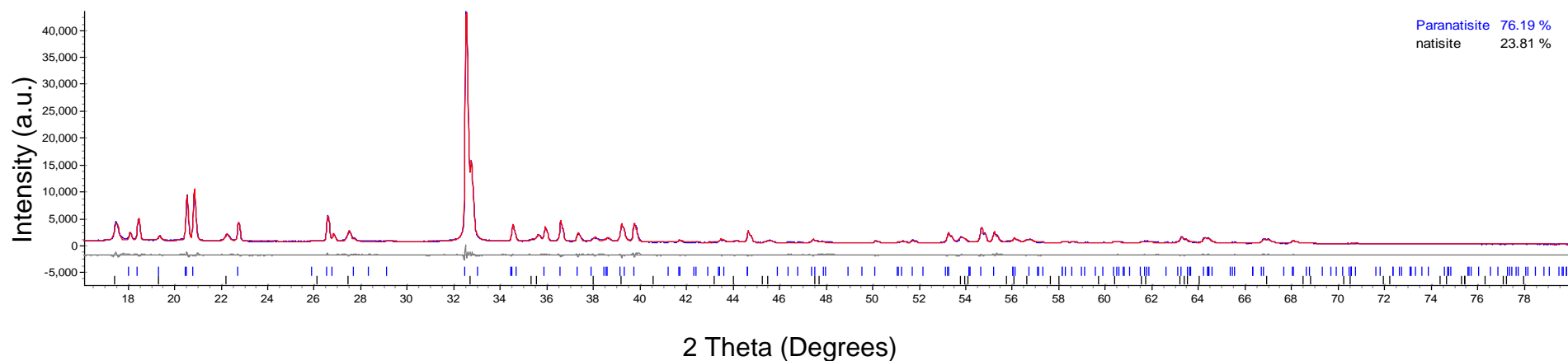


Figure A6.b: Final rietveld fit of 5 day synthesis

A7: Crystallographic Data of 6 Day Synthesis

Table A7.a: Overview of crystallographic data of 6 day synthesis

Parameter	10 %-Vanadium-Paranatisite	10 %-Vanadium-Natisite
System	Orthorhombic	Tetragonal
Space Group	P m m a	P 4 / n m m
a (Å)	9.8352 (2)	6.4917 (2)
b (Å)	9.1922 (3)	6.4917 (2)
c (Å)	4.8178 (1)	5.0918 (2)
V (Å³)	435.57 (2)	214.58 (1)
R_{WP} (%)	6.351	6.351
R_P (%)	2.740	2.740
R_{exp} (%)	4.871	4.871

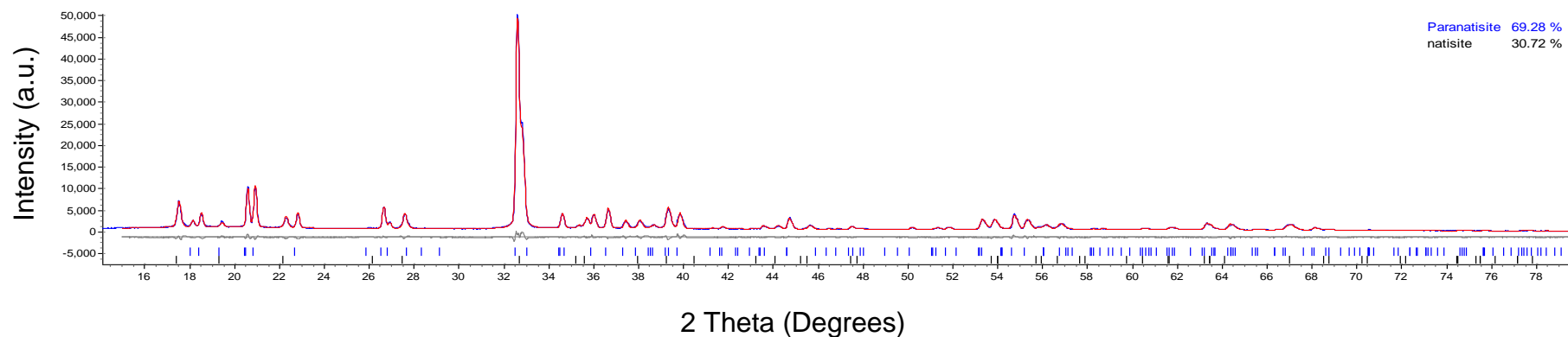


Figure A7.b: Final rietveld fit of 6 day synthesis

A8: Crystallographic Data of 7 Day Synthesis

Table A8.a: Refined lattice parameters and refinement statistics for 7 day synthesis

Parameter	10 %-Vanadium-Paranatisite	10 %-Vanadium-Natisite
System	Orthorhombic	Tetragonal
Space Group	P m m a	P 4 / n m m
<i>a</i> (Å)	9.8457 (3)	6.4873 (2)
<i>b</i> (Å)	9.1738 (3)	6.4873 (2)
<i>c</i> (Å)	4.8061 (2)	5.0946 (2)
<i>V</i> (Å ³)	434.09 (3)	214.41 (1)
R _{WP} (%)	8.291	8.291
R _P (%)	2.878	2.878
R _{exp} (%)	6.325	6.325

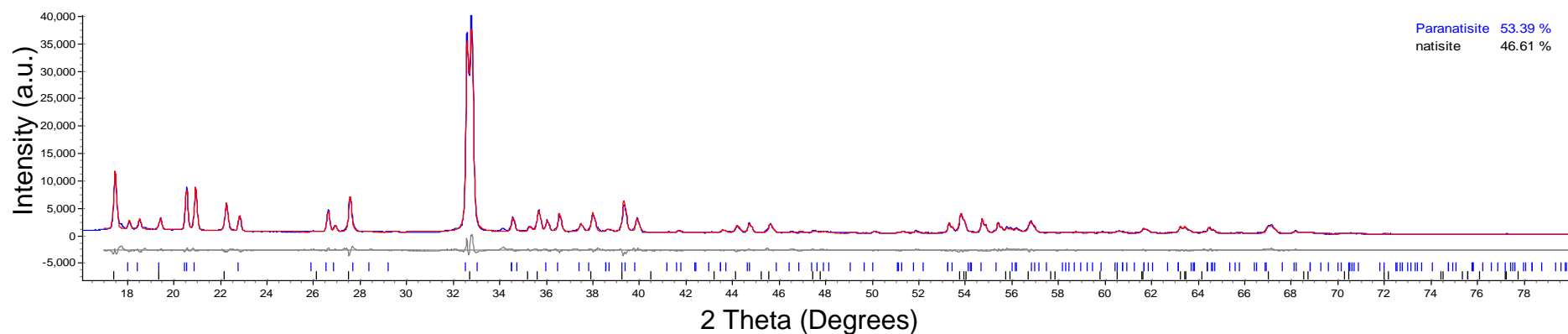


Figure A8.b: Final rietveld fit of 7 day synthesis

A9: Crystallographic Data of 8 Day Synthesis

Table A9.a: Refined lattice parameters and refinement statistics for 8 day synthesis

Parameter	10 %-Vanadium-Paranatisite	10 %-Vanadium-Natisite
System	Orthorhombic	Tetragonal
Space Group	P m m a	P 4 / n m m
<i>a</i> (Å)	9.8389 (4)	6.4924 (2)
<i>b</i> (Å)	9.1834 (5)	6.4924 (2)
<i>c</i> (Å)	4.8119 (2)	5.088 (2)
<i>V</i> (Å ³)	434.78 (3)	214.46 (1)
R _{WP} (%)	8.161	8.161
R _P (%)	2.706	2.706
R _{exp} (%)	6.269	6.269

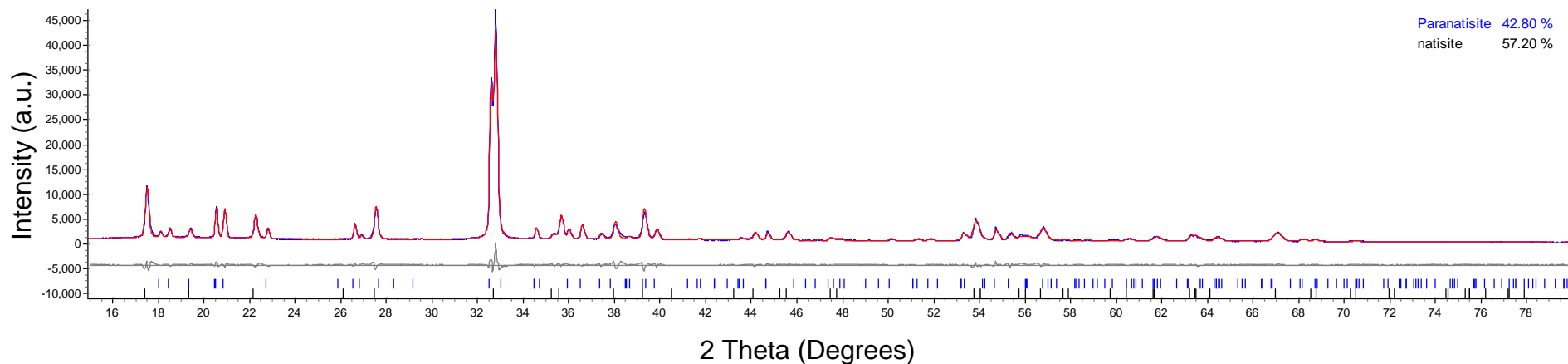


Figure A9.b: Final rietveld fit of 8 day synthesis

A10: Crystallographic Data of 9 Day Synthesis

Table A10.a: Refined lattice parameters and refinement statistics for 9 day synthesis

Parameter	10 %-Vanadium-Paranatisite	10 %-Vanadium-Natisite
System	Orthorhombic	Tetragonal
Space Group	P m m a	P 4 / n m m
<i>a</i> (Å)	9.8435 (3)	6.4868 (1)
<i>b</i> (Å)	9.1740 (3)	6.4868 (1)
<i>c</i> (Å)	4.8058 (1)	5.0932 (1)
<i>V</i> (Å ³)	433.98 (2)	214.312 (9)
R _{WP} (%)	5.860	5.860
R _P (%)	2.765	2.765
R _{exp} (%)	4.507	4.507

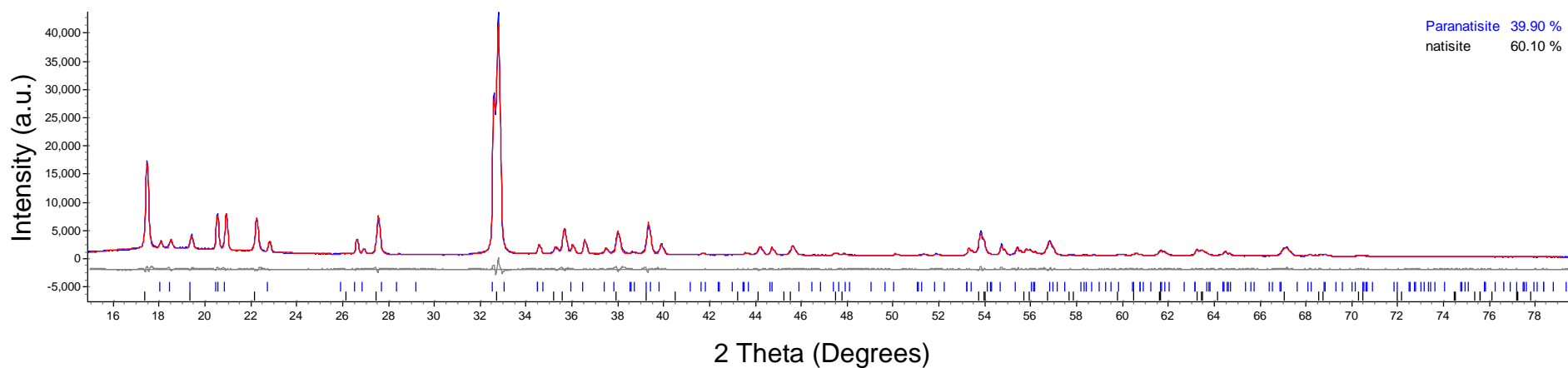


Figure A10.b: Final rietveld fit of 9 day synthesis

A11: Crystallographic Data of 10 Day Synthesis

Table A11.a: Refined lattice parameters and refinement statistics for 10 day synthesis

Parameter	10 %-Vanadium-Paranatisite	10 %-Vanadium-Natisite
System	Orthorhombic	Tetragonal
Space Group	P m m a	P 4 / n m m
a (Å)	9.8412 (3)	6.48381 (9)
b (Å)	9.1714 (4)	6.48381 (9)
c (Å)	4.8040 (2)	5.0934 (1)
V (Å³)	433.59 (3)	214.125 (8)
R_{WP} (%)	5.730	5.730
R_P (%)	2.589	2.589
R_{exp} (%)	4.366	4.366

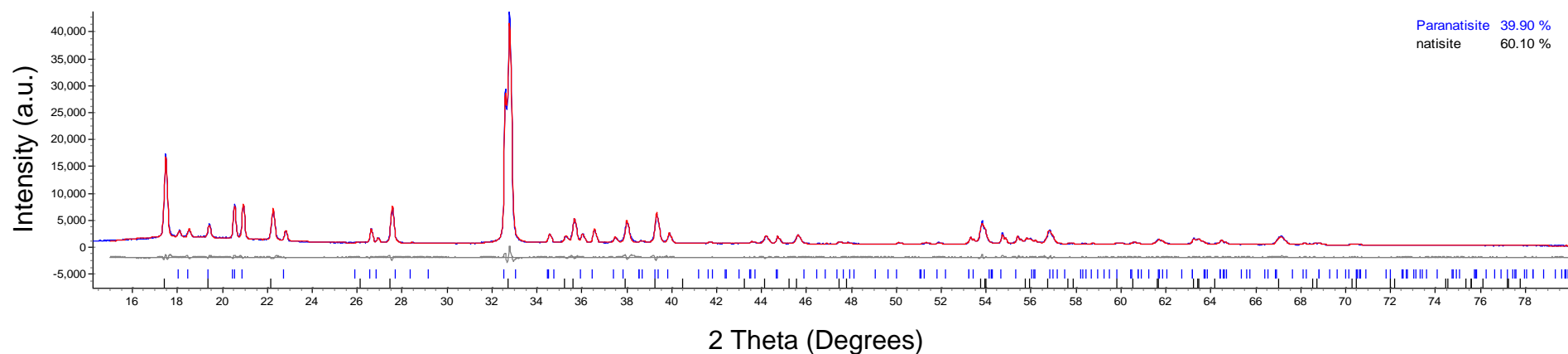


Figure A11.b: Final rietveld fit of 10 day synthesis

A12: Crystallographic Data of 11 Day Synthesis

Table A12.a: Refined lattice parameters and refinement statistics for 11 day synthesis

Parameter	10 %-Vanadium-Paranatisite	10 %-Vanadium-Natisite
System	Orthorhombic	Tetragonal
Space Group	P m m a	P 4 / n m m
a (Å)	9.8479 (5)	6.4877 (2)
b (Å)	7.1714 (6)	6.4877 (2)
c (Å)	4.8045 (3)	5.0945 (2)
V (Å ³)	433.93 (4)	214.43 (1)
R _{WP} (%)	7.533	7.533
R _P (%)	2.979	2.979
R _{exp} (%)	5.696	5.696

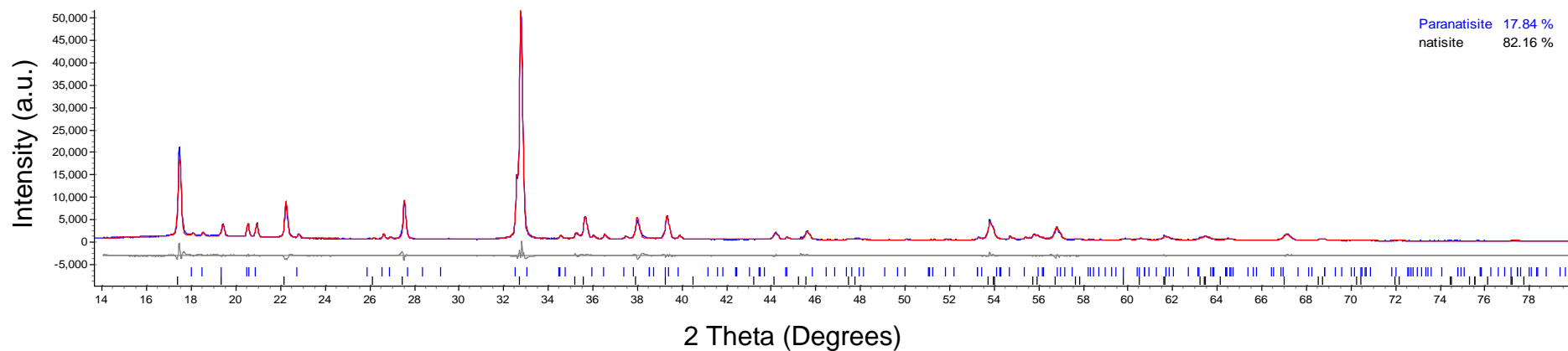


Figure A12.b: Final rietveld fit of 11 day synthesis

A13: Crystallographic data of 12 Day Synthesis

Table A13.a: Refined lattice parameters and refinement statistics for 12 day synthesis

Parameter	10 %-Vanadium-Natisite
System	Tetragonal
Space Group	P 4 / n m m
<i>a</i> (Å)	6.48747 (7)
<i>b</i> (Å)	6.48747 (7)
<i>c</i> (Å)	5.0975 (1)
<i>V</i> (Å ³)	214.538 (6)
R _{WP} (%)	5.605
R _P (%)	4.534
R _{exp} (%)	2.697

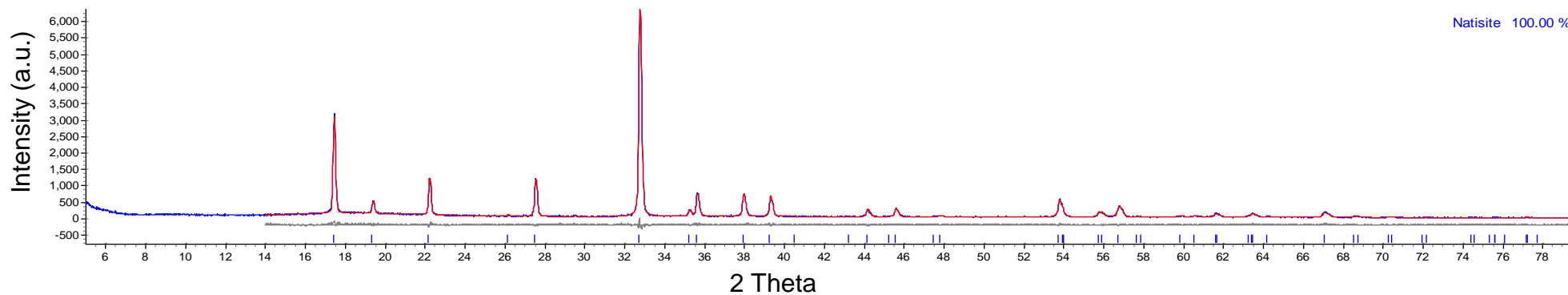


Figure A13.b: Final rietveld fit of 12 day synthesis

A14: Crystallographic Data of 5 %-Vanadium-Paranatisite

Table A14.a: Refined atomic coordinates for 5 %-vanadium-paranatisite

Site	X	Y	Z	Occ	beq
Ti1	0	0	0	0.75	9.6 (2)
Ti2	0.25	0.5	0.539 (9)	1	6.6 (1)
Si1	0	0.250 (6)	0.5	1	5.8 (1)
Na1	0.25	0	0.424 (2)	1	10.0 (3)
Na2	0	0.5	0	1	6.6 (2)
Na3	0.25	0.2452 (6)	0.991 (2)	1	6.4 (1)
O1	0.6139 (4)	0.3517 (7)	0.3568 (8)	1	5.5 (1)
O2	0.4307 (4)	0.1511 (7)	0.2615 (9)	1	5.1 (4)
O3	0.3141 (9)	0	0.842 (2)	0.5	3.7 (4)
O4	0.25	0.5	0.184 (2)	1	4.7 (4)

Table A15.b: Bond lengths of 5 %-vanadium-paranatisite

Bond	Length (Å)	Bond	Length (Å)
Na1-O2	2.387 (6)	Na3-O3	2.450 (7)
Na1-O3	2.111 (1)	Na3-O4	2.523 (7)
Na1-O3	2.881 (1)	O1-Si1	1.613 (6)
O3-O3	1.258 (2)	O2-Si1	1.618 (6)
Na2-O1	2.465 (5)	O2-Ti1	1.997 (6)
Na2-O4	2.610 (3)	O3-Ti1	1.974 (9)
Na3-O1	2.359 (7)	O1-Ti2	1.975 (5)
Na3-O2	2.366 (6)	O4-Ti2	1.714 (9)

Table A15.c: Bond angles of 5 %-vanadium-paranatisite

Bond	Angle (°)	Bond	Angle (°)	Bond	Angle (°)
O3-Na1-O2	122.4 (3)	Na1-O3-Na3	134.1 (5)	Na1-O3-Na1	150.1 (4)
O3-Na1-O2	95.3 (3)	O1-Na3-O3	91.6 (3)	Na3-O3-Na1	70.0 (3)
O3-Na1-O3	175.3 (2)	O1-Na3-O3	108.6 (4)	Ti2-O4-Na3	111.6 (4)
O3-Na1-O3	150.1 (4)	O1-Na3-O4	82.9 (3)	Na3-O4-Na2	82.8 (1)
O2-Na1-O2	141.5 (5)	O2-Na3-O2	97.1 (3)	O1-Si1-O1	109.2 (5)
O2-Na1-O2	71.3 (3)	O2-Na3-O3	91.0 (3)	O1-Si1-O2	108.3 (2)
O2-Na1-O3	80.8 (3)	O2-Na3-O4	82.9 (3)	O2-Si1-O2	111.5 (5)
O2-Na1-O3	61.1 (3)	O3-Na3-O4	164.6 (2)	O2-Ti1-O2	180.0
O2-Na1-O2	96.0 (3)	Si1-O2-Ti1	134.3 (3)	O2-Ti1-O2	88.2 (3)
O2-Na1-O2	71.2 (3)	Si1-O2-Na3	120.1 (4)	O2-Ti1-O3	85.9 (3)
O1-Na2-O1	180.0	Si1-O2-Na1	114.0 (3)	O2-Ti1-O3	94.1 (3)
O1-Na2-O1	112.8 (3)	Ti1-O2-Na3	99.3 (2)	O2-Ti1-O2	180.0
O1-Na2-O1	67.2 (3)	Ti1-O2-Na1	93.2 (2)	O3-Ti1-O3	180.0
O1-Na2-O4	100.9 (2)	Na3-O2-Na1	80.7 (2)	O4-Ti2-O1	104.8 (2)
O1-Na3-O1	69.0 (3)	Ti1-O3-Na1	130.0 (5)	O1-Ti2-O1	87.4 (3)
O1-Na3-O2	165.7 (3)	Ti1-O3-Na3	97.1 (3)	O1-Ti2-O1	85.1 (3)
O1-Na3-O2	96.9 (2)	Ti1-O3-Na1	79.9 (3)	O1-Ti2-O1	150.5 (2)

Table A15.d: Refined lattice parameters and refinement statistics for 5 %-vanadium-paranatisite

Parameter	5 %-Vanadium-Paranatisite
System	Orthorhombic
Space Group	P m m a
<i>a</i> (Å)	9.8172 (2)
<i>b</i> (Å)	9.2017 (2)
<i>c</i> (Å)	4.8260 (7)
<i>V</i> (Å ³)	436.00 (1)
R _{WP} (%)	5.750
R _P (%)	2.899
R _{exp} (%)	4.484

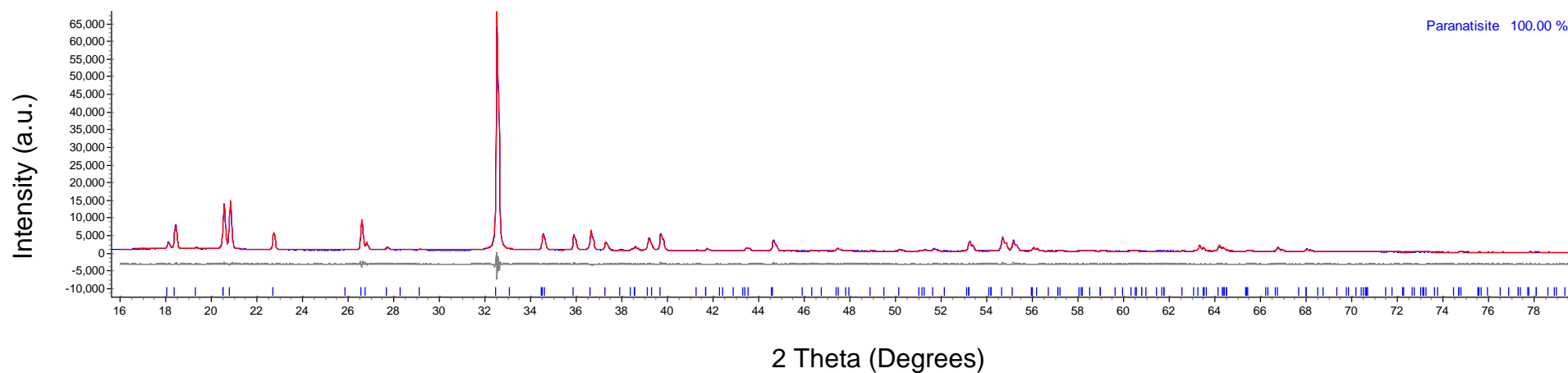


Figure A15.e: Final rietveld fit of 5 %-vanadium-paranatisite

A16: EDX Spectrum of 5 %-Vanadium-Paranatisite

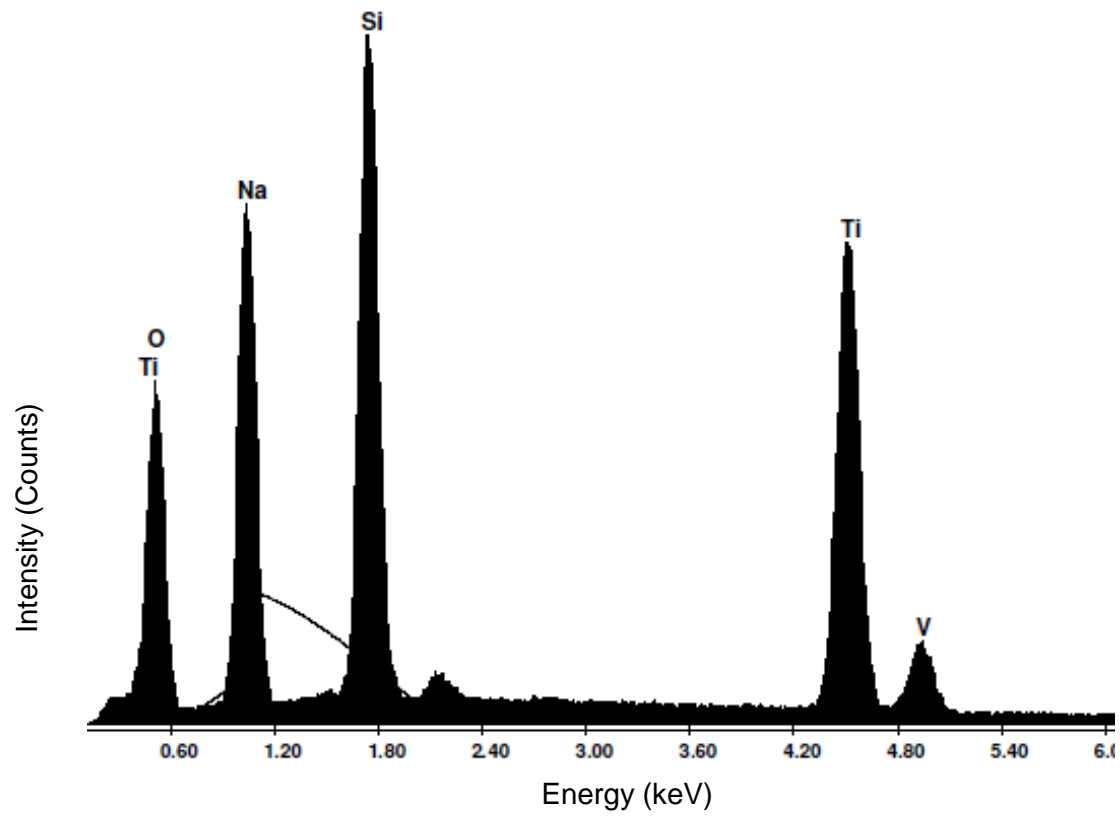


Figure A16: EDX spectrum of 5 %-vanadium-paranatisite

A17: EDX Spectrum of 10 %-Vanadium-Paranatisite

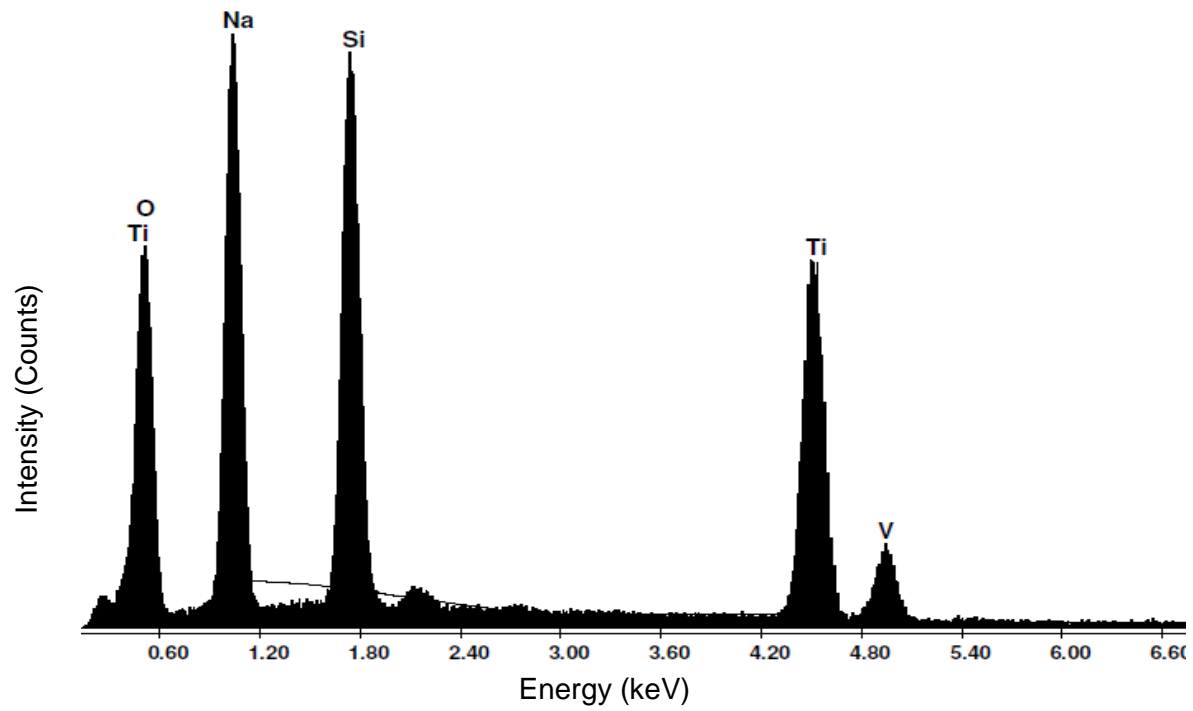


Figure A17: EDX spectrum of 10 %-vanadium-paranatisite

A18: 5 % and 10 %-Vanadium-Percentage in Framework Samples Determined by ICP-MS

Sample : 5 %-Vanadium-Paranatisite	Vanadium (%)
1	4.80
2	4.81
3	4.87
4	4.78
5	4.34
Average:	4.72

Sample : 10 %-Vanadium-Paranatisite	Vanadium (%)
1	8.01
2	7.92
3	8.01
4	7.99
5	7.92
Average:	7.97

A19: Crystallographic data of Phase Aa M1 5 %-Vanadium-Natisite

Table A19.a: Refined atomic coordinates for phase Aa M1 5 %-vanadium-natisite

Site	X	Y	Z	Occ	beq
Na1	0.75	0.2500	0.5000	1	7.8 (3)
O1	1.0000	0.7837 (8)	1.1683 (9)	1	3.2 (2)
O2	1.0000	0.5000	0.746 (4)	1	6.8 (6)
Si1	1.5000	0.5000	1.0000	1	4.8 (3)
Ti1	1.0000	0.5000	1.059 (1)	1	4.4 (2)

Table A19.b: Bond lengths of phase Aa M1 5 %-vanadium-natisite

Bond	Length (Å)
Na1-O1	2.356 (3)
Na1-O2	2.614 (9)
O1-Si1	1.644 (5)
Ti1-O1	1.921 (6)
Ti1-O2	1.60 (2)

Table A19.c: Bond angles of phase Aa M1 5 %-vanadium-natisite

Bond	Angle (°)	Bond	Angle (°)
O1-Na1-O1	68.6 (4)	Ti1-O2-Na1	118.3 (7)
O1-Na1-O1	180.0	Na1-O2-Na1	123.4 (1)
O1-Na1-O1	111.4 (5)	Na1-O2-Na1	77.0 (6)
O1-Na1-O2	89.2 (6)	O1-Si1-O1	106.2 (3)
O1-Na1-O2	90.8 (6)	O1-Si1-O1	116.2 (7)
Si1-O1-Ti1	132.7 (7)	O2-Ti1-O1	105.4 (4)
Si1-O1-Na1	118.4 (4)	O1-Ti1-O1	149.2 (9)
Ti1-O1-Na1	94.8 (4)	O1-Ti1-O1	85.9 (2)
Na1-O1-Na1	86.4 (3)		

Table A19.d: Refined lattice parameters and refinement statistics for phase Aa M1 5 %-vanadium-natisite

Parameter	Phase Aa M1 5 %-Vanadium-Natisite
System	Tetragonal
Space Group	P 4 / n m m
<i>a</i> (Å)	6.4836 (3)
<i>b</i> (Å)	6.4836 (3)
<i>c</i> (Å)	5.1015 (3)
<i>V</i> (Å ³)	214.45 (2)
R _{WP} (%)	6.399
R _P (%)	3.177
R _{exp} (%)	5.271

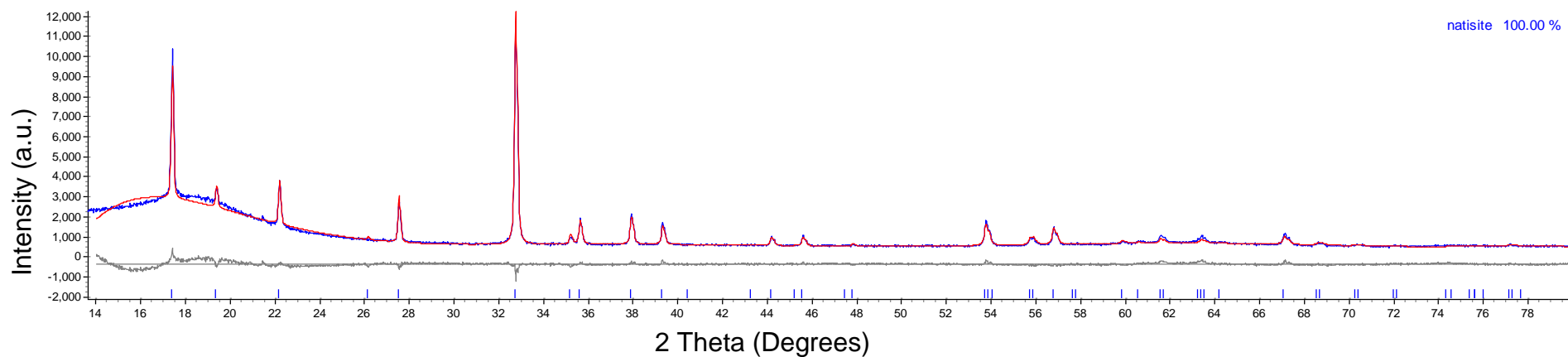


Figure A19.e: Final rietveld fit of phase Aa M15 %-vanadium-natisite

A20: Crystallographic data of Phase Ab M2 10 %-Vanadium-Natisite

Table A20.a: Refined atomic coordinates for phase Ab M2 10 %-vanadium-natisite

Site	X	Y	Z	Occ	beq
Na1	0.75	0.2500	0.5000	1	7.6 (3)
O1	1.0000	0.7924 (8)	1.1691 (1)	1	3.9 (2)
O2	1.0000	0.5000	0.732 (4)	1	8.0 (6)
Si1	1.5000	0.5000	1.0000	1	6.0 (4)
Ti1	1.0000	0.5000	1.052 (2)	1	4.4 (2)

Table A20.b: Bond lengths of phase Ab M2 10 %-vanadium-natisite

Bond	Length (Å)
Na1-O1	2.354 (4)
Na1-O2	2.581 (9)
O1-Si1	1.598 (5)
Ti1-O1	1.989 (5)
Ti1-O2	1.63 (2)

Table A20.c: Bond angles of phase Ab M2-10 %-vanadium-natisite

Bond	Angle (°)	Bond	Angle (°)
O1-Na1-O1	69.4 (2)	Ti1-O2-Na1	117.3 (4)
O1-Na1-O1	180.0	Na1-O2-Na1	125.4 (8)
O1-Na1-O1	110.6 (2)	Na1-O2-Na1	77.9 (3)
O1-Na1-O2	91.9 (3)	O1-Si1-O1	106.8 (2)
O1-Na1-O2	88.1 (3)	O1-Si1-O1	115.1 (4)
Si1-O1-Ti1	130.1 (3)	O2-Ti1-O1	107.4 (2)
Si1-O1-Na1	118.8 (2)	O1-Ti1-O1	84.9 (1)
Ti1-O1-Na1	95.9 (2)	O1-Ti1-O1	145.2 (4)
Na1-O1-Na1	87.1 (2)		

Table A20.d: Refined lattice parameters and refinement statistics for phase Ab M2 10 %-vanadium-natisite

Parameter	Phase Ab M2 5 %-Vanadium-Natisite
System	Tetragonal
Space Group	P 4 / n m m
a (Å)	6.4912 (4)
b (Å)	6.4912 (4)
c (Å)	5.0858 (4)
V (Å ³)	214.29 (3)
R _{WP} (%)	10.129
R _P (%)	3.248
R _{exp} (%)	7.811

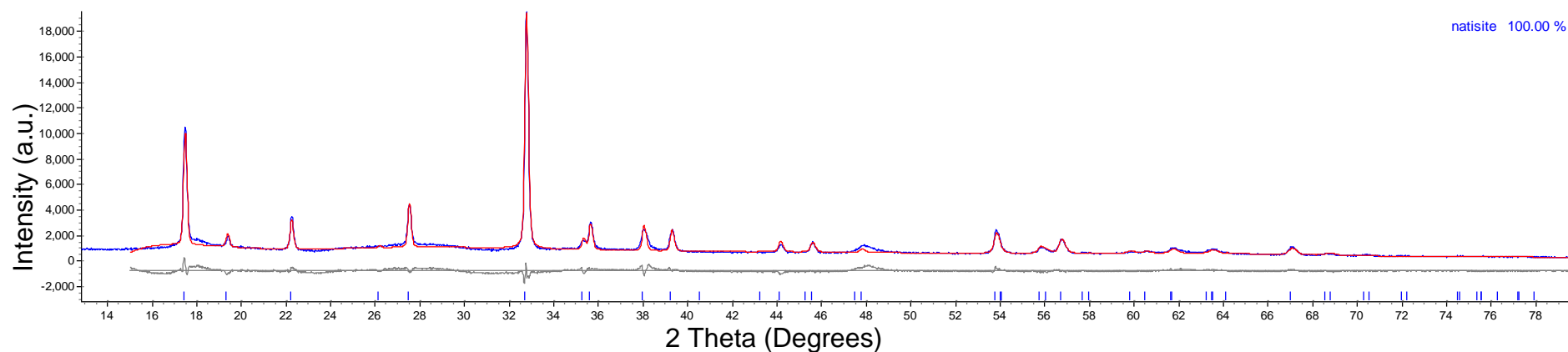


Figure A20.e: Final rietveld fit of phase Ab M2 10 %-vanadium-natisite

A21: Crystallographic Data of Phase B M2 5 %-Vanadium-Natisite

Table A21.a: Refined atomic coordinates for phase B M2 5 %-vanadium-natisite

Site	X	Y	Z	Occ	beq
Na1	0.75	0.2500	0.5000	1	6.14 (7)
O1	1.0000	0.7950 (2)	1.8660 (3)	1	4.67 (6)
O2	1.0000	0.5000	0.7234 (9)	1	5.5 (1)
Si1	1.5000	0.5000	1.0000	1	5.71 (9)
Ti1	1.0000	0.5000	1.0614 (3)	1	5.91 (6)

Table A22.b: Bond lengths of phase B M2 5 %-vanadium-natisite

Bond	Length (Å)
Na1-O1	2.295 (1)
Na1-O2	2.562 (2)
O1-Si1	1.635 (2)
Ti1-O1	2.018 (2)
Ti1-O2	1.722 (5)

Table A22.c: Bond angles of phase B M2 5 %-vanadium-natisite

Bond	Angle (°)	Bond	Angle (°)
O1-Na1-O1	72.3 (7)	Ti1-O2-Na1	116.4 (9)
O1-Na1-O1	180.0	Na1-O2-Na1	78.6 (8)
O1-Na1-O1	107.7 (7)	Na1-O2-Na1	127.2 (2)
O1-Na1-O2	86.7 (8)	O1-Si1-O1	109.8 (5)
O1-Na1-O2	93.3 (8)	O1-Si1-O1	108.9 (1)
Si1-O1-Ti1	126.0 (9)	O2-Ti1-O1	108.4 (6)
Si1-O1-Na1	120.5 (5)	O1-Ti1-O1	84.3 (4)
Ti1-O1-Na1	95.7 (6)	O1-Ti1-O1	143.1 (1)
Na1-O1-Na1	90.0 (6)		

Table A22.d: Overview of crystallographic data of phase B M2 5 %-vanadium-natisite

Parameter	Phase B M2 5 %-Vanadium-Natisite
System	Tetragonal
Space Group	P 4 / n m m
a (Å)	6.48964 (7)
b (Å)	6.48964 (7)
c (Å)	5.09580 (9)
V (Å ³)	214.612 (6)
R _{WP} (%)	5.934
R _P (%)	2.803
R _{exp} (%)	4.562

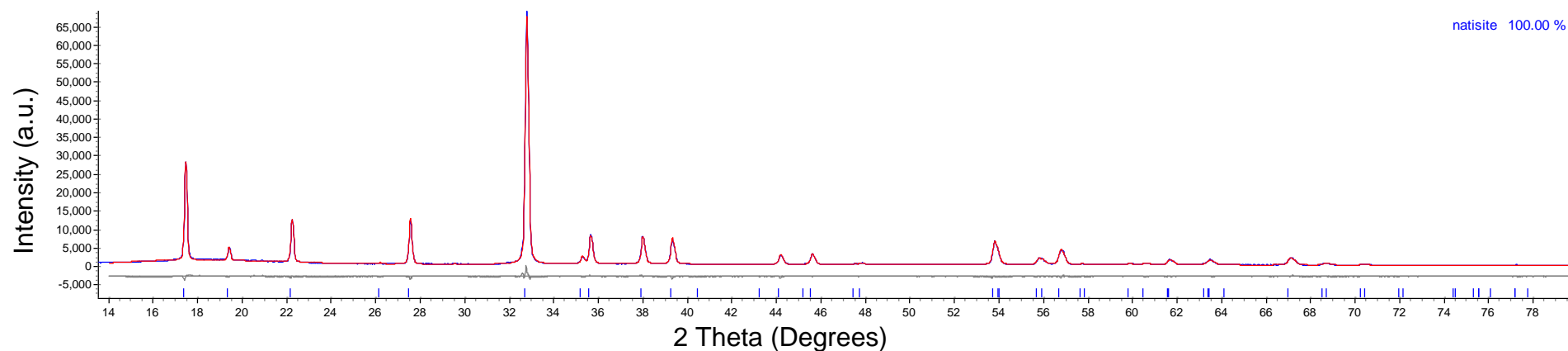


Figure A22.e: Final rietveld fit of phase B M2 5 %-vanadium-natisite

A23: EDX Spectrum of Phase Aa M1 5 %-Vanadium-Natisite

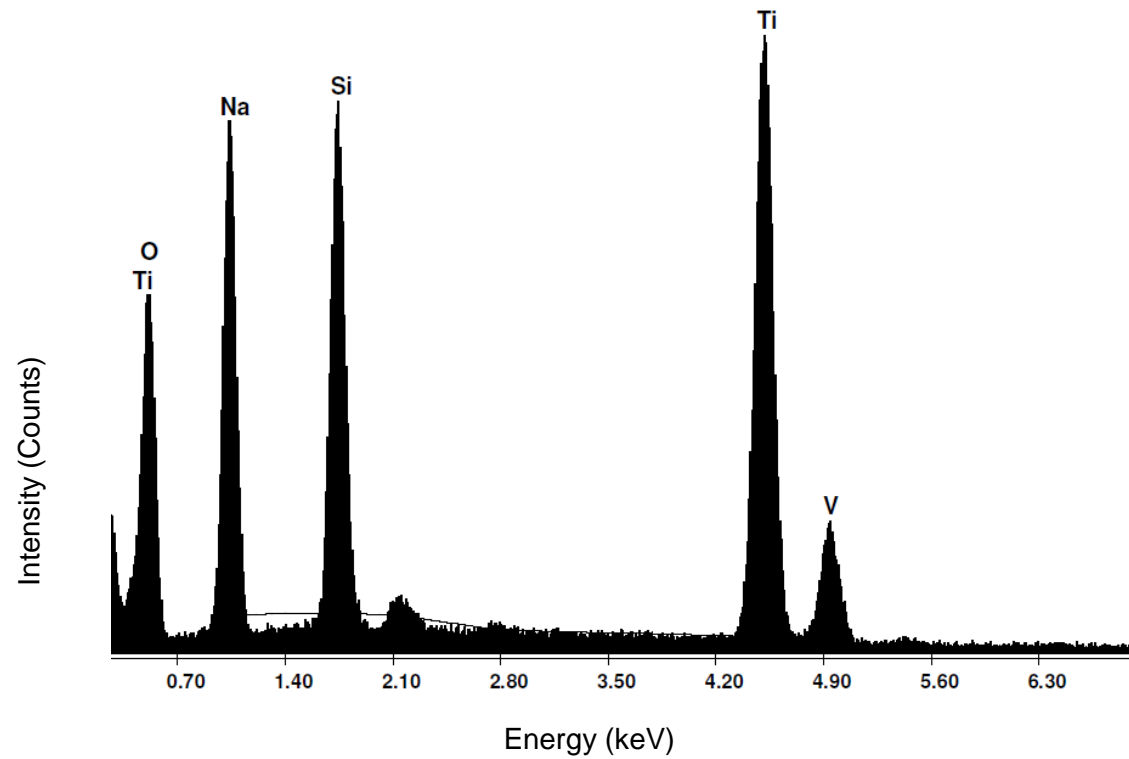


Figure A23: EDX spectrum of phase Aa M1 5 %-vanadium-natisite

A24: EDX Spectrum of Phase Ab M2 10 %-Vanadium-Natisite

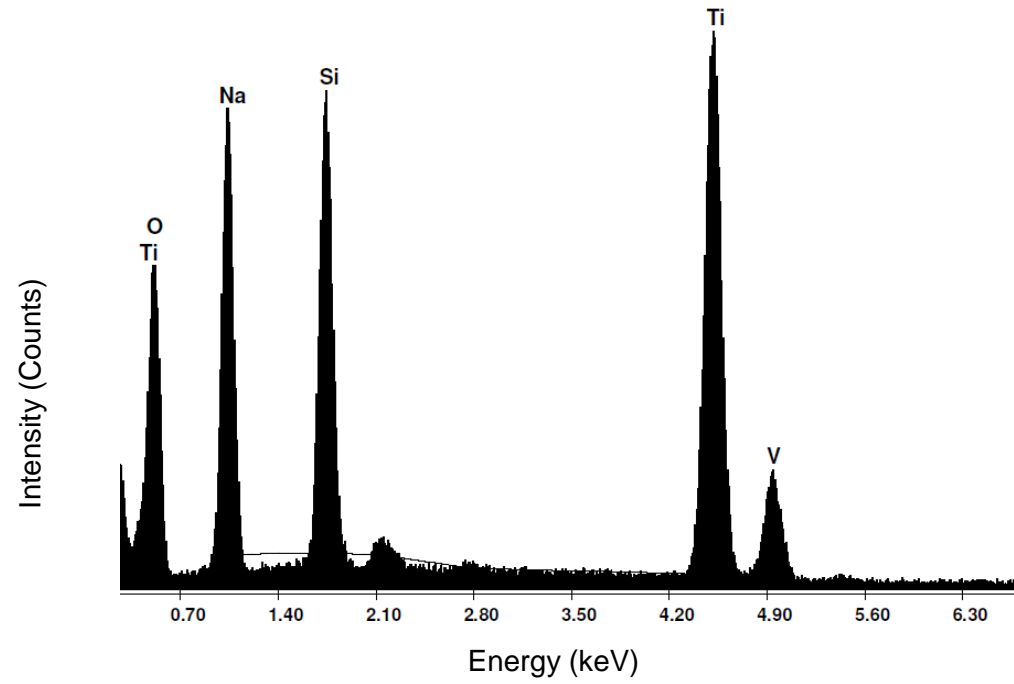


Figure A24: EDX spectrum of phase Ab M2 10 %-vanadium-natisite

A25: EDX Spectrum of Phase B M2 5 %-Vanadium-Natisite

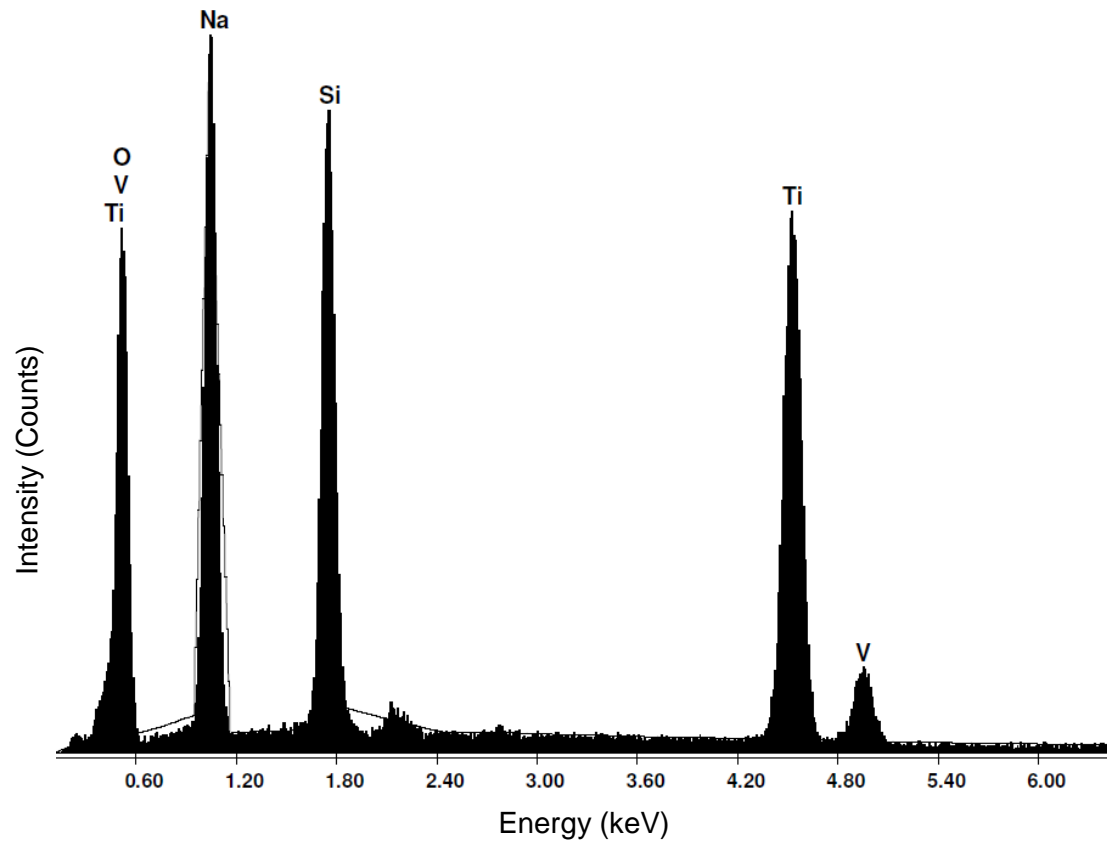


Figure A25: EDX spectrum of phase B M2 5 %-vanadium-natisite

A26: EDX Spectrum of Phase C M2 10 %-Vanadium-Natisite

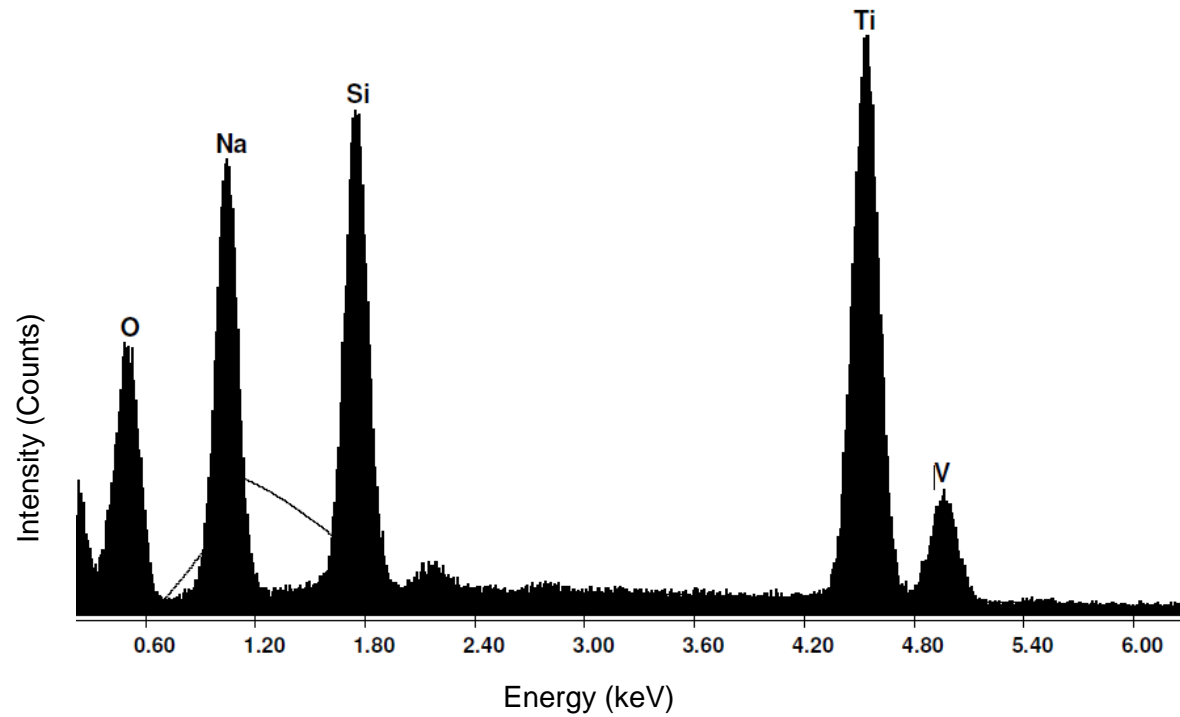


Figure A26: EDX spectrum of phase C M2 10 %-vanadium-natisite

A27: 5 % and 10 %-vanadium-natisite doping in samples as determined by ICP-MS

Sample : 5 %-Vanadium-Natisite	Vanadium (%)
1	4.67
2	4.50
3	4.64
4	4.68
5	4.54
Average:	4.61

Sample : 10 %-Vanadium-Natisite	Vanadium (%)
1	7.79
2	7.91
3	7.81
4	8.16
5	8.17
Average:	7.968

A28: 5 %-Vanadium-Natisite-Cobalt Chloride Ion Exchanged Material

Table A28.a: Refined lattice parameters and refinement statistics for 5 %-vanadium-natisite-cobalt chloride ion exchanged material.

Parameter	5 %-Vanadium-Natisite-Cerium Ion Exchanged Material
System	Tetragonal
Space Group	P 4 / n m m
a (Å)	6.494 (2)
b (Å)	6.494 (2)
c (Å)	5.087
V (Å ³)	214.4 (1)
R _{WP} (%)	4.515
R _P (%)	3.479
R _{int} (%)	2.806

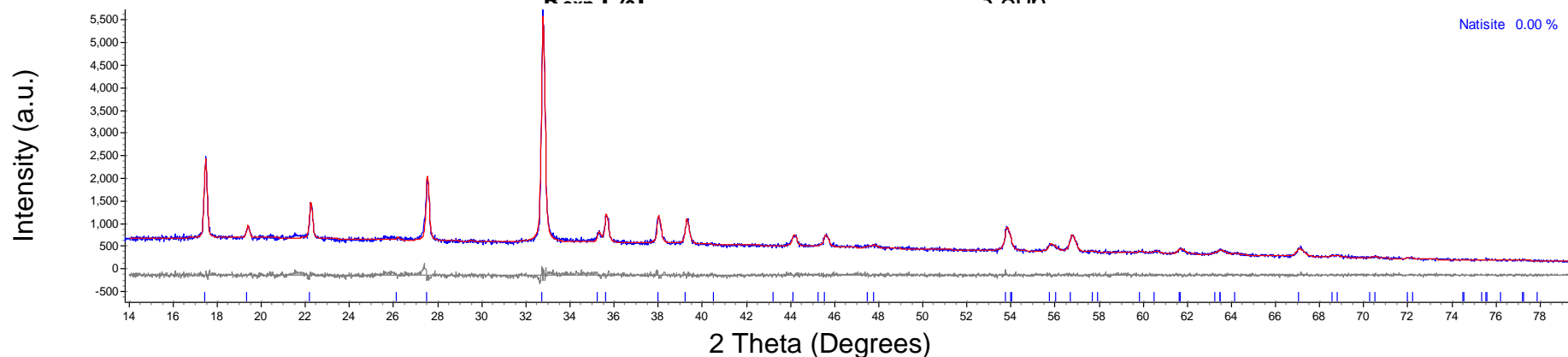


Figure A28.b: Final pawley fit of 5 %-vanadium-natisite-cobalt chloride ion exchanged material

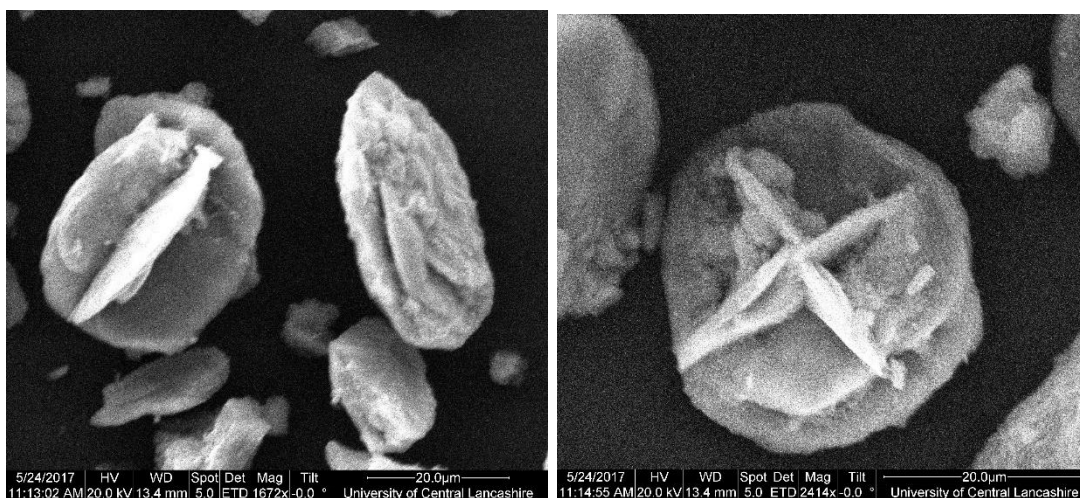


Figure A28.c: SEM imagery of 5 %-vanadium-natisite-cobalt chloride ion exchanged material

Table A28.d: Percentage of cobalt (chloride) ion species exchanged into the framework of 5 %-vanadium-natisite

Ion Exchange Attempt	Percentage Exchanged- into framework (%)
Attempt 1	25 (\pm 0.79)
Attempt 2	24 (\pm 0.92)
Attempt 3	26 (\pm 0.67)
Average	25

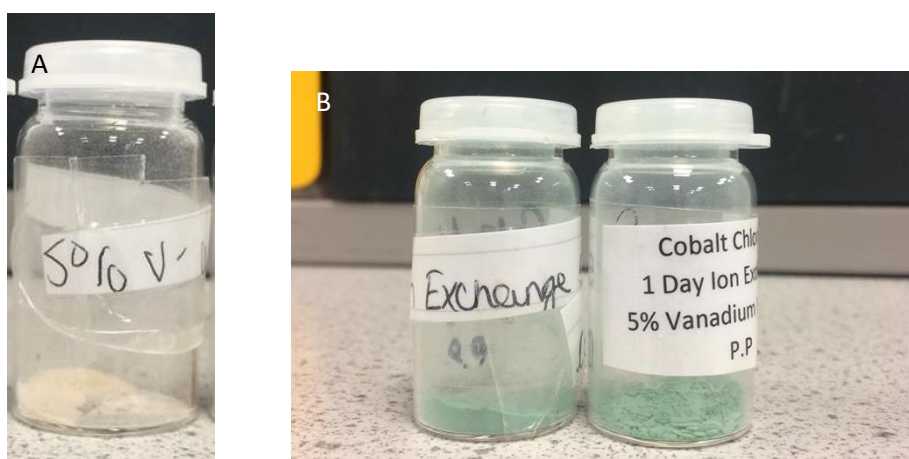


Figure A28.e: Images of A: un-exchanged 5 %-vanadium-natisite and B: exchanged 5 %-vanadium-natisite with cobalt nitrate and cobalt chloride

A29: 5 %-Vanadium-Paranatisite-Cesium Ion Exchanged Material

Table A29.a: Refined lattice parameters and refinement statistics for 5 %-vanadium-paranatisite-cesium ion exchanged material.

Parameter	5 %-Vanadium-Paranatisite-Cesium Ion Exchanged Material
System	Orthorhombic
Space Group	P m m a
<i>a</i> (Å)	9.820 (2)
<i>b</i> (Å)	9.202 (1)
<i>c</i> (Å)	4.8253 (8)
<i>V</i> (Å ³)	436.0 (1)
R _{WP} (%)	10.966
R _P (%)	8.798
R _{exp} (%)	8.756

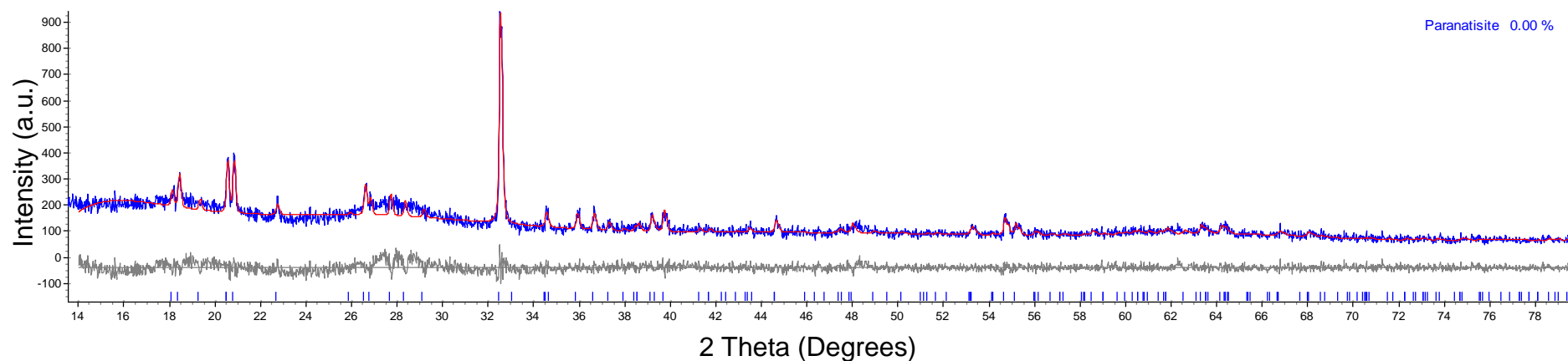


Figure A29.b: Final pawley fit of 5 %-vanadium-paranatisite-cesium ion exchanged material

A30: 5 %-Vanadium-Paranatisite-Cerium Ion Exchanged Material

Table A30.a: Refined lattice parameters and refinement statistics for 5 %-vanadium-paranatisite-cerium ion exchanged material

Parameter	5 %-Vanadium-Paranatisite-Cerium Ion Exchanged Material
System	Orthorhombic
Space Group	P m m a
<i>a</i> (Å)	10.0 (2)
<i>b</i> (Å)	9.2 (2)
<i>c</i> (Å)	4.75 (7)
<i>V</i> (Å ³)	430 (2)
R _{WP} (%)	7.520
R _P (%)	7.008
R _{exp} (%)	5.893

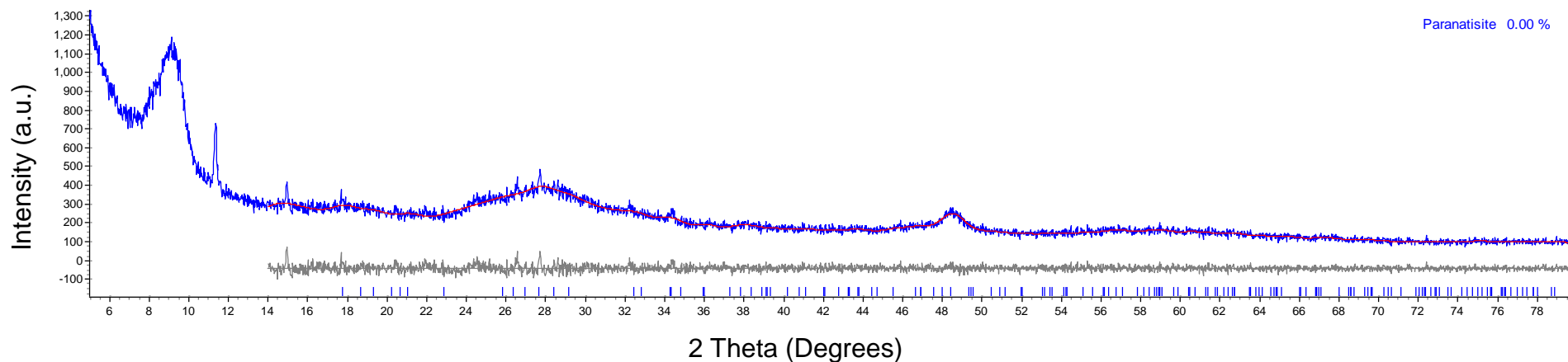


Figure A30.b: Final pawley fit of 5 %-vanadium-paranatisite-cerium ion exchanged material

A31: 5 %-Vanadium-Paranatisite-Cobalt Ion Exchanged Material

Table A31.a: Refined lattice parameters and refinement statistics for 5 %-vanadium-paranatisite-cobalt ion exchanged material

Parameter	5 %-Vanadium-Paranatisite-Cobalt Ion Exchanged Material
System	Orthorhombic
Space Group	P m m a
<i>a</i> (Å)	9.8240 (7)
<i>b</i> (Å)	9.1999 (6)
<i>c</i> (Å)	4.8231 (3)
<i>V</i> (Å ³)	435.91 (5)
R _{WP} (%)	5.742
R _P (%)	5.192
R _{exp} (%)	4.524

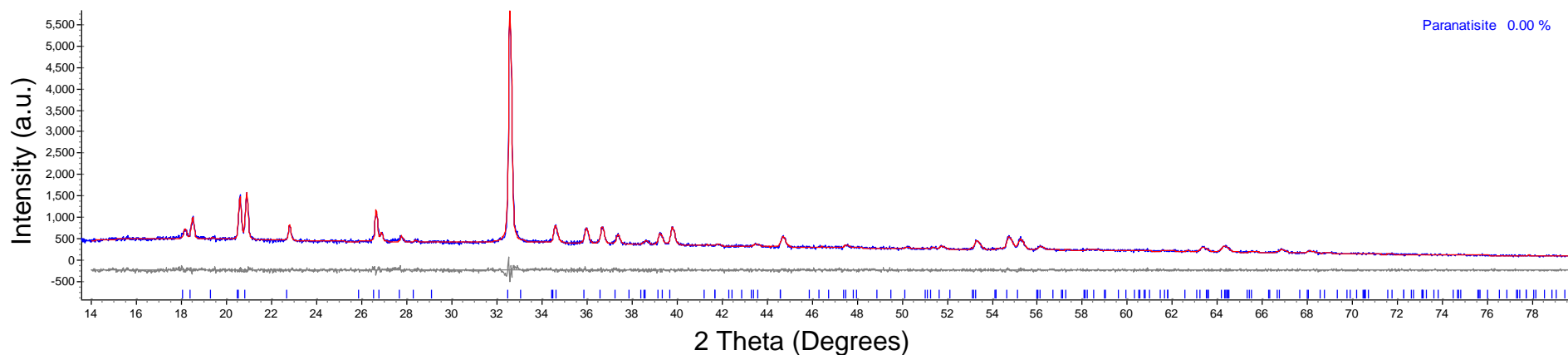


Figure A31.a: Final pawley fit of 5 %-vanadium-paranatisite-cobalt ion exchanged material

A32: 5 %-Vanadium-Paranatisite-Strontium Ion Exchanged Material

Table A32.a: Refined lattice parameters and refinement statistics for 5 %-vanadium-paranatisite-strontium ion exchanged material

Parameter	5 %-Vanadium-Paranatisite-Strontium Ion Exchanged Material
System	Orthorhombic
Space Group	P m m a
<i>a</i> (Å)	9.83 (2)
<i>b</i> (Å)	9.12 (3)
<i>c</i> (Å)	4.82 (1)
<i>V</i> (Å ³)	432 (2)
R _{WP} (%)	18.901
R _P (%)	16.594
R _{exp} (%)	14.803

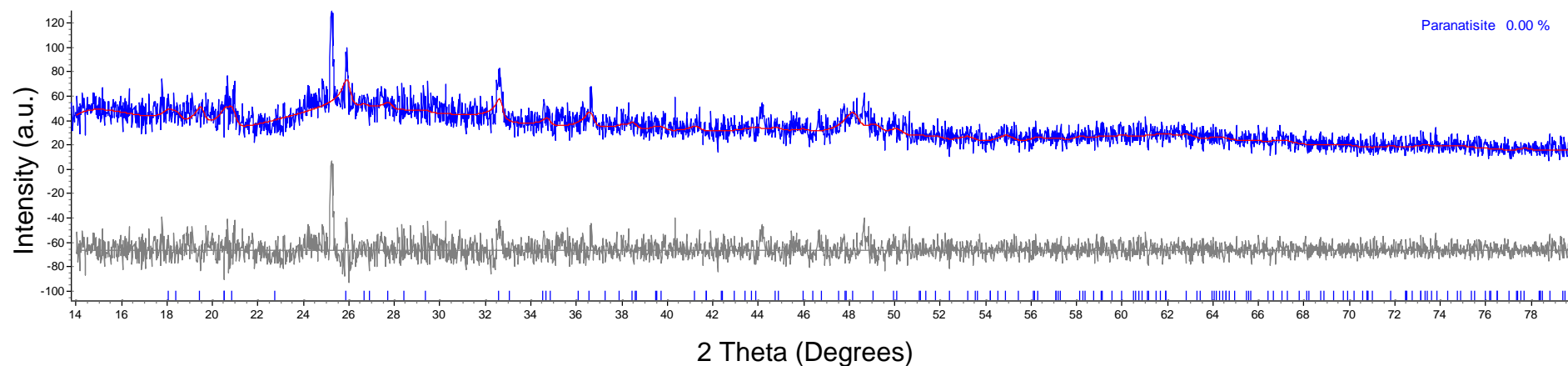


Figure A32.b: Final pawley fit of 5 %-vanadium-paranatisite-strontium ion exchanged material

A33: 5 %-Vanadium-Paranatisite-Neodymium Ion Exchanged Material

Table A33.a: Refined lattice parameters and refinement statistics for 5 %-vanadium-paranatisite-neodymium ion exchanged material

Parameter	5 %-Vanadium-Paranatisite-Neodymium Ion Exchanged Material
System	Orthorhombic
Space Group	P m m a
a (Å)	10.18 (3)
b (Å)	9.15 (2)
c (Å)	4.84 (1)
V (Å ³)	450 (2)
R _{WP} (%)	6.616
R _P (%)	6.316
R _{exp} (%)	5.258

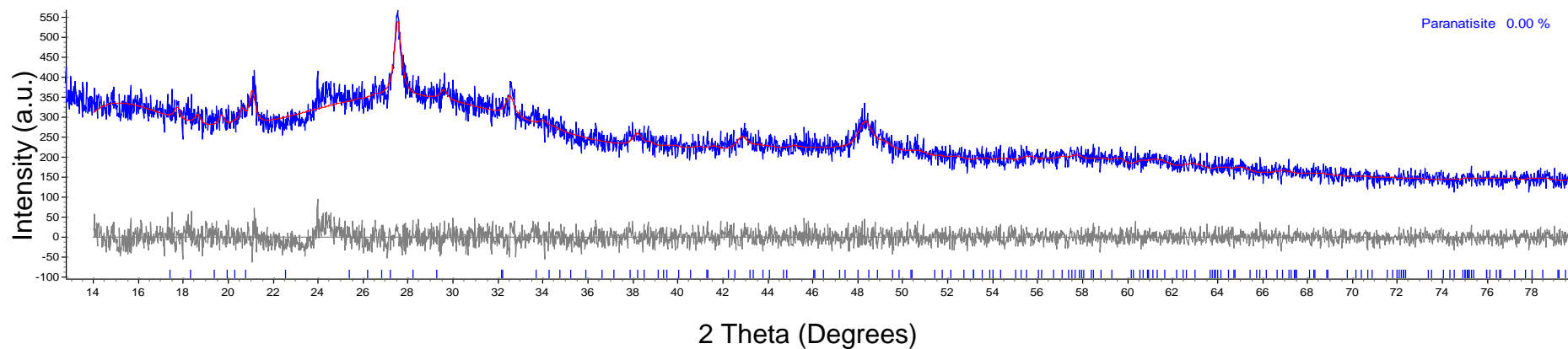


Figure A33.b: Final pawley fit of 5 %-vanadium-paranatisite-neodymium ion exchanged material

A34: 10 %-Vanadium-Paranatisite-Cesium Ion Exchanged Material

Table A34.a: Refined lattice parameters and refinement statistics for 10 %-vanadium-paranatisite-cesium ion exchanged material

Parameter	10 %-Vanadium-Paranatisite-Cesium Ion Exchanged Material
System	Orthorhombic
Space Group	P m m a
<i>a</i> (Å)	9.8328 (4)
<i>b</i> (Å)	9.2028 (4)
<i>c</i> (Å)	4.8211 (2)
<i>V</i> (Å ³)	436.25 (3)
R _{WP} (%)	10.073
R _P (%)	7.704
R _{exp} (%)	7.321

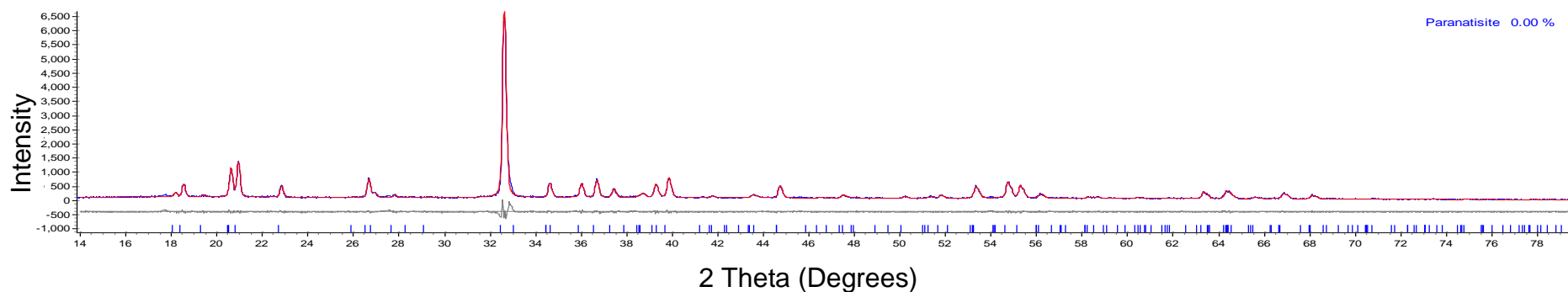


Figure A34.b: Final pawley fit of 5 %-vanadium-paranatisite-cesium ion exchanged material

A35: 10 %-Vanadium-Paranatisite-Cerium Ion Exchanged Material

Table A35.a: Refined lattice parameters and refinement statistics for 10 %-vanadium-paranatisite-cerium ion exchanged material

Parameter	10 %-Vanadium-Paranatisite-Cerium Ion Exchanged Material
System	Orthorhombic
Space Group	P m m a
<i>a</i> (Å)	9.81 (6)
<i>b</i> (Å)	9.192 (4)
<i>c</i> (Å)	4.813 (2)
<i>V</i> (Å ³)	434.0 (4)
R _{WP} (%)	8.379
R _P (%)	7.942
R _{exp} (%)	6.577

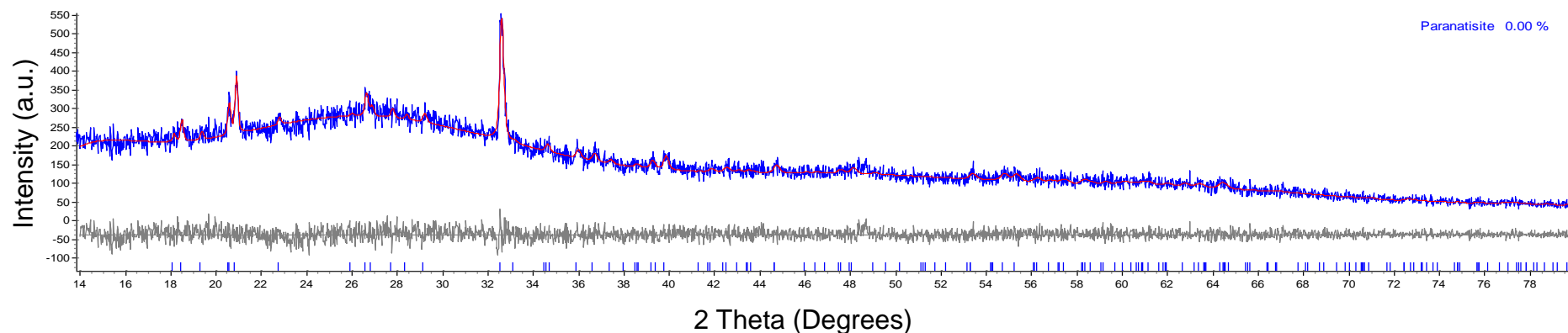


Figure A35.b: Final pawley fit of 10 %-vanadium-paranatisite-cerium ion exchanged material

A36: 10 %-Vanadium-Paranatisite-Cobalt Ion Exchanged Material

Table A36.a: Refined lattice parameters and refinement statistics for 10 %-vanadium-paranatisite-cobalt ion exchanged material

Parameter	10 %-Vanadium-Paranatisite
System	Orthorhombic
Space Group	P m m a
<i>a</i> (Å)	9.8228 (5)
<i>b</i> (Å)	9.1955 (5)
<i>c</i> (Å)	4.8161 (2)
<i>V</i> (Å ³)	434.9 (3)
R _{WP} (%)	6.280
R _P (%)	4.884
R _{exp} (%)	5.543

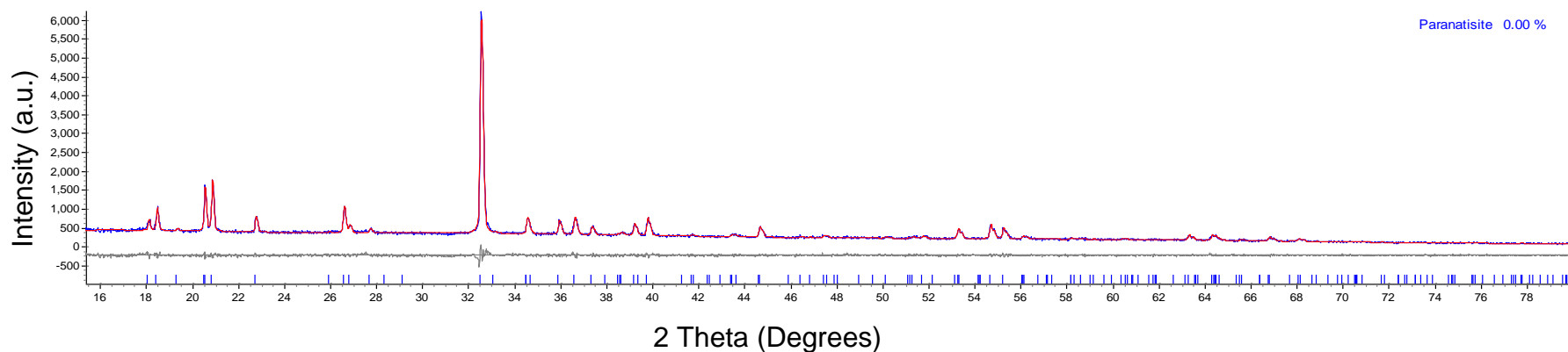


Figure 36.b: Final rietveld fit of 10 %-vanadium-paranatisite-cobalt ion exchanged material

A37: 10 %-Vanadium-Paranatisite-Strontium Ion Exchanged Material

Table A37.a: Refined lattice parameters and refinement statistics for 10 %-vanadium-paranatisite-strontium ion exchanged material

Parameter	10 %-Vanadium-Paranatisite-Strontium Ion Exchanged Material
System	Orthorhombic
Space Group	P m m a
<i>a</i> (Å)	9.8312 (5)
<i>b</i> (Å)	9.1971 (4)
<i>c</i> (Å)	4.8188 (2)
<i>V</i> (Å ³)	435.70 (3)
R _{WP} (%)	10.360
R _P (%)	7.470
R _{exp} (%)	7.667

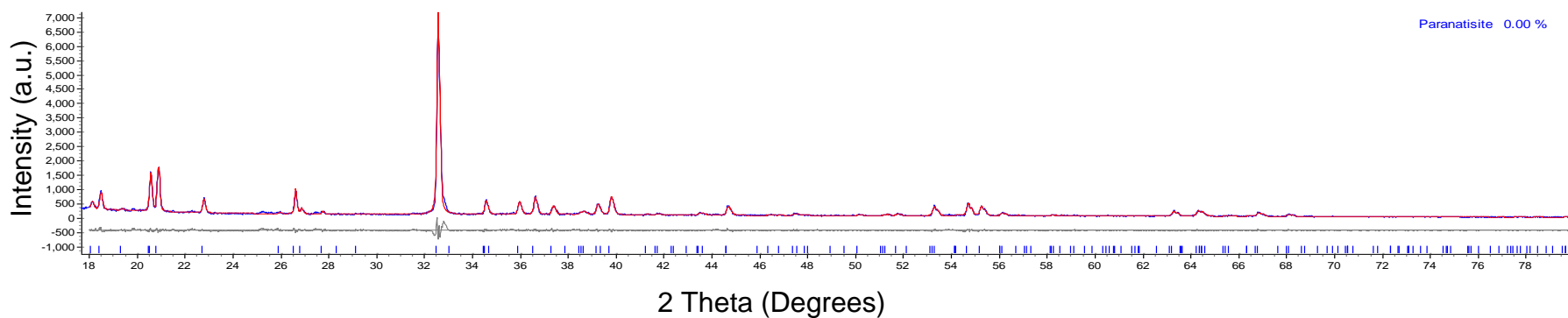


Figure A37.b: Final pawley fit of 10 %-vanadium-paranatisite-strontium ion exchanged material

A38: 10 %-Vanadium-Paranatisite-Neodymium Ion Exchanged Material

Table A38.a: Refined lattice parameters and refinement statistics for 10 %-vanadium-paranatisite-neodymium ion exchanged material

Parameter	10 %-Vanadium-Paranatisite-Neodymium Ion Exchanged Material
System	Orthorhombic
Space Group	P m m a
<i>a</i> (Å)	9.815 (5)
<i>b</i> (Å)	9.194 (4)
<i>c</i> (Å)	4.815 (3)
<i>V</i> (Å ³)	434.6 (4)
R _{WP} (%)	11.584
R _P (%)	7.014
R _{exp} (%)	8.300

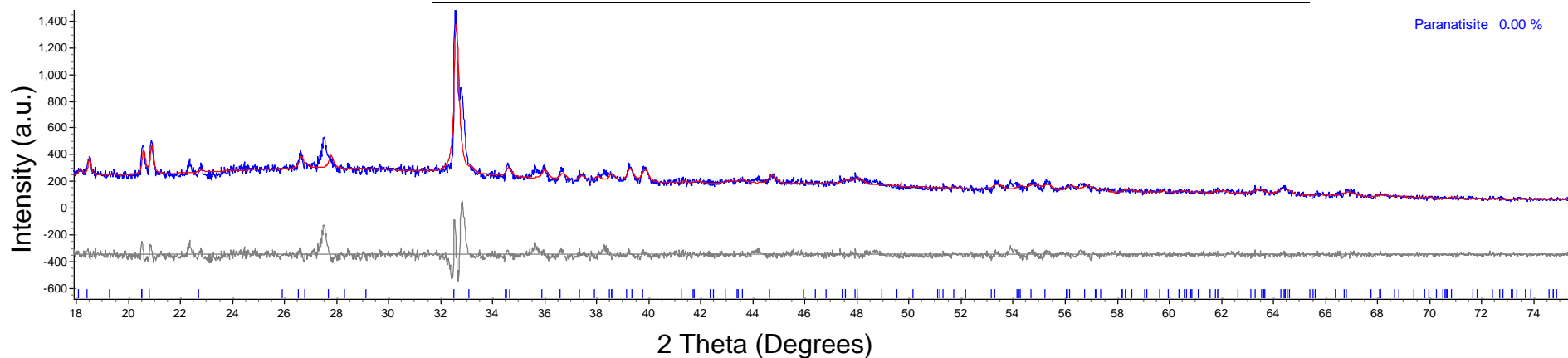


Figure A38.b: Final pawley fit of 10 %-vanadium-paranatisite-neodymium ion exchanged material

A39: EDX Spectrum of 5 %-Vanadium-Paranatisite-Cesium Ion Exchanged Material

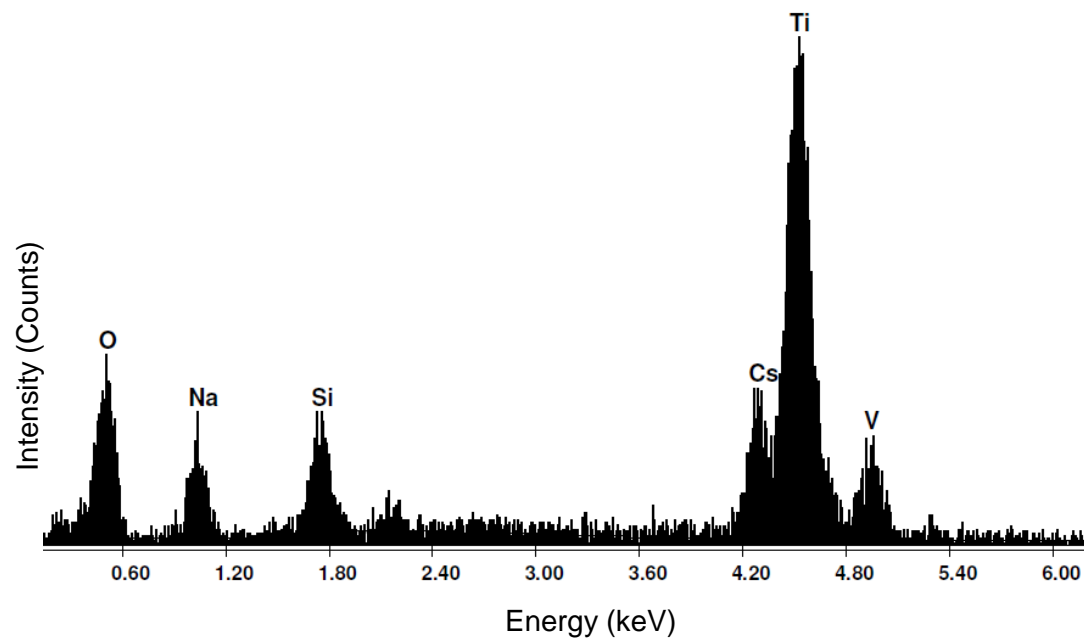


Figure A39: EDX spectrum of 5 %-vanadium-paranatisite-cesium ion exchanged material

A40: EDX Spectrum of 5 %-Vanadium-Paranatisite-Cerium Ion Exchanged Material

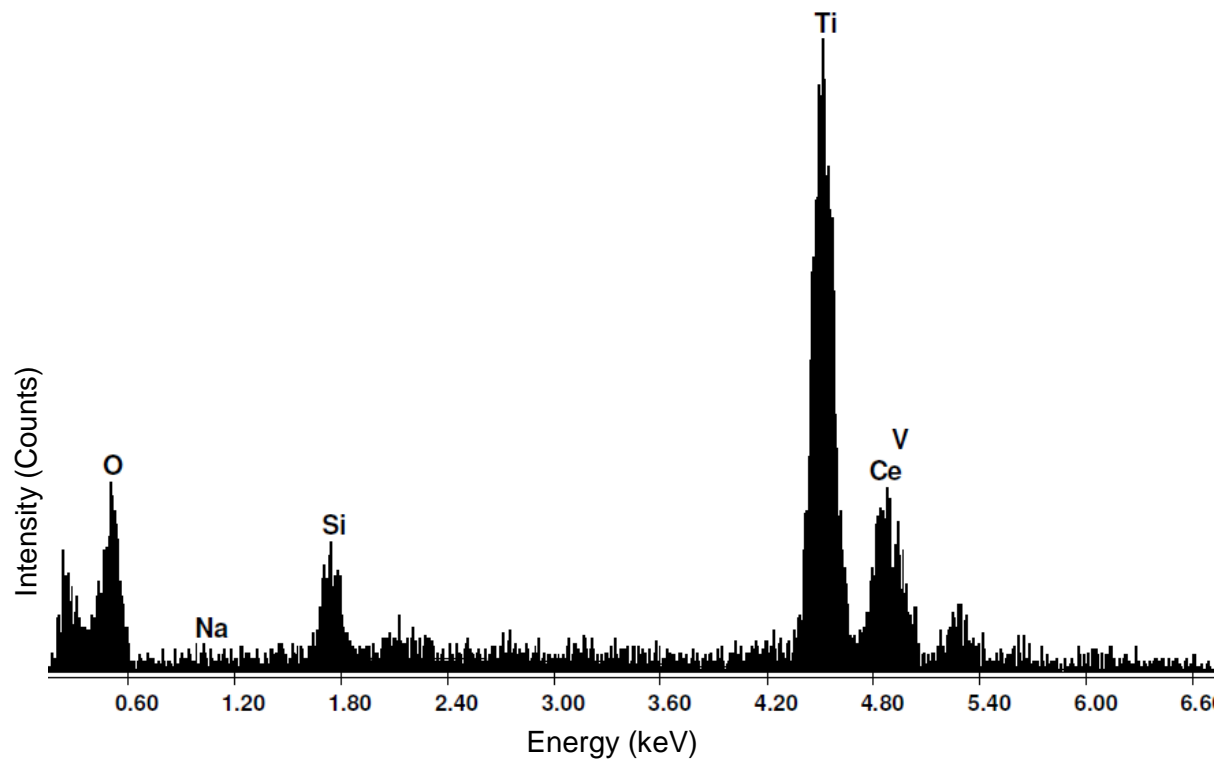


Figure A40: EDX spectra of 5 %-vanadium-paranatisite-cerium ion exchanged material

A41: EDX Spectrum of 5 %-Vanadium-Paranatisite-Cobalt Ion Exchanged Material

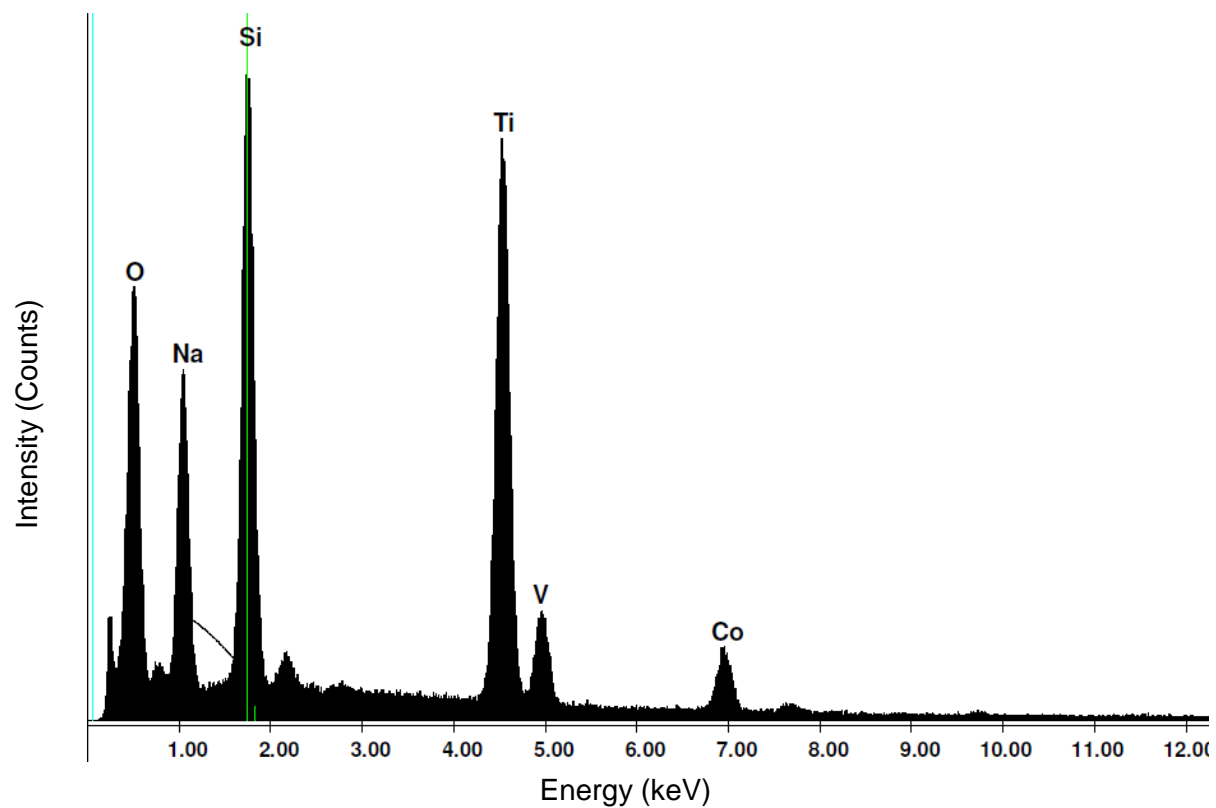


Figure A41: EDX spectrum of 5 %-vanadium-paranatisite-cobalt ion exchanged material

A42: EDX Spectrum of 5 %-Vanadium-Paranatisite-Neodymium Ion Exchanged Material

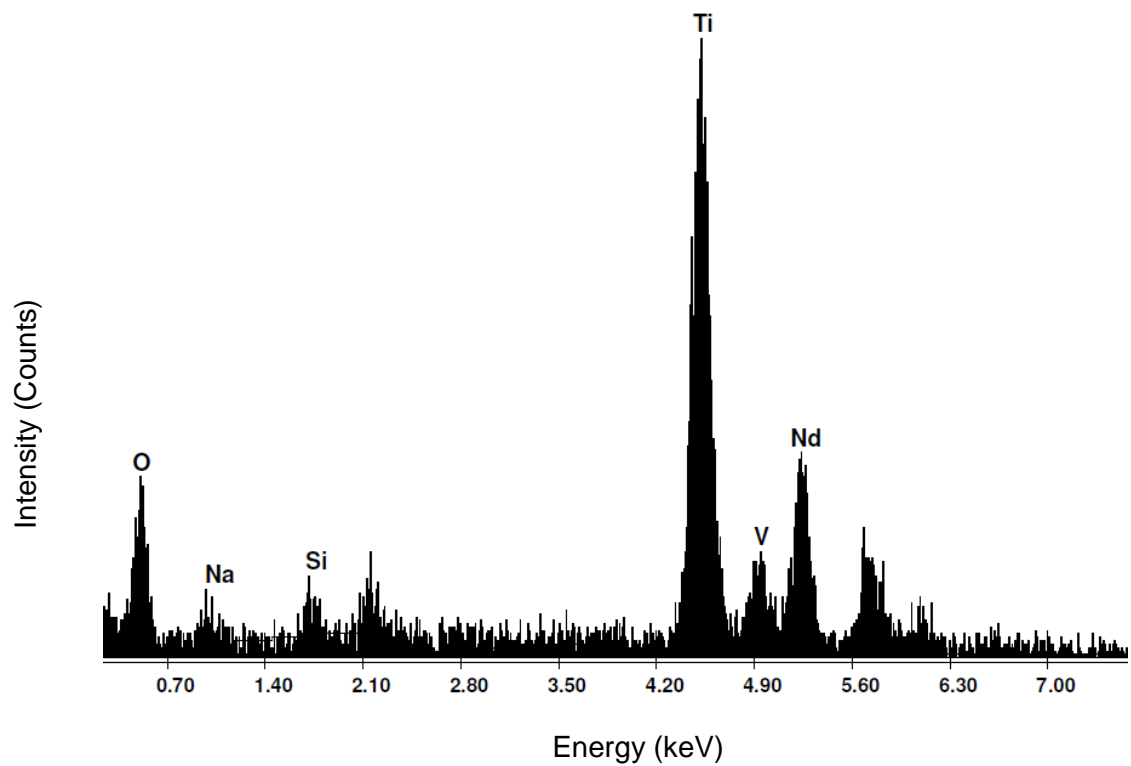


Figure A42: EDX spectrum of 5 %-vanadium-natisite-neodymium ion exchanged material

A43: EDX Spectrum of 5 %-Vanadium-Paranatisite-Strontium Ion Exchanged Material

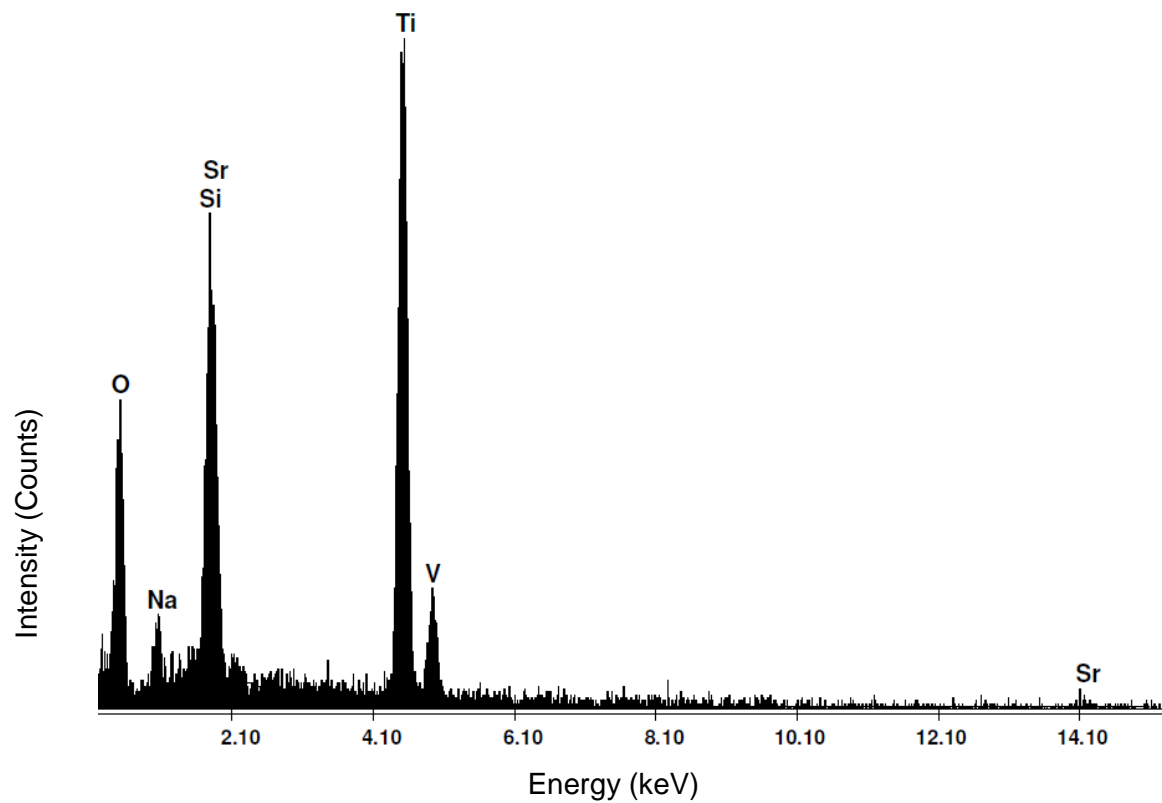


Figure A43: EDX spectrum of 5 %-vanadium-paranatisite-strontium ion exchanged material

A44: XRF Spectra of Ion Exchanged 5 %-Vanadium-Paranatisite

Table A44.a: A list of energies presence within the XRF spectra following cesium, cerium, cobalt, neodymium and strontium ion exchanges.

Element	Energy (keV)	Emission
Cesium	4.41	L _{α1} , L _{α2}
	5.63	L _{β1}
Cerium	4.46	L _{α1} , L _{α2}
	5.87	L _{β2}
	5.20	L _{β1}
Cobalt	6.75	K _{α1} , K _{α2}
	7.45	K _{β1}
Neodymium	4.78	L _{α2}
	5.07	L _{α1}
	5.55	L _{β1}
	6.07	L _{β2}
	6.41	L _{γ1}
Strontium	13.98	K _{α1} , K _{α2}
	15.63	K _{β1}

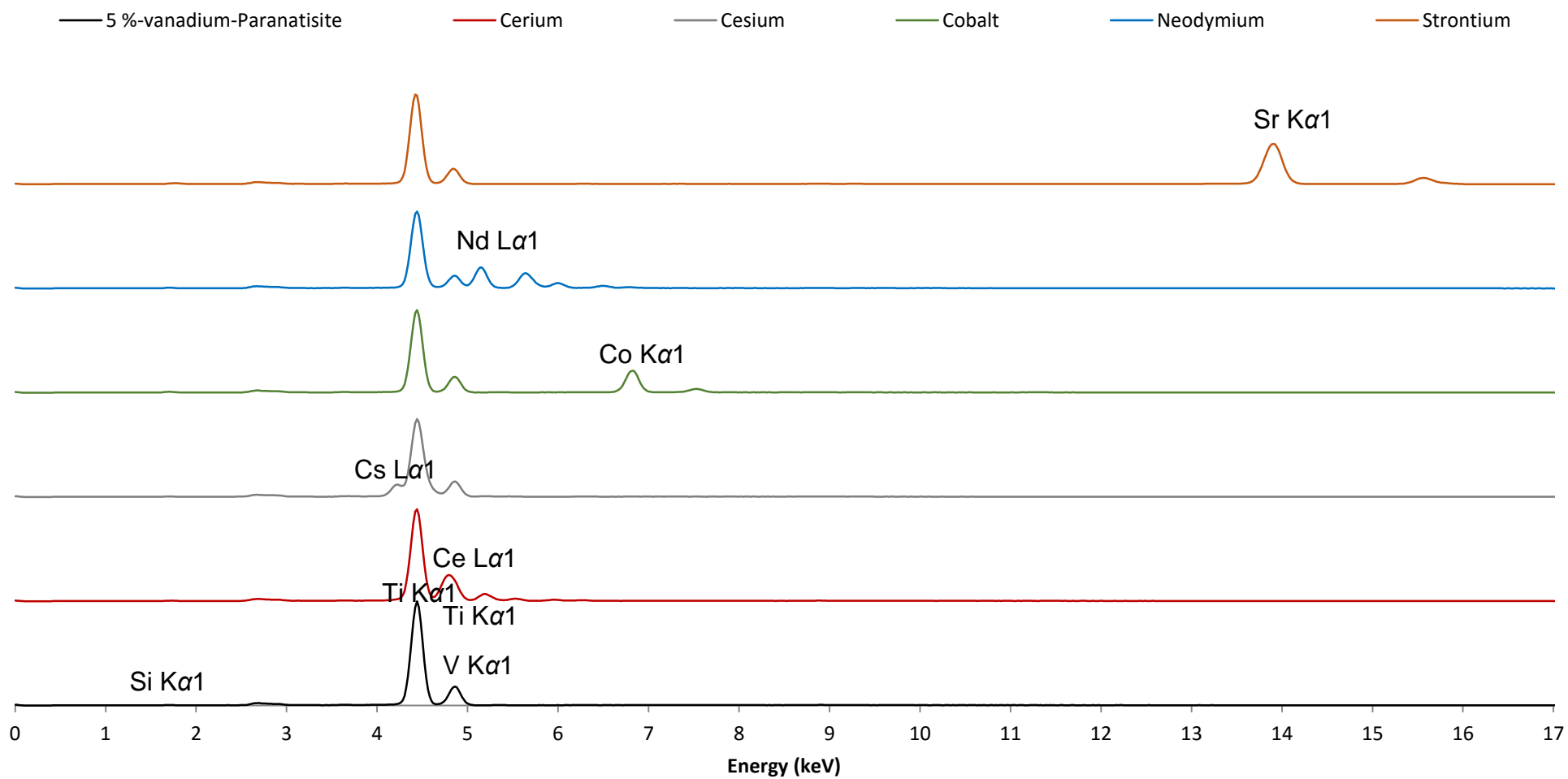


Figure A44.b : Stack view of XRF spectrums collected from 5 %-vanadium-paranatisite, cerium, cesium, cobalt, neodymium and strontium ion exchanged material.

A45: 5 %-Vanadium-Natisite-Cesium Ion Exchanged Material

Table A45.a: Refined lattice parameters and refinement statistics for 10 %-vanadium-natisite-cesium ion exchanged material

Parameter	5 %-Vanadium-Natisite-Cesium Ion Exchanged Material
System	Tetragonal
Space Group	P 4 / n m m
<i>a</i> (Å)	6.4901 (1)
<i>b</i> (Å)	6.4901 (1)
<i>c</i> (Å)	5.0973 (2)
<i>V</i> (Å ³)	214.70 (1)
R _{WP} (%)	9.440
R _P (%)	7.633
R _{exp} (%)	6.939

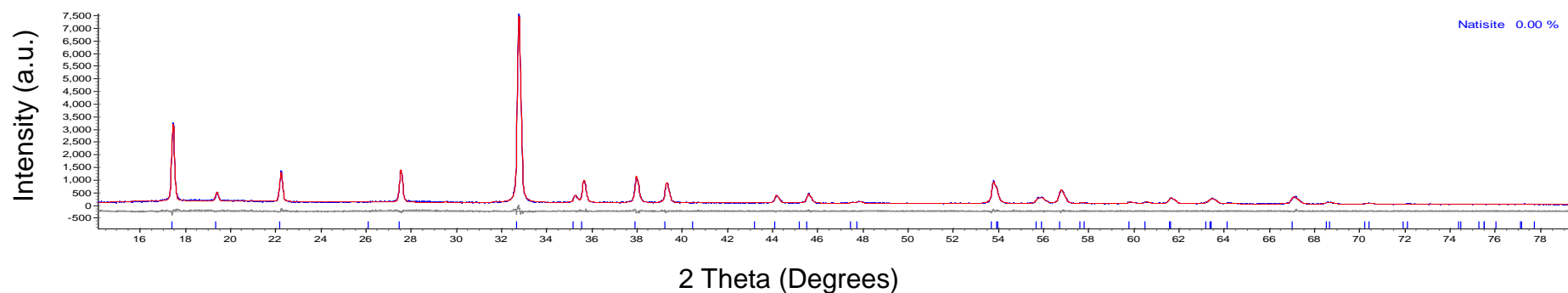


Figure A45.b: Final pawley fit of 5 %-vanadium-natisite-cesium ion exchanged material

A46: 5 %-Vanadium-Natisite-Cerium Ion Exchanged Material

Table A46.a: Refined lattice parameters and refinement statistics for 5 %-vanadium-natisite-cesium ion exchanged material

Parameter	5 %-Vanadium-Natisite-Cerium Ion Exchanged Material
System	Tetragonal
Space Group	P4/nmm
a (Å)	6.508 (3)
b (Å)	6.508 (3)
c (Å)	5.132 (3)
V (Å ³)	217.4 (2)
R _{WP} (%)	10.467
R _P (%)	8.215
R _{exp} (%)	8.290

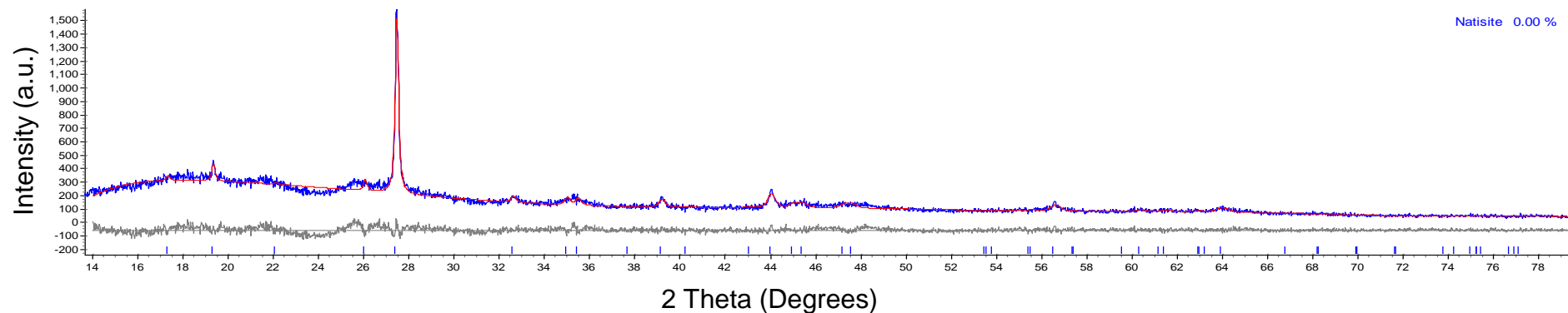


Figure A46.b: Final pawley fit of 5 %-vanadium-natisite-cerium ion exchanged material

A47: 5 %-Vanadium-Natisite-Cobalt Ion Exchanged Material

Table A47.a: Refined lattice parameters and refinement statistics for 5 %-vanadium-natisite-cobalt ion exchanged material

Parameter	5 %-Vanadium-Natisite-Cobalt Ion Exchanged Material
System	Tetragonal
Space Group	P 4 / n m m
a (Å)	6.4925 (4)
b (Å)	6.4925 (4)
c (Å)	5.0927 (4)
V (Å ³)	214.67 (3)
R _{WP} (%)	5.382
R _P (%)	4.593
R _{exp} (%)	4.202

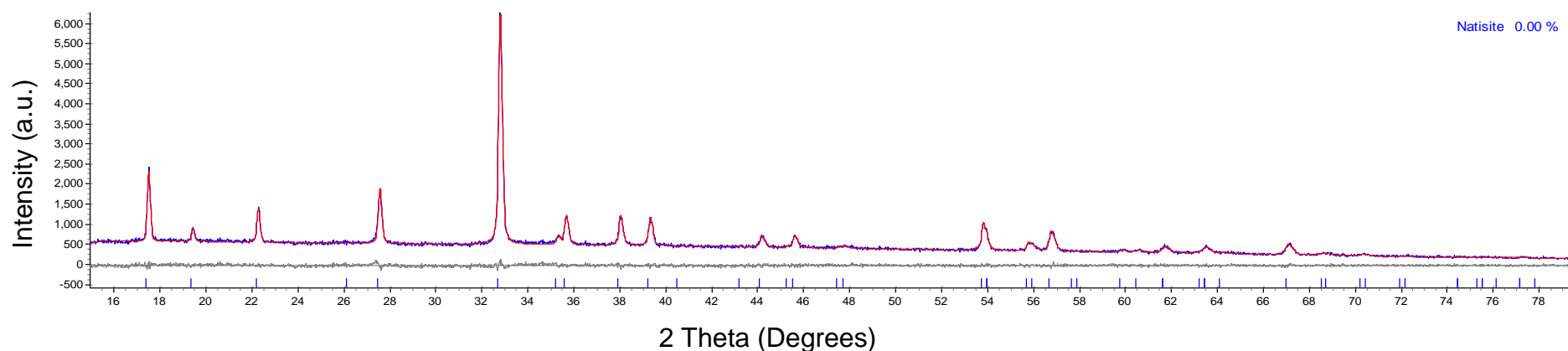


Figure 47.b: Final pawley fit of 5 %-vanadium-natisite-cobalt ion exchanged material

A48: 5 %-Vanadium-Natisite-Strontium Ion Exchanged Material

Table A48.a: Refined lattice parameters and refinement statistics for 5 %-vanadium-natisite-strontium ion exchanged material

Parameter	5 %-Vanadium-Natisite-Strontium Ion Exchanged Material
System	Tetragonal
Space Group	P 4 / n m m
<i>a</i> (Å)	6.4947 (4)
<i>b</i> (Å)	6.4947 (4)
<i>c</i> (Å)	5.0879 (5)
<i>V</i> (Å ³)	214.58 (3)
R _{WP} (%)	10.274
R _P (%)	7.776
R _{exp} (%)	7.947

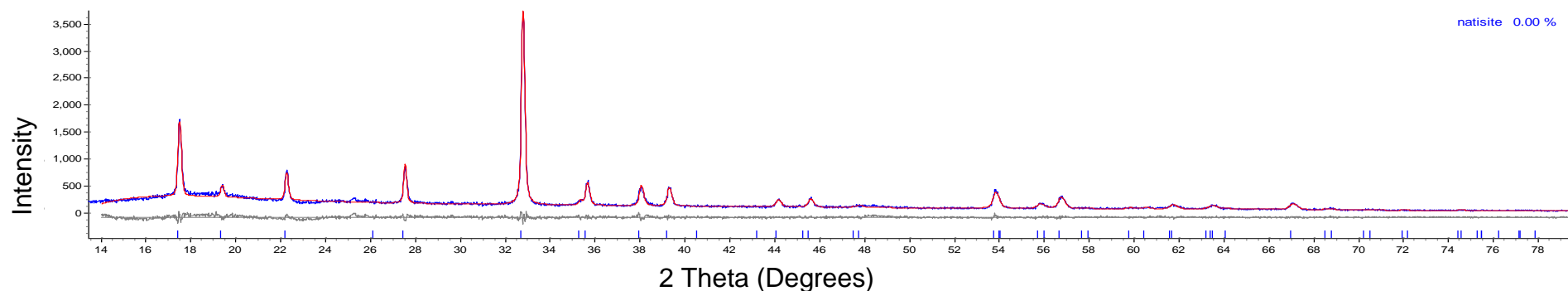


Figure A48.b: Final pawley fit of 5 %-vanadium-natisite-strontium ion exchanged material

A49: 5 %-Vanadium-Natisite-Neodymium Ion Exchanged Material

Table A49.a: Refined lattice parameters and refinement statistics for 5 %-vanadium-natisite-neodymium ion exchanged material

Parameter	5 %-Vanadium-Natisite-Neodymium Ion Exchanged Material
System	Tetragonal
Space Group	P 4 / n m m
a (Å)	6.489 (4)
b (Å)	6.489 (4)
c (Å)	5.094 (4)
V (Å ³)	214.7 (3)
R _{WP} (%)	11.923
R _P (%)	8.464
R _{exp} (%)	9.075

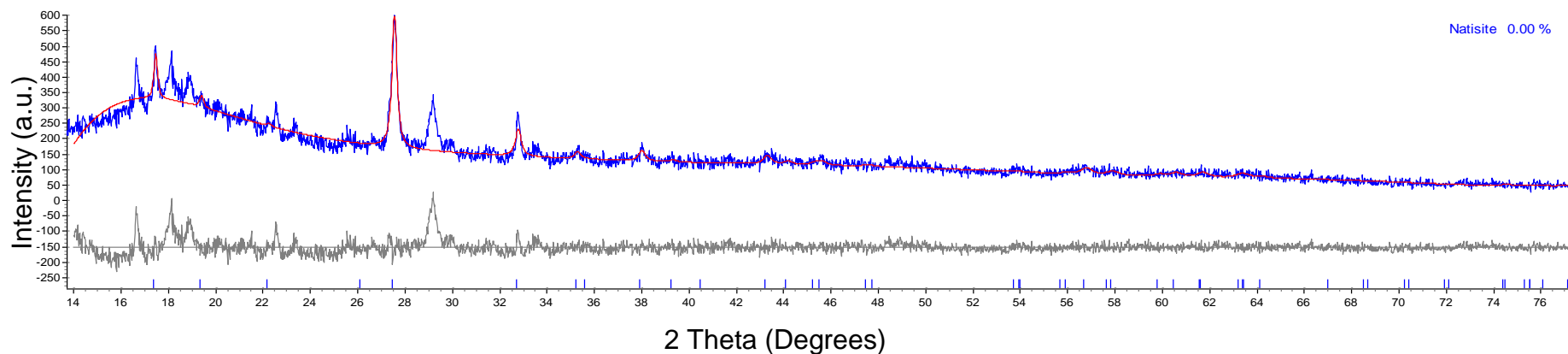


Figure A49.b: Final pawley fit of 5 %-vanadium-natisite-neodymium ion exchanged material

A50: 10 %-Vanadium-Natisite-Cesium Ion Exchanged Material

Table A50.a: Refined lattice parameters and refinement statistics for 10 %-vanadium-natisite-cesium ion exchanged material

Parameter	10 %-Vanadium-Natisite-Cesium Ion Exchanged Material
System	Tetragonal
Space Group	P 4 / n m m
<i>a</i> (Å)	6.4892 (3)
<i>b</i> (Å)	6.4892 (3)
<i>c</i> (Å)	5.0931 (3)
<i>V</i> (Å ³)	214.43 (2)
R _{WP} (%)	10.615
R _P (%)	8.284
R _{exp} (%)	7.895

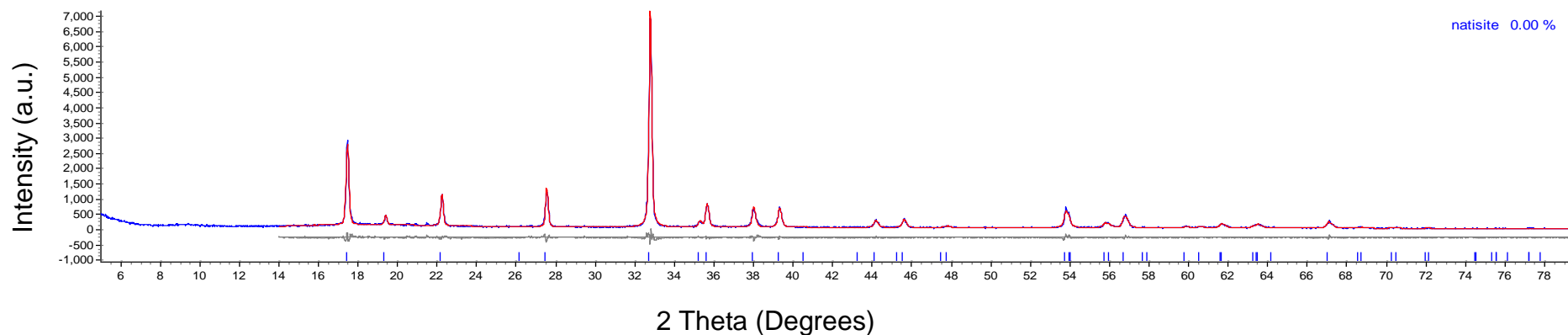


Figure A50.b: Final pawley fit of 10 %-vanadium-natisite-cesium ion exchanged material

A51: 10 %-Vanadium-Natisite-Cerium Ion Exchanged Material

Table A51.a: Refined lattice parameters and refinement statistics for 10 %-vanadium-batisite-cerium ion exchanged material

Parameter	10 %-Vanadium-Natisite-Cerium Ion Exchanged Material
System	Tetragonal
Space Group	P 4 / n m m
a (Å)	6.505 (4)
b (Å)	6.505 (4)
c (Å)	5.132 (4)
V (Å ³)	217.0 (3)
R _{WP} (%)	10.948
R _P (%)	9.453
R _{exp} (%)	8.757

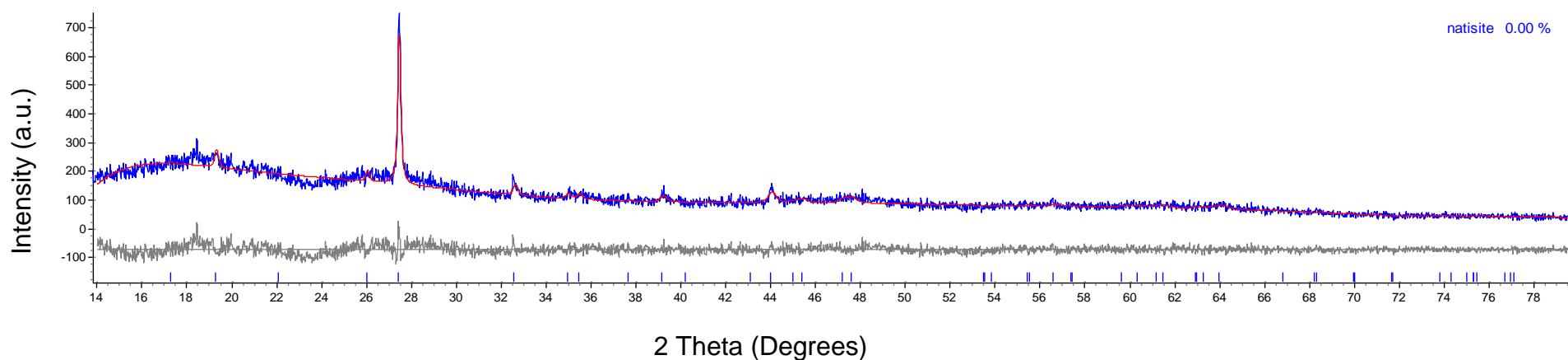


Figure A51.b: Final pawley fit of 10 %-vanadium-natisite-cerium ion exchanged material

A52: 10 %-Vanadium-Natisite-Cobalt Ion Exchanged Material

Table A52.a: Refined lattice parameters and refinement statistics for 10 %-vanadium-natisite-cobalt ion exchanged material

Parameter	10 %-Vanadium-Natisite-Cobalt Ion Exchanged Material
System	Tetragonal
Space Group	P 4 / n m m
a (Å)	6.51 (2)
b (Å)	6.51 (2)
c (Å)	5.07 (1)
V (Å ³)	213.94 (6)
R _{WP} (%)	4.477
R _P (%)	4.010
R _{exp} (%)	3.990

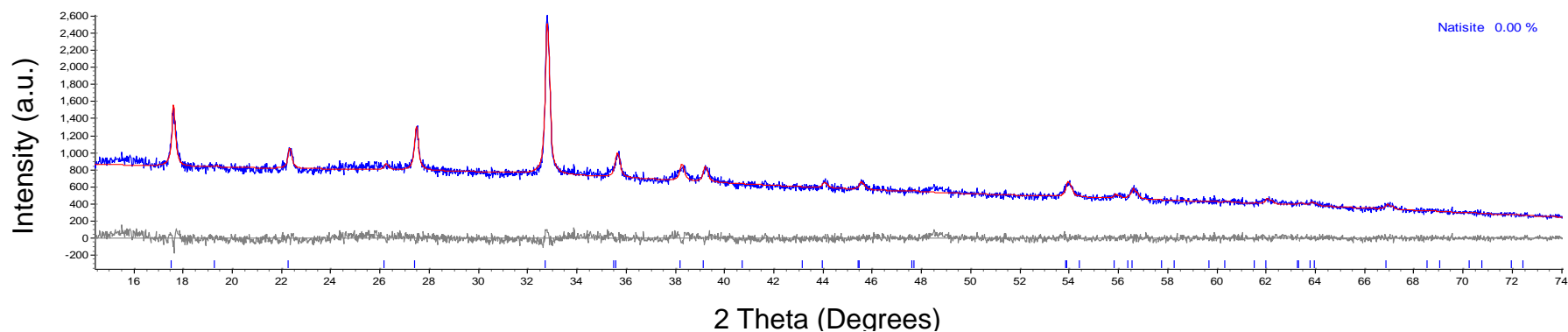


Figure A52.b: Final pawley fit of 10 %-vanadium-natisite-cobalt ion exchanged material

A53: 10 %-Vanadium-Natisite-Strontium Ion Exchanged Material

Table A53.a: Refined lattice parameters and refinement statistics for 10 %-vanadium-natisite-strontium ion exchanged material

Parameter	10 %-Vanadium-Natisite-Strontium Ion Exchanged Material
System	Tetragonal
Space Group	P 4 / n m m
<i>a</i> (Å)	6.4899 (3)
<i>b</i> (Å)	6.4899 (3)
<i>c</i> (Å)	5.0933 (4)
<i>V</i> (Å ³)	214.52 (2)
R _{WP} (%)	10.927
R _P (%)	9.388
R _{exp} (%)	8.290

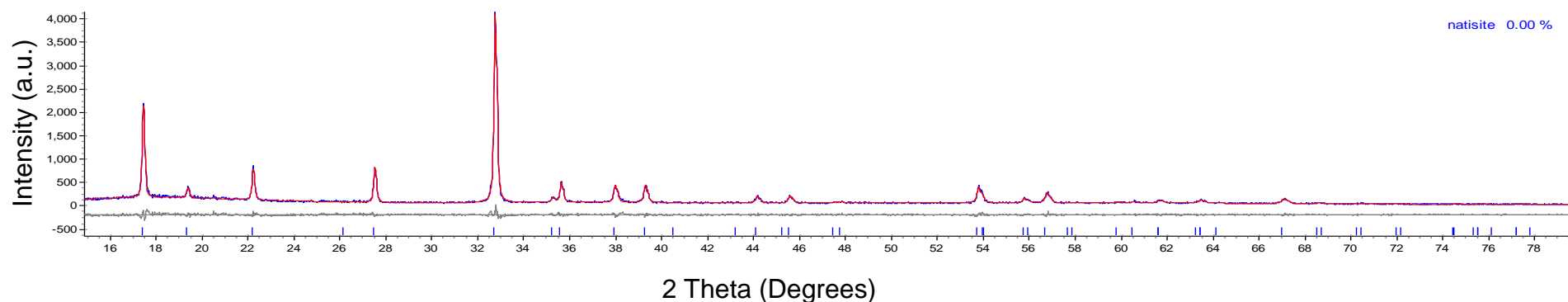


Figure A53.b: Final pawley fit of 10 %-vanadium-natisite-strontium ion exchanged material

A54: 10 %-Vanadium-Natisite-Neodymium Ion Exchanged Material

Table A54.a: Refined lattice parameters and refinement statistics for 10 %-vanadium-natisite-neodymium ion exchanged material

Parameter	10 %-Vanadium-Natisite-Neodymium Ion Exchanged Material
System	Tetragonal
Space Group	P4/nmm
<i>a</i> (Å)	6.493 (3)
<i>b</i> (Å)	6.493 (3)
<i>c</i> (Å)	5.063 (3)
<i>V</i> (Å ³)	213.4 (3)
R _{WP} (%)	7.119
R _P (%)	6.258
R _{exp} (%)	5.649

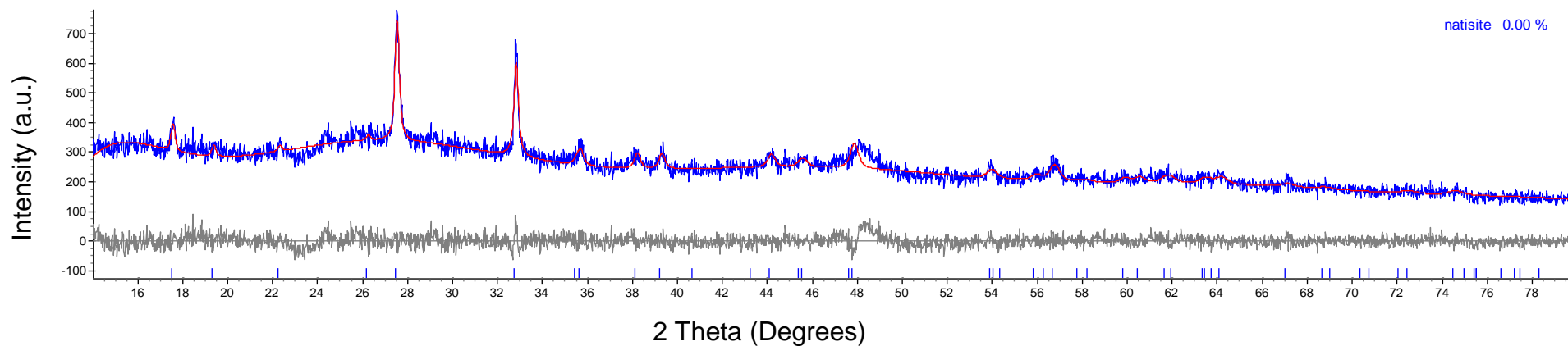


Figure A54.b: Final pawley fit of 10 %-vanadium-natisite-neodymium ion exchanged material

A55: EDX Spectrum of 5 %-Vanadium-Natisite-Cesium Ion Exchanged Material

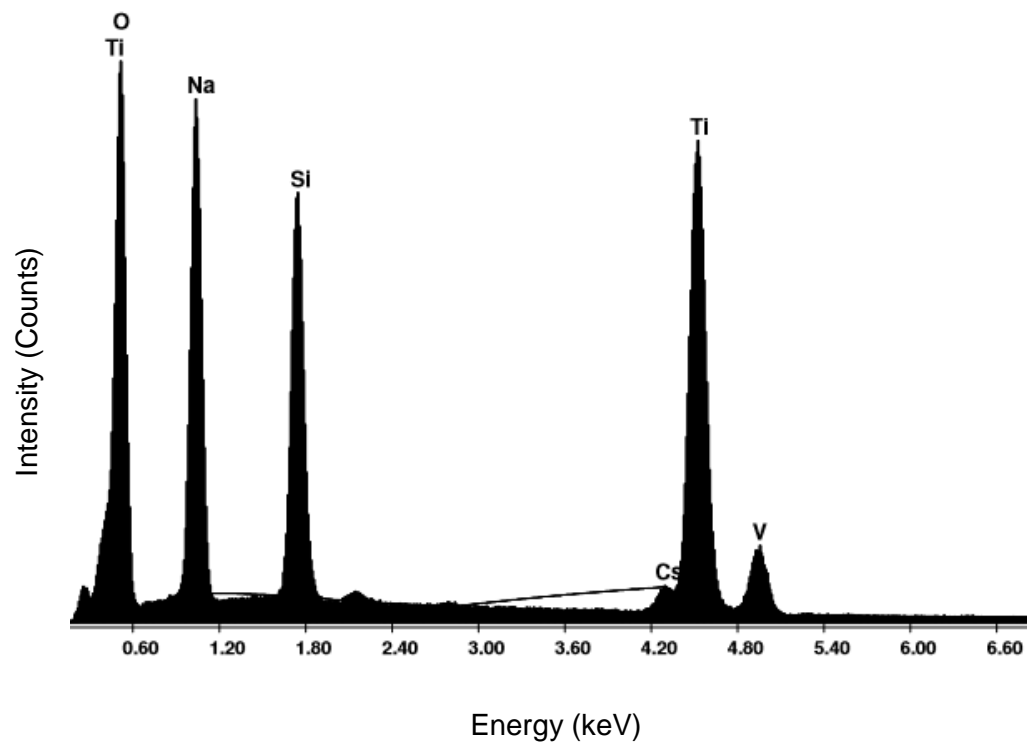


Figure A55: EDX spectrum of 5 %-vanadium-paranatisite-cesium ion exchanged material

A56: EDX Spectrum of 5 %-Vanadium-Natisite-Cerium Ion Exchanged Material

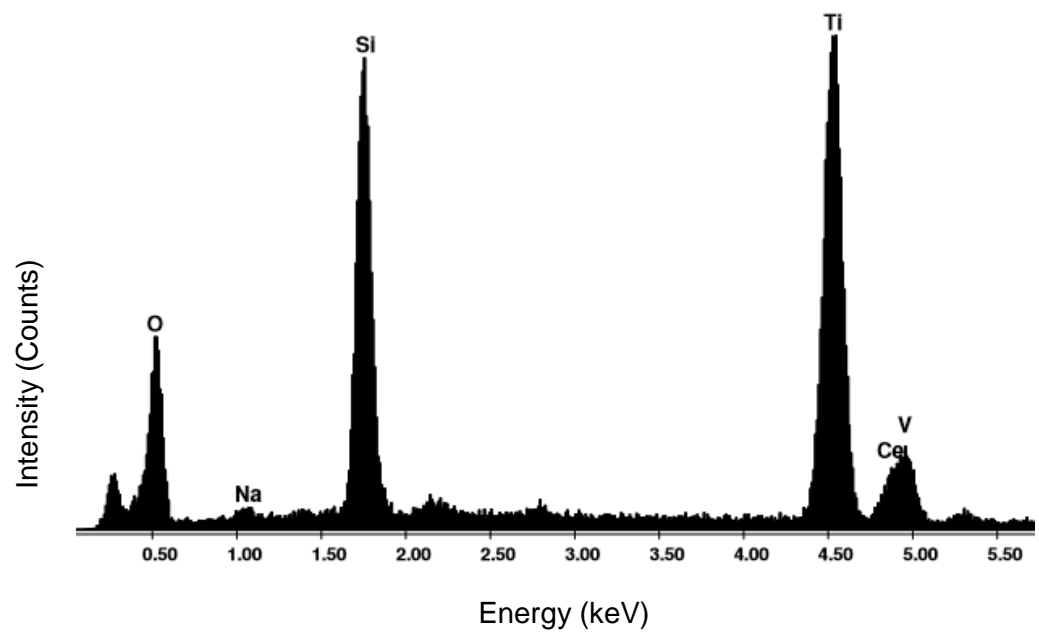


Figure A56: EDX spectrum of 5 %-vanadium-paranatisite-cerium ion exchanged material

A57: EDX Spectrum of 5 %-Vanadium-Natisite-Cobalt Ion Exchanged Data

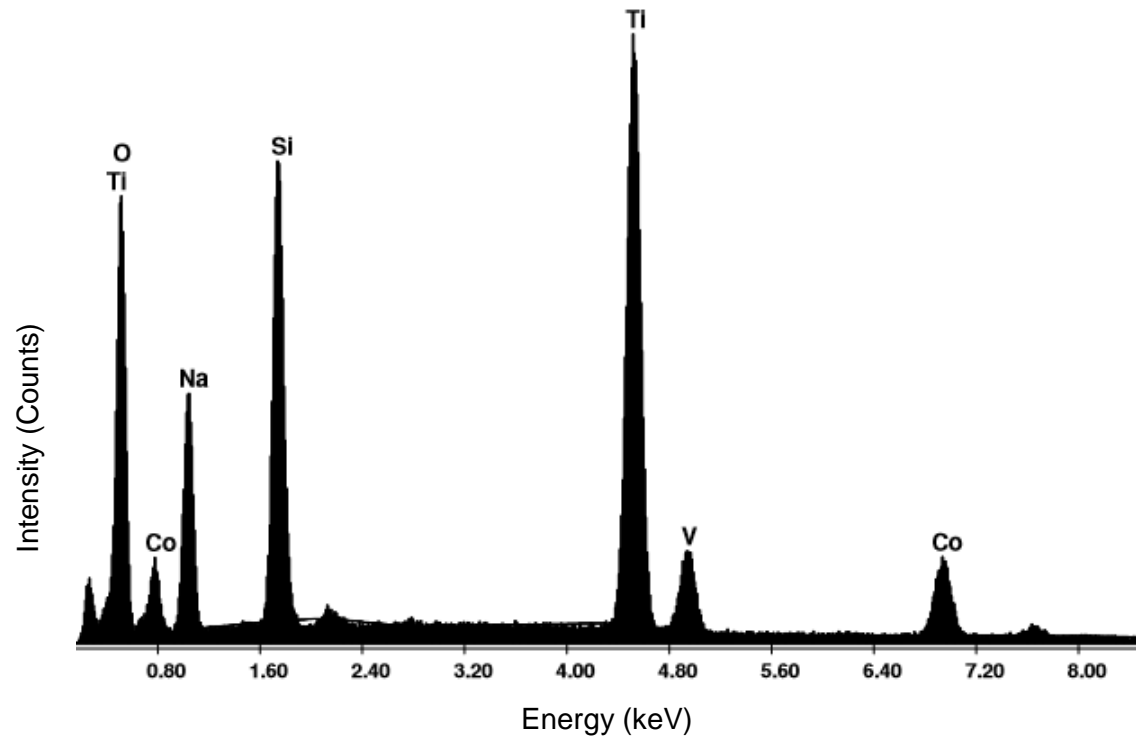


Figure A57: EDX spectrum of 5 %-vanadium-paranatisite-cobalt ion exchanged data

A58: EDX Spectrum of 5 %-Vanadium-Natisite-Strontium Ion Exchanged Material

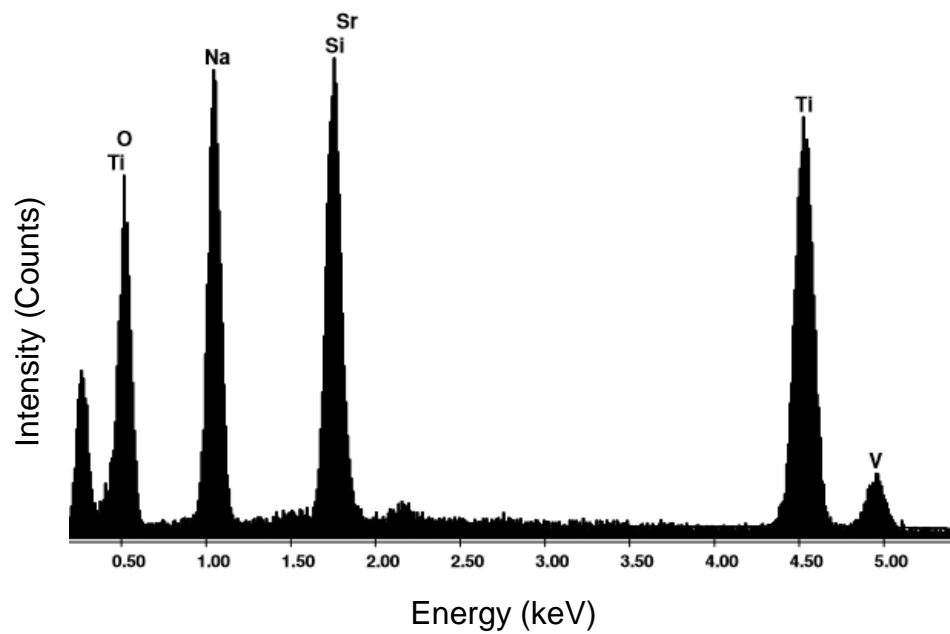


Figure A58: EDX spectrum of 5 %-vanadium-paranatisite-strontium ion exchanged material

A59: EDX Spectrum of 5 %-Vanadium-Natisite-Neodymium Ion Exchanged Material

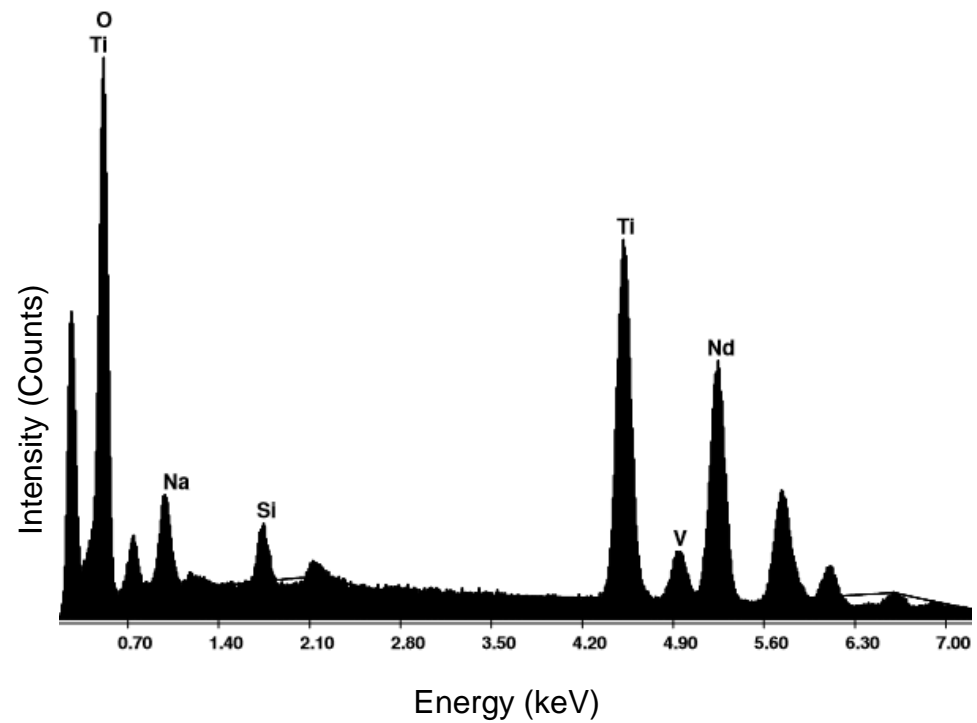


Figure A59: EDX spectrum of 5 %-vanadium-paranatisite-neodymium ion exchanged material

A60: XRF Spectrum of Ion Exchanged 5 %-Vanadium-Natisite

Table A60.a: A list of energies presence within the XRF spectra following cesium, cerium, cobalt, neodymium and strontium ion exchanges

Element	Energy (keV)	Emission
Cesium	4.41	L _{α1} , L _{α2}
	5.63	L _{β1}
Cerium	4.20	L _{α1} , L _{α2}
	5.58	L _{β2}
	5.26	L _{β1}
Cobalt	6.87	K _{α1} , K _{α2}
	7.59	K _{β1}
Neodymium	4.91	L _{α2}
	5.19	L _{α1}
	5.71	L _{β1}
	6.11	L _{β2}
	6.41	L _{γ1}
Strontium	13.98	K _{α1} , K _{α2}
	15.63	K _{β1}

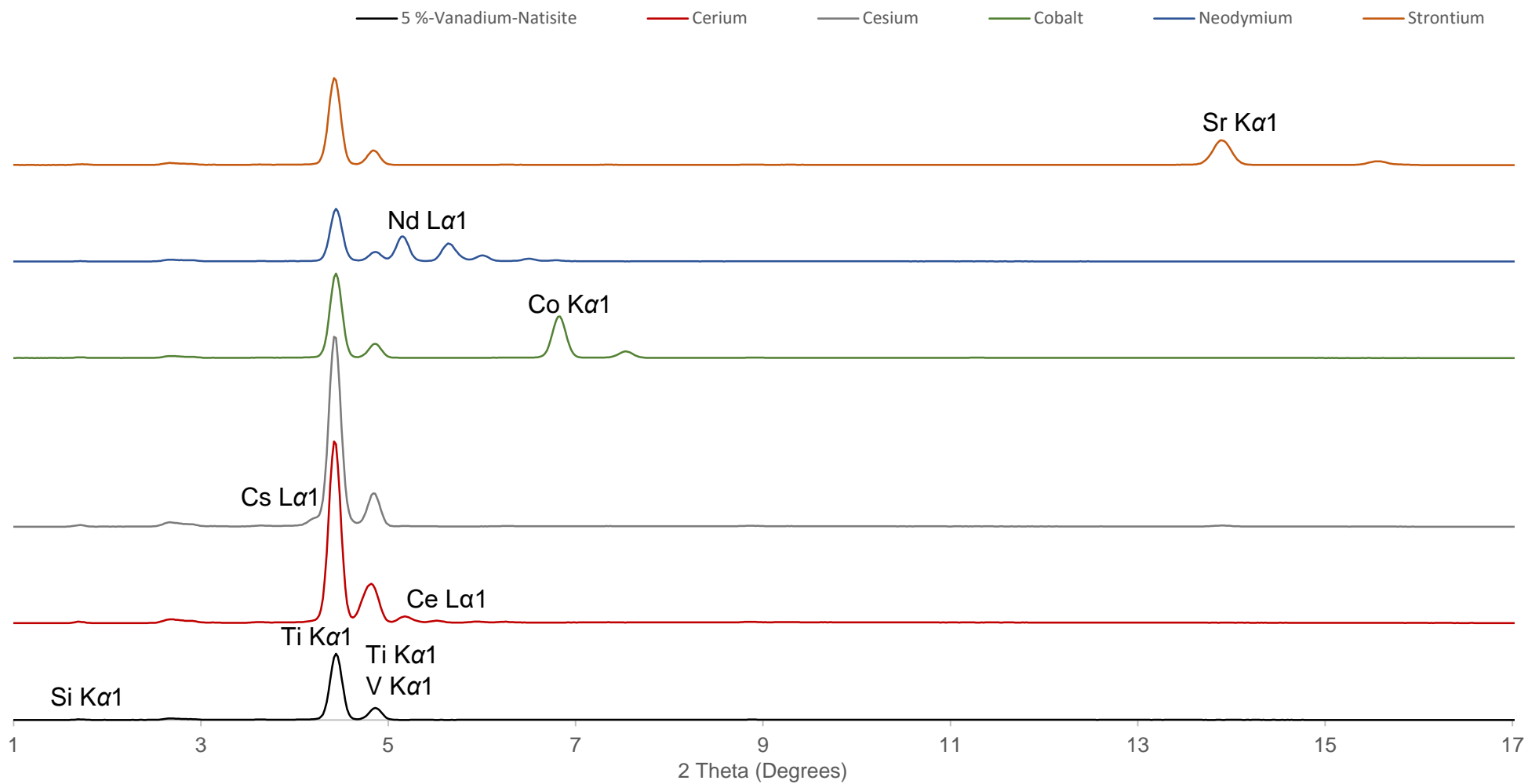


Figure A60.b: Stack view of XRF spectrums collected from 5 %-vanadium-natisite, cerium, cesium, cobalt, neodymium and strontium ion exchanged material.